To İhsan…

MICROBIAL AMYLOIDS AS FUNCTIONAL BIOMATERIALS

A DISSERTATION SUBMITTED TO

THE GRADUATE SCHOOL OF ENGINEERING AND SCIENCE

OF BILKENT UNIVERSITY

IN PARTIAL FULFILLMENT OF THE REQUIREMENTS FOR

THE DEGREE OF

DOCTOR OF PHILOSOPHY

IN

MATERIALS SCIENCE AND NANOTECHNOLOGY

By

EBRU ŞAHİN KEHRİBAR

JANUARY 2021

ABSTRACT

MICROBIAL AMYLOIDS AS FUNCTIONAL BIOMATERIALS

Ebru ŞAHİN KEHRİBAR

PhD in Materials Science and Nanotechnology

Advisor: Urartu Özgür Şafak Şeker

January, 2021

Amyloids are fibrillar aggregations of proteins, dominated by β-sheets in the structure. Although amyloids are historically associated with disorders, they emerged as outstanding biomaterials due to their high mechanical strength and rigidity that provides resistance to physical and chemical stress. Also, amyloids can easily be functionalized with peptide groups using genetic engineering approaches. Ease of functionalization in addition to aforementioned properties makes amyloid fibers excellent candidates for biomaterials with desired characteristics.

In this thesis, we focused on recombinant production, characterization and functionalization of several amyloid proteins from different microorganisms. Binding behavior of amyloid fibrils on medically relevant surfaces are critical for controlling the coating characteristics and desired surface properties of biomaterials. For this reason, we firstly characterized the binding kinetics of CsgA and CsgB curli proteins on silica, gold and hydroxyapatite surfaces to precisely control their surface adhesion. According to the physicochemical properties of surfaces, CsgA, CsgB and

their mixture displayed different binding behavior. Furthermore, functionalization of amyloid fibers to enhance their binding kinetics to surfaces and to organisms may hold great potentials for biomaterial applications. From this perspective, we hypothesized that glycosylation could enhance surface adhesiveness of curli fibers. For this purpose, TasA protein is engineered to obtain a glycosylation site and TasA fibers depicted an increased adhesiveness to gold surfaces upon glycosylation. Finally, we functionalized CsgA curli fibers with RGD peptide to increase adhesiveness to living cells. RGD peptide addition caused a significant increase in the adhesiveness of mammalian cells onto coated surfaces.

In conclusion, amyloid proteins can serve as superior biomaterials with desired functions and characteristics. Physicochemical properties of surfaces and proteins can have essential impacts on their interaction. In order to diversify those properties, amyloid fibers can be functionalized for specific purposes such as improved surface and cell adhesion. Characterization of protein/surface interactions for amyloid proteins provides important clues for optimal biomaterial surface design and functionalization with different peptide groups can extend their application capacity as superior biomaterials.

Keywords: amyloid, curli protein, biofilm, surface adhesion, cell adhesion

ÖZET

MİKROBİYAL AMİLOİTLERİN FONKSİYONEL BİYOMALZEME OLARAK KULLANILMASI

Ebru ŞAHİN KEHRİBAR

Malzeme Bilimi ve Nanoteknoloji, Doktora

Tez Danışmanı: Urartu Özgür Şafak Şeker

Ocak, 2021

Amiloitler, β yaprak yapıları açısından zengin, iplik yapısındaki protein agregasyonlarıdır. Yüksek mekanik güce ve rijitliğe sahip olmaları, amiloitlere fiziksel ve kimyasal stres etmenlerine karşı dayanıklılık sağlamaktadır. Ayrıca, arzu edilen uygulamalara özel olarak, amiloitler peptit gruplarının eklenmesiyle fonksiyonelleştirilebilirler. Bu özellikleri nedeniyle amiloitler biyomalzeme uygulamalarında kullanılmak için oldukça iyi adaylardır.

Körli tabanlı amiloitlerin medikal uygulamalarda kullanılan yüzeylere bağlanma davranışları, kontrol edilebilir biyomalzemeler olarak kullanılabilmeleri bakımından oldukça önemlidir. Ek olarak, körli ipliklerinin yüzeylere ve organizmalara bağlanma kinetiklerinin iyileştirilmesi için peptit grupları ile fonksiyonelleştirilmesi, istenen özelliklere sahip olan biyomalzemeler geliştirilmesi için de oldukça yüksek potansiyele sahiptir.

Bu tezde, CsgA ve CsgB körli proteinlerinin silika, altın ve hidroksiapatit yüzeylere yapışmalarının yüksek hassasiyetle kontrol edilebilmesi için, bu proteinlerin bahsi geçen yüzeylere bağlanma kinetikleri karakterize edilmiştir. Yüzeylerin fizikokimyasal özelliklerine bağlı olarak, CsgA ve CsgB proteinlerinin farklı bağlanma davranışları sergiledikleri gösterilmiştir. İkinci olarak, glikozilasyonun körli ipliklerinin yüzeylere bağlanma eğilimin artıracağı hipotezi test edilmiştir. Bu amaçla, TasA proteini bir glikozilasyon noktası içerecek şekilde fonksiyonelleştirilmiştir ve glikozilasyonun TasA ipliklerinin altın yüzeylere olan bağlanma eğilimini artırdığı gösterilmiştir. Son olarak, CsgA körli ipliklerinin canlı hücrelere bağlanma eğilimi artırmak için, CsgA proteini RGD peptidi içerecek şekilde değiştirilmiştir. Sonuçlar, RGD peptidi eklenmesinin, körli ile kaplanmış yüzeylere bağlanan hücre sayısını anlamlı bir şekilde artırdığını göstermiştir. Sonuç olarak, amiloit proteinleri istenen fonksiyonlara sahip olabilen üstün nitelikli biyomalzemeler olarak kullanılabilir. Yüzeylerin ve proteinlerin fizikokimyasal özellikleri, birbirleri ile olan etkileşimleri üzerinde hayati etkilere sahip olabilir. Sahip oldukları özelliklerin çeşitlendirebilmesi için, amiloit iplikler kolaylıkla modifiye edilebilirler. Çeşitli peptit grupları ile fonksiyonelleştirilerek uygulama kapasiteleri artırılan amiloitler üstün özelliklere sahip biyomalzemeler olarak kullanılma kapasitesine sahiptir.

Anahtar kelimeler: amiloit, körli proteini, biyofilm, yüzey bağlanması, hücre bağlanması

ACKNOWLEDGEMENTS

I would like to start by expressing my gratitude to my advisor Dr. Urartu Özgür Şafak Şeker. Ph.D. is a road full of challenges. In this road, he was a true mentor. He was kind, supportive and always guiding us for better. I am lucky to learn from his research experience and complete my Ph.D. with him.

Next, I thank to my thesis tracking committee members Dr. Özlen Konu Karakayalı and Dr. Sreeperna Banerjee for their valuable advices and helpful discussions during our thesis tracking meetings. Also, I would like to thank to Dr. Bora Garipcan and Dr. Halil İbrahim Okur for being jury members of my thesis defense. Lastly, I thank to all UNAM members.

During my research, I obtained valuable help to shape my ideas, to troubleshoot and to conduct my experiments. I thank to Esra Yuca, Musa Efe Isilak and Eray Ulas Bozkurt for their valuable contributions to this project. I especially thank Esra Yuca for her support and guidance. I also thank Recep Erdem Ahan for always sharing his ideas to move my research forward and to troubleshoot my problems. I thank Dr. Raffaele Mezzenga and Dr. Jozef Adamcik for their kind help in AFM experiments.

Six years is a long time, and I am lucky to have valuable friends during this time. I enjoyed the yoga classes and lunch breaks with Elif Duman, Tugce Onur and Zelal Yavuz. It was interesting to work with Musa Efe Işılak thanks to his extraordinary character. I thank him for his friendship and for our fun chats, sometimes on really serious topics. I thank İlkay Çisil Köksaldı for her supportive friendship and kindness. I enjoyed our chats and our plans for trips, trekking adventures and all kind of activities, even though we could not fulfill them all. I thank to Behide Saltepe and Recep Erdem Ahan for enjoyable coffee breaks and fruitful academic and intellectual conversations. I thank all present and former SBL members; Ahmet Hınçer,

Anooshay Khan, Aslıhan Gökaltun, Büşra Merve Kırpat, Cemile Elif Özçelik, Ebru Aras, Ebuzer Kalyoncu, Gökçe Özkul, Julian Ostaku, Merve Erden Tüçer, Merve Yavuz, Murat Alp Güngen, Nedim Hacıosmanoğlu, Onur Apaydın, Özge Beğli, Sıla Köse, Side Selin Su Yirmibeşoğlu and Tolga Tarkan Ölmez. It was a privilege to work in this productive, supportive and friendly environment.

Last year, we went through very unusual days in the middle of a global pandemic. Even though we had very hard times, we used this pandemic to move our research one step further. I enjoyed working with Çisil, Eray and Recep, making those times endurable and even enjoyable. It was fun, productive and informative. I learnt a lot from them. I thank them for their friendship and support in those dark days.

It is important to have friends that you can share your sorrow as well as your joy. I am lucky to have friendships that do not fade away with distances. I thank my friends Büşra, Hale, Merve and Nesrin for being there for all those years. Having them as my friends during this journey enlightened my days.

Last but not least, I want to express my deep gratitude to my mother Nurten, my father Ruhi and my brother Talha, for their encouragement, support and unrequited love. They supported my decisions and let me go after my dreams. In the dark days, we were always there for each other. In happiness, we celebrated together. I owe my biggest thanks to İhsan. He is my partner in life, my best friend, my dearest supporter. It is valuable to have people supporting you, but to have someone to show you your mistakes is equally important. I thank İhsan for his support, his constructive criticism, his valuable advices about academics and life, his understanding, his encouragement and his endless love. My life would never be the same without him.

This study was supported by TÜBİTAK Project Number 114M163, 216M127 and 119M037.

TABLE OF CONTENTS

1 CHAPTER I

INTRODUCTION 1

1.1 Amyloids 1

1.2 Amyloid formation 3

1.3 Functional amyloids and biofilms 5

1.3.1 Escherichia coli 5

1.3.2 Bacillus subtilis 9

1.3.3 Pseudomonas aeruginosa 11

1.4 Amyloids for biomaterial applications 15

1.5 Protein glycosylation 16

2 CHAPTER II

INTERACTION OF MICROBIAL FUNCTIONAL AMYLOIDS WITH SOLID SURFACES 19

2.1 Introduction 20

2.2 Objective 22

2.3 Materials and Methods 23

2.3.1 Cell strains and cell maintenance 23

2.3.2 Construction of plasmids and transformation 24

2.3.3 Sequence alignments 26

2.3.4 Expression of recombinant proteins in E. coli 26

2.3.5 Purification of recombinant proteins 27

2.3.6 SDS-PAGE and Western Blot 28

2.3.7 Fiber formation and transmission electron microscopy (TEM) 29

2.3.8 Dynamic Light Scattering 30

2.3.9 Circular dichroism (CD) 31

2.3.10 Quartz Crystal Microbalance with Dissipation (QCM-D) 31

2.4 Results and Discussion 33

2.4.1 Cloning, expression and purification 33

2.4.2 Characterization of curli fibers 36

2.4.3 Secondary structure analysis 38

2.4.4 Real-time monitoring of nanofiber assembly with Quartz Crystal Microbalance with Dissipation (QCM-D) 39

2.5 Conclusion 48
3 CHAPTER III
GLYCOSYLATED BIOFILM PROTEINS FOR FUNCTIONAL BIOMATERIALS 50
3.1 Introduction 50
3.2 Objective 51
3.3 Materials and Methods 52
3.3.1 Bacterial strains and cell maintenance 52
3.3.2 Mammalian Cell Lines 53
3.3.3 Plasmid construction 53
3.3.4 Expression and purification of non-glycosylated and glycosylated recombinant proteins in E. coli 54
3.3.5 SDS-PAGE and Western Blot 55
3.3.6 Detection of glycosylation by soybean agglutinin (SBA) blot 56
3.3.7 Fiber formation and scanning transmission electron microscopy (STEM). 57
3.3.8 Fiber characterization by atomic force microscopy (AFM) 57
3.3.9 Secondary Structure Analysis by Circular Dichroism (CD) 58
3.3.10 Quartz Crystal Microbalance (QCM) 58
3.3.11 Cell adhesion 59
3.4 RESULTS AND DISCUSSION 60
3.4.1 Cloning, expression and purification 60
3.4.2 Glycosylation of TasA by SBA blot 67
3.4.3 Effect of glycosylation on secondary structure: CD analysis 68
3.4.4 Analysis of fibrillization and fibril morphology by STEM and AFM ... 71
3.4.5 Analysis of adsorption kinetic and viscoelastic properties with QCM-D……. 76
3.4.6 Effect of glycosylation on cell adhesion 85
3.5 Conclusion 88
4 CHAPTER IV
RGD FUNCTIONALIZED AMYLOIDS AS BIOMATERIALS WITH ENHANCED CELL ADHESION CAPACITY 91
4.1 Introduction 91
4.2 Objective 92
4.3 Materials and Methods 93

4.3.1 Bacterial strains and cell maintenance 93
4.3.2 Mammalian cell lines 93
4.3.3 Plasmid construction 93
4.3.4 Expression and purification of non-functionalized and functionalized biofilm proteins 97
4.3.5 Extracellular expression of biofilm proteins 98
4.3.6 SDS PAGE and Western Blot 99
4.3.7 Crystal violet (CV) and congo red (CR) staining 100
4.3.8 Immunocytochemistry (ICC) 101
4.3.9 Biofilm Formation verification by SEM and TEM 102
4.3.10 Surface coating verification by SEM and TEM 102
4.3.11 Cell adhesion 103
4.4 Results and Discussion 104
4.4.1 Cloning, expression and purification of functionalized proteins 105
4.4.2 Characterization of fibers by SEM and TEM 107
4.4.3 Cell adhesion on coated surfaces 109
4.4.4 Cloning and expression of secreted biofilm proteins 110
4.4.5 Cloning and expression of His-tagged secreted biofilm proteins 117
4.4.6 Verification of biofilm formation by TEM and ICC 121
4.4.7 Cloning and expression of functionalized biofilms as fibers 127
4.4.8 Verification of fiber purification 129
4.4.9 Cell adhesion on purified fibers 130
4.5 Conclusion 131
5 CHAPTER V 133
CONCLUSION 133
6 BIBLIOGRAPHY 138
7 APPENDIX A 150
DNA SEQUENCES OF GENES AND GENE FRAGMENTS 150
8 APPENDIX B 168
LIST OF PRIMERS 168
9 APPENDIX C 175
PLASMID MAPS 175
10 APPENDIX D 185
SANGER SEQUENCING RESULTS 185

11 APPENDIX E 195
AMINO ACID SEQUENCES OF PROTEINS 195
12 APPENDIX F 202
REACTION CONDITIONS 202
13 APPENDIX G 204
ADDITIONAL RESULTS 204

LIST OF TABLES

Table A.1. Nucleotide sequences of *csgA* and *csgB* genes. 150
Table A.2. Nucleotide sequences of *tasA* and *tasA-DQNAT* genes 152
Table A.3. Nucleotide sequences of *csgA-RGD* and *csgB-RGD* genes 154
Table A.4. Nucleotide sequences of *tasA, tapA, csgA* and *csgB* genes with N42 signal sequence 156
Table A.5. Nucleotide sequences of *tasA, tapA, csgA*, *csgB, fapC* and *fapB* genes with N42 signal sequence and N-terminal 6X His tag. 160
Table A.6. Nucleotide sequences of *csgA* genes with N42 signal sequence, RGD peptide tag and N-terminal 6X His tag. 166
Table B.1. Nucleotide sequences of primers used in cloning of *csgA* and *cgsB* genes into pEt22b. 168
Table B.2. Nucleotide sequences of primers used in *tasA* and *tasA DQNAT* genes into pEt22b (+). 169
Table B.3. Nucleotide sequences of primers used in cloning of *csgA-RGD* and *csgB-RGD* genes into pET22b (+) vector. 170
Table B.4. Nucleotide sequences of primers used in cloning of *csgA*, *cgsB, tasA* and *tapA* genes with N42 signal sequence into pZa pBAD vector. 171
Table B.5. Nucleotide sequences of primers used in cloning of *csgA*, *cgsB, tasA, tapA, fapC* and *fapB* genes with N42 signal sequence and with C terminal 6X His tag into pZa pBAD vector. 173
Table B.6. Nucleotide sequences of primers used in cloning of *csgA and cgsA RGD* genes with N42 signal sequence and with C terminal 6X His tag into pZa atc vector. 174
Table E.1. Amino acid sequences of proteins used in Chapter 2. 195
TableE.2. TasA Amino acid sequences of proteins used in Chapter 3. 196
Table E.3. Amino acid sequences of proteins used in Chapter 4. 197
Table F.1. PCR reaction setup of Q5 DNA Polymerase 202
Table F.2. PCR conditions of Q5 DNA Polymerase 202
Table F.3. Restriction digestion reaction setup with NEB restriction enzymes 203
Table F.4. T4 (NEB) ligation reaction setup 203

Table G.1. Dynamic light scattering analysis of CsgA protein at different concentrations and at different maturation times. 204
Table G.2. Dynamic light scattering analysis of CsgB protein at different concentrations and at different maturation times 205
Table G.3. Desorption constant (k_d) of matured TasA, TasA D and TasA DP samples 208
Table G.4. Gibbs free energy (ΔG^o) calculations of matured TasA, TasA D and TasA DP samples 208

LIST OF FIGURES

Figure 1. Schematic of amyloid formation. 3
Figure 2. Structure of amyloids. 4
Figure 3. Schematic diagram of curli secretion system. 7
Figure 4. Schematic of molecular details if CsgA and CsgB. 8
Figure 5. Schematic diagram of fap secretion system. 14
Figure 6. Amyloids as biomaterials for several applications. 16
Figure 7. Schematic representation of N-linked glycosylation pathway in C. jejuni 18
Figure 8. Schematic diagram of CsgA and CsgB expression cassette. 33
Figure 9. Amplification of *csgA* and *csgB* genes from bacterial genomic DNA 34
Figure 10. Agarose gel electrophoresis of pEt22b(+) plasmid digestion. 35
Figure 11. Purification of CsgA and CsgB by IMAC 36
Figure 12. TEM analysis of CsgA and CsgB fibers 38
Figure 13. CD spectrum measurement for secondary structure analysis. 39
Figure 14. QCM measurement of 2 days old CsgA fibers 41
Figure 15. QCM measurement of 2 days old CsgB fibers. 42
Figure 16. QCM measurement of 2 days old CsgA-CsgB mix fibers 43
Figure 17. Binding free energy of polymerized CsgA, CsgB and CsgA-CsgB mix on gold, silica and HA. 48
Figure 18. A schematic representation of glycosylation effecting gold binding affinity and viscoelastic properties of TasA fibrils. 61
Figure 19. Schematic diagram of TasA and TasA DQNAT expression cassette 62
Figure 20. Cloning of *tasA* gene to pEt22b (+) plasmid. 63
Figure 21. Cloning of *tasA* gene to pEt22b DQNAT plasmid. 64
Figure 22. Verification of pEt22b TasA and pEt22b TasA DQNAT constructs 65
Figure 23. Western Blot and SDS-PAGE of TasA, TasA D and TasA DP samples . 67
Figure 24. SBA Blot of TasA D and TasA DP samples 68
Figure 25. Secondary structure analysis of TasA, TasA D and TasA DP samples 69
Figure 26. Circular dichroism spectra and percentages of secondary structures calculated by BestSel online tool for TasA, TasA-Dand TasA-DP samples 70
Figure 27. Morphological characterization of 14 days old TasA, TasA D and TasA DP fibrils using scanning transmission electron microscopy (STEM). 72

Figure 28. Morphological characterization of TasA, TasA D and TasA DP fibrils using scanning transmission electron microscopy (STEM) 73
Figure 29. Morphological characterization of 14 days old TasA, TasA D and TasA DP fibrils using atomic force microscopy (AFM). 75
Figure 30. Morphological characterization of 28 days old TasA, TasA D and TasA DP fibrils using Atomic force microscopy (AFM) 75
Figure 31. QCM D measurements for adsorption kinetics analysis of 14 days old TasA, TasA D and TasA DP samples 78
Figure 32. QCM frequency shifts with respect to time and concentration 79
Figure 33. k_d and ΔG^o graphs of samples 80
Figure 34. Analysis of viscoelastic properties of 14 days old TasA, TasA D and TasA DP samples on gold surface by QCM D 81
Figure 35. The recorded dissipation shifts in QCM-D upon adsorption with increasing concentrations of TasA, TasA-D and TasA-DP proteins 83
Figure 36. Adhesion of HeLa S3 cells on surfaces coated with 7 days, 14 days and 28 days old TasA, TasA D and TasA DP 87
Figure 37. Schematic of the cell adhesion on functionalized and non-functionalized curli fibers. 104
Figure 38. Schematic diagram of CsgA and CsgB RGD expression cassette 105
Figure 39. Amplification of *csgA* and *csgB* genes with and without RGD peptide. 106
Figure 40. Expression and purification of CsgA, CsgB, CsgA RGD and CsgB RGD by IMAC 107
Figure 41. SEM analysis of functionalized CsgA and CsgB fibers 108
Figure 42. TEM analysis of RGD functionalized CsgA and CsgB fibers 109
Figure 43. Cell adhesion results of HEK293 cells on curli coated surfaces 110
Figure 44. Schematic diagram of biofilm protein expression cassettes from pZa pBAD plasmid. 112
Figure 45. Amplification of genes for biofilm expression cassettes in pZa pBAD . 113
Figure 46. Crsytal violet staining TasA, TapA, CsgA and CsgB pZa pBAD plasmids in ΔcsgAB. 115
Figure 47. SEM imaging of as well as pZa pBAD CsgA, CsgB, TasA and TapA constructs in ΔcsgAB with their 1:1 mix samples. 115
Figure 48. SEM imaging of ΔcsgAB as well as CsgA, CsgB, TasA and TapA pZa pBAD constructs in ΔcsgAB; prepared from YESCA agar plates 117

Figure 49. Schematic diagram of biofilm protein expression cassettes from pZa pBAD plasmid with 6 X His tag. 118
Figure 50. Amplification of genes for His-tagged biofilm expression cassettes in pZa pBAD 119
Figure 51. The western blot analysis of csgA-His, csgB-His, (N42) TasA-His, (N42) TapA-His, (N42) FapC-His and (N42) FapB-His constructs in ΔcsgAB 120
Figure 52. Immunocytochemistry of ΔcsgAB cells secreting CsgA, CsgB, TasA, TapA, FapC and FapB proteins 122
Figure 53. TEM images of Ni-NTA-Nanogold labeled, 4 days old in TasA, TapA, CsgA, CsgB, FapC and FapB biofilm forming colonies 123
Figure 54. ICC results of biofilm proteins expressed from pZa pBAD tasA, tapA, fapC, fapB, csgA and csgB constructs in ΔcsgAB, prepared from YESCA agar plates 125
Figure 55. ICC results of biofilm proteins expressed from pZa pBAD tasA, tapA, fapC, fapB, csgA and csgB constructs in ΔcsgA, prepared from YESCA agar plates 126
Figure 56. Schematic diagram of biofilm protein expression cassettes from pZa tetO plasmid with 6 X His tag. 127
Figure 57. Amplification of genes for His-tagged and RGD tagged expression of CsgA in pZa tetO 128
Figure 58. Congo Red staining of cell pellets of CsgA His and CsgA RGD samples after induction in M63 medium. 129
Figure 59. SEM analysis of His-tag and RGD functionalized CsgA fibers. 130
Figure 60. Adhesion of HEK293 cells on surfaces coated with filter purified CsgA-His and CsgA-RGD fibers 131
Figure C.1. Schematic representation of pEt22b-CsgA plasmid. 175
Figure C.2. Schematic representation of pEt22b-CsgB plasmid. 176
Figure C.3. Schematic representation of pEt22b-TasA plasmid. 176
Figure C.4. Schematic representation of pEt22b-TasA DQNAT plasmid. 177
Figure C.5. Schematic representation of pEt22b-CsgA RGD plasmid. 177
Figure C.6. Schematic representation of pEt22b-CsgB RGD plasmid. 178
Figure C.7. Schematic representation of pZa pBAD CsgA plasmid. 178
Figure C.8. Schematic representation of pZa pBAD CsgB plasmid. 179
Figure C.9. Schematic representation of pZa pBAD TasA plasmid. 179

Figure C.10. Schematic representation of pZa pBAD TapA plasmid..... 180
Figure C.11. Schematic representation of pZa pBAD csgA His plasmid. 180
Figure C.12. Schematic representation of pZa pBAD csgB His plasmid. 181
Figure C.13. Schematic representation of pZa pBAD tasA His plasmid. 181
Figure C.14. Schematic representation of pZa pBAD tapA His plasmid. 182
Figure C.15. Schematic representation of pZa pBAD fapC His plasmid. 182
Figure C.16. Schematic representation of pZa pBAD fapB His plasmid. 183
Figure C.17. Schematic representation of pZa tetO csgA His plasmid. 183
Figure C.18. Schematic representation of pZa tetO csgA RGD plasmid..... 184
Figure D 1. Sequencing alignment of pEt22b-CsgA construct. 185
Figure D 2. Sequencing alignment of pEt22b-CsgB construct 186
Figure D.3. Sequencing alignment of pEt22b-TasA construct 186
Figure D.4. Sequencing alignment of pEt22b-TasA DQNAT construct. 187
Figure D.5. Sequencing alignment of pEt22b-CsgA RGD construct 187
Figure D.6. Sequencing alignment of pEt22b-CsgB RGD construct..... 188
Figure D.7. Sequencing alignment of pZa pBAD CsgA construct 188
Figure D.8. Sequencing alignment of pZa pBAD CsgB construct 189
Figure D.9. Sequencing alignment of pZa pBAD TasA construct 189
Figure D.10. Sequencing alignment of pZa pBAD TapA construct 190
Figure D.11. Sequencing alignment of pZa pBAD csgA His construct 190
Figure D.12. Sequencing alignment of pZa pBAD csgB His construct..... 191
Figure D.13. Sequencing alignment of pZa pBAD tasA His construct 191
Figure D.14. Sequencing alignment of pZa pBAD tapA His construct..... 192
Figure D.15. Sequencing alignment of pZa pBAD fapC His construct..... 192
Figure D.16. Sequencing alignment of pZa pBAD fapB His construct..... 193
Figure D.17. Sequencing alignment of pZa tetO csgA His construct..... 193
Figure D.18. Sequencing alignment of pZa tetO csgA RGD construct 194
Figure G.1. Intensity distribution of CsgA samples with different aging times 206
Figure G.2. Intensity distribution of CsgB samples with different aging times 207

1 CHAPTER I

INTRODUCTION

1.1 Amyloids

Amyloids are proteins that form elongated fiber with β sheet rich structures. Amyloid forming proteins are generally associated with neurodegenerative diseases such as Alzheimer's disease and Huntington's disease (Eisenberg & Jucker, 2012). However, amyloids also play physiological roles, known as functional amyloids. Functional amyloids have been identified in a variety of organisms, but they are most abundant in microorganism. Microbial functional amyloids are well characterized for their roles in biofilm formation and surface adhesion (Levkovich, Gazit, & Laor Bar-Yosef, 2020). Another class of amyloids, called artificial amyloids can be described as amyloids formed under artificial conditions using normally non-amyloidogenic proteins (Ke et al., 2020).

Amyloids produced in bacterial biofilms are named as functional amyloids, in contrast to pathogenic amyloids discovered in human diseases such as Alzheimer's or Parkinson's disease. However, functional amyloid fibers produced by bacteria are important determinants of pathogenesis during the infectious process (Blanco, Evans, Smith, Badtke, & Chapman, 2012). The role of functional amyloids in attachment

and invasion of host cells, as well as the interaction of amyloids in immune systems have been described by several reports.

Studies with E. coli curli fibers demonstrated that curli binds to extracellular matrix proteins fibronectin and laminin to mediate attachment to host cells (Barnhart & Chapman, 2006; Olsén, Arnqvist, Hammar, Sukupolvi, & Normark, 1993; Olsén, Jonsson, & Normark, 1989). In addition, curli interacts with several other proteins to facilitate host invasion, such as plasminogen and tissue type plasminogen activator (t-PA). Curli interaction activates plasminogen, a serine protease, and it is speculated that since fibrinogen degrades the soft tissue, it might allow bacteria to penetrate deeper in the tissue during host invasion (Sjöbring, Pohl, & Olsén, 1994). Curli is also thought to have a role in sepsis, as CsgA is detected in the blood serum of sepsis patients (Bian, Brauner, Li, & Normark, 2000).

Mycobacterium tuberculosis expresses M. tuberculosis pili (MTP) that produces amyloid fibers similar to curli. Similar to E. coli curli fibers, antibodies against MTPs are detected in the serum of patients infected with M. tuberculosis, which implies a role of MTPs in infection and immune response. Although the exact role of MTPs for pathogenesis remains unknown, MTP fibers are shown to bind laminin that suggests a role in host attachment (Alteri et al., 2007). Even though several components of immune system are depicted to have a role against M. tuberculosis infection, the mechanism of how MTP fibers effect the immune system is still unknown (Mortaz et al., 2015).

1.2 Amyloid formation

Amyloids share a common structural architecture. They form a fiber by aligning the β-strands perpendicular to the long axis of the fiber. As strong as the steel, those fibers then can aggregate into plaque state in diseases (Iadanza, Jackson, Hewitt, Ranson, & Radford, 2018).

The schematic of amyloid formation is depicted in Figure 1. Native proteins in a dynamic equilibrium between unfolded and native state, form oligomers. Those oligomeric structures then assemble into higher order oligomers, which can serve as nucleation points for assembly of amyloid fibers (Xue, Homans, & Radford, 2008).

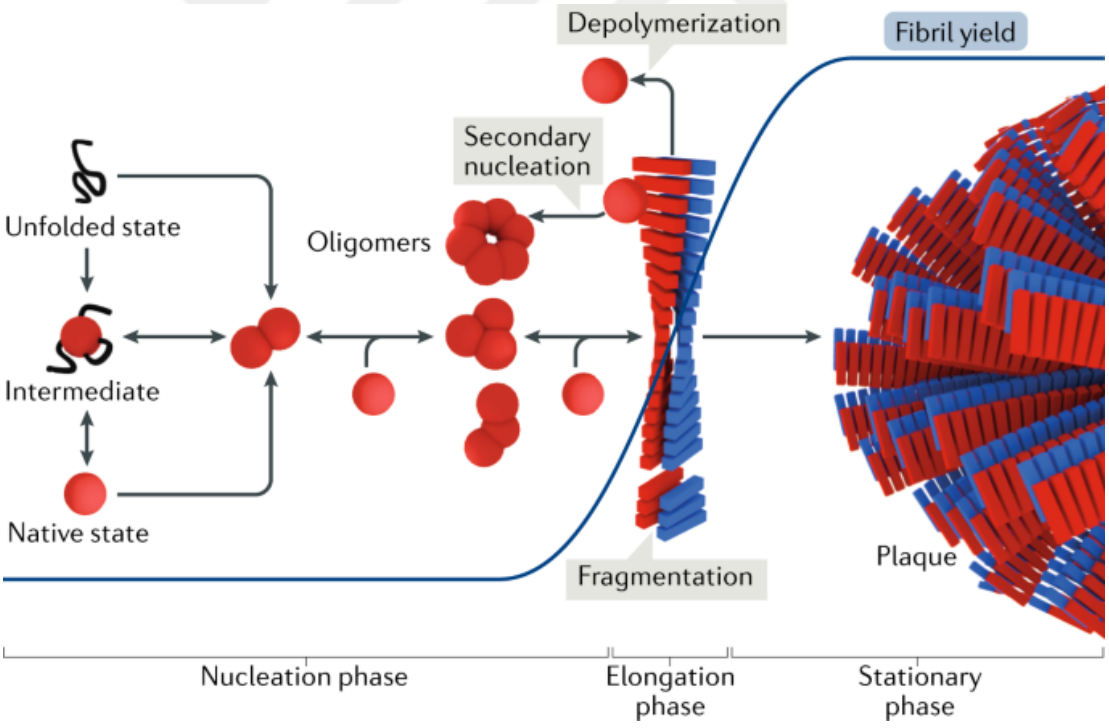


Figure 1. Schematic of amyloid formation. Reprinted by permission from Nature Reviews Molecular Cell Biology Iadanza et al. Copyright 2018.

Amyloids, in brief, are cross β sheets of indefinite length, composed of arrangement of thousands peptide/protein copies. Therefore, they can be visualized easily by electron microscopy (EM), as filaments. Initial characterization of amyloid fibers with EM revealed non-branched structures with a diameter of 6-12 nm and showed that cross β sheet structures results in a characteristic X ray diffraction pattern (Figure 2) (Greenwald & Riek, 2010).

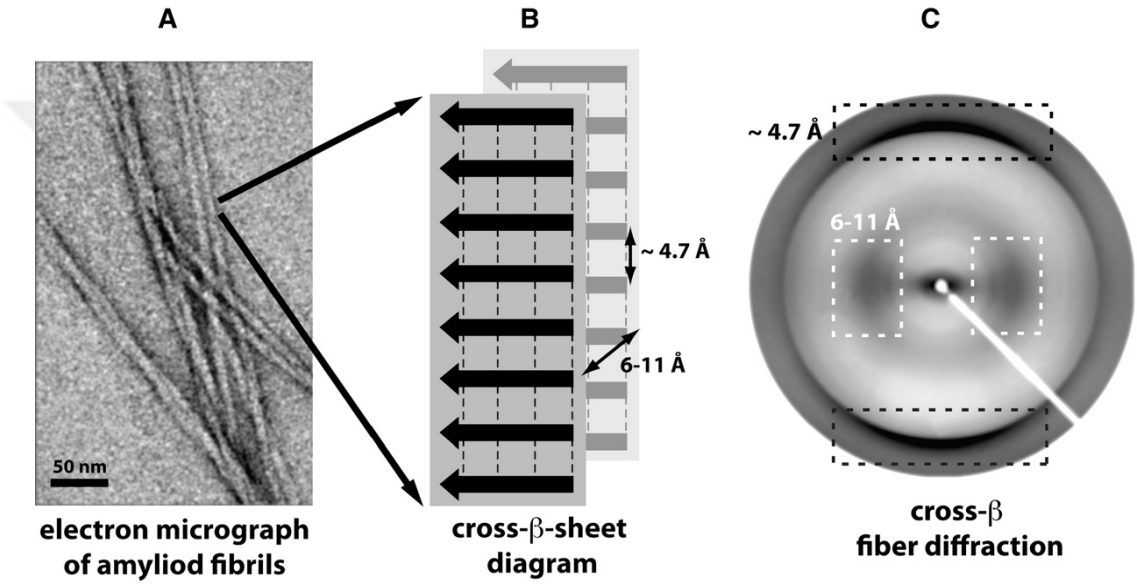


Figure 2. Structure of amyloids. A. Long filaments of amyloids are visualized by EM B. Schematic diagram of cross β sheets in amyloid structure. C. Characteristic X-ray diffraction pattern of cross β sheets in fibrils. Reprinted from Structure Review, Vol 18 , Greenwald & Riek, Biology of Amyloid: Structure, Function, and Regulation, Pages 1244-1260, Copyright 2010, with permission from Elsevier.

1.3 Functional amyloids and biofilms

In nature, functional amyloids have several functions such as mechanical resistance, antimicrobials and cell adhesion, especially in biofilm formation. In the biofilms, communities of cells are sticked together by an extracellular matrix composed of several exopolysaccharides, proteins, DNA and RNA molecules, small peptides etc. (Levkovich et al., 2020). The regulation of biofilm formation in response to environmental cues is facilitated via different cellular machineries. The main regulatory systems responsible for biofilm formation are quorum sensing and several two component systems. Quorum sensing signaling has been reported to be involved in attachment, maturation and aggregation phases of biofilm formation (Davies et al., 1998).

Biofilms provide resistance to nutritional, chemical, physical and mechanical stress. Even though numerous functional amyloids were defined in different microorganisms, not all of them are well understood. In this thesis, I focused on amyloid proteins of biofilms from three extensively studied bacterial species, which were discussed in following sections.

1.3.1 Escherichia coli

Amyloid forming biofilm proteins from *E. coli,* known as curli fibers, are studied widely as model for functional amyloid assembly. Curli secretion system is composed of 7 **c**urli **s**pecific **g**enes (*csg*), controlled by two operons, namely *csgBCA* and *csgDEFG* operon (Levkovich et al., 2020). Expression from *csgBAC* operon is regulated by CsgD protein, a transcriptional regulator.

Production of curli fimbriae starts with *E. coli* switching from planktonic state to biofilm state. During the biofilm state, motility and flagellum formation are turned off and expression of curli are turned on (Ogasawara, Yamamoto, & Ishihama, 2011). CsgD, a FixJ/LuxR family protein, is the master regulator of biofilm formation (Hammar, Arnqvist, Bian, Olsén, & Normark, 1995). It encodes *csg* operons to express and assemble curli fibers, as well as other sets of genes required for adaptation to biofilm state. In laboratory strains, lack of CsgD expression confines biofilm expression, however, *ompR234* mutation is depicted to restore CsgD expression in laboratory strains (Prigent-Combaret et al., 2001).

CsgA is the major protein in curli fibers. It is expressed as a soluble unstructured peptide and secreted to extracellular space by CsgF-CsgG machinery. CsgA has an N terminal signal sequence, represented as N22, which interacts with CsgG during secretion. CsgE interacts both with CsgA and CsgG and provides translocation (Balistreri, Goetzler, & Chapman, 2020). In addition, CsgC also interacts with CsgA and prevents its fibrillization in in the periplasm before secretion (Levkovich et al., 2020; Yan, Yin, Chen, & Li, 2020). CsgB is the minor protein in curli fibers with N terminal 23 amino acid long secretion signal. In nucleates CsgA fibrillization and acts as an anchor between CsgA and cell membrane (Hammer, Schmidt, & Chapman, 2007). The machinery is depicted in Figure 3.

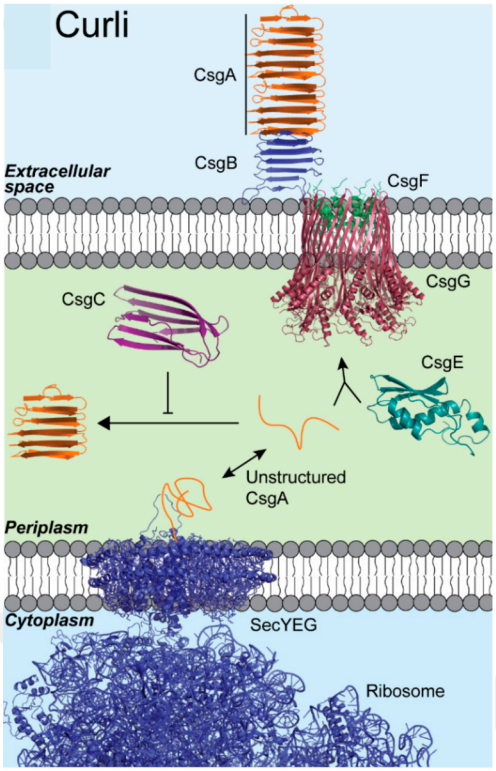


Figure 3. Schematic diagram of curli secretion system. CsgA is secreted through CsgG:CsgF machinery and anchors to membrane via CsgB (Balistreri, Goetzler, et al., 2020)

CsgA is composed of an N terminal signal peptide and C terminal core domain. The core domain is composed of 5 units of imperfect repeats, namely R1 to R5. CsgA has a Ser-X5-Gln-X-Gly-X-Gly-Asn-X-Ala-X3-Gln motif in all units, which forms a β helical cross β structure in overall. Gln and Asn residues in each unit is stacked, resulting in stabilization of amyloid fold (Dueholm et al., 2011; Evans & Chapman, 2014; Shewmaker et al., 2009; Xuan Wang & Chapman, 2008). Repeating units and cross β structures of CsgA and CsgB are summarized in Figure 4.

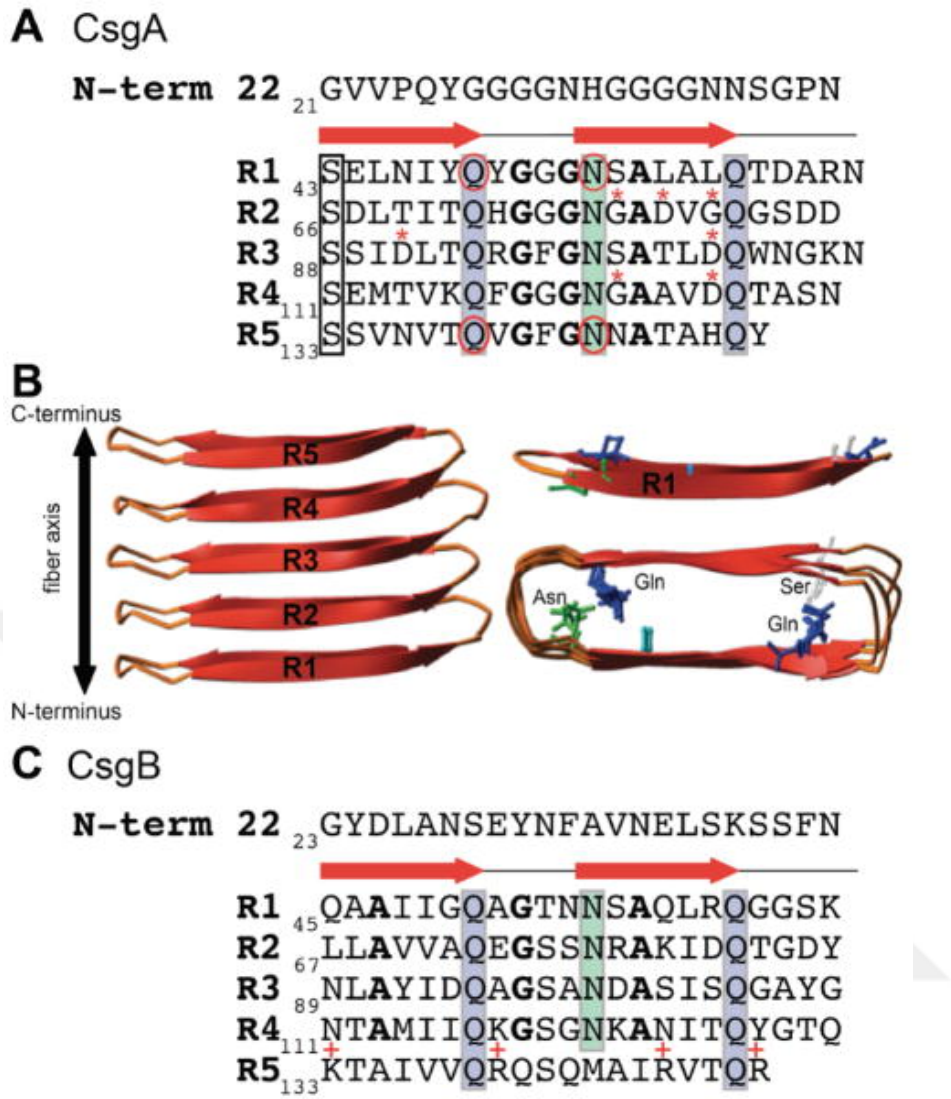


Figure 4. Schematic of molecular details if CsgA and CsgB. A. Amino acid sequences of CsgA N terminal signal sequence and repeat units R1-R5 are depicted. B. A representation of predicted CsgA structure C. Amino acid sequences of CsgB N terminal signal sequence and repeat units R1-R5 are depicted. Reprinted from Biochimica et Biophysica Acta (BBA) - Molecular Cell Research, Vol 1843, Margery L. Evans,Matthew R. Chapman, Curli biogenesis: Order out of disorder, Pages 1551-1558, Copyright 2014, with permission from Elsevier.

1.3.2 Bacillus subtilis

Bacillus subtilis is an endo-spore forming, motile, gram-positive soil bacterium widely used in biofilm formation studies due to its ability to form highly structured, robust biofilms (Branda, González-Pastor, Ben-Yehuda, Losick, & Kolter, 2001). Biofilm formation is regulated by a variety of complex regulatory networks in response to changes in the natural environment of *B. Subtilis*. At the course of biofilm formation, motile cells transform into non-motile cells sticked together by the extracellular matrix secreted from matrix producing cells (Hall-Stoodley, Costerton, & Stoodley, 2004).

Extracellular matrix of *B. Subtilis* biofilms have been extensively characterized so far. The rigid ECM of *B. Subtilis* is mainly constituted from exopolysaccharides (EPS) and proteins (Mielich-Süss & Lopez, 2015). The production of major exopolysaccharide component in *B. Subtilis* biofilms is regulated by the *epsA-O* operon and the exact molecular structure of the EPS regulated by *epsA-O* operon can vary depending on the available substrates in the environment (Y. Chai, Beauregard, Vlamakis, Losick, & Kolter, 2012; Gerwig, Kiley, Gunka, Stanley-Wall, & Stülke, 2014; Jones, Paynich, Kearns, & Knight, 2014).

Protein component of *B. Subtilis* biofilms is mainly composed of three proteins: amyloid-fiber forming proteins TasA and TapA as well as BslA protein responsible for morphology and pellicle formation (Ostrowski, Mehert, Prescott, Kiley, & Stanley-Wall, 2011; Romero, Vlamakis, Losick, & Kolter, 2011). Amyloid fibers in biofilms provide structural stability to biofilms and serve as a robust protein scaffold to hold cells together. TasA is the major component of β-sheet enriched amyloid-like

fibers of B. Subtilis biofilms and TapA is the minor component of fibers required for their assembly and anchors the fibers to the cell wall (Romero, Aguilar, Losick, & Kolter, 2010). Expression of TasA and TapA proteins are regulated from *tapA-sipW-tasA* operon. The third gene in the operon encodes for signal sequence peptidase SipW. SipW is responsible for the secretion of TasA and TapA into the biofilm matrix subsequent to removal of their signal sequences (Terra, Stanley-Wall, Cao, & Lazazzera, 2012). The other protein component of *B. Subtilis* biofilms is BslA, a bacterial hydrophobin required for the biofilm assembly as well as complexity and hydrophobicity of mature biofilms (Kobayashi & Iwano, 2012).

TasA is a 31 kDa protein with a 27-amino acid N-terminal signal sequence which is removed by SipW during translocation through the membrane. TasA is purified from *B. subtilis* in oligomeric form and requires a stimulus such as a hydrophobic surface to form amyloid fibers. Secondary structure analysis revealed that oligomeric and fiber states of TasA aggregates differ in terms of their secondary structures. Similar to the eukaryotic amyloid-like fibers, the oligomeric state is rich in α-helical structures whereas during the fiber formation the conformation shifts towards a β-sheet rich structure (L. Chai et al., 2013). TapA is a 30 kDa protein with a 32-amino acid N-terminal signal sequnece which is removed by SipW. TapA is required for the amyloid fiber assembly and TasA stability (Romero, Vlamakis, Losick, & Kolter, 2014).

B. subtilis biofilm formation is coordinated by a complex regulatory network, composed of mainly 3 master regulators. Spo0A, DegU and ComA. Activation of Spo0A transcription factor by phosphorylation (Spo0A~P) is essential for the onset of biofilm formation. Kinases KinA, KinB, KinC and KinD contribute to the

phosphorylation of Spo0A, depending on the existing signals (Jiang, Shao, Perego, & Hoch, 2000). Activity of membrane-bound sensor histidine kinases KinC and KinD are responsible for low levels of Spo0A~P. When Spo0A~P is present in low-levels, it triggers matrix production by activating *eps* and *tapA-sipW-tasA* operons via the expression of SinI protein (Y. Chai, Chu, Kolter, & Losick, 2008). SinR functions as a repressor of *eps* and *tapA-sipW-tasA* operons. SinR anti-repressor SinI forms a SinR-SinI complex and eliminates SinR repression, triggering matrix production from *eps* and *tapA-sipW-tasA* operons (Kearns, Chu, Branda, Kolter, & Losick, 2005; Lewis, Brannigan, Smith, & Wilkinson, 1996).

1.3.3 Pseudomonas aeruginosa

Pseudomonas aeruginosa is an opportunistic pathogen associated with several human diseases, especially with chronic infections in the lung of cystic fibrosis (CF) patients. *P. aeruginosa* (PA) infections are the major cause of mortality in CF patients, due to persistent colonization of pathogenic PA associated with antibiotic resistant biofilms (Drenkard & Ausubel, 2002). Several environmental factors are defined to induce biofilm formation and dispersion in P. aeruginosa via different metabolic and signaling pathways; such as changes in the nutrient sources and amount (Sauer et al., 2004), oxygen gradients (An, Wu, & Zhang, 2010; E.-J. Kim, Wang, Deckwer, & Zeng, 2005), nitric oxide produced by anaerobic respiration (Barraud et al., 2006; Yoon et al., 2002) and chemicals such as chelating agents, surfactants or amino acids (S.-K. Kim & Lee, 2016).

In the quorum sensing mechanism of *P. aeruginosa*, acyl-homoserine lactones (AHL) are used as signaling molecules (Fuqua & Greenberg, 2002; Gilbert, Kim,

Gupta, Greenberg, & Schuster, 2009; J.-H. Lee, Lequette, & Greenberg, 2006). In addition to quorum sensing signaling, two-component systems GacS/GacA and RetS/LadS are involved in biofilm formation and additionally, act as regulators of quorum sensing in P. aeruginosa (Rasamiravaka, Labtani, Duez, & El Jaziri, 2015a). Additionally, bis-(3′-5′)-cyclic dimeric guanosine monophosphate (c-di-GMP) levels is reported to have an impact on biofilm regulation via promoting the synthesis of exopolysaccharides Psl and Pel in elevated concentrations (V. T. Lee et al., 2007) or promoting bacterial motility and biofilm dispersion in decreased concentations (Merighi, Lee, Hyodo, Hayakawa, & Lory, 2007).

In biofilms of PA, cells are held together in a matrix of extracellular polymeric substance (EPS). EPS protects the cells inside the biofilm from harsh environments and provides tolerance to antimicrobial agents, as well as functioning as a structural scaffold (Ma et al., 2009; Walters, Roe, Bugnicourt, Franklin, & Stewart, 2003). EPS is composed of exopolysaccharides, extracellular DNA, proteins and other biomolecules, constituting more than 85% of total biofilm mass (Flemming, Neu, & Wozniak, 2007).

PA mainly produces 3 types of exopolysaccharides in the EPS matrix as determinants of the biofilm stability: mannose rich polysaccharide Psl, glucose rich Pel polysaccharide and acetylated polysaccharide alginate. Extracellular DNA is an important component of PA biofilms with several functions. DNAase treatment of young PA biofilms results in biofilm dispersal, depicting the importance of eDNA as a connective component in PA biofilm. However, mature biofilms of PA are not effected by DNAase treatment, possibly due to increased amounts of other EPS components such as polysaccharides (Whitchurch, Tolker-Nielsen, Ragas, & Mattick, 2002).

Several extracellular proteins and proteinaceous surface appendages of PA such as type IV pili, flagella and fimbriae are also considered as components of PA biofilm matrix. In addition to their roles in bacterial swimming and swarming motility; type IV pili, fimbriae and flagella have important roles as adhesins in biofilms, especially for the **irreversible attachment** of the cells to surfaces. Those extracellular appendages are also critical for **microcolony formation** in biofilms (Barken et al., 2008; Rasamiravaka, Labtani, Duez, & El Jaziri, 2015b). Surface adhesin CdrA is another protein component of PA that promotes biofilm formation and auto-aggregation (Borlee et al., 2010). Finally, as the functional amyloid protein of PA, Fap amyloids also contribute to biofilms of PA. Detailed investigation of amyloid fibers in PA biofilms revealed that FapC protein is the major component and FapB protein is the minor component serving as a nucleator. The expression of functional amyloids is controlled by the fap operon in PA (Dueholm, Søndergaard, et al., 2013). In addition to fapB and fapC genes, the fap operon includes 4 other genes: fapA, fapD, fapE and fapF. FapA is a chaperone that affects distribution of Fap proteins in the amyloid fibrils. Bioinformatic analysis suggested that FapF is a β-barrel membrane pore required for the secretion of FapB and FapC proteins into extracellular matrix, and FapD is a protease required for the processing of Fap proteins. Even though small amount of FapE is purified within amyloid fibers and nominated as an extracellular chaperone, its exact function remains unknown (Dueholm, Otzen, & Nielsen, 2013; Dueholm, Søndergaard, et al., 2013). The secretion machinery for FapB and FapC is summarized in Figure 5.

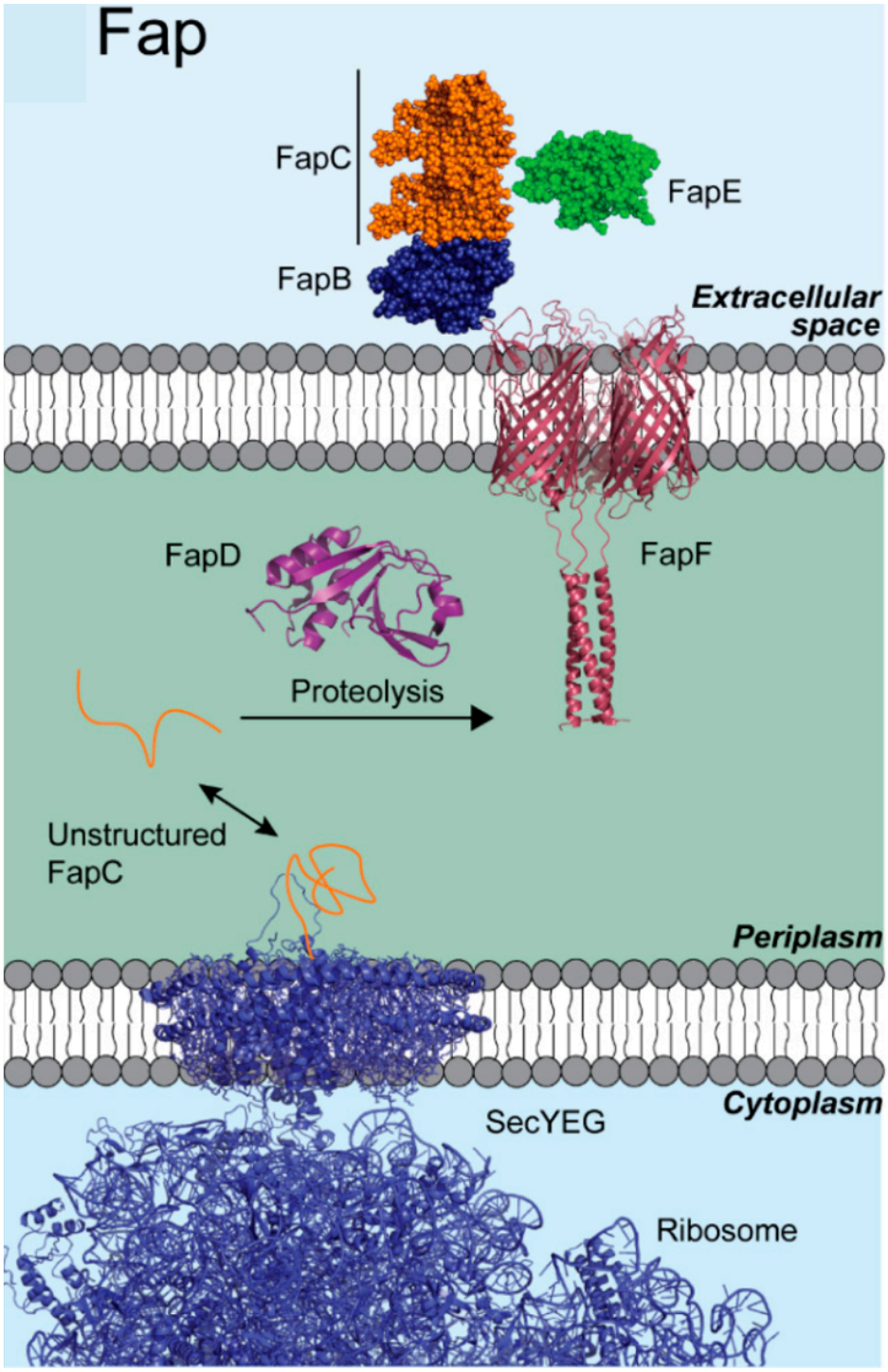


Figure 5. Schematic diagram of fap secretion system. FapC is secreted through FapF machinery and anchors to membrane via FapB (Balistreri, Goetzler, et al., 2020).

1.4 Amyloids for biomaterial applications

In higher organisms, cell adhesion is crucial to enable interaction between cells which is necessary for tissue organization and function. Extracellular matrix (ECM) is responsible for cell-to-cell interactions via several proteins such as collagen, fibronectin etc. ECM proteins have several domains to facilitate cell adhesion, such as RGD domain from fibronectin (Daley & Yamada, 2013; Takahashi et al., 2007). Amyloids can interact with several macromolecules, probably due to the repetitive arrangement of residues on amyloid surfaces (Nilsson, 2009). This capacity is utilized by lower organisms to adhere onto host surfaces, for example curli fibers. Those organisms produce biofilms to adhere host cells to cause disease and obtains protection from host immune system (Das, Jacob, Patel, Singh, & Maji, 2018). The nanofibrillar morphology of amyloids show similarity to ECM structure, therefore it can enhance cell adhesion. Additionally, amyloid fibrils can be functionalized with peptide groups to support cell adhesion further (Gras et al., 2008).

Biomaterials require different properties for different applications. Generally, tissue engineering scaffolds are designed as biomaterials that can mimic natural extracellular matrix to induce cell adhesion and proliferation (Figure 6). Amyloids provide a suitable matrix for cell adhesion; however, amyloids can show toxicity to cells, too. Therefore, characterization of amyloids in terms of biocompatibility is crucial for their utilization as biomaterials (Das et al., 2018).

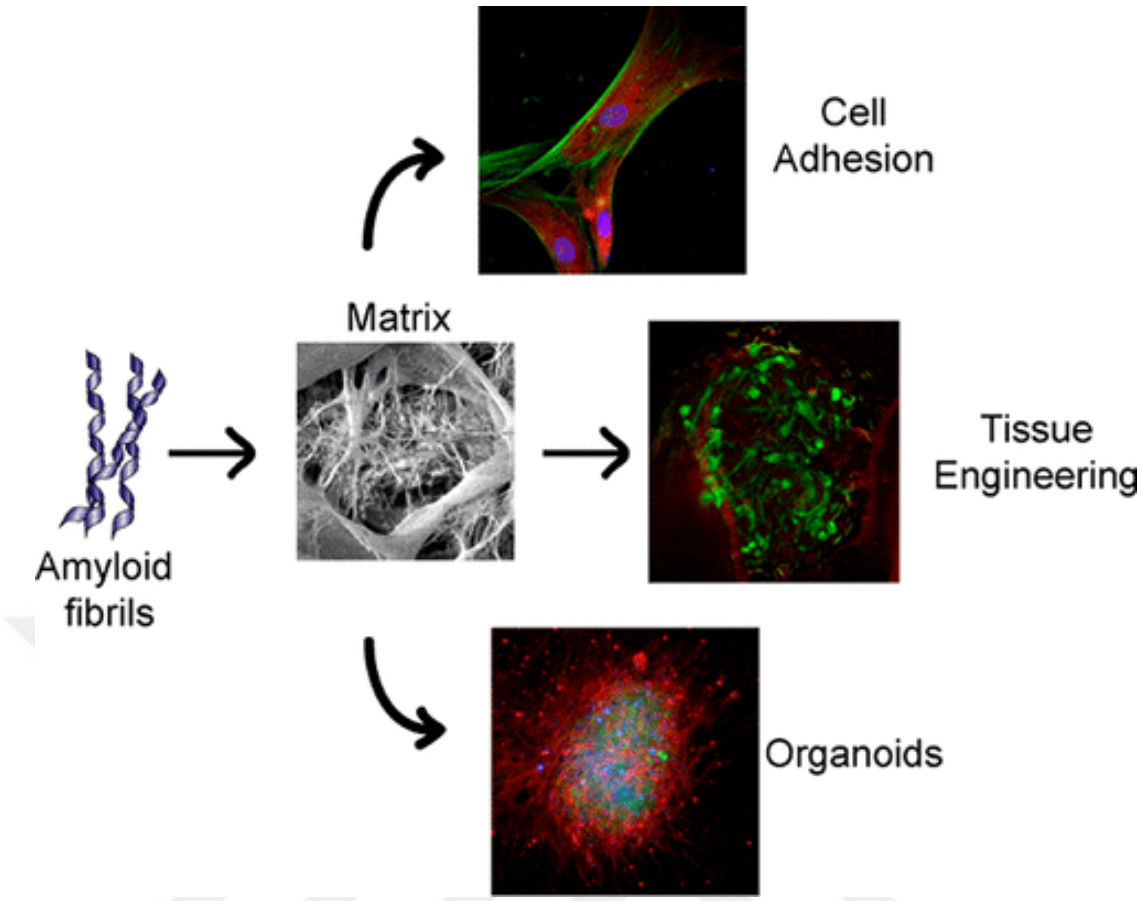


Figure 6. Amyloids as biomaterials for several applications. Reprinted with permission from Biomacromolecules 2018, 19, 6, 1826-1839. Copyright 2018 American Chemical Society.

1.5 Protein glycosylation

Protein glycosylation is enzyme driven attachment of glycan groups to amino acids. It is one of the most common post translational modification in all kingdoms of life. Even though protein glycosylation is identified firstly in eukaryotic cells, bacterial glycosylation is also discovered in the past twenty years, especially in the pathogenic bacteria in association with virulence (Lu, Li, & Shao, 2015).

Glycosylation can be classified into two groups as N-linked glycosylation and O-linked glycosylation. In N-linked glycosylation, glycan groups are attached to amide nitrogen of Asn in the side chain, in Asn-X-Ser/Thr motif (X is any amino acid except proline). In O-linked glycosylation, glycan groups are attached to the hydroxyl group of Ser or Thr (Nothaft & Szymanski, 2010).

*Campylobacter jejun*i, a pathogen that causes bacterial gastroenteritis, is the first prokaryotic species that is discovered to possess N-linked glycosylation (Szymanski, Yao, Ewing, Trust, & Guerry, 1999). Protein glycosylation machinery is expressed by a *pgl* gene cluster in *C. jejuni*. Sugar biosynthesis enzymes expressed by *pgl* operon produces a hepta-saccharide precursor that is transferred to target Asn in the periplasm by PglB. PglB protein acts as an oligosaccharyltransferase that transfers the oligosaccharides to Asn residues of nascent polypeptide chains (Lu et al., 2015). The hepta-saccharide is converted to undecaprenyl-diphosphate (Und-P-P) by the membrane proteins PglC, PglA, PglJ, PglH, and PglI. Following, PglK, a flippase, translocates Und-P-P to periplasmic space for the action of PglB (Hartley, Schneggenburger, & Imperiali, 2013). The mechanism of C. jejuni pgl glycosylation pathway is depicted in Figure 7.

The *pgl* glycosylation pathway is transferred to *E. coli* and successful protein glycosylation was achieved upon transfer of *pgl* cassette, enabling engineering of recombinant glycan structures for research purposes, as well as industrial applications (Wacker et al., 2002).

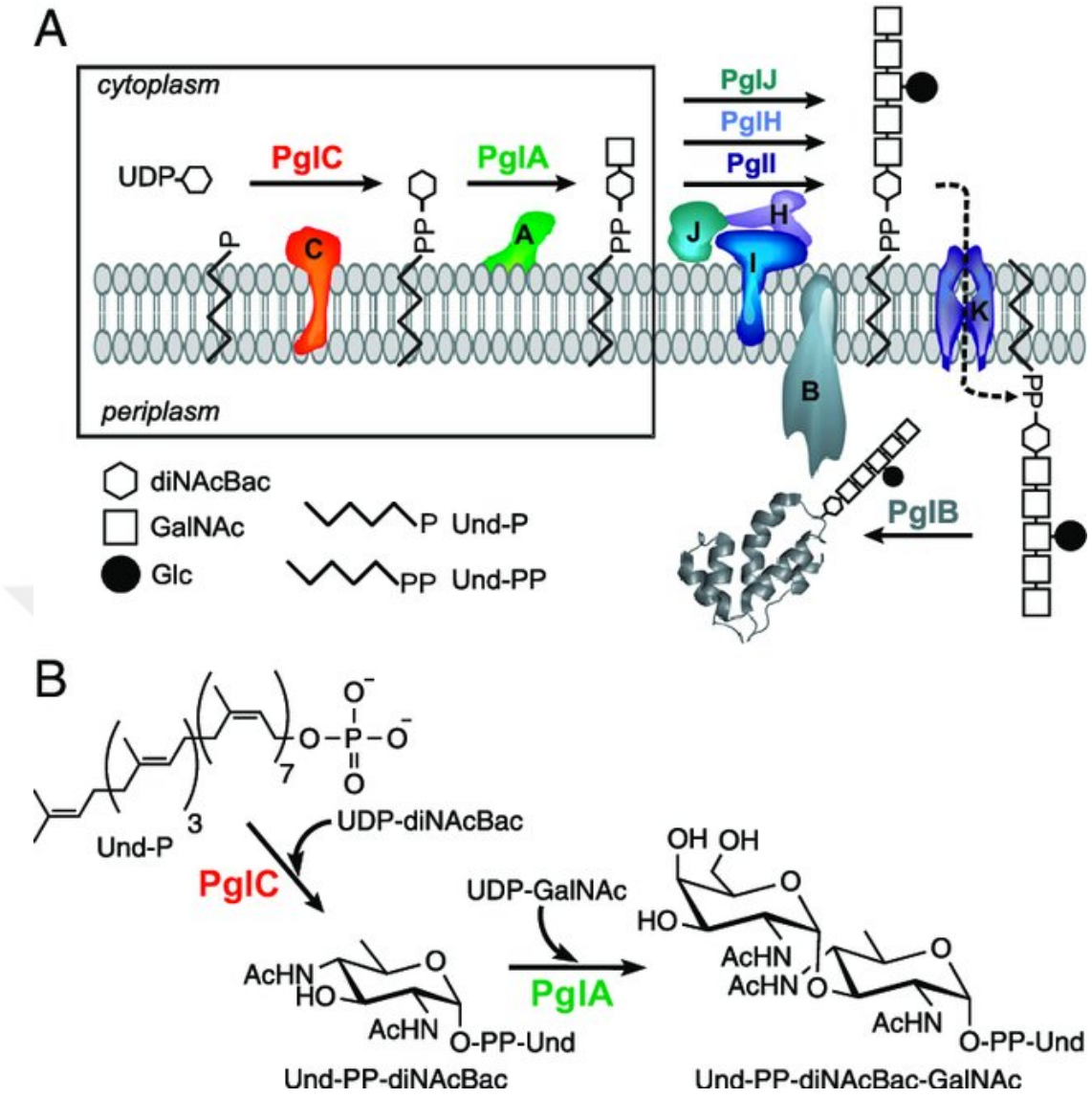


Figure 7. Schematic representation of N-linked glycosylation pathway in C. jejuni. A. production of polyprenyl-diphosphate–linked glycan by membrane bound enzymes. B. Reactions of PglA and PglC enzymes. Reprinted from (Hartley et al., 2013).

2 CHAPTER II

INTERACTION OF MICROBIAL FUNCTIONAL AMYLOIDS WITH SOLID SURFACES

This work is partially described in the following publication (Yuca, Şahin Kehribar, & Şeker, 2020)

Esra Yuca [2#], Ebru Şahin Kehribar [1#], Urartu Özgür Şafak Şeker [1]

1 UNAM−Institute of Materials Science and Nanotechnology, Bilkent University, TR-06800 Ankara, Turkey,

2 Molecular Biology and Genetics Department, Yildiz Technical University, 34210 Istanbul, Turkey

Corresponding Author

Dr. Urartu Ozgur Safak Seker

urartu@bilkent.edu.tr

#These authors have equally contributed

2.1 Introduction

Utilization of self-assembly abilities of protein subunits offers the fabrication of biomolecule-based new generation materials with improved functions. Collagen, actin, knot proteins, protein catenanes (Pieters, van Eldijk, Nolte, & Mecinović, 2016), viral capsid proteins (Jolley, Klem, Harrington, Parise, & Douglas, 2011), scaffold proteins, bacterial flagella, bacterial pili , and amyloids are the examples of protein nanostructures that can self-assemble into an ordered supramolecular structure (Kumar et al., 2014; Yuca et al., 2020).

Amyloid proteins that are resistant to hard physical and chemical conditions can be classified as functional, pathological and artificial amyloids (Pham, Kwan, & Sunde, 2014). Pathologic amyloids are produced as a result of protein aggregation observed in neurodegenerative disease conditions while functional amyloids are produced to form biofilms by following a different developmental process than pathological amyloids. Artificial amyloids are produced from non-toxic proteins under artificial conditions and utilized as functional biomaterials (Cherny et al., 2005). Functional amyloids go beyond the misfolding and aggregation properties of pathologic amyloids and bring the useful properties of amyloids to the forefront in nature (Kalyoncu, Ahan, Ozcelik, & Seker, 2019; Van Gerven, Klein, Hultgren, & Remaut, 2015)

Biofilms are complex microorganism populations embedded in the extracellular matrix (ECM) that protect bacteria from adverse environmental conditions and formed by bacteria attaching to the surface. Resistance to external physical and chemical stresses increases in biofilms compared to planktonic life. Although the

exact content of the biofilm matrix that encapsulates the bacteria varies depending on bacterial strains and environmental conditions, it is generally composed of proteins, nucleic acids, and polysaccharides (Seker, Chen, Citorik, & Lu, 2017). Bacterial biofilms, which are highly regulated, complex and dynamic systems, resistant to harsh environmental conditions with their ECM, have a great potential for the production and development of new generation materials (Knowles & Buehler, 2011; D. Li et al., 2014).

In recent years there is an increasing trend towards the use of amyloids and amyloid-like fibrils as building blocks and as functional biomaterial systems (Xinyu Wang, Li, & Zhong, 2015). Functional amyloid curli fiber, which constitutes an important protein component of the extracellular biofilm matrix, is the most common bacterial amyloid protein genetically manipulated (Botyanszki, Tay, Nguyen, Nussbaumer, & Joshi, 2015; Taglialegna, Lasa, & Valle, 2016). Transcription of bacterial curli amyloid nanofiber subunits is are regulated by csgBAC and csgDEFG operons. Bacterial curli amyloid nanofibers consist of major CsgA and minor CsgB amyloid subunit proteins with N-terminal signal sequences. Use of CsgA and CsgB amyloid subunits for bioinspired materials production and bioinspired processes or device development have been investigated. In our previous study, we optimized the recombinant production and biochemical properties of CsgA and CsgB curli protein mutants (Donlan, 2002). Controlling the production and secretion of CsgA and CsgB amyloid proteins is critical in terms of final mechanical characteristics of the biofilm-based material assembly. From this motivation, morphological and mechanical properties of CsgA and CsgB biofilm proteins have been investigated to provide stiffer or softer amyloid nanofiber assemblies (Balistreri, Kahana, Janakiraman, & Chapman, 2020). Bacterial biofilms were also used to form conductive protein

nanofibers, integrating conductive peptide motifs for biofilm assembly in the previous work (Onur, Yuca, Olmez, & Seker, 2018). In another study, a series of genetic circuits were designed to control the secretion of CsgA-material binding peptide fusions upon extracellular signal processing of the available metallic nanoparticle precursors (Abdelwahab, Kalyoncu, Onur, Baykara, & Seker, 2017). In addition to control the assembly of biofilm amyloids, patterning of them can also be controlled using genetic logic gates to build up organized living material system upon inducing the coexpression of different CsgA fibers. Zhang et al. has have developed a coarse-grained curli fiber model to provide insight into adhesion mechanisms of curli subunit (Zhang, Wang, DeBenedictis, & Keten, 2017). Keten group has examined CsgA adsorption onto graphene and silica surfaces through atomistic simulation (DeBenedictis, Liu, & Keten, 2016). Although there are is an increasing number of efforts to use biofilm proteins as intelligent materials (Nguyen, Botyanszki, Tay, & Joshi, 2014), advanced characterization studies for biological nanofibers protein subunits of biofilm structures will increase their applications to the higher level in terms of producing by design.

2.2 Objective

In this part of the thesis project, binding kinetics of curli functional amyloids to solid materials such as gold, hydroxyapatite, and silica, which are used commonly used in biomedical applications (Cobley, Chen, Cho, Wang, & Xia, 2011; Vivero-Escoto, Huxford-Phillips, & Lin, 2012) are investigated to produce well-defined, controllable and tunable next- generation biomaterials.

Curli, the adhesive protein that provides attaching to surfaces during biofilm formation, is an essential precursor for development of innovative materials with its adherent feature. The development of functional materials based on the adhesion of the fibrils to the desired surfaces by using amyloid fibrils obtained as a result of processing globular proteins has been reported in other studies. For example, layered hybrid nanocomposites were developed as a result of combining these amyloid fibrils with hydroxyapatite (Dong, Zhou, Wu, & Wang, 2008). In addition, hybrid nanocomposites produced by combining gold nanoparticles and single-crystal platelets with amyloid fibrils and their superior utilization potential have been reported (Hoefling, Iori, Corni, & Gottschalk, 2010; Ozboyaci, Kokh, & Wade, 2016). On the other hand, in our approach the development of functional structures by purifying directly from the living host of well-characterized fibrils, which are improved by genetic engineering and fine-tuned in order to be controlled, directed and fine-tuned, and even the direct use potential of microorganisms that produce these fibrils are followed. For this purpose, we monitored the binding affinity of the fiber samples for biomedically relevant surfaces namely gold, silica and hydroxyapatite.

2.3 Materials and Methods

2.3.1 Cell strains and cell maintenance

In this study, *E. coli* DH5α strain (NEB) was utilized for cloning. *E. coli* DH5α strain contains mutations in recA1 and endA1 genes which increase transformation

efficiency via reduced plasmid recombination and increased plasmid stability by recA1, as well as increased plasmid yield by endA1 (Borja et al., 2012; Singer, Eiteman, & Altman, 2009). Cells were grown overnight in Lysogeny Both (LB) medium (1% (w/v) tryptone, 0.5% (w/v) yeast extract, 0.5% (w/v) NaCl) with proper antibiotics in Erlenmeyer flasks at 37 °C, 200 rpm. Cell stocks were prepared in freezing medium containing 25% glycerol in LB medium for long term storage at -80 °C.

E. coli BL21 DE3 strain (NEB) which encodes T7 polymerase under the control of Lac promoter and is deficient of proteases (Jeong et al., 2009, p. 606) was used for protein expression. This strain was maintained at the same conditions as for *E. coli* DH5α, as described above.

2.3.2 Construction of plasmids and transformation

CsgA and CsgB are biofilm proteins of *E. coli.* Therefore, *csgA* and *csgB* genes without signal sequences and C terminal flexible GS linker (GGSG) were amplified from *E. coli* K12 MG1655 genomic DNA using the primers listed in Table B.1. Q5 High-Fidelity DNA Polymerase (NEB) was used for all PCR reactions (Reaction conditions were described in APPENDIX F).

pET22b(+) vector with removed pelB periplasmic space localization signal peptide was used for cloning. Plasmid maps were shown in Figure C.1 and Figure C.2.

KpnI-HF (NEB.) and XhoI (NEB) was used to digest the plasmid. (Reaction conditions were described in APPENDIX F). Same restriction enzymes were used to digest PCR amplified *csgA* and *csgB* genes. All PCR products and digested plasmids

were verified on 1 % agarose gel stained with SYBR Safe DNA Gel Stain (Thermo Fisher Scientific). NucleoSpin Gel and PCR Clean-up kit (Macherey-Nagel) was used according to the manufacturer's instructors to isolate DNA from agarose gels. Digested plasmid (vector) and PCR products (insert) were assembled into a plasmid using T4 ligase (NEB) at 1:3 insert to vector molar ratio (Reaction conditions were described in APPENDIX F). The ligation mix was transformed into chemically competent *E. coli* DH5α bacteria. After overnight incubation, single colonies were selected and positive clones containing *csgA* and *csgB* genes were verified by Sanger sequencing. (Figure D.1, Figure D.2).

For chemical transformation, competent cells were prepared. Bacterial cells grown overnight were diluted in LB to 1:100 ratio. The cells were incubated at 37°C and 180 rpm shake in Erlenmeyer flasks till OD_{600} reaches 0.2-0.5. Here, the cells were incubated on ice for 10 min and collected by centrifugation at 1000 ×g, +4 ºC for 10 minutes. Following, the pellet was resuspended in 1:10 volume of TSS (Transformation and Storage Solution) buffer (PEG 8000 20% (w/v), DMSO 10% (w/v), $MgCl_2$ 100 mM, pH 6.5 in LB) and aliquoted. Ligation reaction was mixed with competent cells and incubated on ice for 20-30 minutes. The mixture were incubated at 42ºC for 45 seconds for heat-shock and cooled down on ice for 2 minutes. LB medium was added on the cooled cells and the cells were incubated at 37 ºC 200 rpm for 30-60 minutes without any antibiotics. After the incubation, cells were spread onto antibiotic containing LB-agar plate and incubated at 37 ºC, overnight.

All genetic part sequences used this chapter was introduced in Table A.1 and the amino acid sequences of each design were listed in Table E.1.

2.3.3 Sequence alignments

All plasmid maps were designed by Benchling online tool. After cloning, selected colonies were verified by Sanger sequencing (GENEWIZ). The sequencing results were analyzed by Geneious R9.0.5 software by pairwise alignment. Plasmid maps were exported as .gb files and imported in Geneious software together with the sequencing results (abi files).

2.3.4 Expression of recombinant proteins in E. coli

E. coli BL21 DE3 strain was used to express CsgA and CsgB proteins. The plasmids containing these genes were transformed into *E. coli* BL21 DE3 strain via chemical transformation. T7 promoter controlling the expression of CsgA and CsgB was switched on in the presence of a commonly used inducer, Isopropyl β-D-1-thiogalactopyranoside (IPTG). Bacteria harboring CsgA and CsgB expressing plasmid constructs were grown in LB medium supplemented with antibiotics at 37 ºC. After overnight incubation, cell culture was diluted to 1:50 in fresh LB medium. At OD_{600} ~0.9, CsgA and CsgB expressions were induced with IPTG (Amresco 0487) addition to a final concentration of 0.5 mM. Following two hours incubation at 37 ºC 200 rpm, bacterial culture was centrifuged at 8000 RCF and the pellets were kept at -80 ºC until purification.

2.3.5 Purification of recombinant proteins

For cell lysis, pellets were thawed and resuspended in phosphate buffer saline (PBS, 2.7 mM KCl, 137 mM NaCl, 2 mM KH2PO4, 10 mM Na2HPO4) at pH 7.0 that contained 6 M GdnHCl, 10 mM imidazole. After 1 hour incubation at +4 ºC, lysed cells were centrifuged at 10000 g for 20 min at 4 ºC to separate intact components from soluble proteins, and the remaining cellular debris was removed. A cobalt resin-based affinity method was applied for the purification of the proteins.

During affinity chromatography, his-tagged proteins were isolated from the rest of proteins in cell debris. 6 x His tag of the recombinant proteins interacts with cobalt ions specifically. Before loading to cobalt resin, the supernatant was filtered with 0.45 µm syringe and the resin was equilibrated in lysis buffer (PBS, 2.7 mM KCl, 137 mM NaCl, 2 mM KH2PO4, 10 mM Na2HPO4 at pH 7.0 that contained 6 M GdnHCl, 10 mM imidazole). Soluble cellular fraction was mixed with cobalt resin and incubated at 4 ºC in an end-over-end rotator for 1 h. The resin was centrifuged at 700 RCF for 2 minutes and sample solution was removed. Resin was washed with 2 bed volumes (BV) of lysis buffer 2-3 times to remove all non-specific proteins. CsgA and CsgB proteins were eluted from the resin with elution buffer (PBS at pH 7.0, 6 M GdnHCl, 150mM imidazole) since high imidazole concentration in elution buffer replaces His-tagged proteins from resin. CsgA and CsgB proteins were transferred to PBS pH 7.0 using centrifugal filter units (Thermo Scientific™ Pierce) with a molecular weight cutoff of 3 kDa. Purified protein oligomers were separated from monomers using 30 kDa centrifugal filter units (Thermo Scientific™ Pierce) for the following kinetic analyzes.

2.3.6 SDS-PAGE and Western Blot

Since CsgA and CsgB are amyloid forming proteins, they tend to form amyloid fibers. GdnHCl provides the strong denaturing conditions required for their monomerization during purification, however, upon the removal of GdnHCl CsgA and CsgB starts to form fibers. Since those fibers cannot be monomerized in SDS-PAGE sample buffer even in the presence of denaturants such as dithiothreitol (DTT), purified CsgA and CsgB protein samples were treated with 100 % formic acid at room temperature for 10 minutes, to break down protein oligomers and were freeze- dried to remove formic acid.

Formic acid treated and lyophilized CsgA and CsgB proteins were dissolved in 2x Laemmli sample buffer (6X Laemmli sample buffer contains 1.2 g SDS (sodium dodecyl sulfate), 6 mg bromophenol blue, 4.7 ml glycerol, 1.2 ml Tris (0.5M, pH 6.8), 2.1 ml ddH_2O). 15% SDS gel was used to separate CsgA and CsgB since their molecular weights were as low as 13-15 kDa. 1×SDS Running Buffer (25 mM Tris-HCl, 200 mM Glycine, 0.1% (w/v) SDS) was used during the run.

15 % SDS resolving gel was prepared with BioRad SDS Gel casting system using the following recipe: 2.2 ml ddH_2O, 2.6 ml 1.5 M Tris-HCl (Sigma) (pH 8.8), 100 µl 10% (w/v) SDS, 5 ml Acrylamide/ Bisacrylamide (VWR) (30%/0.8% w/v), 100 µl 10% (w/v) APS (Biorad Ammonium persulfate), 10 µl tetramethylethylenediamine (TEMED) (Biorad). Stacking gel was prepared using the following recipe: 2.975 ml ddH_2O, 1.25 ml 0.5 M Tris-HCl (pH 6.8), 50 µl 10% (w/v) SDS, 0.67 ml Acrylamide/Bisacrylamide (30%/0.8% w/v), 50 µl 10% (w/v) APS, 5 µl TEMED.

For SDS-PAGE, the gels were stained staining in Coomassie brilliant blue R-250 to detect the protein bands (45 MetOH%, 10% glacial acetic acid, 3 g/L CBB R250), and destained in destaining buffer (10% acetic acid, 30% methanol).

For detecting his-tagged proteins immunoblot analysis, the proteins on gel were transferred to a PVDF (Thermo Scientific 88520) membrane using Transblot Turbo Transfer System (Biorad) at following transfer conditions: 25 kV, 1.3 A for 7 min. The membrane was blocked in 5% milk powder in 0.1 % TBS-T for 2 hours on a rotator at room temperature. After blocking, the membrane was incubated in primary antibody solution (1: 5000 dilution of mouse anti-6X-His Tag mAb (Proteintech Europe) in 5% milk powder in 0.1 % TBS-T), for 1 h at room temperature or for overnight at +4 ˚C on a rotator. The membrane was washed 3 times in 0.1 % TBS-T for 5, 15, 5 min on a rotator at room temperature. Then, membrane was incubated in secondary antibody solution (1: 5000 dilution of Goat anti-mouse IgG H&L (HRP) (Abcam ab6789) in 5% milk powder in 0.1 % TBS-T) at room temperature for 1 h on a rotator. The membrane was washed in 0.1 % TBS-T as described previously. ECL Substrate (Biorad 170-5060) was used for visualization according to manufacturer's instructions and the membrane was imaged immediately in ChemiDoc MP Imaging System (Biorad) with Image Lab Software.

2.3.7 Fiber formation and transmission electron microscopy (TEM)

Protein concentrations were determined using BCA Assay (Thermo Fisher Scientific) according to manufacturer's instructions and absorbance values were recorded in SpectraMax M5 spectrophotometer (Molecular Devices).

Concentrations of freshly purified CsgA and CsgB monomers were diluted to 4 μM, immediately after buffer exchange of proteins into PBS, pH 7.4. Prepared CsgA, CsgB, and equimolar mix of both proteins (4 μM each) were incubated at room temperature for two days to induce fiber formation. Biofilm protein fibers with histidine tags were labeled with nickel nitrilotriacetic acid- conjugated gold nanoparticles (5 nm, Nanoprobes). Briefly, the biofilm fibers were formed from freshly purified biofilm proteins in PBS (phosphate buffer saline) solution at room temperature. The droplets containing biofilm fibers were placed on a piece of parafilm, and TEM grids (formvar carbon-coated 200 mesh nickel grids (Electron Microscopy Sciences) were placed on droplets and incubated for five minutes. Then, TEM grids were washed with ddH_2O twice and selective binding buffer twice (1x PBS, 300 mM NaCl, 80 mM imidazole, 0.2% (v/v) tween-20). Following, TEM grids were placed on 90 μL of 10 nM of 5 nm Ni-NTA Au-NP dissolved in selective binding buffer for 90 min, at room temperature at dark. Then, TEM grids were washed with selective binding buffer (1x PBS, 300 mM NaCl, 80 mM imidazole, 0.2% (v/v) tween-20) 5 times, with PBS twice and with ddH_2O twice. Lastly, grids were put on a droplet of 2 % uranyl acetate (UA) for 25 seconds and air dried at room temperature. The samples were visualized using TEM (FEI Tecnai) at 200kV power setting.

2.3.8 Dynamic Light Scattering

Concentrations of freshly purified CsgA and CsgB monomers were diluted to 400 nM, 40 nM and 4 nM immediately after buffer exchange of proteins into PBS, pH

7.4. Dynamic light scattering (DLS) was performed (Nano-ZS Zetasizer Dynamic Light Scattering, Malvern Instruments) to determine Z-average size of the formed fibers immediately after buffer exchange to PBS (Day 0) and after 24 hours incubation for fibrillization (Day1). Each measurement was carried out in duplicate at 25 °C.

2.3.9 Circular dichroism (CD)

CD Spectra Measurement Device (Jasco J-815) was used to analyze the secondary structures of CsgA and CsgB. Proteins prepared in PBS were diluted to 1 uM in ddH_2O, right after buffer exchange and after 48 hours following buffer exchange. Measurements were taken using the following parameters: 25 ºC, 300 sec delay time, 1 mm band width. Secondary structure percentage were calculated using BestSel online tool.

2.3.10 Quartz Crystal Microbalance with Dissipation (QCM-D)

To induce fiber formation, CsgA, CsgB and equimolar concentration mix of both proteins were prepared in PBS buffer at concentrations of 1 µM, 2 µM, 2.5 µM, 3 µM, and 4 µM. Before each measurement, QCM-D sensor surfaces (Biolin Scientific) were treated with Piranha solution (1:3 Hydrogen peroxide: Ammonia) at 70°C for 30 minutes. Then, sensor surfaces were washed with ddH2O and dried with nitrogen stream. After baseline equilibration using PBS buffer, CsgA, CsgB, and equimolar mix protein samples were introduced to QCM-D (QCM Q-Sense E1)

chamber in a sequential order of increasing concentration (1 μM, 2 μM, 2.5 μM, 3 μM, and 4 μM), with washing steps between administration of each concentration. The absorption and material interaction behavior of the protein samples were evaluated on hydroxyapatite, silica, and gold sensor surfaces in three experimental sets using a QCM-D system. After the delivery of each protein concentration to the system and the washing step, frequency and dissipation changes were recorded at all harmonics (F1, F3, F5, F7, F9, F11 and F13).

To characterize the adsorption of protein samples onto different sensor surfaces, data from three different overtone orders were analyzed using the Langmuir equilibrium model, as reported in the literature previously (Tolga T. Olmez et al., 2018; Onur et al., 2018; Seker et al., 2017). This model relates the frequency change to the desorption strength by the following equation.

Eq. (1) $\Delta f = (f_{max} \times C)/(k_d + C)$

C is the protein concentration, f_{max} value was estimated by the Langmuir isotherm, and k_d value was determined by least-squares fitting.

Gibbs free energy is calculated using the following formula.

Eq. (2) $\Delta G^o = -RT \ln(k_{eq})$

R is the gas equilibrium constant (1.987 kcal K^{-1} mol^{-1}), T is the reaction temperature in K (298 K) and k_{eq} is $1/k_d$.

Significance is determined by Student's t-test. $p \leq 0.5$ is depicted as*, $p \leq 0.01$ as **, $p \leq 0.001$ as *** and $p \leq 0.0001$ as ****.

2.4 Results and Discussion

2.4.1 Cloning, expression and purification

Commercial pet22b (+) plasmid contains 6X His-tag sequence at the 3' end of the multiple cloning site. A GS linker was added between CsgA/CsgB and C-terminal His-tag sequence in order to provide flexibility to His-tag. Schematic diagrams of the construct designs are depicted in Figure 8.

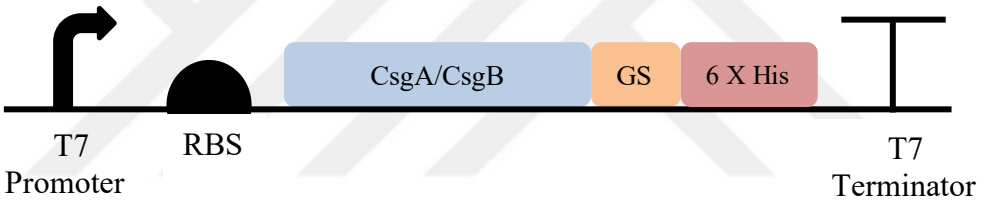


Figure 8. Schematic diagram of CsgA and CsgB expression cassette. His tag was added to the C terminal of proteins. GS linker was added to provide flexibility to His-tag. T7 promoter and terminator were used for expression by T7 polymerase.

Since CsgA and CsgB are *E. coli* biofilm proteins, the *csgA* and *csgB* genes were amplified from the genomic DNA of the *E. coli* K-12 strain (Figure 9) with the primers listed in Table B.1 and cloned into KpnI-XhoI digested pET22b(+) plasmid (Figure 10). (Figure C.1, Figure C.2).

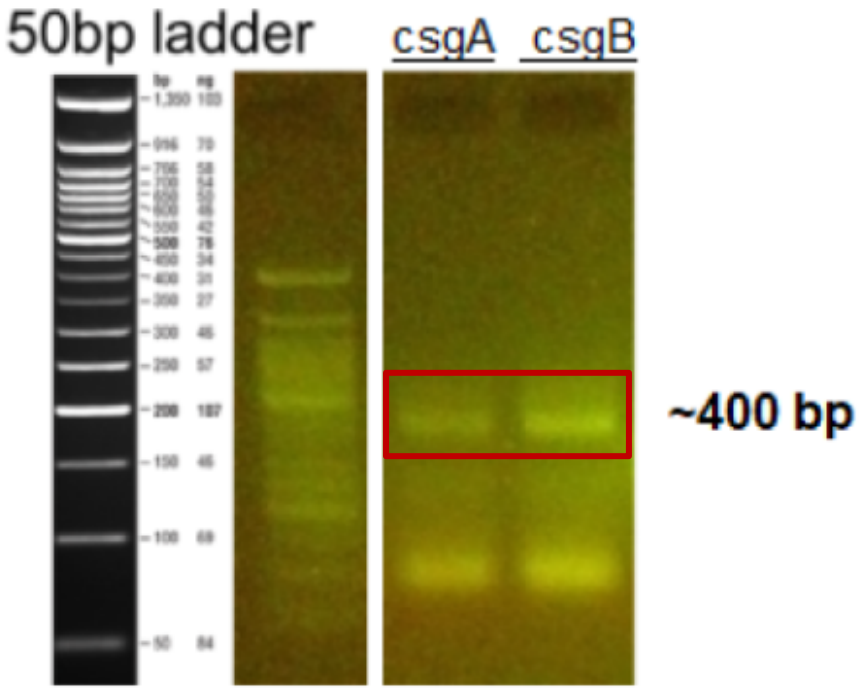


Figure 9. Amplification of *csgA* and *csgB* genes from bacterial genomic DNA. DH5α genomic DNA was used as a template to amplify *csgA* (lane 2) and *csgB* (lane3) genes. PCR reaction was performed according to the protocol of Q5 Polymerase (NEB). 50 bp DNA ladder (NEB) was used for detection (Lane1).

Clonings were verified by Sanger sequencing. Sequencing result was aligned with corresponding gene sequences at Geneious software. (Figure D.1, Figure D.2) and the match was 100 %.

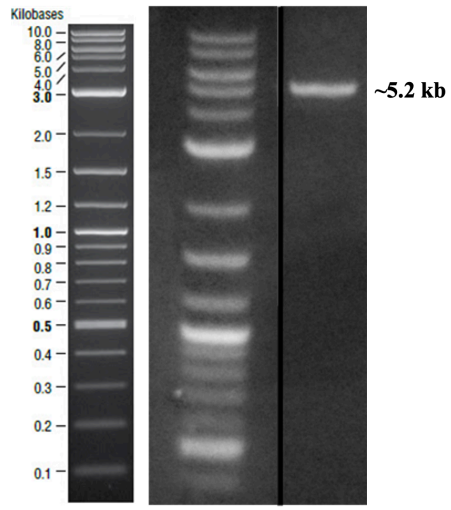


Figure 10. Agarose gel electrophoresis of pEt22b(+) plasmid digestion with KpnI-XhoI restriction enzymes. Bands ~ 5200 bp corresponds to digested plasmid (Lane 2). The ladder was 2-log DNA ladder (NEB) in Lane 1.

E. coli BL21 DE3 cells harboring pEt22b-CsgA and pEt22b-CsgB plasmids were induced with 0.5 mM IPTG at 37 °C for 2 hours. CsgA and CsgB proteins were purified with immobilized metal affinity chromatography (IMAC) under denaturing conditions. Purified CsgA and CsgB protein were desalted into PBS and treated with formic acid for monomerization, then verified using SDS-PAGE and Western blotting using antibodies against polyhistidine tag. Theoretical molecular weights of the recombinant CsgA and CsgB proteins were calculated as 15.52 kDa and 13.34 kDa, respectively, using the Swissprot Expasy tool. In Western Blot, CsgA band appeared at ~17 kDa and CsgB band appeared ~15 kDa, with small deviations from calculated molecular sizes (Figure 11).

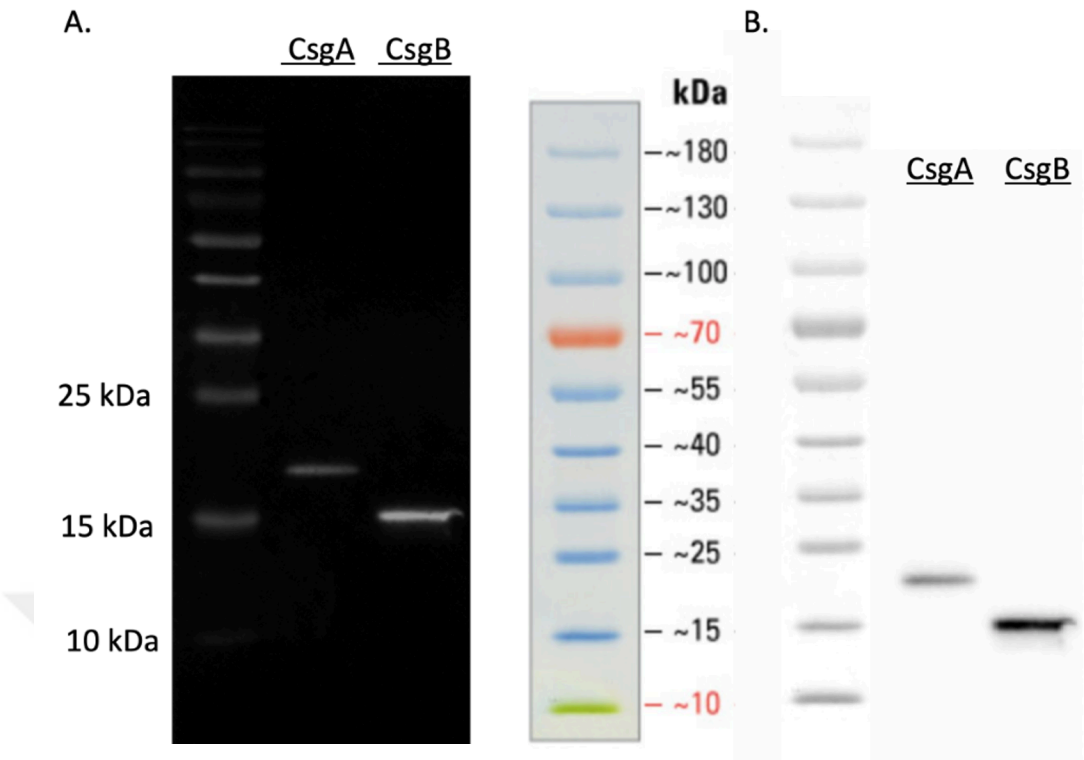


Figure 11. Purification of CsgA and CsgB by IMAC. A. Western Blot analysis. Lane 1 Page Ruler (NEB) ladder, Lane 2 purified CsgA, Lane 3 purified CsgB. B. SDS-PAGE analysis Lane 1 Page Ruler ladder, Lane 2 purified CsgA, Lane 3 purified CsgB.

2.4.2 Characterization of curli fibers

Dynamic light scattering measures the size distribution of small particles in a solution. Since the CsgA and CsgB monomers form oligomers by time, size distribution of CsgA and CsgB monomers and oligomers are expected to change over the course of incubation. Therefore, fibrillization of purified CsgA and CsgB monomers were detected by dynamic light scattering (DLS). The results for DLS analysis with different concentrations of CsgA and CsgB were summarized in Table

G.1 and Table G.2. The intensity distribution of those samples was also depicted in Figure G.1 and Figure G.2.

For CsgA at 400 nM, DLS analysis revealed a polydispersity index (PdI) of 0.366 (±0.007) and a Z-Average size of 262 (±7.0) nm right after dialysis (Day0) and a PdI of 0.421 (±0.05) and a Z-Average size of 485 (±18.8) nm after 1 day incubation (Day1). The increase in Z-average values indicated an increase in size, due to polymerization of CsgA during incubation. Additionally, PdI values suggested a polydispersed state for both days and indicated an increase in polydispersity upon incubation.

For CsgB samples at 400 nM, DLS analysis revealed a polydispersity index (PdI) of 0.339 (±0.02) and a Z-Average size of 263 (±8.8) nm at Day0 and a PdI of 0.415 (±0.001) and a Z-Average size of 2166 (±55) at Day1. Similar to CsgA, the increase in Z-average values indicated an increase in size, due to polymerization of CsgB. PdI values suggested a polydispersed state for both days and indicated an increase in polydispersity upon incubation.

In addition, assemblies of the CsgA and CsgB fibers were visualized by TEM analyses. 6X His tags of CsgA and CsgB fibers were labeled with Ni-NTA conjugated gold nanoparticles and nanofiber structures formed by CsgA and CsgB was shown by gold nanoparticle labelling (Figure 12). Assemblies of the nanoparticles on the nanofibers displaying His-tags were visualized by TEM. The TEM images validated that CsgA and CsgB proteins in PBS form fiber structures in the course of 2 days incubation at room temperature.

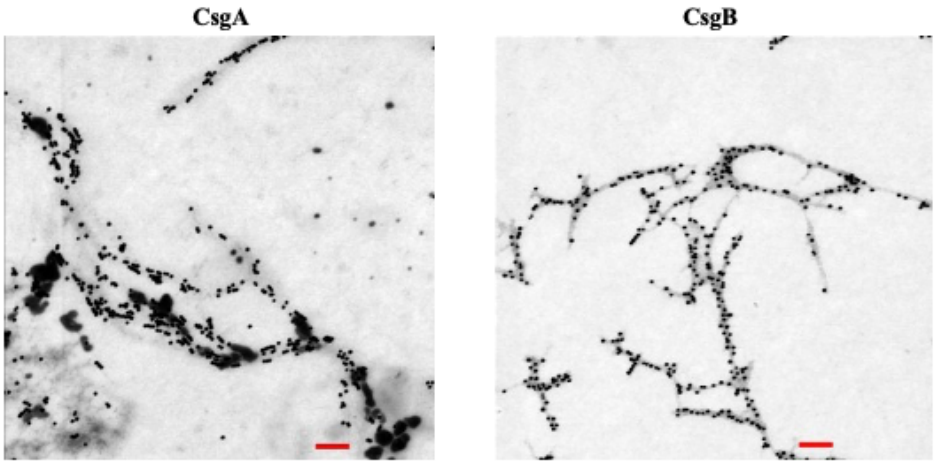


Figure 12. TEM analysis of CsgA and CsgB fibers. 2 days old CsgA and CsgB nanofibers (4 μM) were labeled with Ni-NTA-conjugated gold nanoparticles (lines represent 100 nm scale bar).

2.4.3 Secondary structure analysis

CD measures the absorption of differences in right and left circularly polarized light from samples and structural elements (α helix, β-sheet, turns, random coils) in a protein gives a characteristic excitation in spectrum. This way, secondary structure elements in proteins can be determined by CD (Micsonai et al., 2015).

In order to observe the secondary structural elements in CsgA and CsgB, CD analysis was performed with monomers (1 hr) and oligomers/fibers (48 hrs) with different incubation times. Bestsel online tool was used to calculate percentages of each structural element and results were summarized in Figure 13. For both CsgA and CsgB, ratio of alpha helices decreased, and ratio of anti-parallel beta sheets increased upon incubation, which correlates with the formation of beta-sheet rich amyloid fibers during the course of incubation.

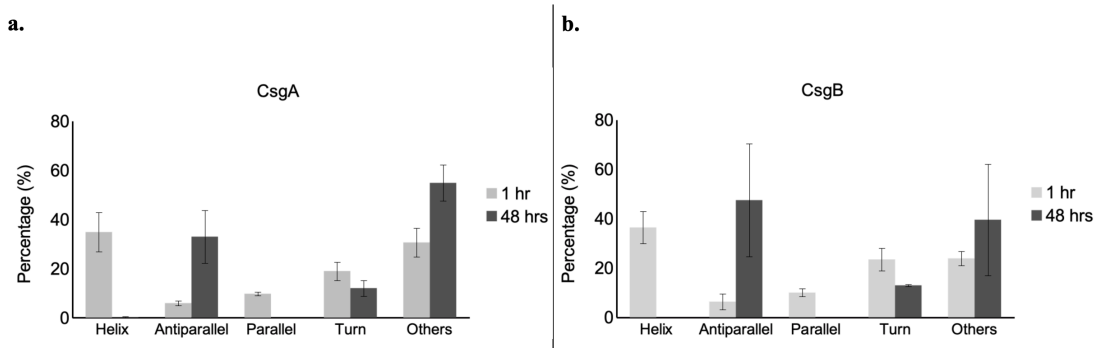


Figure 13. CD spectrum measurement for secondary structure analysis. Change in secondary structure elements by time was calculated by BestSel for a. purified CsgA protein and b. purified CsgB protein. n=3.

2.4.4 Real-time monitoring of nanofiber assembly with Quartz Crystal Microbalance with Dissipation (QCM-D)

QCM-D is a powerful tool to track interactions of proteins with solid surfaces by providing real-time data for protein binding as well as dissipated energy upon protein / surface interaction (Hnilova et al., 2008). The binding equilibrium constant and binding free energy of the proteins were calculated by measuring the frequency changes during protein addition processes and washing steps.

CsgA, CsgB and CsgAB mix nanofibers were used for QCM D analysis. Those samples were obtained by incubating the CsgA protein, CsgB protein and their equimolar mixture (CsgAB) for two days at room temperature. Each of the polymerized CsgA, CsgB, and CsgAB proteins were deposited on three different types of QCM sensors, and the frequency change versus concentration graphs was drawn. Langmuir isotherm model provides a direct model to quantify protein adsorption. Using this model, dissociation constants (k_d) were calculated by Eq. (1),

relating the frequency change to desorption strength. In this equation, Δf is the frequency change recorded by QCM D at each step following protein administration with increased concentrations. C corresponds to protein concentration at the step where Δf was recorded. f_{max} value is the maximum theoretical frequency change and it was estimated by the Langmuir isotherm, using recorded frequency changes upon differing protein concentrations.

Upon addition of increasing concentrations of polymerized CsgA through the QCM-D system a drop in frequency for all three surfaces (Figure 14) was recorded. Except for CsgA, other incubated protein samples have highest binding affinity to hydroxyapatite (HA) surface compared to gold and silica. CsgB and CsgA-CsgB equimolar mixture polymers have higher binding affinity to gold than silica (Figure 15, Figure 16), while CsgA polymer exhibits approximately similar affinity for the two surfaces (Figure 14).

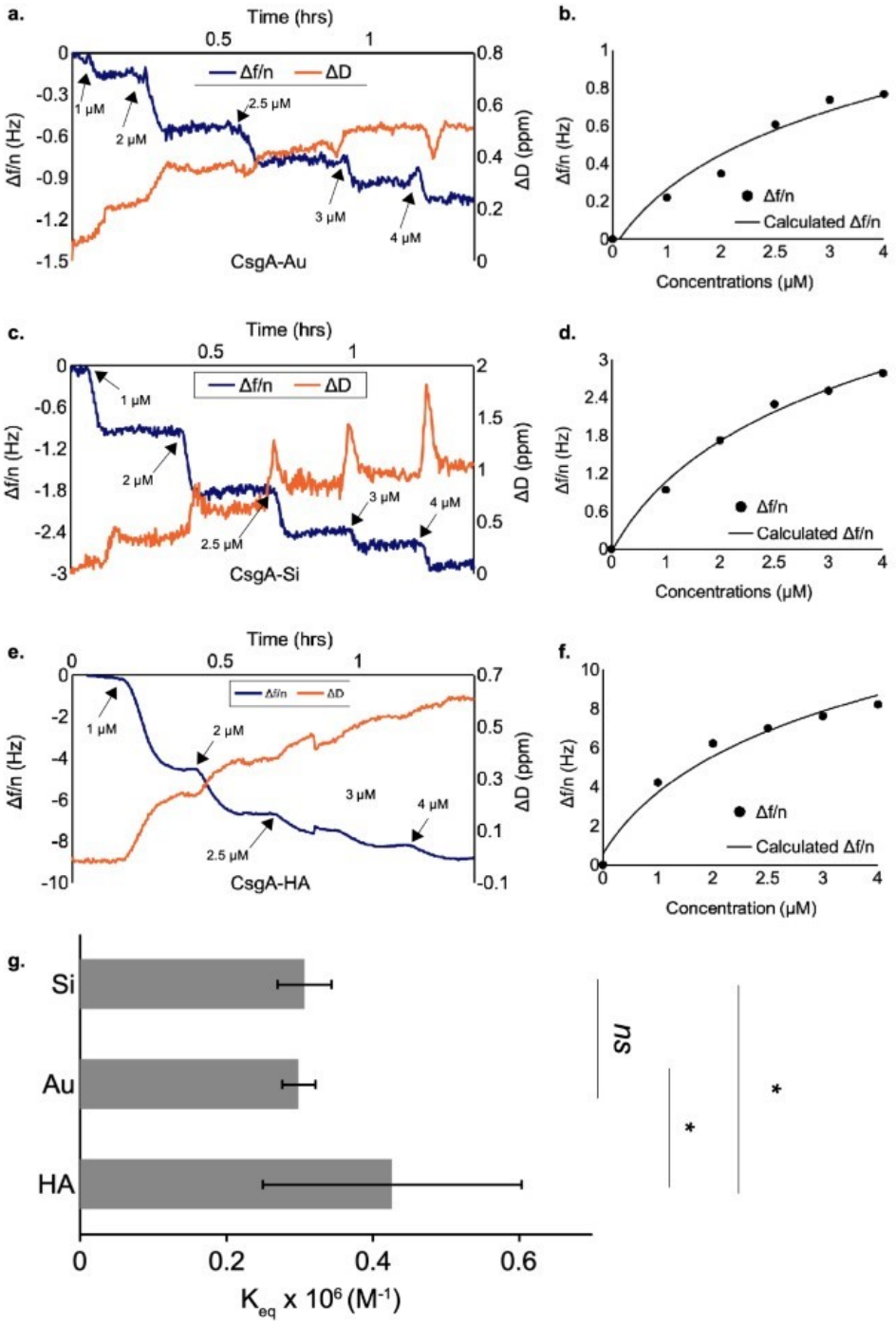


Figure 14. QCM measurement of 2 days old CsgA fibers. Binding kinetics to the (a) gold, (b) silica, and (c) HA coated quartz surface is shown as a resonance frequency change. d. Binding equilibrium constants of polymerized CsgA on gold, silica, and HA coated surfaces. Significance values are calculated by t-test, n=3.

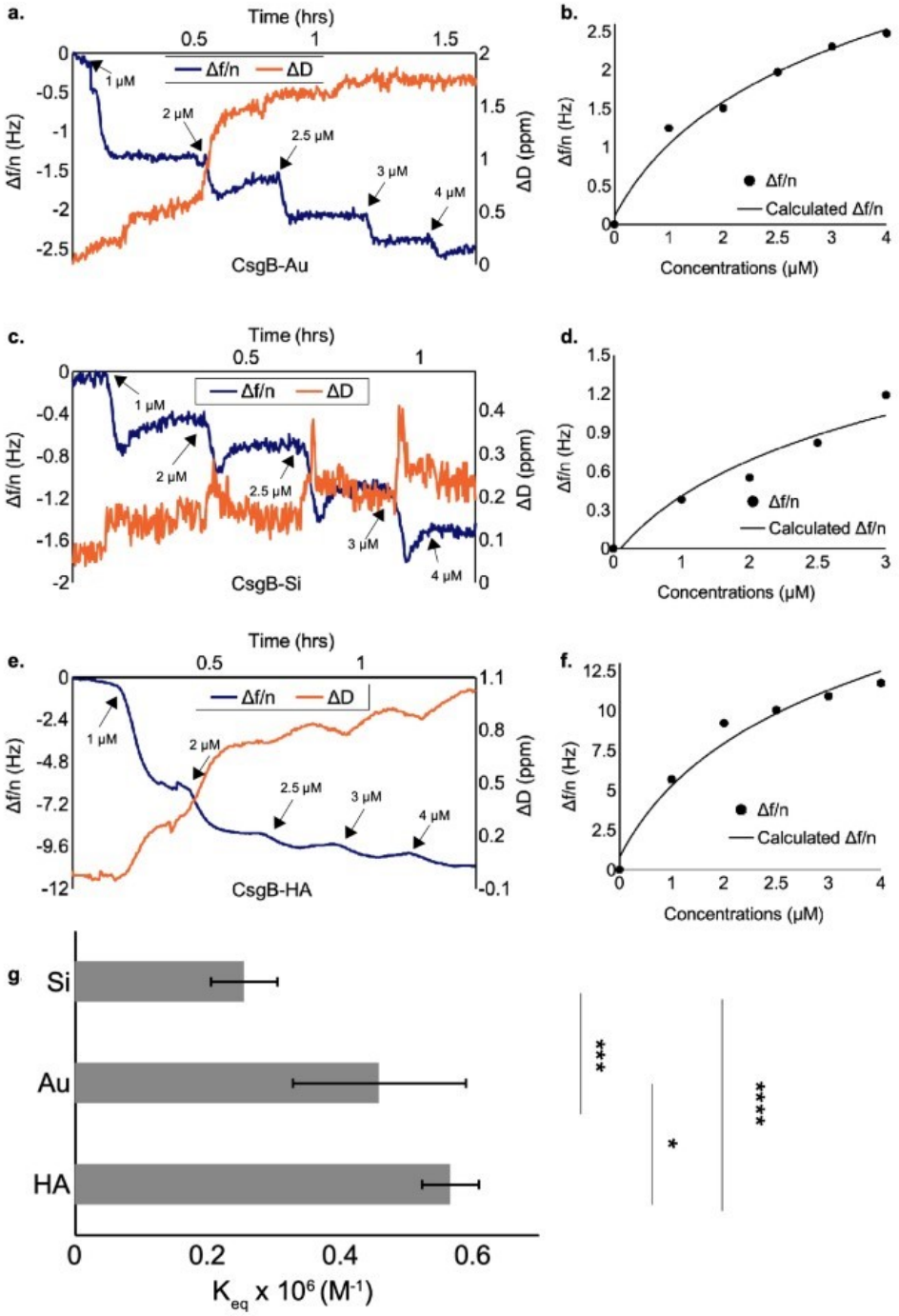


Figure 15. QCM measurement of 2 days old CsgB fibers. Binding kinetics to the (a) gold, (b) silica, and (c) HA coated quartz surface is shown as a resonance frequency change. d. Binding equilibrium constants of polymerized CsgB on gold, silica, and HA coated surfaces. Significance values are calculated by t-test, n=3.

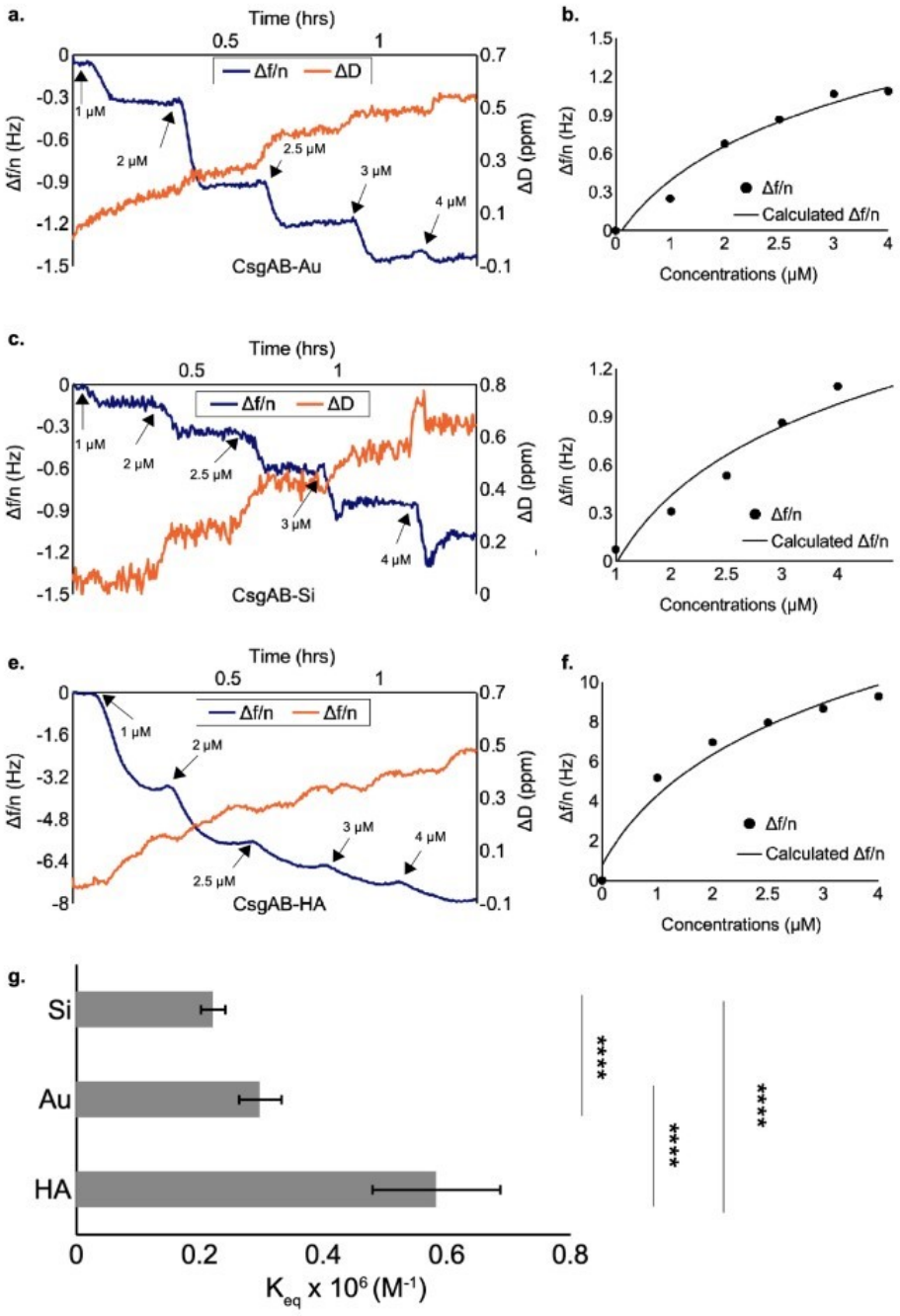


Figure 16. QCM measurement of 2 days old CsgA-CsgB mix fibers. Binding kinetics to the (a) gold, (b) silica, and (c) HA coated quartz surface is shown as a resonance frequency change. d. Binding equilibrium constants of polymerized CsgA-CsgB mix on gold, silica, and HA coated surfaces. Significance values are calculated by t-test, n=3.

In assessing surface binding characteristics, it should be noted that proteins and peptides vary in length, amino acid contents, as well as their charge (neutral or positive) and polarity or hydrophobicity. Based on diversity of peptides and proteins, it has been possible to identify common adsorption motifs on specific surfaces (John et al., 2019). Another contributing factor in binding of a given protein is the properties of targeted surfaces. In a previous study, which examined the adsorption of CsgA subunit to graphene and silica surfaces by atomic simulation, it was reported that structural and sequence characteristics of CsgA affect the adhesive strength and consequently provide strong adhesion to both polar and non-polar surfaces (DeBenedictis et al., 2016).

Silica surface is composed of silanol groups (Si-OH) and siloxane bridges (Si-O-Si), and at pH values higher than 3 silanol groups tend to be deprotonated (Mathé et al., 2013). Therefore, in our experimental setup, silica chips have a negative surface charge at pH 7. Surface charge is an essential parameter in terms of protein adsorption onto surfaces. The consensual view suggests that the reversible first step of protein adhesion onto silica results from the electrostatic properties of proteins (Fenoglio, Fubini, Ghibaudi, & Turci, 2011). Therefore, at neutral pH, positively charged amino acids Arg, Lys, and His are considered essential for the electrostatic interactions with the negatively charged silica surface.

Interestingly, instead of the net charge of the protein, the total number of negatively and positively charged amino acids affect the binding affinity of proteins onto silica, probably due to increased polarity and hydrophilicity (Mathé et al., 2013). Comparing our constructs in this study, CsgB contains more charged residues than CsgA. Even though we expect CsgB to have a higher affinity than CsgA, calculated binding free energies of CsgA, CsgB, and CsgA-CsgB mix on gold, silica, and HA

surfaces suggests the opposite (Figure 17). Here, considering the second step of protein adhesion can provide more detailed insight for those observations.

The second step, generally considered irreversible, depends on the ability of proteins to form structural changes on the surface. Tightly structured (or rigid) proteins do not induce conformational changes on the surface, so they are not very prone to adsorption. Proteins with weak internal interactions (or soft proteins), on the other hand, can structurally rearrange themselves on the surface more easily and efficiently, and maximize the number of protein-surface interactions (Ikeda & Kuroda, 2011). In addition to the aforementioned electrostatic interactions, hydrophobic residues exposed to protein surface during the conformational changes may interact with the hydrophobic siloxane bridges on the silica surface. Therefore, in addition to the interaction with the charged residues, rigidity/softness of the protein structure is crucial for adhesion onto the silica surface. It has been demonstrated that curli fibers composed of only CsgB proteins exhibit more stiffness than curli fibers composed of only CsgA protein (Abdelwahab et al., 2017). Besides, combined secretion of CsgA and CsgB proteins in biofilms can produce mechanically stiffer nanofibers. Therefore, the stiffer nature of CsgAB fibers is in correlation with the behavior of mixture protein on the silica surface, which exhibits the highest Gibbs free energy, and therefore lowest silica affinity (Figure 17). Similarly, CsgA possessing the highest affinity to silica surface is in correlation with its lower stiffness compared to CsgB and mixture fibers. Therefore, the rigidity of the fibers appears to be a crucial parameter for adhesion onto the silica surface.

Hydroxyapatite (HA) is a naturally occurring mineral with the chemical formula Ca5(PO4)3(OH)]. HA has a high affinity for proteins and other biomolecules (Zhou, Wu, Dong, Wang, & Shen, 2007). Studies suggest that the pH and mechanical

properties of proteins, as well as the surface topology of HA, can affect the protein-HA interactions (Q. Wang et al., 2017). Computational studies suggested that –COO– and -NH2 are the main interactions sites with HA and play crucial roles in the protein adsorption onto the HA surfaces by forming O-Ca-O connections and hydrogen bonds (H-bonds). Adsorption of proteins onto the Ca-rich HA surface can be mainly regulated by strong electrostatic interactions involving Ca atoms of HA and O atoms of carboxyl groups (Azzopardi et al., 2010). Those strong electrostatic interactions also occur between PO4-3 anions in HA structure and the -NH+ and -C(NH)+ groups in the protein structure (Dong et al., 2008). Therefore, acidic amino acid residues Asp and Glu can serve as primary interaction sites with Ca, whereas basic amino acid residues Arg, Lys, and His can serve as interaction sites with PO4-3 anions. Overall, CsgA is more acidic (pI value 5.20) than CsgB (pI value 6.57), and CsgA has more acidic residues than CsgB. In contrast, CsgB has more basic amino acids than CsgA. ΔG calculations suggest that the interaction of CsgB with the HA surface is significantly higher than of CsgA (Figure 17). The strength of those interactions is ruled by interaction distances, as well as the number of interaction sites (Azzopardi et al., 2010; Q. Wang et al., 2017). The higher affinity of CsgB can be due to the stronger interactions of basic amino acids with HA surface, rather than the number of interacting residues. The binding affinity of CsgB and CsgAB is not significantly different, indicating the forces that dominate CsgB interaction with HA is also governing CsgAB interaction with the surface.

Cysteines in proteins can interact with gold surfaces via irreversible chemisorption, however molecular dynamic simulations suggest that initial steps of recognition are due to electrostatic interactions. Computational studies suggested that histidine (His) and methionine (Met) residues have high gold binding propensity and can facilitate

the initial adsorption of proteins onto gold surfaces, creating interactions approaching covalent bonds (Ozboyaci et al., 2016). Other molecular dynamics simulation studies proposed that aromatic residues form strong interactions with gold, possibly due to π electron mediated effects. Besides, positively charged amino acids also have strong binding affinities, whereas apolar aliphatic amino acids and negatively charged amino acids have weak interactions with the gold surface (Hoefling et al., 2010, p. 111). Experimental studies showed that arginine (Arg), tryptophan (Trp), tyrosine (Tyr), and cysteine (Cys) amino acids are overrepresented in peptide groups with strong gold binding affinities (Hnilova et al., 2008).

CsgA and CsgB do not have any Cys in their structure; therefore, chemisorption of fibers onto gold surfaces is not affecting the binding affinity. Additionally, the number of aromatic groups in both CsgA and CsgB is the same; hence the aromatic group-Au surface interactions are not expected to contribute significantly to the difference in their surface binding affinity. To determine the charge of the proteins at pH 7.0, isoelectronic points were calculated using ExPASy. CsgA has a theoretical pI value of 5.20, and CsgB has a theoretical pI value of 6.57 that indicates both proteins are negatively charged at pH 7.0. CsgB has more positively charged amino acid residues than CsgA. Correspondingly, CsgB is expected to have a higher Au binding affinity than CsgA, because of the strong binding affinity of positively charged amino acids to Au. Besides, as the Met is reported to have a high gold binding propensity, five Met groups in CsgB can contribute to the Au binding affinity more than in CsgA, which has only two met groups in its structure. Histidine groups can also contribute to gold binding affinity, however both CsgA and CsgB have the same number of His groups. Therefore, His groups are not expected to have a role in the difference of gold binding affinity for CsgA and CsgB. As anticipated, calculated ΔG

values indicated that the affinity of CsgB to Au surface is significantly higher than of CsgA and CsgAB equimolar mix ($p < .001$) (Figure 17). ΔG values of CsgA and CsgAB mix do not show a significant difference, indicating that the binding pattern of CsgA dominates the interaction of the mixture with the gold surface.

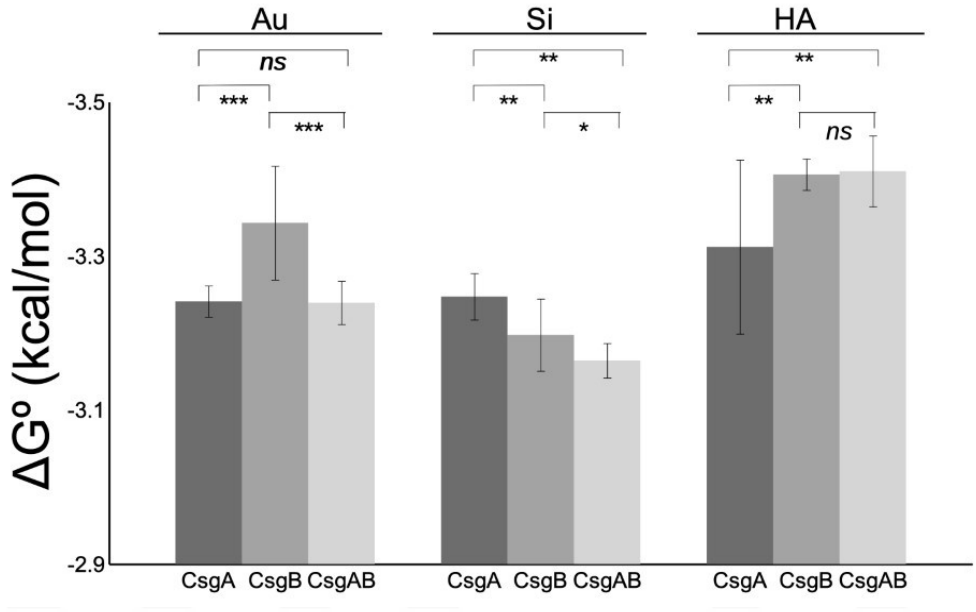


Figure 17. Binding free energy of polymerized CsgA, CsgB and CsgA-CsgB mix on gold, silica and HA. Significance values are calculated by t-test, n=3.

2.5 Conclusion

CsgA and CsgB proteins are excellent candidates for nanomaterial synthesis due to their self-assembly capabilities, and their easy manipulation by genetic engineering. Depending on the intended purpose, binding of proteins to selected surfaces at controlled and adjustable levels is essential in the design and development of various amyloid-based functional materials. To obtain controlled and adjustable binding, it is

necessary to examine and characterize systems, including proteins and target surfaces.

Here we reported that CsgA, CsgB and their mixture behave differently in terms of binding and interaction with gold, silica and HA surfaces. According to our observation CsgB protein is the key protein that dictates the final adhesiveness of the final CsgAB protein mixture on HA and silica surfaces. In contrast to this observation, CsgA is the key component in controlling the behavior of CsgAB mixture on gold surface. Our findings provide an understanding of binding behavior of CsgA, CsgB and their mixture to gain a better control on their adhesion on a targeted surface.

3 CHAPTER III

GLYCOSYLATED BIOFILM PROTEINS FOR FUNCTIONAL BIOMATERIALS

3.1 Introduction

Protein glycosylation is a common form of post-translational modification in all domains of life. Glycosylation is crucial for adhesiveness of proteins, and many adhesive proteins such as spider silk are heavily glycosylated (Hennebert, Maldonado, Ladurner, Flammang, & Santos, 2015). Glycosylation in prokaryotes is generally associated with but not restricted to pathogenicity, due to increased adhesiveness to host cells (Schmidt, Riley, & Benz, 2003; Tan, Tang, & Exley, 2015). Glycans can be covalently attached to the amide nitrogen of Asn (N-linked glycosylation) or hydroxyl oxygen of Ser and Thr (O-linked glycosylation) (Nothaft & Szymanski, 2010). *Campylobacter jejuni* is the first bacteria discovered with N-linked glycosylation. *C. jejuni* glycosylation pathway became the most extensively studied bacterial glycosylation mechanism due to the transfer of protein glycosylation (*pgl*) operon into *Escherichia coli* (Szymanski et al., 1999; Wacker et al., 2002). *pgl* is a 17 kb long operon with 12 genes. Glycan molecules are synthesized in the cytoplasm,flipped to the periplasm by PglK and transferred to the nitrogen of Asn in D/E-X1-N-X2-S/T motif (X1 and X2 can be any amino acid

except proline) in the periplasm to complete glycosylation process (H. Li et al., 2017; Linton et al., 2005).

Biofilms are multicellular assemblies formed by many bacterial species in nature to help them tolerate harsh environmental conditions and mediate substrate adhesion. Bacteria in biofilms secrete a cohesive and protective extracellular matrix composed of nucleic acids, polysaccharides, other biomolecules, and protein fibers as scaffolds (Flemming & Wingender, 2010). Amyloid and amyloid-like fibrils serve several functions in biofilms, especially during adhesion onto different surfaces and host cells (DeBenedictis et al., 2016).

Amyloid biofilms are emerging functional biomaterials with broad applications. Recent efforts exploited the functionalization of amyloid fibrils for applications such as waste-water treatment (Bolisetty & Mezzenga, 2016), material synthesis (Kalyoncu et al., 2019; Nguyen et al., 2014; Tolga Tarkan Olmez, Sahin Kehribar, Isilak, Lu, & Seker, 2019), enzyme immobilization (Ahan, Saltepe, Apaydin, & Seker, 2019), and biomineralization (C. Li et al., 2014; Yang et al., 2018) due to their exquisite mechanical properties and ease of manipulation via genetic engineering. As an example, curli fibrils fused with mussel foot proteins (Mfps) are reported as strong underwater adhesives (Zhong et al., 2014). Since *Bacillus subtilis* is generally regarded as safe (GRAS), its amyloid-like protein TasA is also used to create living materials with desired functionalities (J. Huang et al., 2019).

3.2 Objective

Up to date, several functional groups are attached to proteins to incorporate desired modifications and functions (Ahan et al., 2019; Bolisetty & Mezzenga, 2016; J.

Huang et al., 2019; Yang et al., 2018). Most adhesive proteins being heavily glycosylated can imply many opportunities for glycosylation in protein-based biomaterial applications. *de novo* glycosylation may increase the adhesiveness of biofilm fibers, since the biofilm proteins already formed rigid, robust and adhesive fibrillar structures (Axpe et al., 2018). Given the fact that amyloid-like TasA fibrils are utilized in biomaterial research, glycosylation appears to be a practical tool to alter adhesive properties. Consequently, the feasibility of TasA protein fibrils as adhesive materials may be utilized in several areas.

In this part of this thesis, I introduced and characterized glycosylation on TasA fibrils in terms of fibril structure, binding kinetics and adhesive properties. TasA protein was engineered to include the D/E-X1-N-X2-S/T (DQNAT) glycosylation motif at the C terminal and expressed it in *E. coli* containing *pgl* circuit. Subsequently, the effect of N-linked glycosylation on fibril formation and viscoelastic properties of fibrils were examined, as well as the time-dependent binding kinetics of matured TasA fibrils on solid surfaces. It was demonstrated that glycosylation can enhance adhesive properties of amyloid-like fibrils without disrupting fibrillization to produce biomaterials with superior adhesive performance.

3.3 Materials and Methods

3.3.1 Bacterial strains and cell maintenance

In this study, *E. coli* DH5α strain (NEB) was utilized for cloning. Cells were maintained at the same conditions as the studies in Chapter 2. *E. coli* BL21 DE3

strain (NEB) was used for protein expression. This strain was maintained at the same conditions as for *E. coli* DH5α.

3.3.2 Mammalian Cell Lines

HeLA S3 cells (ATCC) were cultivated in DMEM (Lonza) containing 2 mM L-glutamine, 1 g/L glucose, 10% FBS (Gibco, South America origin), penicillin (5000 U/mL) and streptomycin (100 mg/mL) (Gibco) in 5% CO_2 humidified incubator at 37ºC (Binder).

3.3.3 Plasmid construction

The *tasA* gene without signal sequence and with C terminal flexible GS linker (GGSG) was retrieved from the genome of wild-type *B. subtilis 168* strain. Cells were grown overnight, and genomic DNA was isolated according to the manufacturer's guidelines (QIAamp genomic DNA kit). Genomic DNA was amplified using Q5 DNA polymerase (NEB) with primers targeting the *tasA* open reading frame, which were listed in Table B.2 (Reaction conditions were described in APPENDIX F). To create a pET-22b (+) plasmid with *pgl* glycosylation recognition site after polyhistidine tag, DQNAT motif was added to pET-22b (+) plasmid via PCR using forward primers with DQNAT motif at the overhang region. Primer sequences used for PCR reactions were listed in Table B.2. For TasA cloning, resulting DNA fragments and the pET-22b (+) plasmid were restriction digested by high fidelity KpnI (NEB) and XhoI (NEB) enzymes (Reaction conditions were

described in APPENDIX F). For TasA-DQNAT cloning, *tasA* PCR fragments with suitable restriction sites and pet22b (+) PCR fragments with DQNAT were restriction digested by HF SacI (NEB) and AvrII (NEB).

All PCR products and digested plasmids were verified and isolated as explained in Section 2.3.2. Digested DNA fragments were ligated by T4 DNA ligase (NEB) (Reaction conditions were described in APPENDIX F) and transformed into DH5α chemically competent cells, as described in 2.3.2. Plasmid maps were shown in Figure C.3 and Figure C.4. After overnight incubation, single colonies were selected and positive clones containing *tasA* and *tasA-DQNAT* genes were verified by Sanger sequencing (Genewiz, USA) (Figure D.3, Figure D.4). All genetic part sequences used this chapter was introduced in Table A.2 and the amino acid sequences of each design were listed in Table E.2.

All plasmid maps were designed by Benchling online tool. After cloning, selected colonies were verified by Sanger sequencing (GENEWIZ). The sequencing results were analyzed by Geneious R9.0.5 software.

3.3.4 Expression and purification of non-glycosylated and glycosylated recombinant proteins in E. coli

E. coli BL21 DE3 strain was used to express non-glycosylated TasA (TasA WT) and TasA-DQNAT (TasA D) proteins. pEt22b (+) TasA and pEt22b (+) TasA-DQNAT plasmids were transformed into *E. coli* BL21 DE3 strain via chemical transformation. To obtain TasA proteins with glycosylation (TasA DP), TasA-DQNAT construct was transformed to *E. coli* BL21 DE3 strain containing *pgl*

pathway from *C. jejuni*, a kind gift from Markus Aebi (Wacker et al., 2002). Expression of TasA and TasA-DQNAT were controlled by T7 promoter and switched on in the presence of IPTG. Bacteria harboring TasA and TasA-DQNAT expressing plasmids were grown in the auto-induction medium (Fox & Blommel, 2009) for 24 hours at 37 °C, 200 rpm. Following incubation, bacterial culture was centrifuged at 8000 RCF and the pellets were kept at -80 ºC until purification.

For purification, cell pellets were resuspended in lysis buffer (1X PBS pH 7.4 containing 6M guanidine hydrochloride and 20mM imidazole and 0.2% Tween-20). The suspensions were incubated at +4 ºC for 1 hour, on an end-to-end rotator, then sonicated at 30% power for 5 minutes with 10 s on/20 s off cycles. Sonicated suspensions were centrifuged at 21.500g for 1 hour and supernatant was filtered with 0.45µm filter. Filtered lysate was loaded on HisTrap nickel column (GE life sciences 17524701) that was pre-equilibrated with wash buffer (1X PBS pH 7.4 containing 6M guanidine hydrochloride and 20mM imidazole and 0.2% Tween-20). The column was washed with 10 column bed volumes of wash buffer. Finally, proteins were eluted with 5 column bed volumes of elution buffer (1X PBS pH 7.4 containing 6M guanidine hydrochloride and 500mM imidazole). To remove Gdn HCl and induce fibrillization of proteins, samples were dialyzed against ddH_2O for 2 hours at room temperature and then for O/N at +4 °C in fresh ddH_2O, with gentle stirring.

3.3.5 SDS-PAGE and Western Blot

Since TasA is an amyloid-like protein, it tends to form amyloid-like fibers. GdnHCl provides the strong denaturing conditions required for purification and upon the

removal of GdnHCl, TasA starts to form oligomers/fibers. However, TasA fibers are not as strong as CsgA or CsgB fibers, therefore incubating TasA fibers at 95 ºC in SDS-PAGE sample buffer for 1 hour is sufficient to break down protein oligomers for SDS-PAGE analysis (L. Chai et al., 2013). TasA and TasA-DQNAT proteins were dissolved in 2x Laemmli sample buffer and incubated at 95 ºC for 1 hour. 12% SDS gel was used to separate ~ 35 kDa TasA proteins. 12 % SDS-PAGE was casted as described in 2.3.6. 1×SDS Running Buffer was used during the run.

For SDS-PAGE, the gels were stained staining in Coomassie brilliant blue R-250 and for destaining the gel was incubated in destaining solution until the bands were clearly visible. For detecting his-tagged proteins by Western blot was conducted as explained in Section 2.3.6.

3.3.6 Detection of glycosylation by soybean agglutinin (SBA) blot

For SBA blot, TasA proteins were electrophoresed on 12 % SDS-PAGE and proteins were transferred to PVDF membrane using Trans Blot Turbo (Biorad). Following, the membrane was blocked with 5% bovine serum albumin (BSA) (Sigma) in TBS-T (0.1 % Tween 20) for 2 hours with rocking at room temperature. After blocking, the membrane was transferred into 5% BSA in TBS-T containing 1:2500 HRP conjugated SBA (Sigma Aldrich, L1395) and incubated for 1 hour at room temperature with rocking. The membrane was washed with TBS-T for 5 minutes, a total of 5 times with shaking. ECL Substrate (Biorad 170-5060) was used for visualization according to manufacturer's instructions and the membrane was imaged immediately in ChemiDoc MP Imaging System (Biorad) with Image Lab Software.

3.3.7 Fiber formation and scanning transmission electron microscopy (STEM)

Protein concentrations were determined using BCA Assay as explained in previous chapter. Concentrations of freshly purified TasA WT, TasA D and TasA DP monomers were diluted to 10 μM, immediately after dialysis of proteins into ddH_2O. Prepared TasA WT, TasA D and TasA DP proteins were incubated at room temperature for 28 days to induce fiber formation.

Fiber formation characteristics and fiber morphologies of TasA WT, TasA D and TasA DP samples were analyzed by scanning electron microscopy (STEM) at Day1, Day7, Day14 and Day 28 of fibrillization. For STEM analysis, biofilm protein fibers with histidine tags were labeled with nickel nitrilotriacetic acid- conjugated gold nanoparticles (5 nm, Nanoprobes) on TEM grids (formvar carbon-coated 200 mesh nickel grids (Electron Microscopy Sciences), as described previously in 2.3.7. The samples were visualized using STEM module of environmental scanning electron microscope (SEM) (FEI Quanta 200 FEG) with varying voltages.

3.3.8 Fiber characterization by atomic force microscopy (AFM)

For atomic force microscopy (AFM) analysis of fiber morphology and fiber kinetics, following affinity chromatography, size exclusion chromatography was performed using HiPrep 16/60 Sephacryl S-200 HR SEC column (GE lifesciences) according to the manufecterer's protocol. 1X PBS pH 7.4 containing 6M guanidine hydrochloride was used as mobile phase. Then, proteins were desalted into 25 mM NaCl using HiTrap desalting column (GE lifesciences), according to manufacturer's instructions.

Desalted proteins were incubated at room temperature over the period of 28 days. At day 21 and 28, samples were prepared for imaging. 100 µl protein sample was incubated for 3 minutes on freshly cleaved mica surface. Treated mica was rinsed with ddH_2O, then dried with nitrogen stream. The AFM was operated at tapping mode using silica cantilevers. The acquired images are used for height and length analysis of fibrils with the open-source software FiberApp (Usov & Mezzenga, 2015). The fibril height and length distributions of TasA, TasA D and TasA DP were compared with each other using the Kolmogorov–Smirnov statistic test. p values were calculated, and distributions were accepted as the same if p value is greater than 0.05.

3.3.9 Secondary Structure Analysis by Circular Dichroism (CD)

For CD analysis, 1 µM of each protein was prepared at Day1, Day7, Day 14 and Day 28 of incubation. The CD spectra of samples was measured from 300nm to 190nm with 5 repeats (Jasco J-815) at room temperature with 300 sec delay time, 1 mm band width. Data was analyzed using the Bestsel online tool for secondary structure analysis (Micsonai et al., 2018, 2015).

3.3.10 Quartz Crystal Microbalance (QCM)

The gold QCM sensors were cleaned with basic piranha solution (1:3 Hydrogen peroxide: Ammonia) at 70°C for 30 minutes, washed in ddH_2O and dried with N_2 stream before each measurements. QCM sensor was equilibrated with the ddH_2O.

Proteins were diluted to 1µM, 2µM, 5µM and 10µM samples and sonicated at sonic baths just before use. Samples with increasing concentrations were applied with 30 µL/minute flow rate for 3 minutes at 25°C. Between each concentration, QCM sensor was equilibrated with the ddH_2O for 10 minutes. F1, F3, F5, F7, F9, F11 and F13 harmonics were collected during the experiments on QSense explorer QCM device with gold coated sensor (Biolin Scientific). QCM data were collected for all TasA, TasA D and TasA DP samples at Day7, Day 14 and Day28.

To characterize the effect of glycosylation on the adsorption of each TasA samples onto gold sensor surfaces, data from five different overtone orders were analyzed using the Simple adsorption model:

$\Delta f = (f_{max} \text{ x } C)/(k_d + C)$

where C was the protein concentration, f_{max} value was estimated by the adsorption isotherm, and k_d value was determined by least-squares fitting.

ΔG^o values were calculated according to the formula:

$\Delta G^o = -RT\ln(k_{eq})$

where R was ideal gas constant (1.987 kcal/ K. Mol), T was temperature at Kelvin scale, and k_{eq} was $1/k_d$. Statistical significance between experimental sets were calculated using student t-test.

3.3.11 Cell adhesion

Non-treated 96 well plates were coated with 10 µM of matured TasA, TasA D and TasA DP samples at Day7, Day14 and Day28 of maturation. 50 µl of samples were dried on the wells, as triplicates. The wells were blocked by 0.1 % BSA in low glucose DMEM, overnight at +4 ºC. Next day, 5 X 10^4 HeLa S3 cells were added to

each well in FBS free low glucose DMEM with 0.1% BSA and allowed to adhere onto coated surfaces for 90 minutes in 37 ºC, 5% CO_2 incubator. Following, non-adherent cells were washed with 1 X PBS three times and for recovery, adhered cells were incubated in 10 % FBS low glucose DMEM for 4 hours in 37 ºC, 5% CO_2 incubator. Wells were washed with 1 X PBS 3 times, and alive cells adhered onto coated surfaces were dyed with 1 μM Calcein AM for 30 minutes. The adhered cells were visualized with an inverted fluorescent microscope and cells were counted from 3 different points for each well. Experiments were conducted in triplicates. Statistical significance between experimental sets were calculated using student t-test.

3.4 RESULTS AND DISCUSSION

3.4.1 Cloning, expression and purification

In this study, we focused on TasA amyloid-like protein due to its functionalization capacity with peptide/protein inserts without losing its self-assembling properties, therefore allowing production of nanofibrils with additional desired functions (J. Huang et al., 2019). Even though amyloid and amyloid-like proteins of biofilms were functionalized with several peptide/protein groups previously, their recombinant glycosylation has not been reported before. We examined the effect of glycosylation on adhesive and viscoelastic properties of purified TasA fibrils, as depicted in Figure 18.

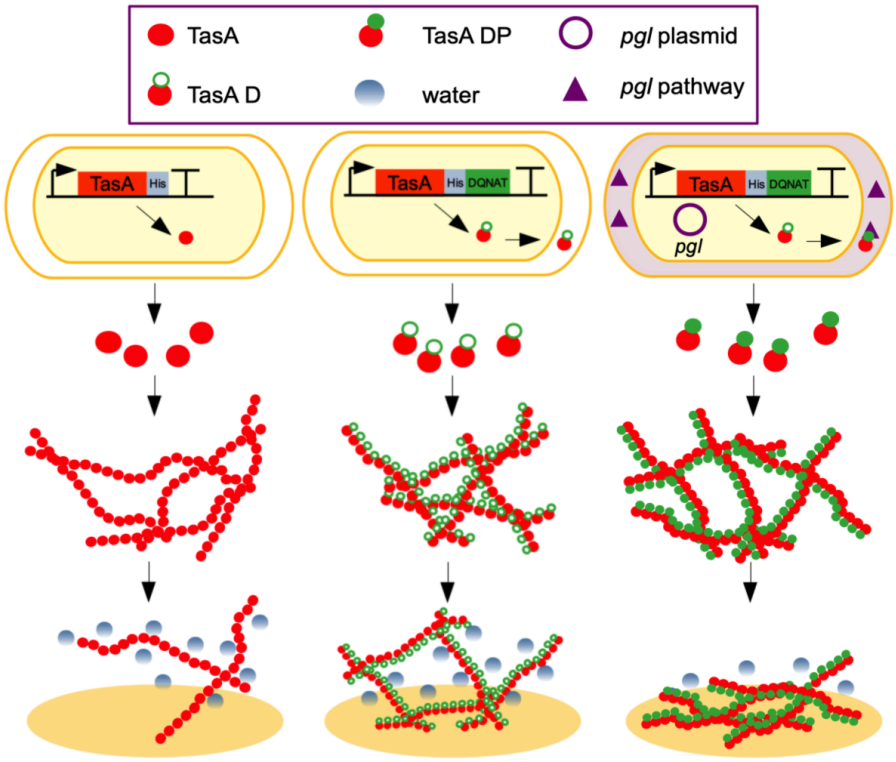


Figure 18. A schematic representation of glycosylation effecting gold binding affinity and viscoelastic properties of TasA fibrils.

For this purpose, tasA gene was cloned into pEt22b (+) vector for inducible expression. A GS linker was added between TasA and C-terminal His-tag sequence in order to provide flexibility to His-tag. DQNAT motif was added to pET-22b (+) plasmid harboring pelb leader sequence for periplasmic expression via PCR using primers with DQNAT motif at the overhang region in order to create pEt22b (+) plasmid with DQNAT glycosylation tag at the C terminal of 6X His tag. A GS linker was added between His-tag andC-terminal DQNAT-tag sequence in order to provide flexibility DQNAT glycosylation motif. pelb leader sequence directs the expressed proteins to periplasmic space, where glycosylation via *pgl* pathway takes place at DQNAT motif. Schematic diagrams of the construct designs are depicted in Figure 19.

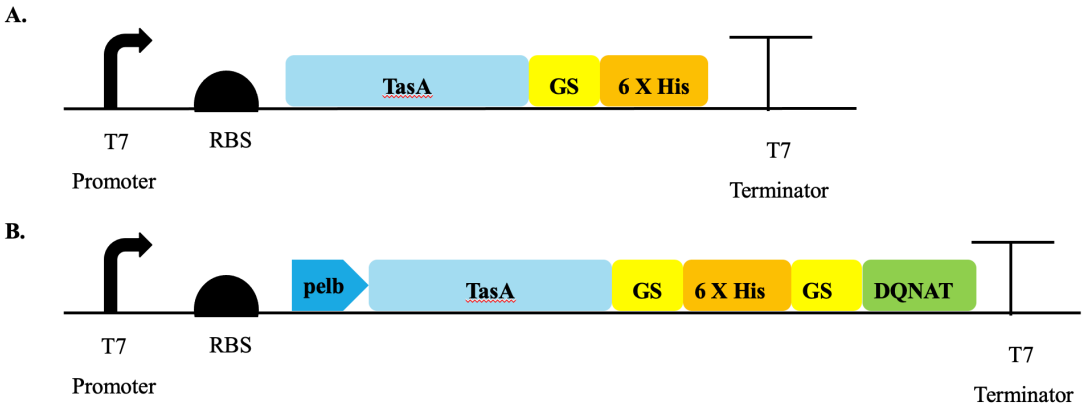


Figure 19. Schematic diagram of TasA and TasA DQNAT expression cassette. His tag was added to the C terminal of proteins and N terminal of DQNAT tag. GS linker was added to provide flexibility to His-tag and DQNAT tag. T7 promoter and terminator were used for expression by T7 polymerase.

Since tasA is one of *B. subtilis* biofilm proteins, the *tasA* gene was amplified from the genomic DNA of the *B. subtilis* 168 strain (Figure 20.A) with the primers listed in Table B.2 and cloned into KpnI-XhoI digested pET22b(+) plasmid (Figure 20.B) (Figure C.3, Figure C.4)

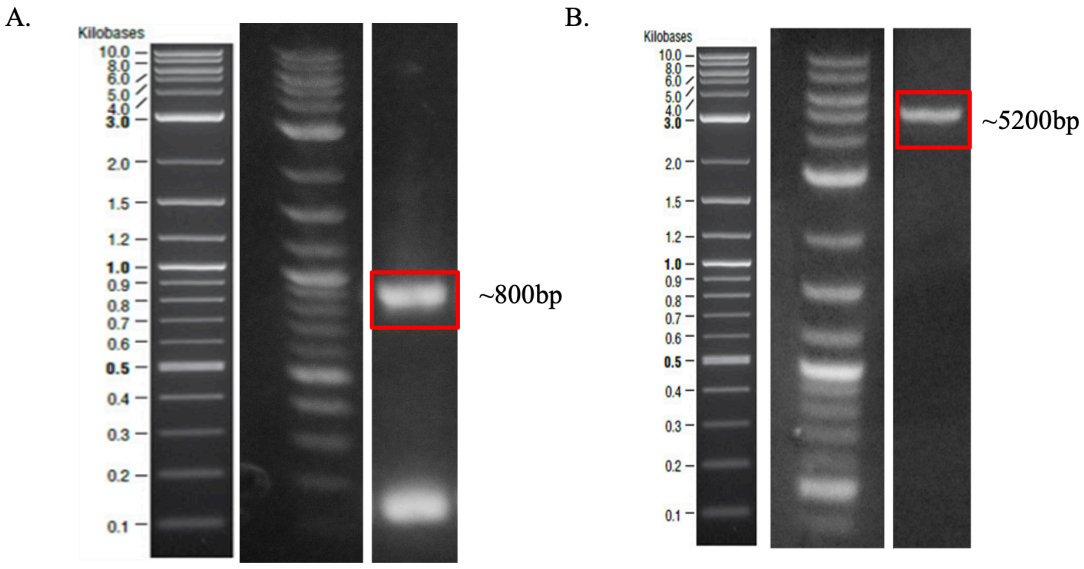


Figure 20. Cloning of *tasA* gene to pEt22b (+) plasmid. A. Agarose gel electrophoresis of *tasA* PCR. *Bacillus subtilis 168* genomic DNA was used as a template to amplify *tasA* gene (lane 2). PCR reaction was performed with Q5 Polymerase (NEB). 2-log DNA ladder (NEB) was used for detection (Lane1). B. Agarose gel electrophoresis of pEt22b (+) plasmid digestion with KpnI-XhoI restriction enzymes. Bands ~ 5200 bp corresponds to digested plasmid (Lane 2). The ladder was 2-log DNA ladder (NEB) in Lane 1.

For insertion of DQNAT tag as well as AvrII and SacI restriction digestion sites, pEt22b (+) plasmid with pelb leader sequence was amplified with PCR using the primers listed in Table B.2 and were restriction digested by high fidelity SacI (NEB) and AvrII (NEB) enzymes (Figure 21.B). *tasA* gene with suitable restriction enzymes (AvrII and SacI) was also PCR amplified using the primers listed in Table B.2 and were restriction digested by high fidelity SacI and AvrII enzymes (Figure 21.A). Digested fragments were extracted from agarose gel and used for cloning by T4 Ligase ligation reaction.

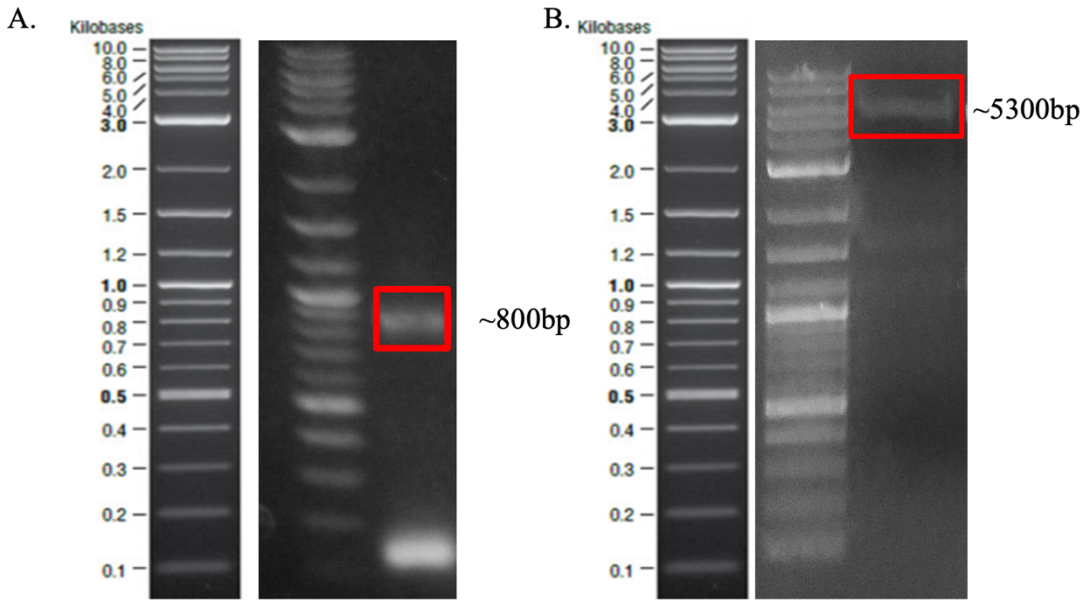


Figure 21. Cloning of *tasA* gene to pEt22b DQNAT plasmid. A. Agarose gel electrophoresis of *tasA* PCR. pEt22b TasA plasmid DNA was used as a template to amplify *tasA* gene with suitable restriction digestion sites (lane 2). PCR reaction was performed with Q5 Polymerase (NEB). 2-log DNA ladder (NEB) was used for detection (Lane1). B. Agarose gel electrophoresis of pEt22b (+) PCR with primers to insert DQNAT tag and suitable restriction digestion sites. Bands ~5300 bp corresponds to PCR product of the plasmid (Lane 2). The ladder was 2-log DNA ladder (NEB) in Lane 1.

In order to confirm cloning, 4 colonies from each were selected and verified by colony PCR with primers used for TasA cloning and visualized on agarose gel (Figure 22). Purified plasmids from colony PCR verified colonies were sent to sequencing and one of the clones were selected for further use. Sequencing results were shown in Figure D.3 and Figure D.4.

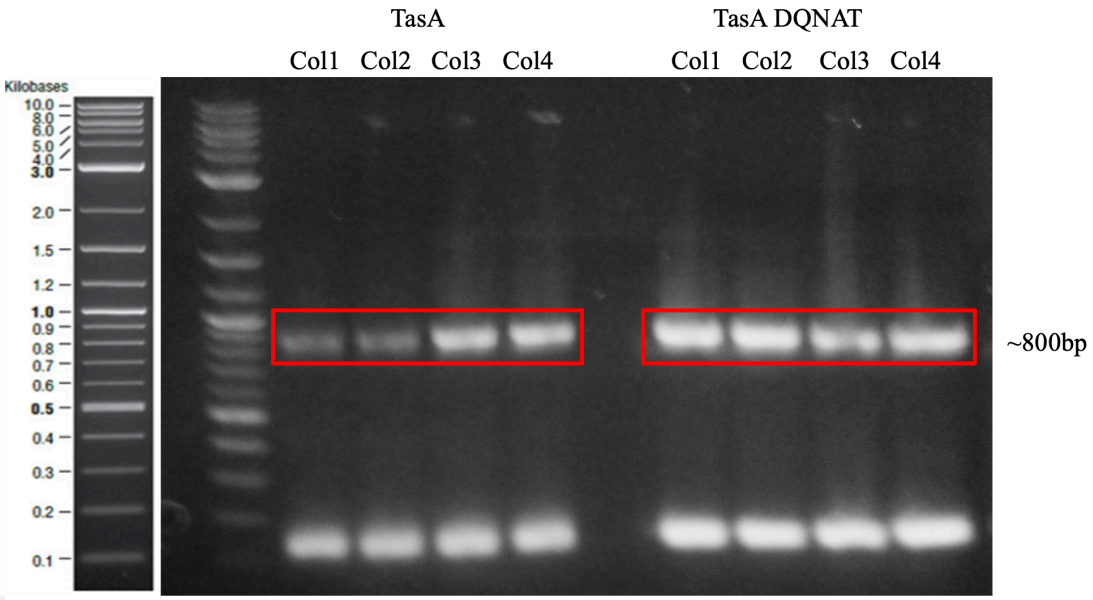


Figure 22. Verification of pEt22b TasA and pEt22b TasA DQNAT constructs. Colony PCR were conducted using the primers for TasA amplification from genome. Lane 1: 2-log DNA Ladder, Lane 2-5: colonies selected for pEt22b TasA cloning and their colony PCR products on agarose gel. Lane 6: Empty. Lane 7-10: colonies selected for pEt22b TasA DQNAT cloning and their colony PCR products on agarose gel.

Sanger sequencing verified pEt22b TasA and pEt22b TasA DQNAT plasmids were transformed into *E. coli* BL21 DE3 competent cells by chemical transformation to induce protein expression. In order to obtain glycosylated protein expression, TasA DQNAT construct was transformed into *E. coli* BL21 DE3 competent cells harboring *pgl* glycosylation pathway. TasA without DQNAT tag (TasA WT), non-glycosylated TasA DQNAT (TasA D) and glycosylated TasA DQNAT (TasA DP) proteins were induced for 24 hours at 37 ºC 200 rpm in auto-induction medium. Auto induction medium can be used to induce T7 promoter instead of IPTG without a need to monitor OD_{600}. The media has glucose, glycerol and glucose as carbon source. Cells

prefer glucose initially and following depletion of glucose, cells are forced to consume lactose, which drives expression from T7 promoter (Studier, 2014). Following cell lysis under denaturing conditions (with 6M guanidine HCl), TasA WT, TasA D and TasA DP proteins were purified with immobilized metal affinity chromatography (IMAC) under denaturing conditions. Purified proteins were dialyzed against ddH_2O and verified using SDS-PAGE and Western blotting using antibodies against polyhistidine tag (Figure 23.A). Theoretical molecular weights of the recombinant TasA WT and TasA D/TasA DP proteins were calculated as 27.2 kDa and 28.4 kDa, respectively, using the Swissprot Expasy tool. In Western Blot and SDS PAGE, TasA bands appeared at ~35 kDa. There are additional bands at lower molecular weights which are thought to correspond to translations from in-frame AUG codons in *tasA* gene or degradation products.

For analysis of fibrillization kinetics and fibril characteristics in AFM, highly pure protein samples are needed. For this purpose, TasA proteins were further purified with size exclusion chromatography (SEC) and displayed single bands at ~35 kDa for SDS-PAGE (Figure 23.B).

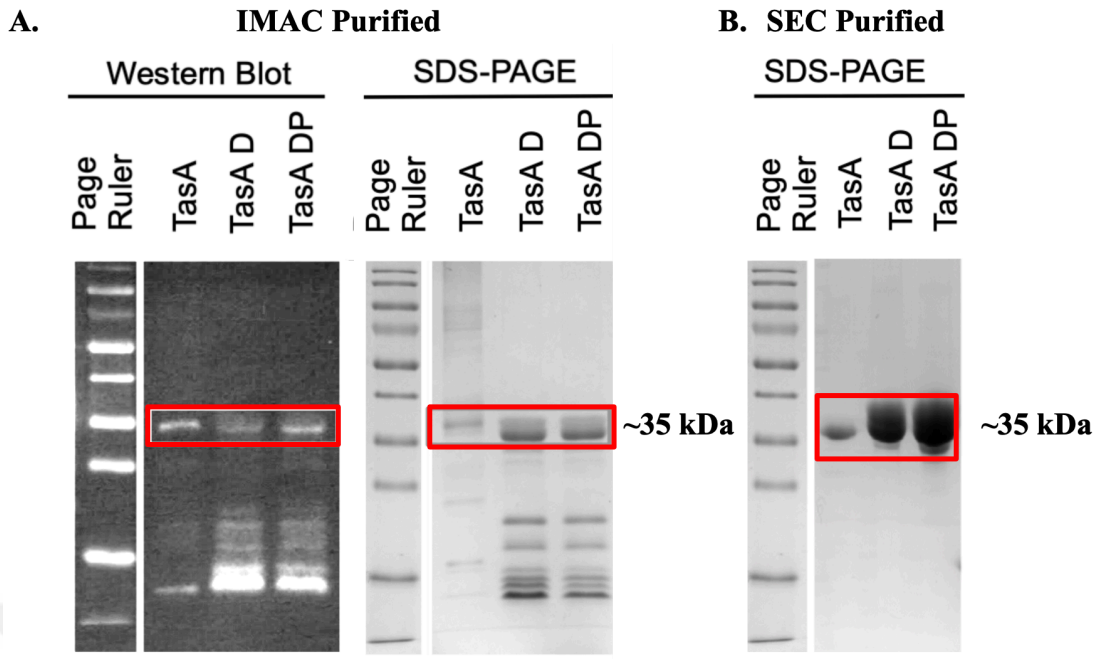


Figure 23. Western Blot and SDS-PAGE of TasA, TasA D and TasA DP samples. A. Affinity chromatography purified samples and B. SDS PAGE analysis of SEC purified samples. Page ruler was used as ladder.

3.4.2 Glycosylation of TasA by SBA blot

Following verification of expression and purification, glycosylation status of TasA D with *pgl* pathway using soybean agglutinin (SBA) lectin blot was investigated. *pgl* is the N-linked glycosylation system from *C. jejuni* that was successfully transferred to *E. coli* (Feldman et al., 2005). SBA is a lectin that has specific affinity to terminal GalNAc of *C. jejuni* glycan (Kelly et al., 2006). In SBA blot, therefore, HRP conjugated SBA was used instead of antibodies to detect protein glycosylation. Glycosylated TasA (TasA DP) was detected at ~35 kDa, ~20 kDa and ~15 kDa only in cells co-transformed with pEt22b TasA-DQNAT plasmid and *pgl* pathway, in

correlation with the western blot (Figure 24.A). These results indicated the successful glycosylation of TasA D protein in the periplasmic space by *pgl* pathway. Proteins further purified by size exclusion chromatography displayed single bands at ~35 kDa for SBA blot (Figure 24.B).

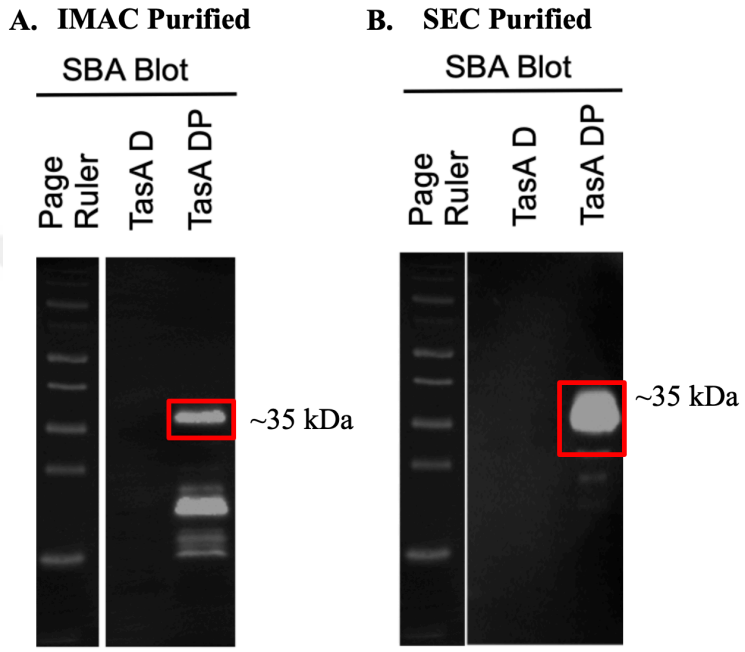


Figure 24. SBA Blot of TasA D and TasA DP samples. A. Affinity chromatography purified samples and B. SEC purified samples. Page ruler was used as ladder.

3.4.3 Effect of glycosylation on secondary structure: CD analysis

To observe the effects of DQNAT motif addition and glycosylation on structure of TasA fibrils, changes in the secondary structures of 14 days old fibrils were analyzed using circular dichroism (CD). CD spectra of TasA displayed a minimum ~200 nm, a shoulder ~220 nm and a maximum ~190nm, which is in correlation with the previously reported CD analysis of TasA oligomers (L. Chai et al., 2013) and purified TasA fibrils (Romero et al., 2010) (Figure 25.a).

TasA samples lack a high beta-sheet content which is typical for amyloid-like fibrils represented by a single minimum ~216 nm and a maximum ~197 nm, however a decrease in ellipticity in the range of 220-200 nm and an increase ~190 nm suggests the presence of beta-sheets in TasA fibrils. Additionally, two minima ~ 220 and ~ 200 nm indicate alpha helical characteristics. 14 days old TasA, TasA D and TasA DP display very similar CD spectra, indicating that addition of DQNAT motif or glycan groups did not alter the secondary structure significantly. In order to quantify structural elements, secondary structures were determined from CD data using BestSel online tool (Micsonai et al., 2018, 2015) (Figure 25.b). BestSel calculations also revealed no significant change in the percentage of β-sheets or α-helices.

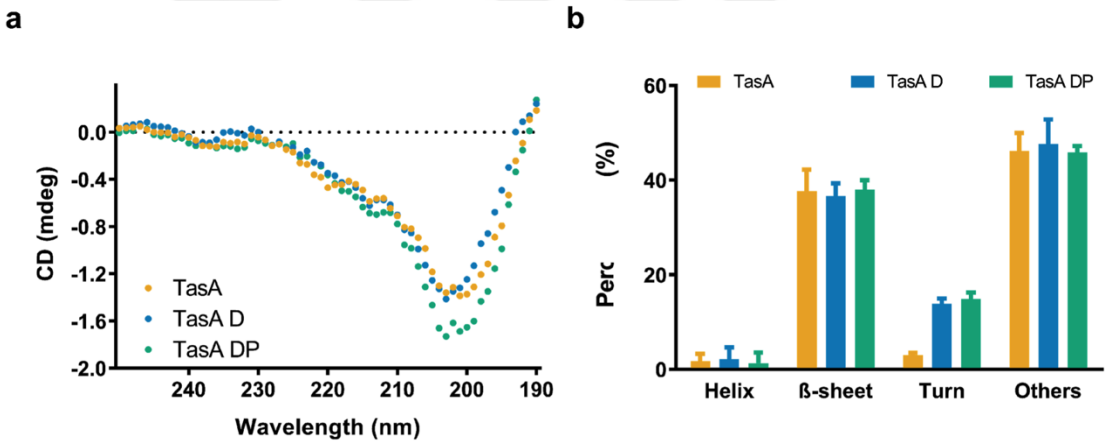


Figure 25. Secondary structure analysis of TasA, TasA D and TasA DP samples. a. Circular dichroism spectra of 14 days old TasA (orange dots), TasA D (blue dots) and TasA DP (green dots) samples. b. Percentages of secondary structures calculated by BestSel online tool for 14 days old TasA (orange bars), TasA D (blue bars) and TasA DP (green bars) samples. Significance values are calculated by t-test, n=3.

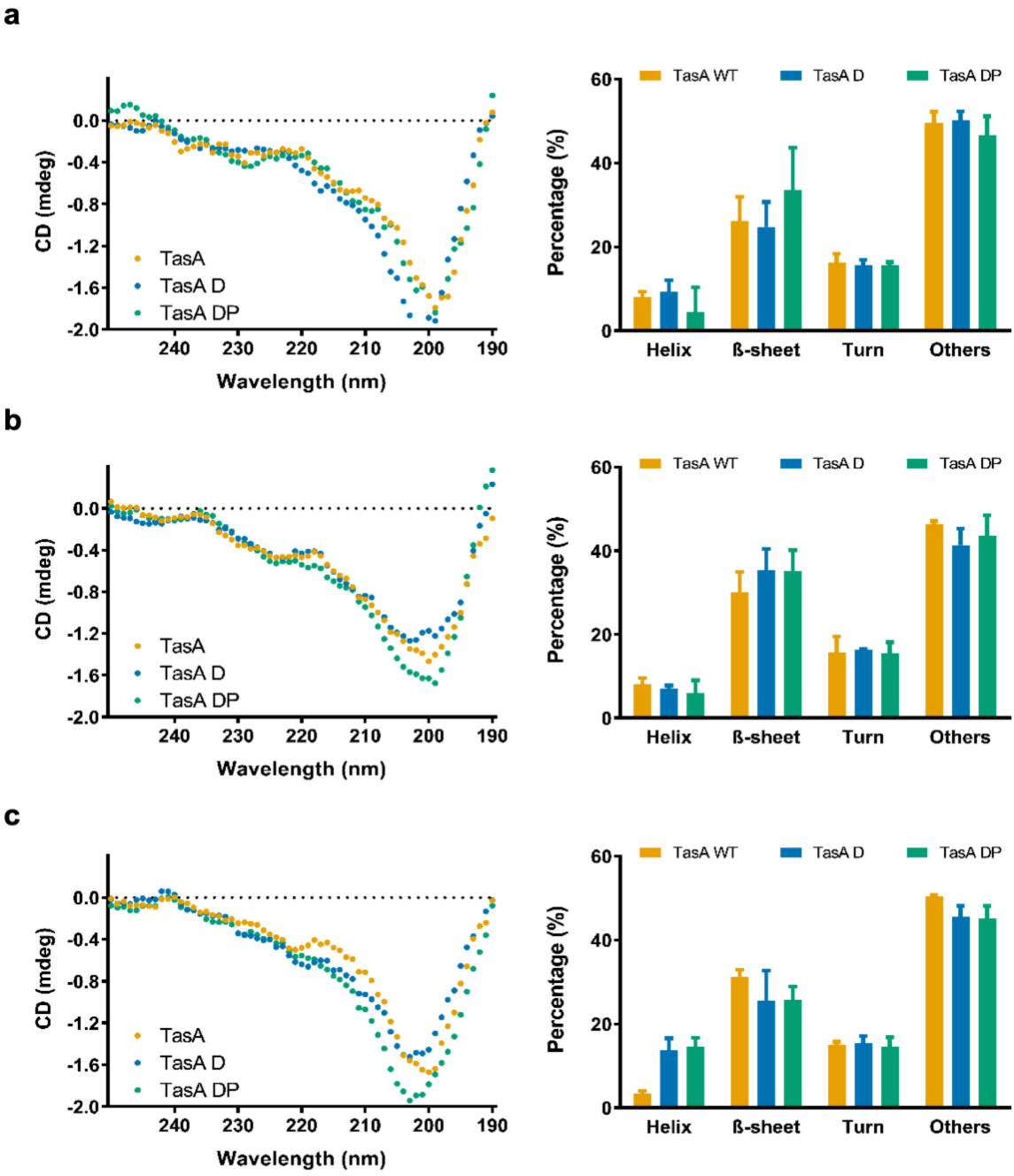


Figure 26. Circular dichroism spectra of TasA (orange dots), TasA-D (blue dots) and TasA-DP (green dots) samples and percentages of secondary structures calculated by BestSel online tool for TasA (orange bars), TasA-D (blue bars) and TasA-DP (green bars) with aging durations of a. 1 day b. 7 days and c. 28 days. Significance values are calculated by t-test, n=3.

CD spectrum and Bestsel secondary structure calculations of 1 day old, 7 days old and 28 days old TasA fibrils depicted similar structural behavior in response to DQNAT motif and glycan addition, indicating that maturation duration has no effect on the structural behavior of TasA, TasA D and TasA DP samples (Figure 26).

3.4.4 Analysis of fibrillization and fibril morphology by STEM and AFM

Despite the fact that CD analysis indicated no significant effect of glycosylation on secondary structure, fibril formation or morphology could still be disrupted by DQNAT motif or glycan groups. Matured samples were examined with scanning transmission electron microscopy (STEM) (Figure 27). STEM images of 14 days old samples revealed the surfaces are coated with wide film-like agglomerations and smaller aggregates and upon DQNAT motif or glycan addition, however film-like coatings are not disrupted. STEM images of 1 day, 7 days and 28 days old samples revealed similar structures (Figure 28).

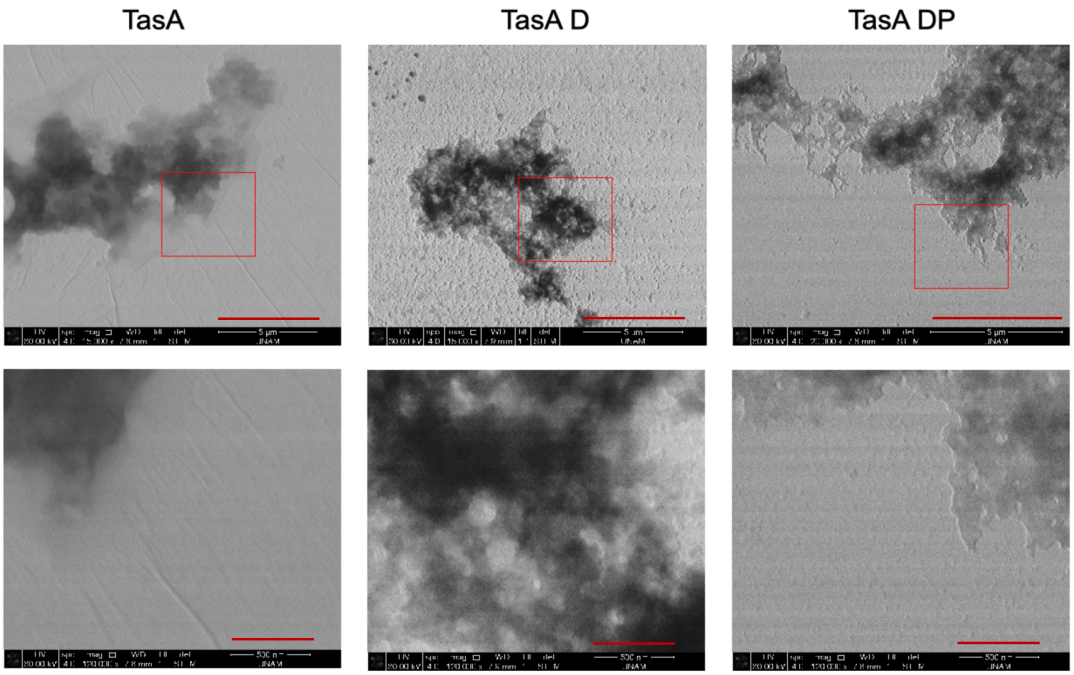


Figure 27. Morphological characterization of 14 days old TasA, TasA D and TasA DP fibrils using scanning transmission electron microscopy (STEM). Upper images are higher magnification versions of the areas in red boxes from lower images. Scale bars correspond to 5 µm for upper images and 500 nm for lower images.

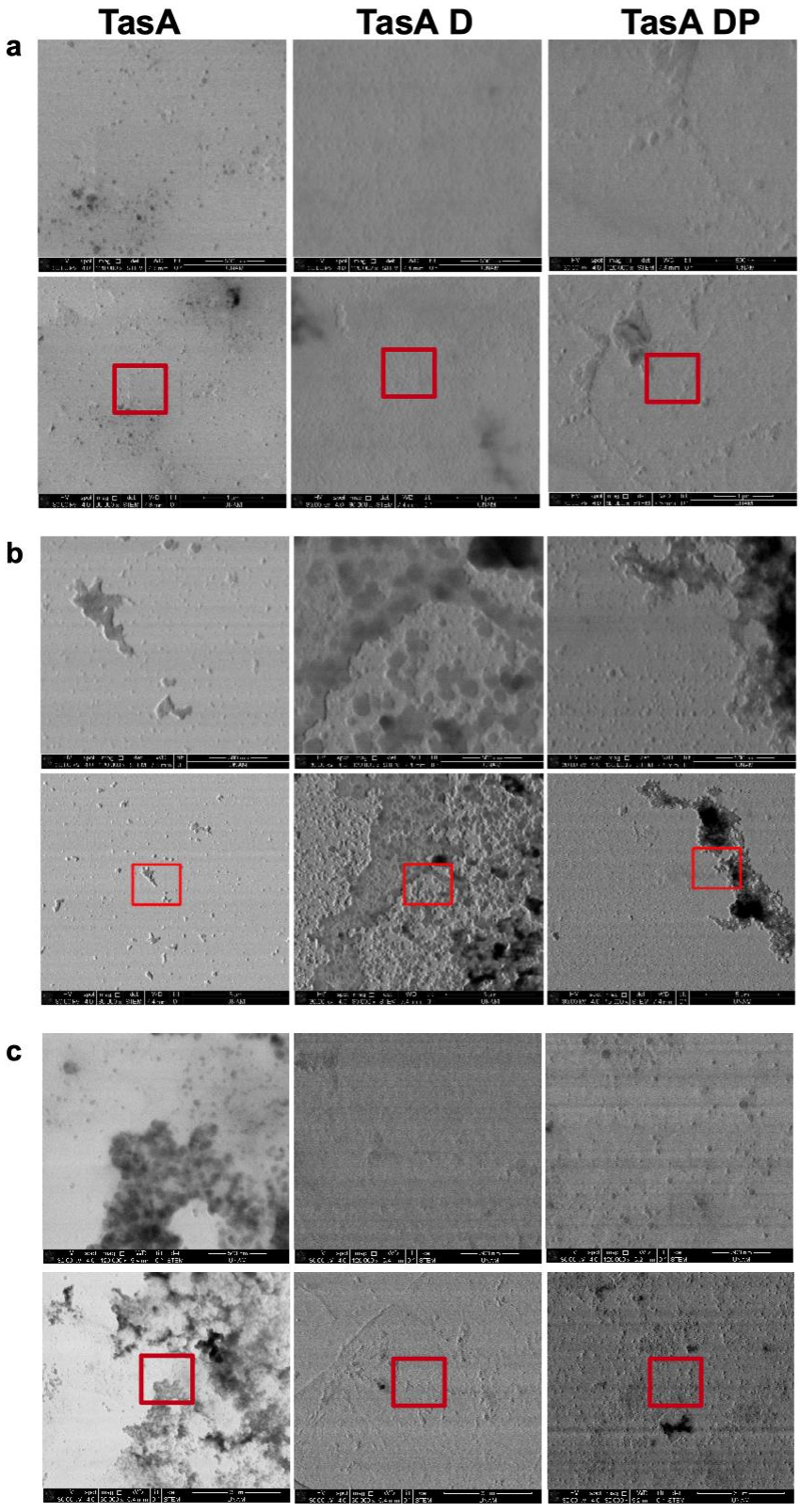


Figure 28. Morphological characterization of TasA, TasA D and TasA DP fibrils using scanning transmission electron microscopy (STEM) at aging time of a. 1 day, b. 7 days and c. 28 days. Upper images are higher magnification versions of the areas in red boxes from lower images.

For analysis with better resolution, we characterized the 21 and 28 days old fibrils by atomic force microscopy (AFM). 3D AFM images of 28 days old TasA, TasA D and TasA DP samples exhibited small fibrillary structures (Figure 29.a). The height and length distribution of those fibril-like structures are analyzed with open source software FiberApp (Usov & Mezzenga, 2015) (Figure 29.b), and the similarity of distributions are tested using Kolmogorov–Smirnov statistic. p values are greater than 0.05, therefore the distributions did not change significantly upon glycosylation. The average height is around 3 nm for all types of fibrils. The average length of formed fibrils where TasA fibrils are shortest while TasA DP fibrils are longest, however the difference was not significant. Similarly, for 21 days old sample, the same pattern in fibril height and contour length is observed (Figure 30). The analysis depicted that DQNAT motif or glycans did not significantly affect structures of small fibrils.

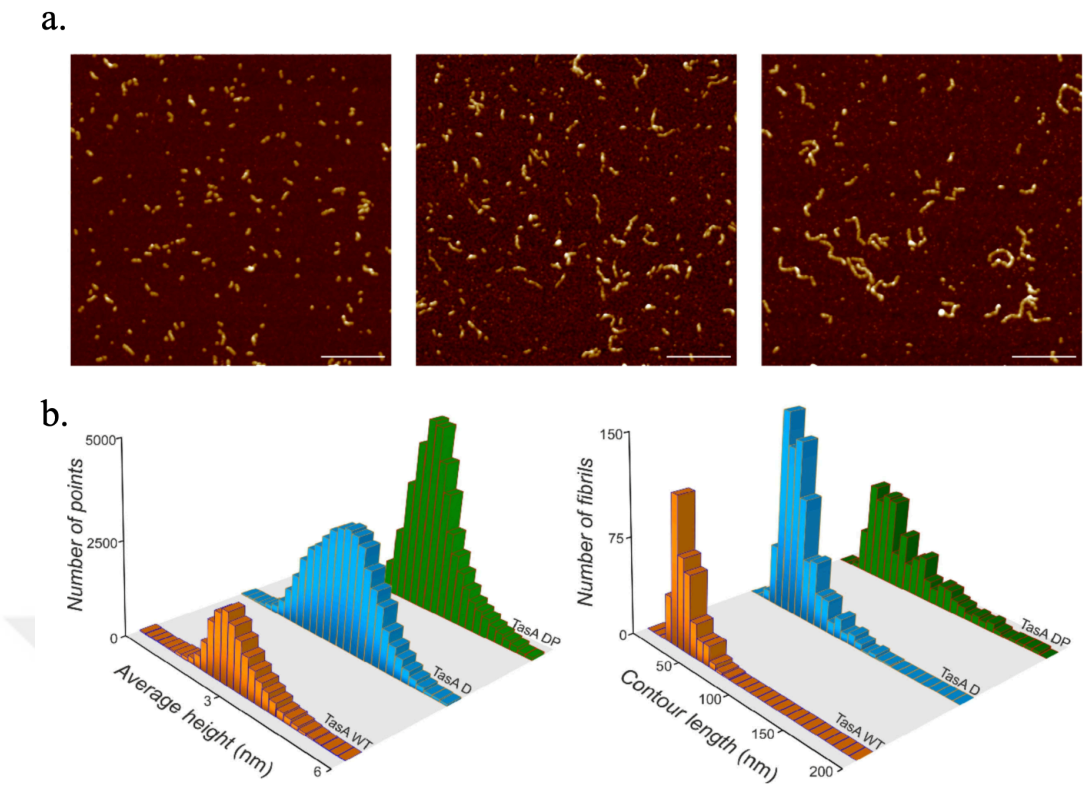


Figure 29. Morphological characterization of 14 days old TasA, TasA D and TasA DP fibrils using atomic force microscopy (AFM). a. AFM images of 14 days old protein samples. Scale bar:200 nm. b. AFM images analyzed by FiberApp software for quantification of average fibril height and length. The similarity of distributions is tested using Kolmogorov–Smirnov statistic.

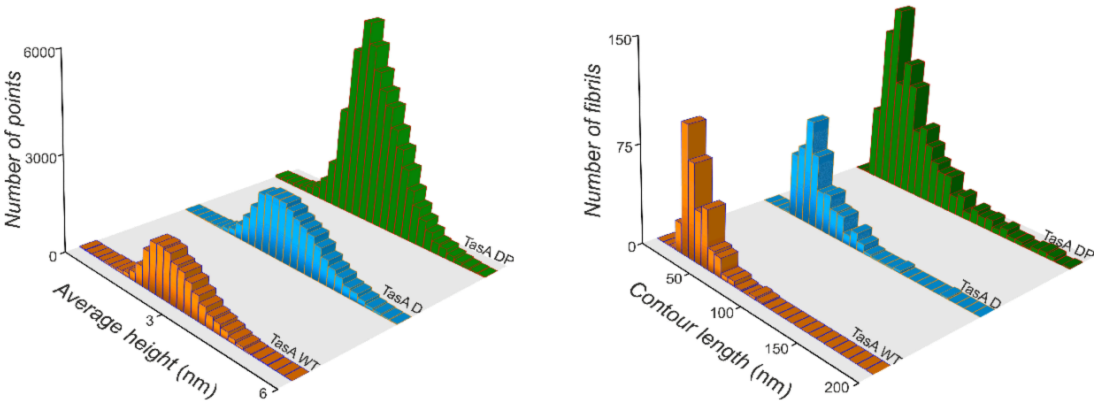


Figure 30. Morphological characterization of 28 days old TasA, TasA D and TasA DP fibrils using Atomic force microscopy (AFM). AFM images were analyzed by FiberApp software for quantification of average fibril height and contour length. The similarity of distributions is tested using Kolmogorov–Smirnov statistic.

3.4.5 Analysis of adsorption kinetic and viscoelastic properties with QCM-D

Proteins, in general, tend to adhere more effectively on hydrophobic surfaces (Anand, Sharma, Dutta, Kumar, & Belfort, 2010). Glycoproteins, on the other hand, extensively adsorb on hydrophilic surfaces since the hydrophobic domains are masked by hydrophilic glycan groups (Rabe, Verdes, & Seeger, 2011). Therefore, glycosylation of TasA could enhance its adsorption on hydrophilic surfaces. Since gold surfaces are used for several biomedical applications due to their biocompatibility and ease of functionalization (Elahi, Kamali, & Baghersad, 2018), we analyzed the adsorption kinetics of matured TasA fibrils on gold surfaces with Quartz Crystal Microbalance with Dissipation (QCM-D) to assess the applicability of TasA protein as surface coating material. QCM-D records the frequency and dissipation change of a quartz crystal as a function of mass deposited on the surface at all the harmonics (n=1,3,5,…,13), and provides real-time quantitative monitoring of surface-protein interactions as well as the viscoelastic properties of the deposited film (S. Huang et al., 2017).

Figure 31.a shows frequency shifts upon adsorption of 14 days old TasA, TasA D and TasA DP samples on gold QCM-D chips. Interaction of 1 μM samples resulted in a rapid initial decrease in the frequency, indicating the deposition of proteins on the sensor surface. Sequential administration of samples with increased concentrations (2 μM, 5 μM and 10 μM) caused further but slower drops in the frequency, as the surface coverage approaches saturation. Small changes in frequency were recorded upon rinsing, indicating that some of the adsorption was

reversible in the studied time-scale. Applied protein concentration to the sensor surface correlates with resonance frequency shifts (Figure 31.b). This correlation indicates the strength of binding. Frequency shifts upon adsorption and their correlation with protein concentration for 1 day, 7 days and 28 days old samples are depicted in Figure 32.

Data collected from QCM-D experiments is used to calculate desorption constant (k_d) of matured TasA, TasA D and TasA DP samples (Table G.3), as reported in the literature before (Tolga T. Olmez et al., 2018; Onur et al., 2018; Seker et al., 2017). The least squares curve fitting was used to fit the simple adsorption model to experimental data in Figure 31.b to calculate f_{max} and k_d. Calculated desorption constants of 14 days old samples are demonstrated in Figure 31.c. DQNAT motif addition (TasA D) readily caused a significant ($p \leq 0.01$) decrease in k_d values compared to TasA samples. Furthermore, glycosylation (TasA DP) resulted in a more significant ($p \leq 0.0001$) decrease in k_d values, compared to TasA D samples. k_d calculations of 1 day, 7 days and 28 days old samples also displayed the same behavioral pattern (Figure 33) indicating that maturation durations did not alter the effect of glycosylation on adsorption kinetics.

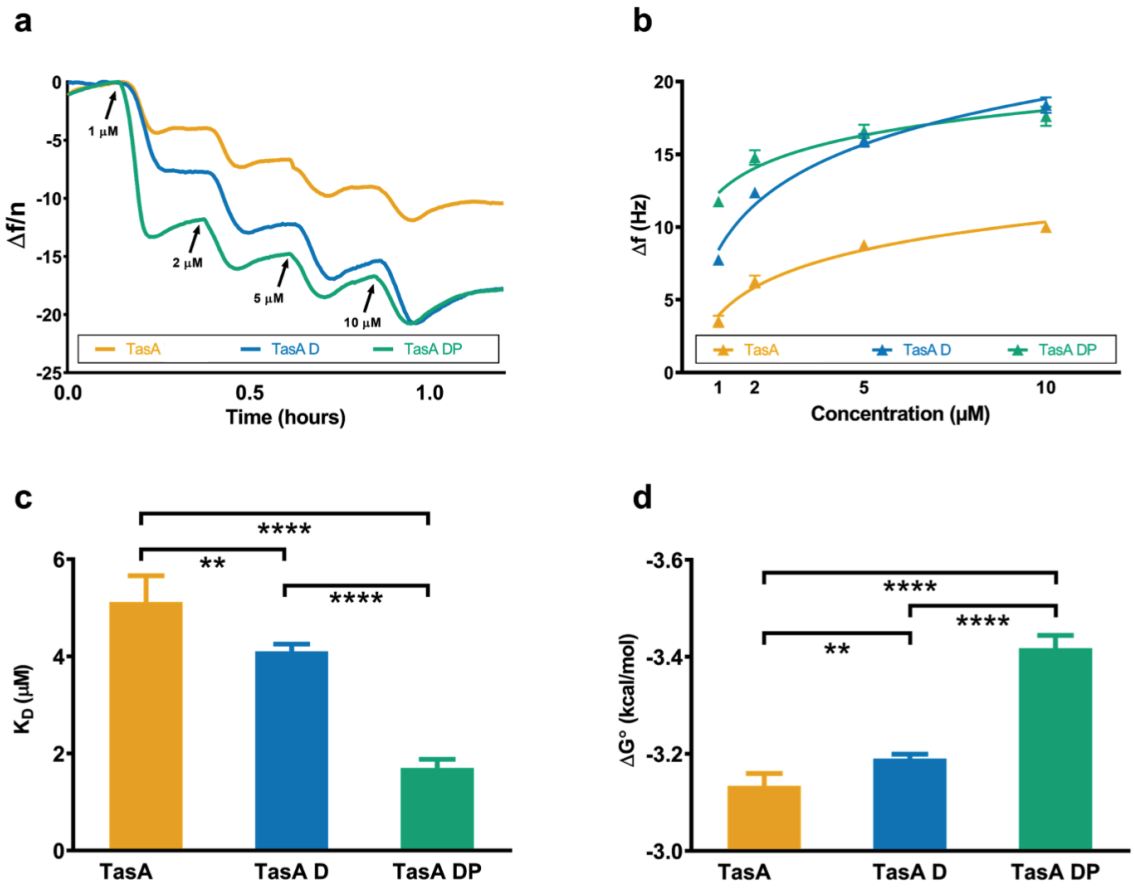


Figure 31. QCM D measurements for adsorption kinetics analysis of 14 days old TasA, TasA D and TasA DP samples. a. The recorded frequency shifts in QCM-D upon adsorption with increasing concentrations b. Frequency shifts with respect to applied protein concentrations c. Calculated desorption constants (k_d) and d. Calculated Gibbs free energy (ΔG^o). Significance values are calculated by t-test, n=3.

In addition, Gibbs free energy (ΔG^o) of adsorption is calculated for matured samples (Table G.4). Correspondingly, ΔG^o calculations revealed that TasA DP has significantly lower ΔG^o, implying that the adsorption of TasA DP onto gold surface is thermodynamically more favorable and more stable, compared to TasA and TasA D for 14 days old samples (Figure 31.d). ΔG^o calculations of 1 day, 7 days and 28 days samples also displayed the same behavioral pattern (Figure 33).

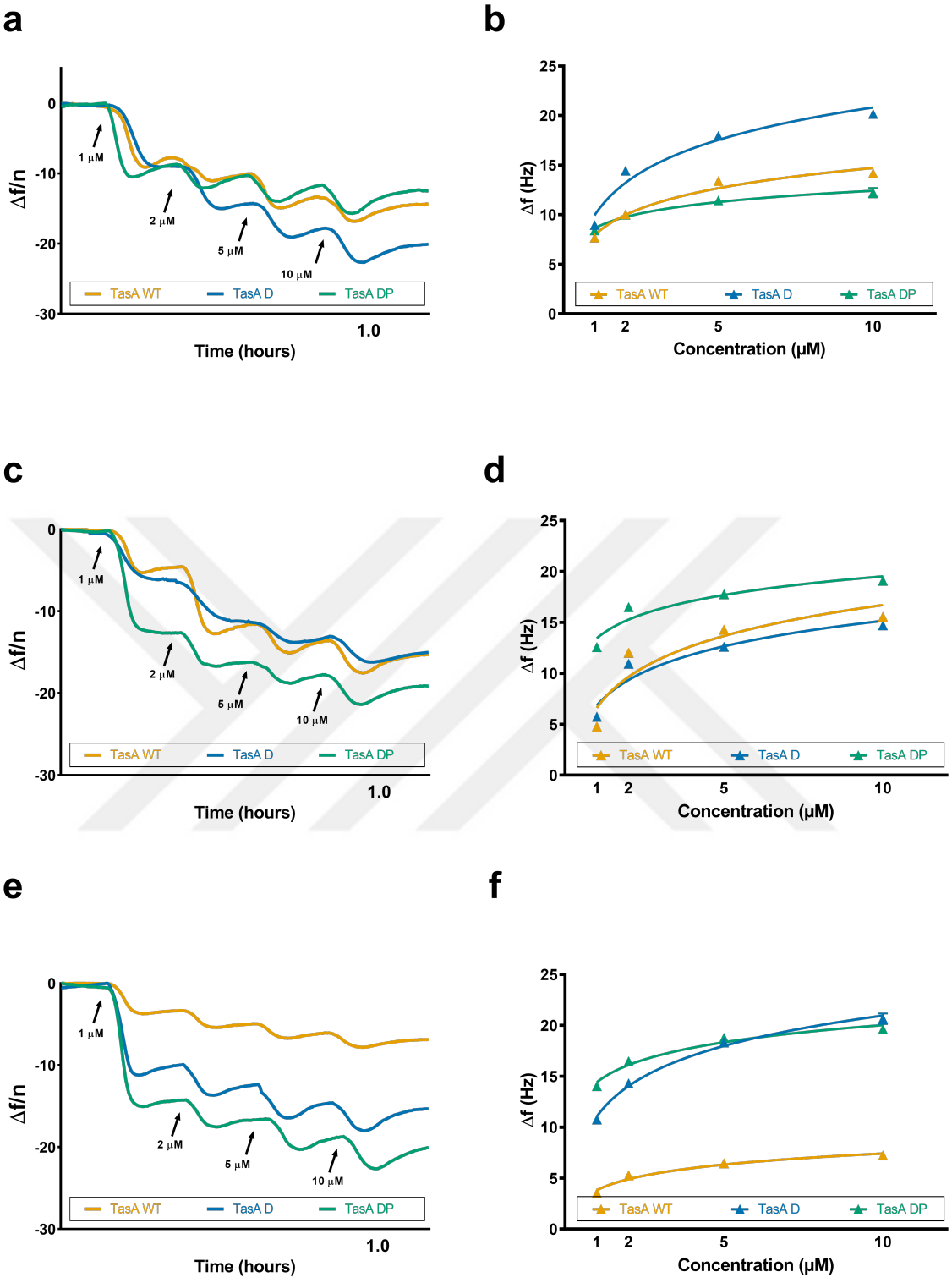


Figure 32. QCM frequency shifts with respect to time and with respect to protein concentration for (a-b). 1 day old, (c-d). 7 days old and (e-f). 28 days old samples.

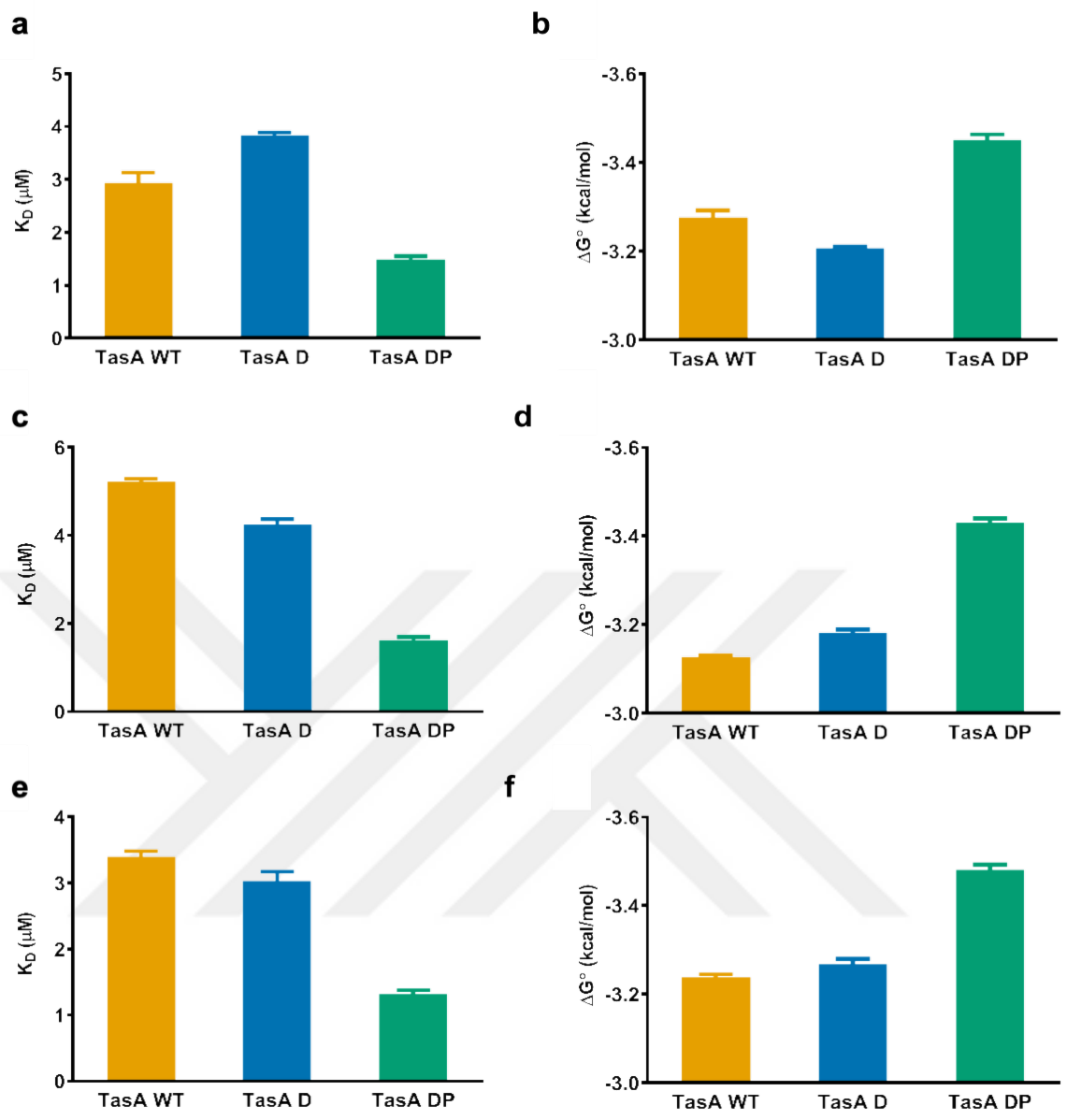


Figure 33. k_d and ΔG^o graphs of (a-b). 1 day old, (c-d). 7 days old and (e-f). 28 days old samples. n=3.

The frequency and dissipation change recorded with QCM-D measurements holds information about the amount of deposited mass and viscoelastic properties of deposited films, in addition to binding kinetics (Vogler, 2012). Proteins adsorbed on QCM chip surface can be quantified with Δf, however protein layers have structural flexibility and viscoelasticity, which requires frequency and dissipation

determination. The change of dissipation (*ΔD)* over the course of time are depicted in Figure 34.a for 14 days old TasA, TasA D and TasA DP samples on gold chips. Negative *Δf* (Figure 31.a) and positive *ΔD* (Figure 34.a) is characteristic for mass deposition, in our case protein adsorption. The decrease in dissipation during washing steps indicates that a fraction of adsorption is reversible. Dissipation changes over time for 1 day, 7 days and 28 days old samples are depicted in Figure 35 and display a similar behavior.

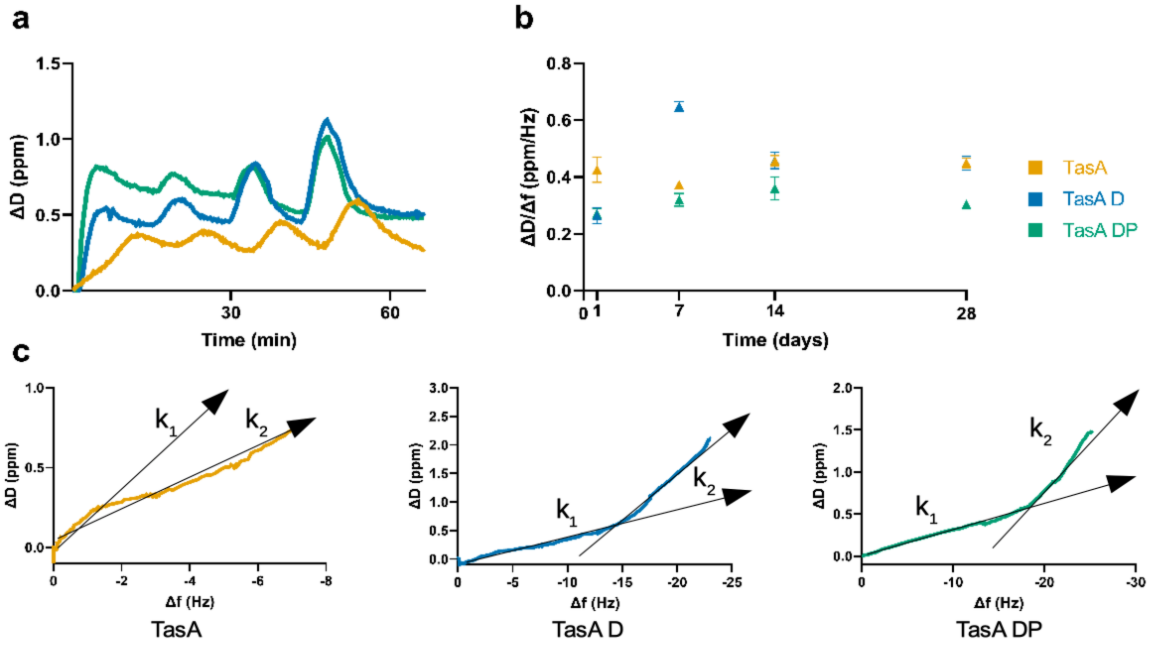


Figure 34. Analysis of viscoelastic properties of 14 days old TasA, TasA D and TasA DP samples on gold surface by QCM D. a. The recorded dissipation shifts in QCM-D upon adsorption with increasing concentrations of 14 days old TasA, TasA-D and TasA-DP proteins b. Total *ΔD/Δf* ratios of matured TasA, TasA-D and TasA-DP fibrils. Significance values are calculated by t-test, n=3. c. *ΔD vs Δf* plots of 14 days old TasA, TasA D and TasA DP proteins, with corresponding color codes.

QCM-D measures the mass of both protein and coupled water. Mass of the trapped, intra-layer or hydrodynamically coupled water also affects the viscoelastic response of the adsorbed layer (Vogler, 2012). Increase in dissipation corresponds to enhanced viscous behavior and conversely, decrease in dissipation corresponds to enhanced elasticity (Clegg, Ludolph, & Peppas, 2020). Therefore, $\Delta D/\Delta f$ ratio can be used to determine flexibility of the deposited film, where larger $\Delta D/\Delta f$ ratio is indicative of more viscous and flexible films (Aung, Ho, & Su, 2008). Glycan groups are reported to structure water molecules in their vicinity and even in longer ranges (Espinosa-Marzal et al., 2013), therefore glycosylated TasA samples are expected to represent a more viscous behavior. Viscosity can enhance cell adhesion on surfaces (Valentin et al., 2019) and the viscoelastic properties of coating materials influence cellular behavior (Charrier, Pogoda, Wells, & Janmey, 2018). Therefore, characterization of viscoelastic properties can hold important clues in terms of designing functional surfaces. In order to understand the differences between viscoelastic properties of deposited films, we assessed $\Delta D/\Delta f$ ratios of TasA, TasA D and TasA DP samples with different maturation times (Figure 34.b). $\Delta D/\Delta f$ ratios are calculated from the end point of ΔD and Δf values after protein addition at different concentrations. Addition of the DQNAT motif significantly affects $\Delta D/\Delta f$ ratio for 1 day old and 7 days old samples. At day 1, TasA has the higher ratio and at day 7, TasA D has a significantly higher ratio than TasA. However for day 14 and 28, no significant difference is observed between $\Delta D/\Delta f$ ratios of TasA and TasA D samples.

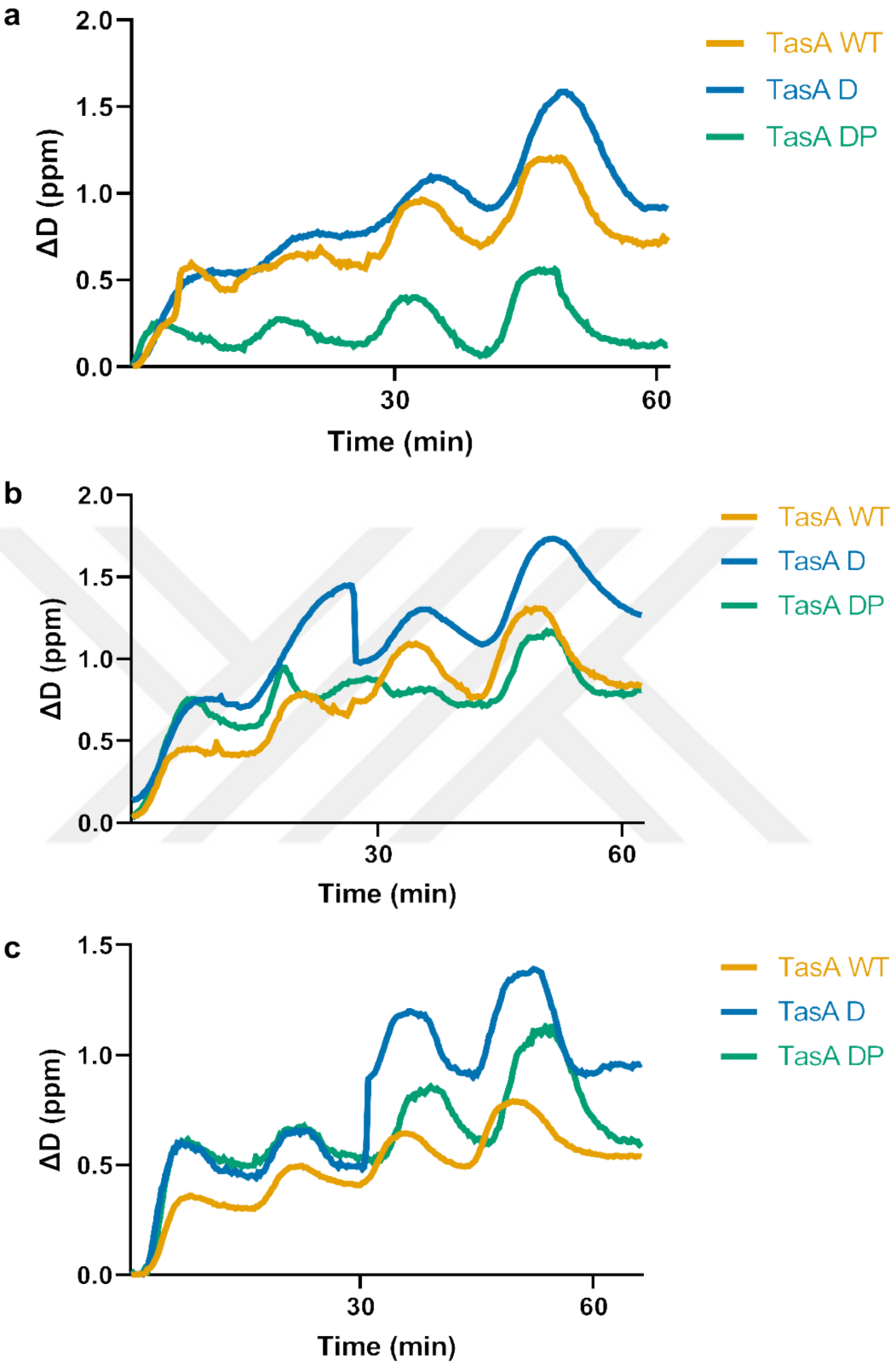


Figure 35. The recorded dissipation shifts in QCM-D upon adsorption with increasing concentrations of TasA, TasA-D and TasA-DP proteins with aging durations of a. 1 day b. 7 days and c. 28 days.

ΔD/Δf ratio does not only vary between samples, but also varies with maturation time (Figure 34.b). The viscoelastic behavior of different samples over the time show some discrepancies. For TasA, *ΔD/Δf* ratio does not change significantly in day 7, increases significantly ($p<0.01$) at day 14 and then does not display any further significant change. Overall, the *ΔD/Δf* ratio of TasA fibrils is not affected by maturation from day 1 to day 28. For TasA D, *ΔD/Δf* ratio increases significantly in day 7 ($p<0.0001$) unlike TasA, but shows a sharp decrease at day 14 ($p<0.001$) and then does not display any further significant change. However, between day 1 and day 28, the *ΔD/Δf* ratio of TasA D fibrils increased significantly ($p<0.001$). TasA DP, on the other hand, shows an increase in *ΔD/Δf* ratio at day 7 with respect to day 1 ($p<0.05$), then does not display any further significant change in day 14 and day 28. Overall, there is no significant change in 1 day old and 28 days old TasA DP fibrils in terms of *ΔD/Δf* ratio. Even though only TasA D samples demonstrated a significant change in viscoelastic properties between day 1 and day 28 samples, all samples displayed alterations at different time points during the maturation process. Overall, viscoelastic properties of TasA and TasA DP fibril did not change significantly, whereas TasA D fibrils showed increased viscosity and flexibility over the course of time.

In order to understand the viscoelastic properties of deposited films over time with increasing concentration, we plotted *ΔD* vs *Δf* graphs of TasA, TasA D and TasA DP samples with different maturation times. The plots for 14 days old samples are depicted in Figure 34.c. *ΔD* vs *Δf* plots can reveal differences between adsorption behavior of proteins, not directly observed from time dependent *ΔD* or *Δf* plots. For all proteins, *ΔD* vs *Δf* graphs display two different phases with different slopes along the adsorption process, indicated with black arrows. Those different slopes depicted

as k_1 and k_2, indicate at least two different kinetic processes (Valentin et al., 2019). For TasA, the initial slope is much higher and the slope after the break point is lower than other proteins (k_1 =0.93 and k_2 =0.41). This data depicts that a flexible layer is formed initially and the flexibility of the layer is decreased with increasing protein concentration. For TasA D and TasA DP samples, the initial slope k_1 and the slope after the break point k_2 is very similar (k_1 TasA D=0.25 and k_1 TasA DP=0.27, k_2 TasA D=0.92 and k_2 TasA DP=1) indicating a similar adsorption kinetics for glycosylated and non-glycosylated samples. In contrast to TasA, larger k_2 values indicate a rigid initial layer and increased flexibility with increasing protein concentration. The biphasic adsorption kinetics indicates an initial adsorption onto surfaces, followed by the rearrangements/conformational changes within the adsorbed layer (Höök, Rodahl, Kasemo, & Brzezinski, 1998). As explained previously, proteins separated on the surface results in higher dissipation at low surface coverages. The higher k_1 value of TasA can arise from lower surface coverage at low protein concentrations, in correlation with its higher k_d value. As the surface coverage increases with high protein concentrations, close packing results in more rigid films and less dissipation.

3.4.6 Effect of glycosylation on cell adhesion

Understanding cell adhesion behavior on a surface is of crucial importance for biomaterial studies, as desired cell adhesion properties may be different for each application. For example, biomaterials that interact with blood such as artificial vessels are required to be non-adherent to cells, whereas scaffolds for tissue generation studies need to promote cell adhesion to the material (W. Huang, Anvari,

Torres, LeBaron, & Athanasiou, 2003; Khalili & Ahmad, 2015). Thus, we determined the cell adhesion capacity for matured TasA, TasA D and TasA DP fibrils using HeLa S3 cells to analyze the effect of maturation and glycosylation on cell adhesive properties. Representative fluorescent microscopy images of Calcein AM labeled adhered cells are depicted in Figure 36.a and the total number of adhered cells are summarized in Figure 36.b.

Even though the number of adhered cells appears to decrease by DQNAT motif addition and increase by glycan addition, the high variation between each experimental set leads to an insignificant change in cell adhesion capacity of glycosylated samples. However, glycosylated or non-glycosylated, all samples have cell adhesion capacity in the range of positive control. This data suggests that glycosylated TasA fibrils possess improved affinity to gold surfaces and can be utilized in applications that require cellular adhesion.

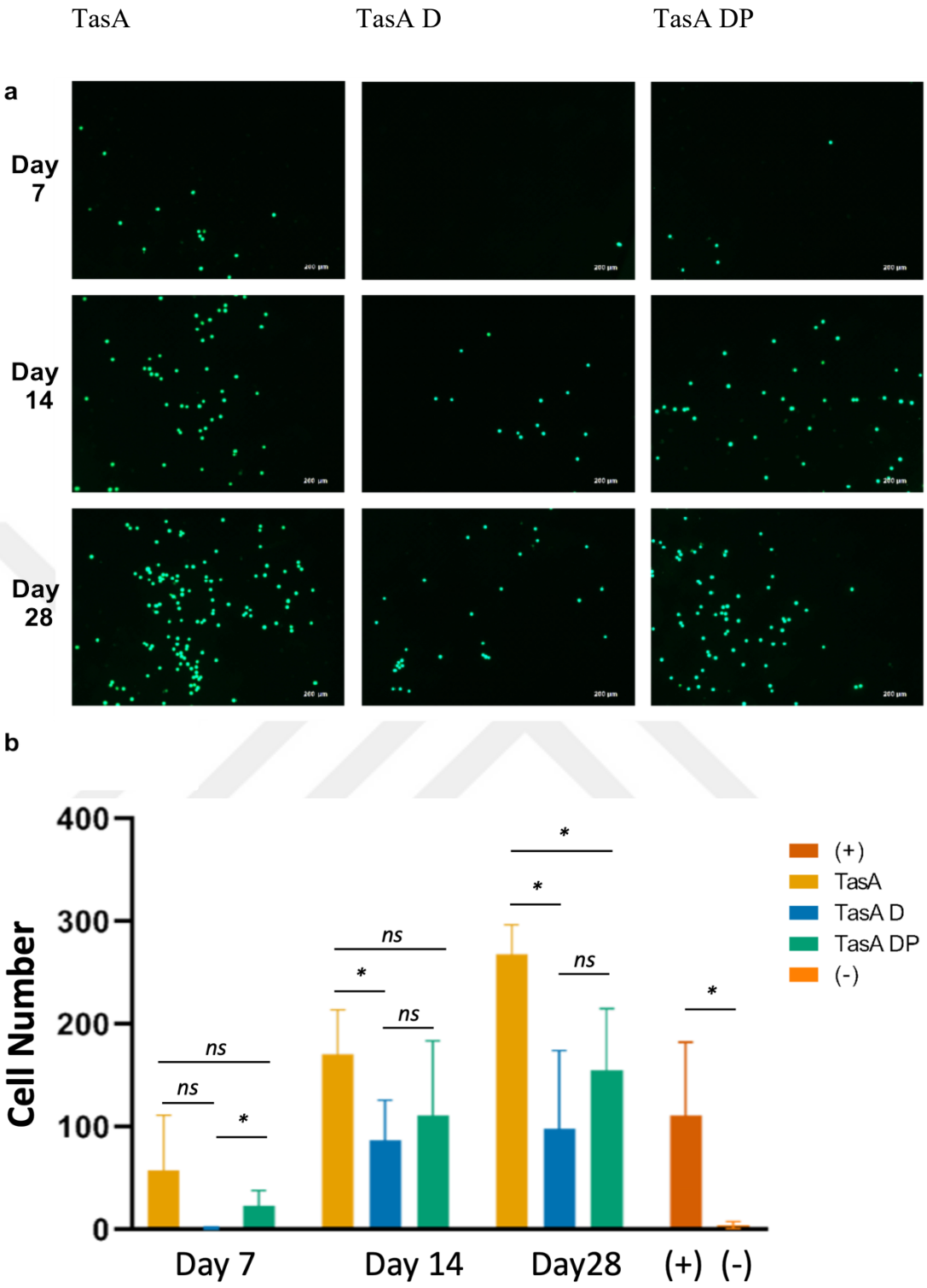


Figure 36. Adhesion of HeLa S3 cells on surfaces coated with 7 days, 14 days and 28 days old TasA, TasA D and TasA DP. a. Representative images of Calcein AM labelled adhered cells and b. Quantitative analysis of adhered number of cells. Positive control is tissue culture treated well and negative control is non-treated well. Significance values are calculated by t-test, n=3.

3.5 Conclusion

Biofilms are widely utilized adhesive materials composed of both living and nonliving components. In nature, these self-assembling multilayer structures protect bacteria from challenging environments and are often linked to pathogenicity due to enhanced adhesiveness to host cells. Its adhesiveness, along with many other properties, has been utilized in many applications. When other adhesive proteins in nature are envisioned, such as silk and mussel foot proteins (Mfps), they are found highly glycosylated. Here, we combined two pro-adhesiveness components, *B. subtilis* biofilm protein TasA and *C. jejuni* glycosylation pathway and successfully produced recombinant glycosylated TasA proteins as a novel method to enhance adhesive properties. We calculated desorption constant (k_d) and Gibbs free energy (ΔG^o) of adsorption and found that TasA DP has lower k_d and ΔG^o, suggesting that glycosylation significantly improved adsorption characteristics of TasA to gold surface. This enhancement in the surface adsorption can be due to the interaction of hydrophilic glycan groups on the surface of the proteins with oxidized gold surface . This can also explain the enhanced adsorption upon addition of hydrophilic DQNAT motif. CD, STEM and AFM data suggested that glycosylation of biofilm proteins did not affect the secondary structure. Even though the contour length of the fibrils has changed upon DQNAT motif or glycan addition, height of the fibrils remain unchanged and film-like coatings are not disrupted.

We also investigated viscoelastic properties of TasA, TasA D and TasA DP by analyzing $\Delta D/\Delta f$ plots and observed that glycosylated TasA forms a more compact and rigid layer, compared to TasA and TasA D. Normally, glycan groups are known to interact with water molecules, therefore, expected to increase hydration and

viscosity. However, the amount of coupled water is also related with how protein packs within the interface (Vogler, 2012). If the interaction of the protein with the surface is stronger than the interaction within the protein, proteins can form a closely packed, rigid thin layer on the surface resulting in higher surface coverage, therefore, entrapping less water within the film. In addition, this could result in reduced film flexibility due to electrostatic repulsion between the densely packed groups[35]. Noting that glycosylated samples result in high affinity to gold surface, lower dissipation values of glycosylated samples suggest the formation of a denser thin layer and higher surface coverage due to increased surface affinity, which results in less water entrapment and reduced flexibility. In addition, charge of glycans may also contribute to the reduced flexibility of densely packed films, due to electrostatic repulsion.

Conformational rearrangements during the maturation process can alter secondary structures. When $\Delta D/\Delta f$ plots and secondary structure predictions are co-analyzed, a significant increase in $\Delta D/\Delta f$ ratio of TasA is observed (Figure 34.b) between day 7 and day 14, which is in correlation with a significant increase in anti-parallel beta sheets and a significant decrease in alpha helical structures. On day 28, the percentage of anti-parallel beta sheets decreases significantly and displays no significant difference between day 1 and day 28. TasA D has an increased $\Delta D/\Delta f$ ratio between day 1 and day 7 and a significant increase in anti-parallel beta sheets, similar to TasA. A decreased $\Delta D/\Delta f$ ratio is accompanied with a decrease in alpha helical structure between day 7 and day 14, while the anti-parallel beta sheet content remains the same. Between day 1 and day 28, no significant change is observed in the percentage of secondary structures, however the $\Delta D/\Delta f$ ratio is significantly increased. For TasA DP, alpha helix and beta sheet content of the sample is altered

significantly between day 14 and day 28, however those changes are not detected as a change in *ΔD/Δf* ratio. Similarly, the small increase in *ΔD/Δf* ratio between day 1 and day 7 is not detected as a significant change in secondary structures. This data suggests that the differences in viscoelastic properties are not solely due to structural rearrangements but also differences in hydration capacity contributions to viscous and elastic properties of the samples. Taken together, the fluctuation in percentages of secondary structure elements along with the associated water molecules can alter *ΔD/Δf* ratios.

Biocompatibility of a surface is generally related with cell adhesion onto the surface (Lord et al., 2006). Glycosylated TasA fibrils with different maturation times are reported to support cell adhesion. In conclusion, glycosylated TasA fibrils hold a potential as biocompatible coating or scaffold materials for applications that require enhanced cell adhesion such as tissue engineering, wound sealants and medical devices. Due to their higher adsorption affinity and higher surface coverage, glycosylated TasA fibrils may be utilized as superior coating materials.

4 CHAPTER IV

RGD FUNCTIONALIZED AMYLOIDS AS BIOMATERIALS WITH ENHANCED CELL ADHESION CAPACITY

4.1 Introduction

For tissue development and maintenance, cell adhesion is a fundamental process with great importance. Therefore, it is critical to consider cell adhesion properties of different materials during biomaterial design and development, as specific applications can require various cell and tissue adhesion characteristics. For instance, during the design of as artificial valves or vessels, the utilized biomaterials are required not to adhere to blood cells or plasma proteins to avoid esuchmbolism or similar disorders. However, production and design of other biomaterials can require enhanced adherence to cells for cell proliferation on contact surfaces, such as tissue scaffolds, implantable sensors or artificial bones(Khalili & Ahmad, 2015).
Amyloids are protein aggregates that self assemble into highly ordered fibrillar structures. Amyloids are generally associated with toxicity in neurological disorders such as Huntington's and Alzheimer's disease. However, numerous functional amyloid structures are found in nature with defined functions in organisms. For

example, curli proteins of biofilms from several microorganisms such as *E. coli*, *B. subtilis, P. aeruginosa* are examples of functional amyloids, that provide resistance to harsh environmental conditions (Fowler, Koulov, Balch, & Kelly, 2007). Their high mechanical strength, stiffness, stability and ease of functionalization via alteration of amino acid sequences make amyloid fibrils suitable candidates as nanostructured biomaterials for various applications (Jacob et al., 2015; Mankar, Anoop, Sen, & Maji, 2011)

4.2 Objective

In this section, I proposed that curli proteins CsgA and CsgB from *E. coli*, TasA and TapA from *B. subtilis* as well as FapC and FapB from *P. aeruginosa* can be utilized to develop tissue scaffolds to support cell adhesion and they can be modified via addition of functional motifs for specific applications, to enhance their adhesive capacity. For this purpose, I characterized their recombinant production and secretion capacity in *E. coli*, using its native biofilm secretion pathway. Here, I aim to characterize the cell adhesion capacity of *E. coli* curli proteins with and without addition of RGD functional peptide motif and analyze the differences in cell adhesion capacity following fusion of functional peptide groups with curli proteins.

4.3 Materials and Methods

4.3.1 Bacterial strains and cell maintenance

In this study, *E. coli* DH5α strain (NEB) was utilized for cloning and *E. coli* BL21 DE3 strain (NEB) was used for protein expression, as explained in more detail in Chapter 2. For biofilm secretion, *E. coli K12* strains devoid of *csgA* gene *(*Δ*csgA* strain) and *E. coli K12* strains devoid of *csgA* and *csgB* genes (Δ*csgAB* strain). This strain was maintained at the same conditions as for *E. coli* DH5α.

4.3.2 Mammalian cell lines

HEK293 cells (ATCC) were maintained using the same conditions as HeLa S3 cells as explained in Section 3.2.2. Briefly, the cells were cultivated in DMEM with 2 mM L-glutamine, 1 g/L glucose, 10% FBS, penicillin and streptomycin in 5% CO_2 humidified incubator at 37ºC.

4.3.3 Plasmid construction

Firstly, pET22b csga-RGD and peET22b csgB-RGD plasmids were constructed for inducible expression of genes of interest. The *csgA* and *csgB* genes without signal sequences were amplified from *E. coli K12 MG1655* genomic DNA using the primers listed in Table B.3. pET22b (+) plasmid without pelb leader sequence and with C terminal 6 X His-tag, flexible GS linker (GGSG) and RGD peptide were

amplified from previously constructed (in Chapter 3) pET22b (+) plasmid without pelb leader sequence using the primers RGD_F (66) and RGD_R (68), listed in Table B.3. DNA was amplified using Q5 DNA polymerase (NEB) (Reaction conditions were described in APPENDIX F). PCR products of inserts and vector were verified on 1% agarose gel. NucleoSpin Gel and PCR Clean-up kit (Macherey-Nagel) was used according to the manufacturer's instructors to isolate DNA from agarose gels. PCR fragments were digested using HF KpnI (NEB) and XhoI (NEB) restriction enzymes. NucleoSpin Gel and PCR Clean-up kit (Macherey-Nagel) was used to isolate digested DNA from reaction mix. Digested DNA fragments were ligated by T4 DNA ligase (NEB) (Reaction conditions were described in APPENDIX F). The ligation product was transformed into DH5α chemically competent cells, as described in 2.3.2. Plasmid maps were shown in Figure C.5 and Figure C.6. After overnight incubation, single colonies were selected and positive clones containing *csgA-RGD* and *csgB-RGD* genes were verified by Sanger sequencing (Genewiz, USA). The sequencing results were analyzed by Geneious R9.0.5 software by alignment (Figure D.5, Figure D.6). All genetic part sequences used this chapter was introduced in Table A.3 and the amino acid sequences of each design were listed in Table E.3. All plasmid maps were designed by Benchling online tool.

Secondly, pZa pBAD csgA, pZa pBAD csgB, pZa pBAD tasA and pZa pBAD tapA plasmids were constructed for secretion of biofilm proteins. The *csgA* and *csgB* genes with signal sequences were amplified from *E. coli Nissle* genomic DNA using the primers listed in Table B.4. The *tasA* and *tapA* genes without native signal sequence were retrieved from the genome of wild-type *B. subtilis 168* strain using the primers listed in Table B.4. After first amplification with those primers, N42 signal sequence was added to both *tasA* and *tapA* gene by sequential PCR reactions

using P2 FWD, P3 FWD and P4 FWD primers, listed in Table B.4. Genomic DNA was amplified using Q5 DNA polymerase. PCR products of inserts and pZa pBAD vector digested by HF KpnI (NEB) and XhoI (NEB) enzymes were verified on 1% agarose gel. NucleoSpin Gel and PCR Clean-up kit was used to isolate DNA from agarose gels. PCR fragments were digested using the same restriction enzymes and digested inserts were isolated by NucleoSpin Gel and PCR Clean-up kit. Digested DNA fragments were ligated by T4 DNA ligase. The ligation product was transformed into DH5α chemically competent cells. Plasmid maps were shown in Figure C.7, Figure C.8, Figure C.9 and Figure C.10. After overnight incubation, single colonies were selected and positive clones were verified by Sanger sequencing (Genewiz, USA). The sequencing results were analyzed by Geneious R9.0.5 software by alignment (Figure D.7, Figure D.8, Figure D.9 and Figure D.10). All genetic part sequences used this chapter was introduced in Table A.4 and the amino acid sequences of each design were listed in Table E.3. All plasmid maps were designed by Benchling online tool.

Following, pZa pBAD csgA His, pZa pBAD csgB His, pZa pBAD tasA His, pZa pBAD tapA His, pZa pBAD fapC His and pZa pBAD fapB His plasmids were constructed for easier verification of biofilm protein secretion. The *csgA* and *csgB* genes with native signal sequences as well as *tasA* and *tapA* genes with N42 signal sequences were amplified from previously constructed plasmids using the primers listed in Table B.5. The *fapC* and *fapB* genes of *P. aeruginosa* without signal sequences were codon optimized for *E. coli* expression and synthesized from GenScript Inc. (USA). N42 signal sequence was added to both *fapC* and *fapB* genes by sequential PCR reactions using primers listed in Table B.5, using Q5 DNA polymerase. PCR products of inserts and pZa pBAD vector digested by HF KpnI

(NEB) and XhoI (NEB) enzymes were verified on 1% agarose gel. NucleoSpin Gel and PCR Clean-up kit was used to isolate DNA from agarose gels. PCR fragments were digested using the same restriction enzymes and digested inserts were isolated by NucleoSpin Gel and PCR Clean-up kit. Digested DNA fragments were ligated by T4 DNA ligase. The ligation product was transformed into DH5α chemically competent cells. Plasmid maps were shown in Figure C11, Figure C.12, Figure C.13, Figure C.14, Figure C.15 and Figure C.16. After overnight incubation, single colonies were selected and positive clones were verified by Sanger sequencing (Genewiz, USA). The sequencing results were analyzed by Geneious R9.0.5 software by alignment (Figure D11, Figure D.12, Figure D.13, Figure D.14, Figure D.15 and Figure D.16.). All genetic part sequences used this chapter was introduced in Table A.5 and the amino acid sequences of each design were listed in Table E.3. All plasmid maps were designed by Benchling online tool.

Lastly, in order to increase biofilm secretion yield under an anhydrotetracycline (aTc) inducible promoter, pZa tetO csgA His and pZa tetO csgA RGD plasmids were constructed. The *csgA His* and *csgA RGD* genes with native *csgA* signal sequence were amplified from previously constructed plasmids with sequential PCR reactions using the primers listed in Table B.6 using Q5 DNA polymerase. PCR products of inserts and pZa tetO vector digested by HF KpnI (NEB) and HF MluI (NEB) enzymes were verified on 1% agarose gel. NucleoSpin Gel and PCR Clean-up kit was used to isolate DNA from agarose gels. PCR fragments were digested using the same restriction enzymes and digested inserts were isolated by NucleoSpin Gel and PCR Clean-up kit. Digested DNA fragments were ligated by T4 DNA ligase. The ligation product was transformed into DH5α chemically competent cells. Plasmid maps were shown in Figure C.17 and Figure C.18. After overnight incubation, single

colonies were selected and positive clones were verified by Sanger sequencing (Genewiz, USA). The sequencing results were analyzed by Geneious R9.0.5 software by alignment (Figure D.17 and Figure D.18). All genetic part sequences used this chapter was introduced in Table A.6 and the amino acid sequences of each design were listed in Table E.3. All plasmid maps were designed by Benchling online tool.

4.3.4 Expression and purification of non-functionalized and functionalized biofilm proteins

E. coli BL21 DE3 strain was used to express CsgA His, CsgA RGD, CsgB His and CsgB RGD proteins from pET22b (+) plasmid. T7 promoter was induced by IPTG. Bacteria harboring plasmid constructs were grown in LB medium supplemented with antibiotics at 37 ºC. After overnight incubation, cell culture was diluted to 1:50 in fresh LB medium. At OD_{600} ~0.6, expressions were induced with IPTG addition to a final concentration of 1 mM. Following two hours incubation at 37 ºC 200 rpm, bacterial culture was centrifuged at 8000 RCF. For purification, HisTrap nickel column was used as described in Section 3.3.4. To remove guanidine hydrochloride and induce fibrillization of proteins, samples were dialyzed against ddH_2O for 2 hours at room temperature and then for O/N at +4 °C in fresh ddH_2O, with gentle stirring. Purified proteins were incubated at room temperature for aging.

.

4.3.5 Extracellular expression of biofilm proteins

In order to induce biofilm formation from pZa pBAD csgA, pZa pBAD csgB, pZa pBAD tasA, pZa pBAD tapA, pZa pBAD csgA His, pZa pBAD csgB His, pZa pBAD tasA His, pZa pBAD tapA His, pZa pBAD fapC His and pZa pBAD fapB His constructs, plasmids were transformed into Δ*csgA* and Δ*csgAB* competent cells by chemical transformation. Bacteria harboring plasmid constructs were grown in LB medium supplemented with antibiotics at 37 ºC. After overnight incubation, cell culture was diluted to 1:25 in fresh LB medium and grown till OD_{600} ~0.6. The cells were centrifuged, and pellet was resuspended in equal volume of M63 medium (Amresco) supplemented with $MgSO_4$ (Sigma) (1 mM), glycerol (Sigma) (0.02 %) and casein hydrolaysate (Sigma) (0.02%). Following, cells were induced with L (+) arabinose (Sigma) to a final concentration of 0.2 %. CsgA His and CsgA RGD expressions were induced with IPTG addition to a final concentration of 1 mM. Cells were induced at 30 ºC for 4 days. Cells were centrifuged at 8000 RCF, pellet was kept at -20 ºC and supernatant was kept at +4 ºC for further analysis. For biofilm formation on solid media, YESCA agar (1 g/L yeast extract, 10 g/L casein hydrolayse, 20 g/l agar) plates including 0.2 % L (+) arabinose were prepared as minimal medium instead of M63. 10 µl of overnight culture was inoculated onto YESCA agar plate and incubated at 30 ºC for 4 days. Cells were scraped from plate and resuspended in 1X PBS for analysis.

In order to induce biofilm formation from pZa tetO csgA His and pZa tetO csgA RGD constructs, plasmids were transformed into Δ*csgA* competent cells. Overnight cultures of cells were diluted to 1:100 in M63 medium supplemented with $MgSO_4$

(1mM), glycerol (0.02 %) and casein hydrolaysate (0.02%), then induced with anhydrotetracycline (aTc) to a final concentration of 214 nM. Cells were incubated at 30 ºC for 4 days.

Produced biofilm fibers were purified as reported previously (Dorval Courchesne, Duraj-Thatte, Tay, Nguyen, & Joshi, 2017). In summary, Gdn-HCl was added to the cultures to a final concentration of 0. 8 M and incubated at +4ºC for 2 hours prior to filtration. Samples were vacuum filtered onto 47 mm polycarbonate filter membranes with 10 µm pores (EMD Millipore). The mass on the filter was incubated with 5 ml 8M Gdn-HCl for 5 minutes and then vacuum filtered. The filter was rinsed with 5 ml ddH_2O 3 times with vacuum filtration. Finally, the filter was incubated with 5 % (m/v) SDS in water for 5 minutes and rinsed with 5 ml ddH_2O 5 times with vacuum filtration. Purified fibers were scraped from the filter by a spatula. Their wet weight was measured on a microbalance and 1.5 mg/ml solutions were prepared in ddH_2O for further analysis.

4.3.6 SDS PAGE and Western Blot

Since CsgA, CsgB, FapC and FapB are amyloid forming proteins, they tend to form amyloid fibers. Therefore, purified protein samples were prepared as explained in Section 2.3.6. Briefly, samples were treated with 100 % formic acid at room temperature for 10 minutes, to break down protein oligomers and were freeze- dried to remove formic acid. Formic acid treated and lyophilized proteins were dissolved in 2x Laemmli sample buffer. Incubating TasA and TapA fibers at 95 ºC in SDS-PAGE sample buffer for 1 hour is sufficient to break down protein oligomers for

SDS-PAGE analysis. TasA and TapA proteins were dissolved in 2x Laemmli sample buffer and incubated at 95 ºC for 1 hour. 15% SDS gel was used to separate proteins. 15 % SDS-PAGE was casted as described in 2.3.6. 1×SDS Running Buffer was used for the run. SDS-PAGE and Western Blot analysis were carried out as described previously.

For secreted samples trichloroacetic acid (TCA) precipitation prior to Western blot was applied. 1 volume of TCA was added onto 4 volume of sample and incubated at room temperature for 10 minutes, centrifuged at 14.000 rpm for 5 minutes and the supernatant was removed. The protein pellet was washed twice by cold acetone the dried at 95 ºC for 10 minutes, mixed by SDS sample buffer and boiled for 5 minutes before SDS PAGE run.

For monomerization of biofilm proteins, the precipitated protein/cell pellet was resuspended in 100% hexafluoroisopropanol (HFIP), incubated for 10 minutes and dried under a nitrogen stream. The HFIP treated pellets were mixed by SDS sample buffer and boiled for 5 minutes prior to run.

4.3.7 Crystal violet (CV) and congo red (CR) staining

First, the biofilm formation in M63 medium on the surface of 24-well plates were quantified by crystal violet (CV) staining. Media was removed from the plates and the plates were washed in ddH_2O twice, to remove unbound cells from the surface. Afterwards, the wells were covered with 0.5% crystal violet in 25 % methanol, and incubated at room temperature, on shaker for 10 minutes. After crystal violet was removed, wells were again washed with ddH_2O twice, to remove excess crystal violet. In order to have quantitative results, the stained cells in the wells were treated

with 30% acetic acid at room temperature for 30 min, with shaking. Then, the acetic acid was collected and absorbance values at 600nm are measured in Microplate Reader.

Crystal violet staining is an indirect method of biofilm measurement, as it binds to cells attached to the surface. Congo red is a more amyloid specific dye that binds to β-sheet rich regions in amyloids (Reichhardt et al., 2015). Therefore, I conducted a congo red (CR) assay. The cells were resuspended in ice-cold PBS and incubated with 1 mg/ml CR at room temperature for 30 minutes. OD_{600} values were measured and then the cells were centrifuged down at 10.000g for 5 minutes. The OD_{480} values of the supernatant were measured. Blanks were taken and OD_{480}/OD_{600} graph was drawn.

4.3.8 Immunocytochemistry (ICC)

In order to observe proteins on the cell surface, I performed immunocytochemistry (ICC) experiments. Cells were collected and washed once with PBS. For fixation, cells were incubated in 4 % formaldehyde in PBS for 10 minutes on rotator at room temperature. Formaldehyde was removed and cells were washed in PBS, twice. Following, cells were resuspended in 1 % BSA in PBS for blocking for 2 hours at room temperature. Cells were centrifuged to remove BSA and incubated in 1:250 primary mouse anti-his 6X antibody in 1 % BSA at +4 ºC for overnight. Cells were washed 3 times with PBS, then incubated in 1:500 anti-mouse secondary antibody DyLight 550 in 1 % BSA for 90 minutes at room temperature. After washing 5 times with PBS, the cells were seeded on microscope glass coverslips and with an upright fluorescent microscope.

4.3.9 Biofilm Formation verification by SEM and TEM

For SEM sample preparation, the cells were washed with 1X PBS twice, then the cells were collected into 2.5 % glutaraldehyde for fixation, placed onto cleaned Si-wafers for 30 minutes at room temperature for attachment. Then, cells were removed and the Si-wafers with attached cells were fixated with increasing concentrations of ethanol (30%, 50%, 80% and then 100% ethanol), 15 minutes at each concentration. At the end, the wafers were dried using critical point drying (CPD). The wafers were then coated with 5 nm Au/Pd and imaged using SEM. FEI Quanta 200 FEG scanning electron microscopy was used for imaging.

TEM samples of biofilm produced *E. coli* cells were also prepared. Cells resuspended and washed twice in PBS were placed on TEM grids for 5 minutes, washed for 5 minutes with ddH_2O and selective binding buffer once, then incubated in 10 nM 5 nm Ni-NTA-Nanogold for 90 minutes at dark. Then the grid was washed for 5 minutes with selective binding buffer 5 times, with PBS twice and with ddH_2O twice. Then, the grid was incubated in 2 % uranyl acetate (UA) for 25 seconds and air dried at room temperature. The samples were visualized using TEM (FEI Tecnai) at 200kV power setting.

4.3.10 Surface coating verification by SEM and TEM

Concentrations of freshly purified CsgA His and CsgA RGD proteins were determined using BCA Assay (Thermo Fisher). Freshly purified monomers were diluted to 20 µM, immediately after dialysis of proteins to PBS pH 7.4. Prepared proteins were incubated at room temperature for 48 hours to induce fiber formation.

For scanning electron microscopy (SEM) imaging of purified fibers, silica surfaces were cleaned firstly in acetone for 15 minutes on a shaker, and then in isopropanol for 15 minutes. Surfaces were then washed in ddH_2O and left to dry. Then 20 µl protein sample was dropped onto the cleaned surface and left to dry. Coated surfaces were placed on SEM stubs and coated with 5 nm gold/palladium prior to SEM imaging. FEI Quanta 200 FEG scanning electron microscopy was used for imaging. For transmission electron microscopy (TEM) imaging of purified fibers, 20 µM of biofilm protein fibers with histidine tags were labeled with nickel nitrilotriacetic acid- conjugated gold nanoparticles (5 nm, Nanoprobes) on TEM grids (formvar carbon-coated 200 mesh nickel grids (Electron Microscopy Sciences), as described previously in 2.3.7. The samples were visualized using TEM (FEI Tecnai) at 200kV power setting. For all analysis, equimolar mix of CsgA and CsgB constructs were also prepared.

4.3.11 Cell adhesion

Non-treated 96 well plates were coated with 20 µM of CsgA His, CsgA RGD, CsgB His and CsgB RGD samples as well as their equimolar mixture. 50 µl of samples were dried on the wells, as triplicates. For purified fibers, non-treated 24 well plates were coated with 100 µM of CsgA His and CsgA RGD. 300 µl of samples were dried on the wells, as triplicates. Cell adhesion assay was conducted as explained in Section 3.3.11. Briefly, 5 X 10^4 HEK293 cells in FBS free media were added to each well to adhere onto coated surfaces for 90 minutes in 37 ºC, 5% CO_2 incubator. Non-adherent cells were washed with 1 X PBS three times and for recovery, adhered cells were incubated in media with 10 % FBS for 4 hours in 37 ºC, 5% CO_2 incubator.

Wells were washed with 1 X PBS 3 times, and alive cells were dyed with 1 µM Calcein AM for 30 minutes. The adhered cells were visualized with an inverted fluorescent microscope and counted. Experiments were conducted in triplicates.

4.4 Results and Discussion

In this study, we focused on optimal production of RGD functionalized biofilm proteins with optimal conditions. Even though amyloid and amyloid-like proteins of biofilms were functionalized with several peptide/protein groups previously, their recombinant functionalization with RGD peptide to increase their cell adhesion capacity has not been reported before. We examined several expression and purification methods to obtain functionalized fibers with enhanced cell adhesion capacity, as depicted in Figure 37.

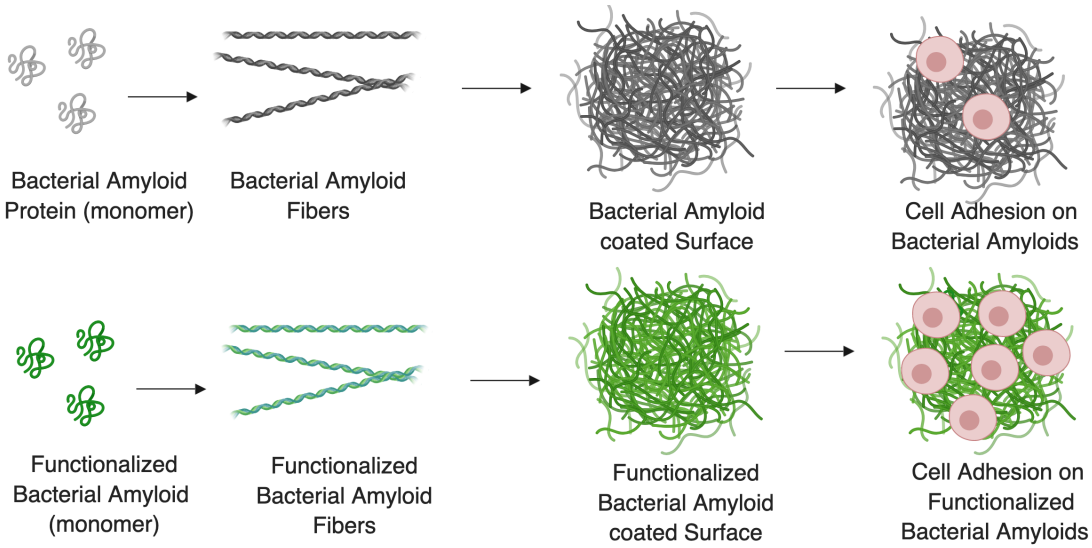


Figure 37. Schematic of the cell adhesion on functionalized and non-functionalized curli fibers.

4.4.1 Cloning, expression and purification of functionalized proteins

CsgA, CsgA RGD, CsgB and CsgB RGD genes were cloned into pET22b (+) vector with His-tag. A GS linker was added between CsgA/CsgB and RGD peptide tag, as well as in between C-terminal His-tag and RGD tag. Schematic diagrams of the construct designs were depicted in Figure 38.

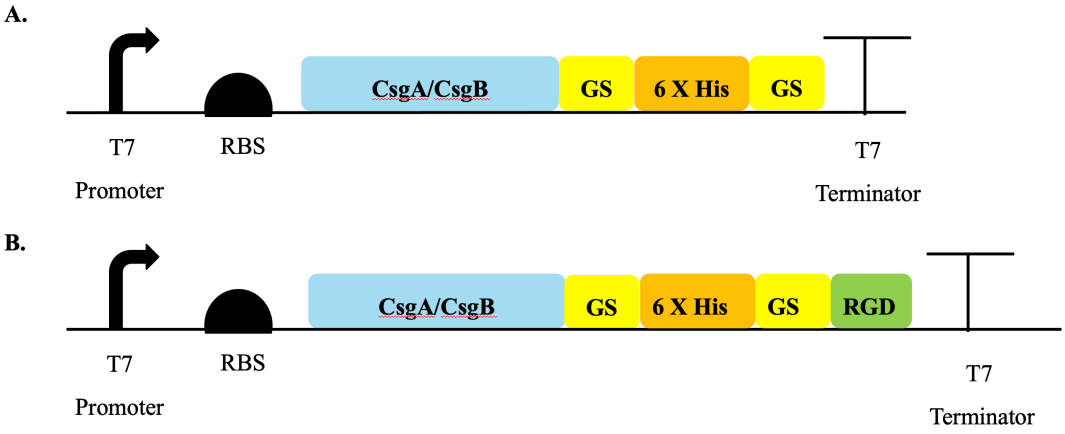


Figure 38. Schematic diagram of CsgA and CsgB RGD expression cassette. GS linker was added to provide flexibility to His-tag and RGD peptide tag. T7 promoter and terminator were used for expression by T7 polymerase.

csgA and *csgB* genes were amplified from the previously constructed plasmids (Figure 39) with the primers listed in Table B.3 and cloned into KpnI-XhoI digested pET22b (+) plasmid (Figure 10) (Figure C.5, Figure C.6).

Clonings were verified by Sanger sequencing. Sequencing result was aligned with corresponding gene sequences at Geneious software. (Figure D.5, Figure D.6) and the match was 100 %.

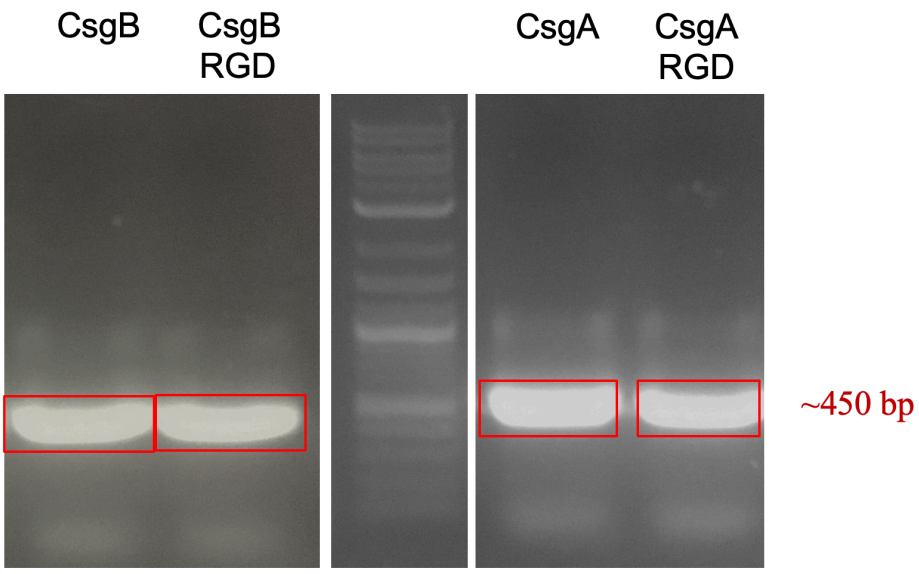


Figure 39. Amplification of *csgA* and *csgB* genes with and without RGD peptide. Previously constructed plasmids were used as templates to amplify *csgA* (lane 4), *csgA RGD* (lane5), *csgB His* (lane1) and *csgB RGD* (lane2) constructs. PCR reaction was performed according to the protocol of Q5 Polymerase (NEB). 2-log DNA ladder (NEB) was used for detection (Lane3).

Proteins were expressed in *E. coli BL21* cells and purified with immobilized metal affinity chromatography (IMAC) under denaturing conditions. Purified proteins were dialyzed against ddH_2O and treated with formic acid for monomerization, then verified using SDS-PAGE and Western blotting using antibodies against polyhistidine tag. In Western Blot, bands appeared ~15 kDa, with small deviations from calculated molecular sizes (Figure 40).

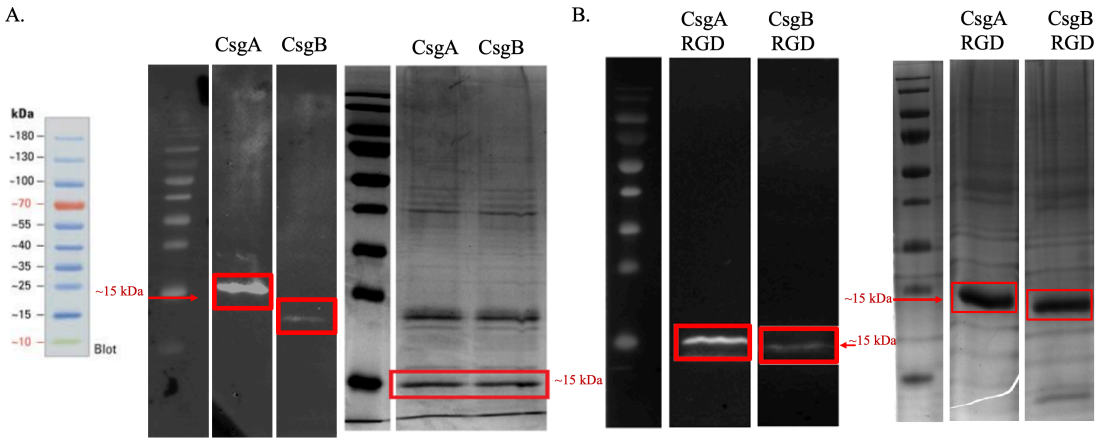


Figure 40. Expression and purification of CsgA, CsgB, CsgA RGD and CsgB RGD by IMAC. A. Western Blot and SDS analysis of CsgA and CsgB. B. Western blot and SDS-PAGE analysis of CsgA RGD and CsgB RGD. Page ruler was used. Bands appeared ~15 kDa with small deviations.

4.4.2 Characterization of fibers by SEM and TEM

Assemblies of the CsgA, CsgA RGD, CsgB and CsgB RGD fibers were visualized by SEM analysis (Figure 41). SEM images indicated a high surface coverage with protein aggregates. Coverage of RGD tagged proteins were lower, however morphologies of functionalized and non-functionalized samples were very similar.

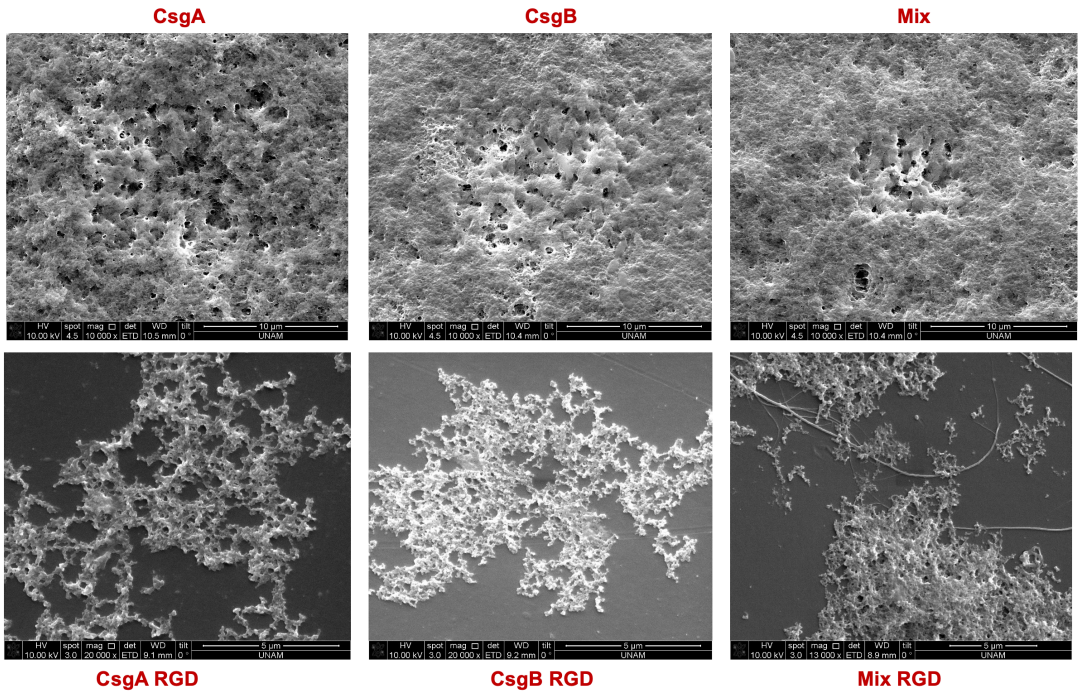


Figure 41. SEM analysis of functionalized CsgA and CsgB fibers. Protein nanofibers (20 µM) were prepared on Si surfaces.

SEM analysis depicted film like aggregates of proteins on coated surfaces, however, it was not clear if those aggregates were fibrillar structures or not. In order to characterize protein aggregates with higher resolution, the protein assemblies were also characterized by TEM. 6X His tags of fibers were labeled with Ni-NTA conjugated gold nanoparticles and nanofiber structures formed by RGD functionalized CsgA and CsgB was shown by gold nanoparticle labelling. Assemblies of the nanoparticles on the nanofibers displaying His-tags were visualized by TEM (Figure 42). The TEM images showed that CsgA RGD and CsgB RGD proteins in PBS form more aggregate like structures instead of thin fibers in the course of 2 days incubation at room temperature. Additionally, gold nanoparticles were clearly visible for CsgB RGD sample and less nanoparticles were visible for

CsgA RGD and mixture samples. Those data might suggest that during dialysis, aggregates of monomers/thin fibers occurred and His-tag of CsgA RGD proteins might not be accessible on the surface of those aggregates

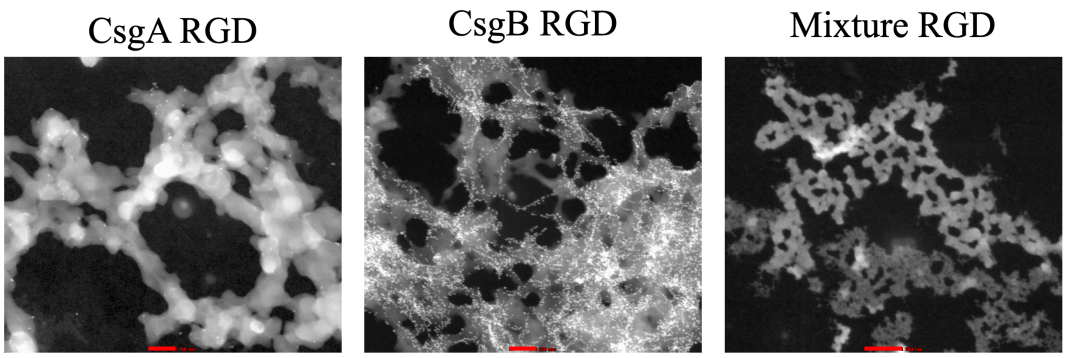


Figure 42. TEM analysis of RGD functionalized CsgA and CsgB fibers. Protein samples (20 μM) were labeled with Ni-NTA-conjugated gold nanoparticles (red lines represent 100 nm scale bar).

4.4.3 Cell adhesion on coated surfaces

As discussed in Section 3.4.6, cell adhesion on a surface is of crucial importance for biomaterial studies. RGD peptide is known to enhance cell adhesion, therefore we functionalized curli proteins to further increase their cell adhesion capacity. Interestingly, TEM results indicate that His tag might be buried in the aggregates for CsgA RGD samples. In this case, RGD group might also be buried in those aggregates and enhancement in cell adhesion may not be obtained. In order to observe the RGD affect, cell adhesion experiments were carried out. Surfaces coated with non-functionalized and functionalized curli proteins were analyzed for their adhesive capacities using HEK293 cells (Figure 43).

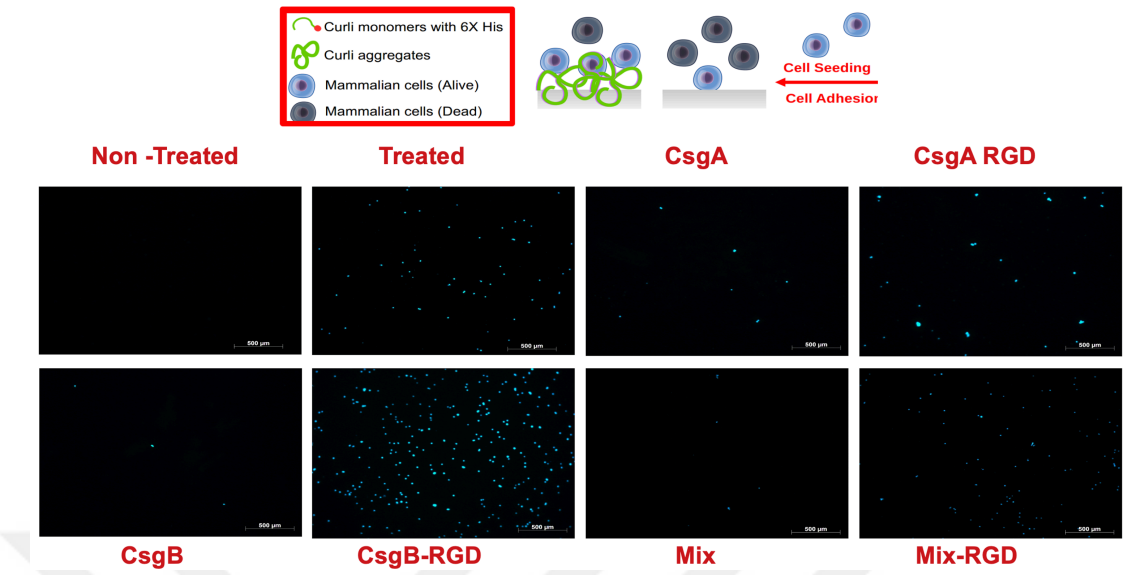


Figure 43. Cell adhesion results of HEK293 cells on curli coated surfaces. Cells adhered onto surfaces were stained with Calcein AM and images are taken with upright fluorescence microscope. (White line represents 500 µm scale bar)

For CsgB and mixture samples, the results were as expected. Addition on RGD peptide group to biofilm proteins enhanced cell adhesion. However, for CsgA, addition of RGD did not cause such a dramatic change in adhesion of HEK293 cells.

4.4.4 Cloning and expression of secreted biofilm proteins

In correlation with TEM data, cell adhesion data suggested that CsgA RGD proteins form aggregates instead of fibers and RGD group was buried inside of those aggregates with His tag. Therefore, IMAC purification of CsgA RGD under denaturing conditions may not be a useful approach to obtain curli fibers as coating materials. Additionally, protein purification yield with IMAC is very low and it is

sometimes troublesome to remove impurities. Besides, purification of biofilm proteins with IMAC columns are problematic, causing clogging of columns. In order to obtain higher yields and to ease purification, I decided to secrete biofilm proteins and purify those secreted biofilm proteins as fibers from extracellular space.

In this section, I constructed plasmids that secrete CsgA and CsgB fibers from *E. coli*, as they are the native biofilm proteins or *E. coli*. However, secretion of other biofilm proteins from *E. coli* using its native biofilm pathway has not been reported before. If other biofilm proteins can also be secreted using the same pathway, their high yield recombinant expression and easy purification from *E. coli* can also be useful. Therefore, I also constructed plasmids that express biofilm proteins TasA and TapA from *B. subtilis*.

Firstly, CsgA, CsgB, TasA and TapA genes were cloned into pZa pBAD vector without His-tag and with N terminal CsgA N42 signal sequence. Schematic diagrams of the construct designs were depicted in Figure 44.

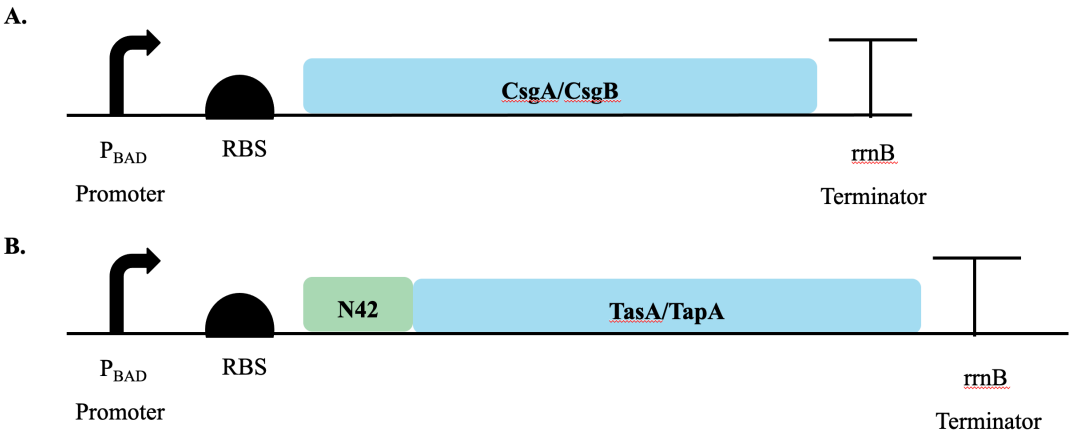


Figure 44. Schematic diagram of biofilm protein expression cassettes from pZa pBAD plasmid. A. CsgA and CsgB expression cassette with native secretion signals. B. TasA and TapA expression cassettes with N42 secretion signal. P_{BAD} promoter and rrnB terminator were used for expression.

csgA and *csgB* genes were amplified from *E. coli Nissle* (EcN) genomic DNA (Figure 45.a) with the primers listed in Table B.4 and cloned into KpnI-XhoI digested pZa pBAD plasmid (Figure C.7, Figure C.8). *tasA* and *tapA* genes with N42 signal sequence were amplified from *B. subtilis* genomic DNA (Figure 45.b, Figure 45.c) with sequential PCR reactions using primers listed in Table B.4 and cloned into KpnI-XhoI digested pZa pBAD plasmid (Figure C.9, Figure C.10).

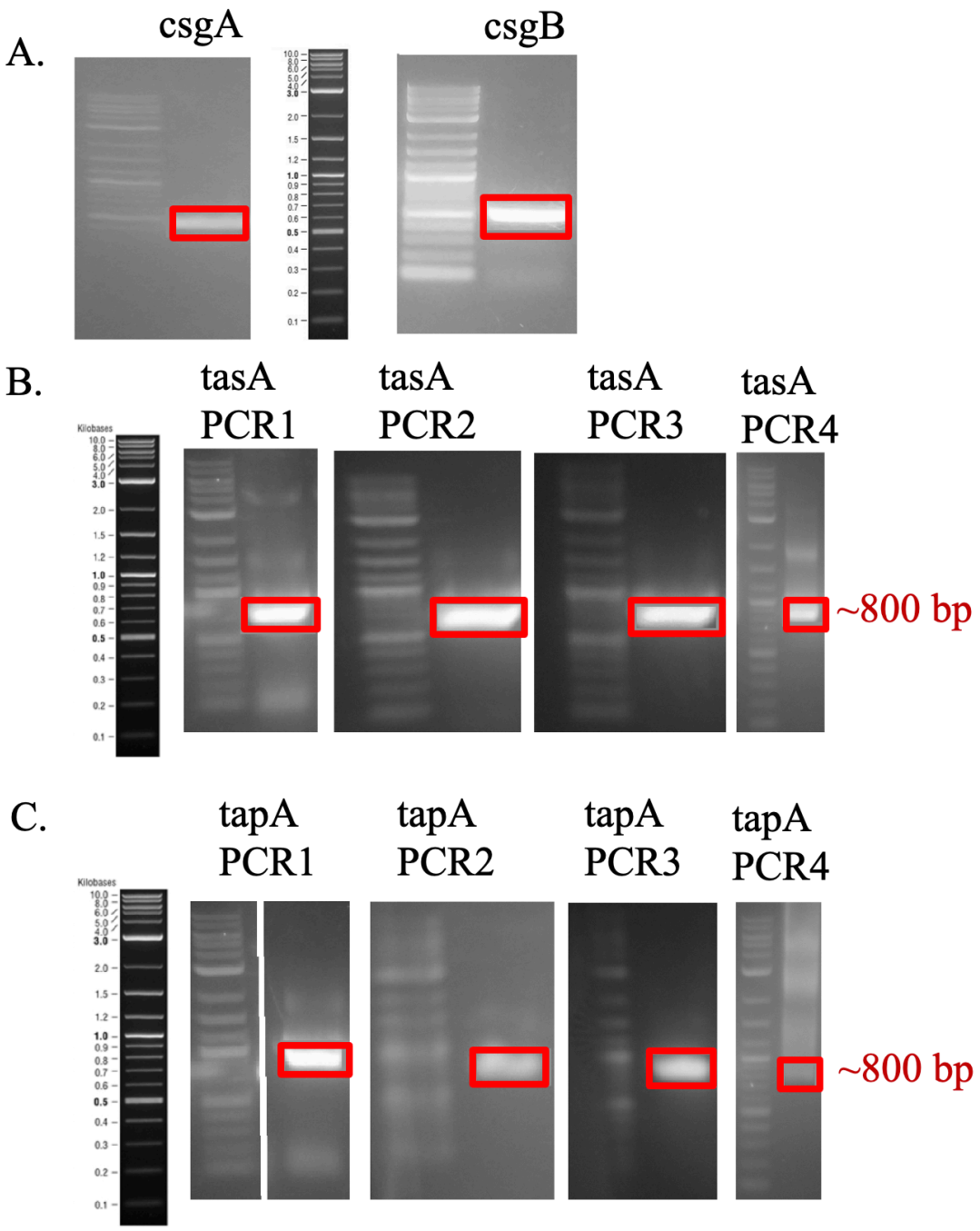


Figure 45. Amplification of genes for biofilm expression cassettes in pZa pBAD. A. PCR products of *csgA* and *csgB* genes from EcN with native signal sequences. Products of consecutive PCR reactions of B. *tasA* and C. *tapA* genes from *B. subtilis* to add N terminal N42 signal sequences. 2-log DNA ladder (NEB) was used for detection.

Clonings were verified by Sanger sequencing. Sequencing result was aligned with corresponding gene sequences at Geneious software. (Figure D.7, Figure D.8, Figure D.9, Figure D.10) and the match was 100 %.

Following the verification of constructs, next step was to observe if curli subunits were secreted and formed biofilms. To investigate this, I transformed TasA, TapA, csgA and csgB pZa pBAD plasmids into ΔcsgAB *E. coli* strain. Biofilm formation was induced in M63 minimal media (with 0.2% glycerol, 1 mM $MgSO_4$ and 0.1% casaminoacids) with L-arabinose to a final concentration of 0.2%. 1:1 v:v mixtures of TasA:TapA and CsgA:CsgB were also prepared. The plates were incubated at 30 ºC for 2 days, without shaking to induce biofilm formation and adhered cells were dyed with crystal violet (CV). 24-well plate wells after crystal violet staining were shown in Figure 46.A. Cells attached to surface were observable in violet color in induced samples, compared to uninduced samples. Quantified CV absorbance values were depicted in Figure 46.B. Those results indicated a significant increase in number of surface adhered cells, suggesting that all CsgA, CsgB, TasA and TapA proteins were successfully secreted and formed biofilms. There was no significant difference between the CV absorbance values of induced and uninduced ΔcsgAB cells without any plasmids, verifying that the difference in cells harboring the plasmids was due to protein expression. Mixture samples did not cause a noteworthy change in the CV absorbance signals.

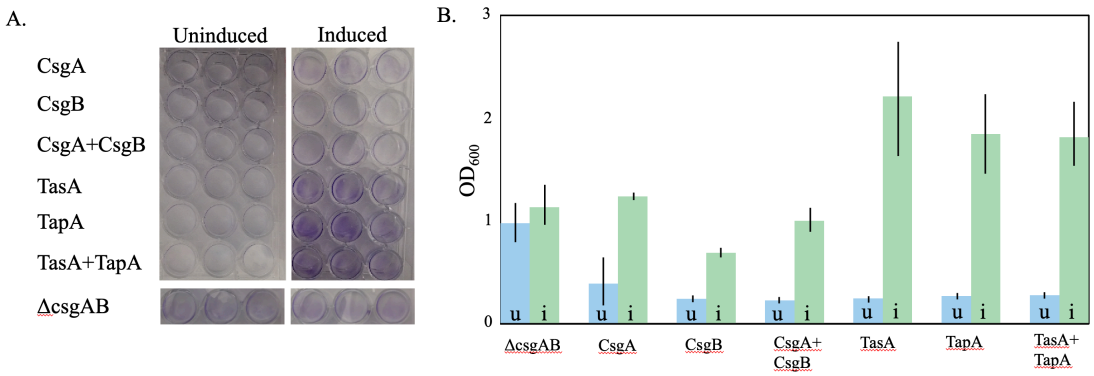


Figure 46. Crsytal violet staining TasA, TapA, CsgA and CsgB pZa pBAD plasmids in ΔcsgAB. A. Cells adhered onto wells were dyed with CV. B. Quantitative analysis of CV staining. u corresponds to uninduced samples and i corresponds to induced samples, n=3.

CV dyes the cells adhered onto wells; therefore, it can be considered as an indirect method to determine biofilm formation. In order to observe biofilm fibers directly, I conducted SEM analysis. I collected the cells from wells in 2.5 % glutaraldehyde for fixation and prepared SEM samples on Si surfaces. SEM images for each sample were summarized in Figure 47.

.

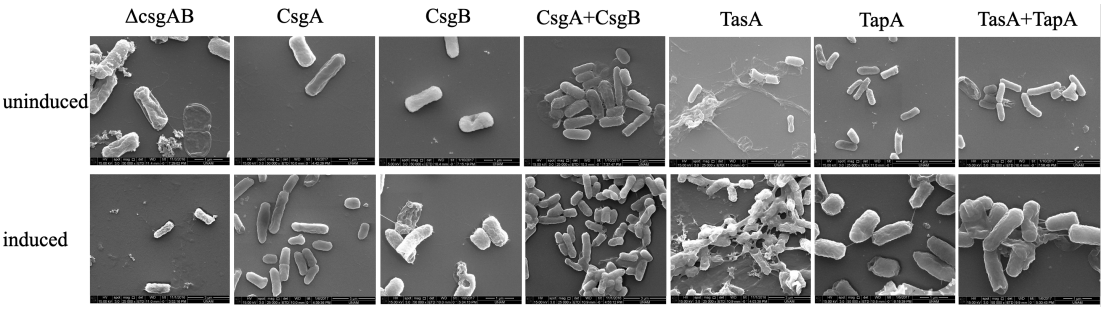


Figure 47. SEM imaging of as well as pZa pBAD CsgA, CsgB, TasA and TapA constructs in ΔcsgAB with their 1:1 mix samples.

In its finest, I expected to see biofilm fibers that were extended from cell surfaces. The figures depicted sticky structures for CsgA:CsgB mix, TasA and TasA:TapA mix constructs, whereas ΔcsgAB, CsgA, CsgB and TapA samples revealed none of those structures. These results were in contradiction with CV results, in which induction caused a significant increase in CV signal in all constructs. Additionally, those sticky structure were also observed in uninduced samples. Leaky expression may cause those structures; however, they may also be cytoplasmic content of lysed cells.

Since CV and SEM results were not in correlation and biofilms were not observed clearly, I decided to induce biofilm formation on YESCA plates in case M63 induction was problematic. Cells on YESCA agar plates with L-arabinose for induction were incubated at 30 ºC for 4, 6, and 9 days long. Then, SEM samples were prepared as described previously and imaged. SEM images from YESCA plates were depicted in Figure 48.

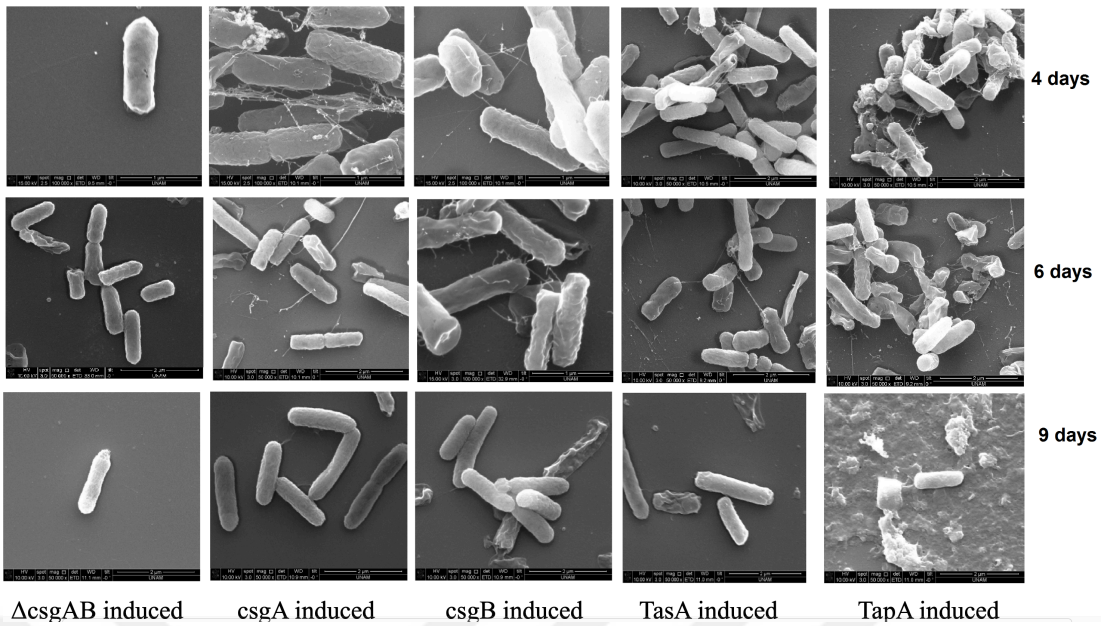


Figure 48. SEM imaging of ΔcsgAB as well as CsgA, CsgB, TasA and TapA pZa pBAD constructs in ΔcsgAB; prepared from YESCA agar plates. The samples were prepared after 4 days, 6 days and 9 days of inoculation. 3 different images were represented for each sample.

4.4.5 Cloning and expression of His-tagged secreted biofilm proteins

Even though some fiber like structures were observed on YESCA SEM samples, most of the cells on prepared SEM samples was not in a biofilm structure. Those results were not conclusive, therefore same constructs with 6X His tags were constructed to observe biofilm secretion/formation using methods targeting His tag such as Western Blot, Ni-NTA conjugated gold nanoparticle labeling and immunocytochemistry (ICC). In this section, I also constructed plasmids that express His tagged biofilm proteins FapC and FapB from *P. aeruginosa* with N terminal N42 signal sequence. Schematic diagrams of the construct designs were depicted in Figure 49.

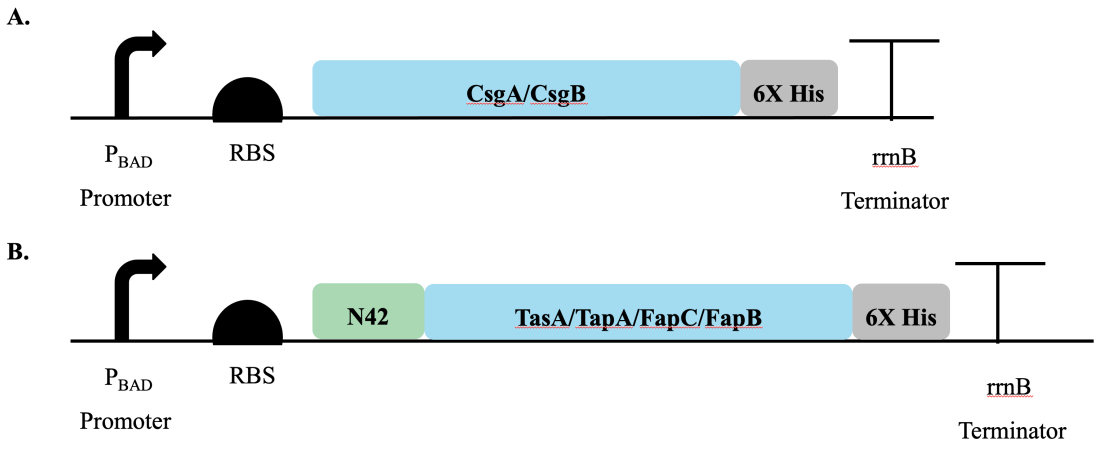


Figure 49. Schematic diagram of biofilm protein expression cassettes from pZa pBAD plasmid with 6 X His tag. A. CsgA and CsgB expression cassette with native secretion signals. B. TasA, TapA, FapC and FapB expression cassettes with N42 secretion signal. P_{BAD} promoter and rrnB terminator were used for expression.

csgA, csgB, tasA and *tapA* genes with N42 signal sequence were PCR amplified (Figure 50.A) using constructs from Section 4.4.4 with the primers listed in Table B.5 and cloned into KpnI-XhoI digested pZa pBAD plasmid (Figure C.11, Figure C.12, Figure C.13, Figure C.14). *fapC* and *fapB* genes with N42 signal sequence were amplified from synthesized gene fragments with sequential PCR (Figure 50.B) with the primers listed in Table B.5 and cloned into KpnI-XhoI digested pZa pBAD plasmid (Figure C.15, Figure C.16).

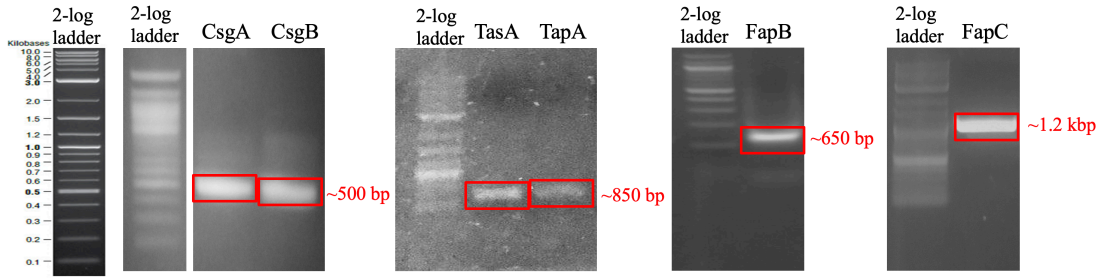


Figure 50. Amplification of genes for His-tagged biofilm expression cassettes in pZa pBAD. Previously constructed plasmids were used as template for CsgA, CsgB, TasA, TapA, FapC and FapB with N42 signal sequence. 2-log DNA ladder (NEB) was used for detection.

Clonings were verified by Sanger sequencing and the result was aligned with corresponding gene sequences at Geneious software. (Figure D.11, Figure D.12, Figure D.13, Figure D.14, Figure D.15, Figure D.16) and the match was 100 %.

To investigate if curli subunits were secreted and formed biofilms, I transformed TasA, TapA, CsgA, CsgB, FapC and FapB pZa pBAD His plasmids into ΔcsgAB competent cells by chemical transformation. Biofilm formation was induced in M63 minimal media as explained in Section 4.4.4.

For verification with western blot, I collected the supernatant and precipitated the secreted proteins via TCA precipitation. CsgA, CsgB, TasA, TapA, FapC and FapB samples were treated with HFIP. At the same time, the cells were collected from the bottom of the wells, treated with HFIP, resuspended in SDS sample buffer, boiled for 5 minutes and proceeded with Western blot against 6 X His tag. For TasA and TapA samples, samples boiled in SDS buffer without HFIP treatment for 1 hour was also used, to compare effect of HFIP and boiling (Figure 51).

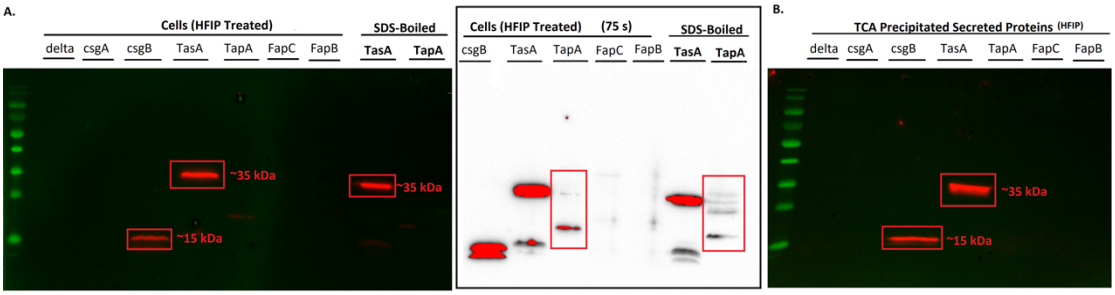


Figure 51. The western blot analysis of ΔcsgAB cells as control and csgA-His, csgB-His, (N42) TasA-His, (N42) TapA-His, (N42) FapC-His and (N42) FapB-His constructs in ΔcsgAB. The western analysis was done for A. the cells and for B. the supernatant to detect secreted proteins.

In the cell samples, TasA proteins were observed ~35 kDa, around its expected sizes. TapA sample was only observed with increased exposure time (~75 seconds). It can mean lower expression of TapA or a smaller number of cells. In each case, TapA was shown to be expressed. In secreted proteins, TasA was observed very nicely however TapA was not observed. The results suggest that TasA was secreted however TapA aggregates probably sticked to the cell wall, or not secreted. For csgA samples, interestingly, no bands were observed. CsgB band was observed at ~15 kDa for both cells and secreted protein portions, as expected. Interestingly FapC and FapB proteins were absent both in cell and supernatant portions. Since the induction mechanism was the same as the other proteins, FapC and FapB were probably expressed in the cells and cannot be secreted. Since amyloid accumulation is toxic to the cells, their accumulation may lead death of cells expressing the proteins.

4.4.6 Verification of biofilm formation by TEM and ICC

In order to observe if proteins were present on the cell surface, I performed immunocytochemistry (ICC) experiments using DyLight 550 antibody for labeling of cell surface and imaged the cells using fluorescence microscope. The ICC results were depicted in Figure 52.

Even though red signals and cells co-localized, the fluorescent signal was not very strong. To observe amyloid fibers located on cells with better resolution and to obtain a labeling with higher magnification, Au-labeled TEM samples from 4 days old biofilm samples were prepared as explained previously. TEM images were taken to observe biofilm fibers around bacterial cells and Au nanoparticles localized on those fibers. Results were demonstrated in Figure 53.

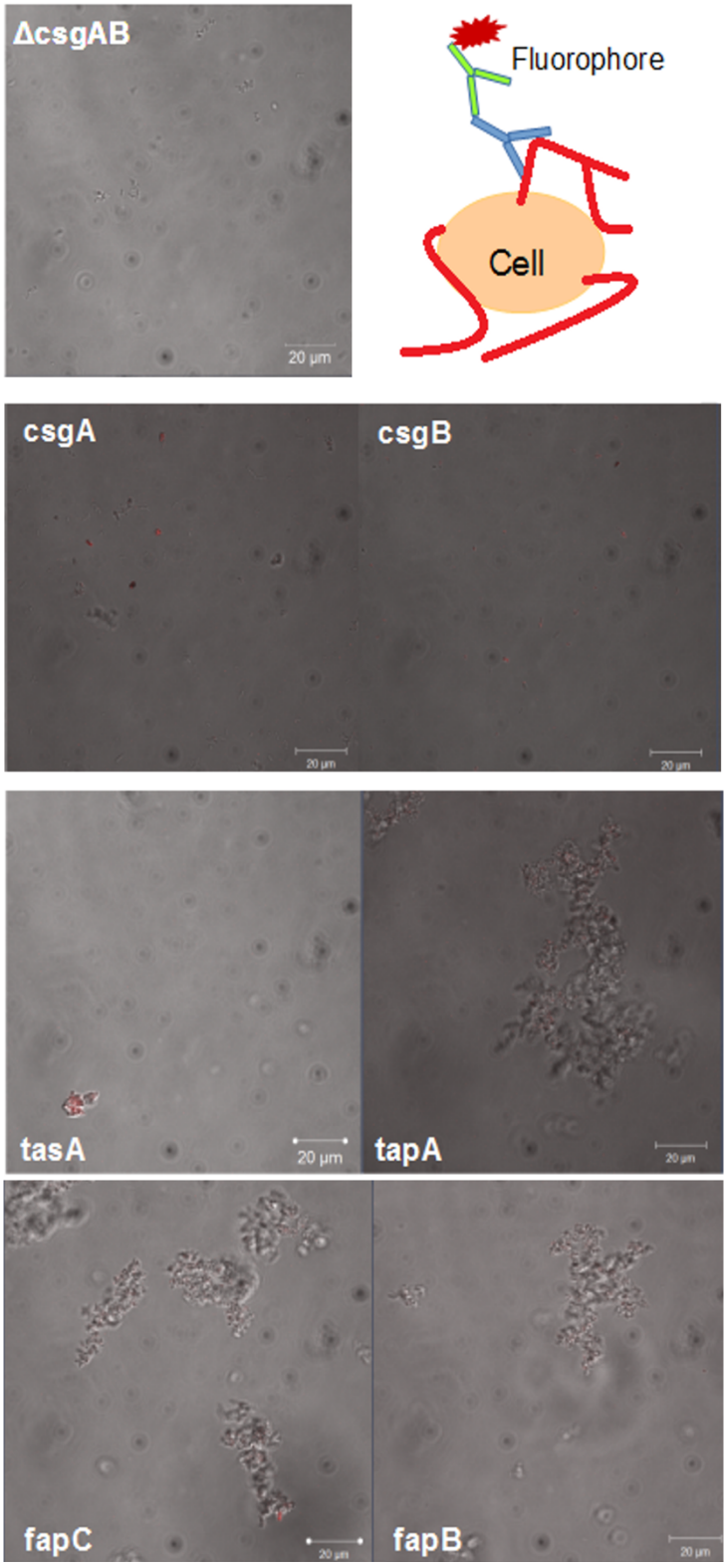


Figure 52. Immunocytochemistry of ΔcsgAB cells secreting CsgA, CsgB, TasA, TapA, FapC and FapB proteins. His-tagged proteins in the amyloid fibers around the cells are recognized by anti-his 1º antibody and then detected via DyLight 2º antibody.

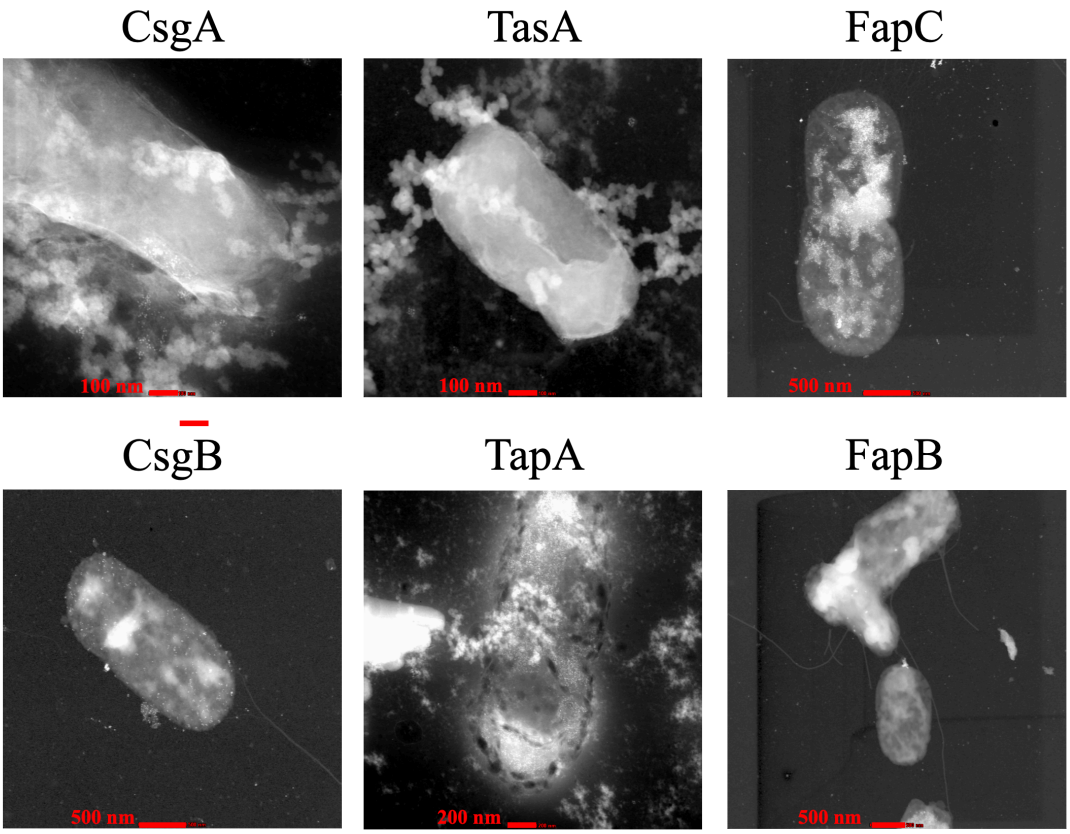


Figure 53. TEM images of Ni-NTA-Nanogold labeled, 4 days old in TasA, TapA, CsgA, CsgB, FapC and FapB biofilm forming colonies after L-arabinose induction. Red lines were used as scale bar.

In TEM images, Au particles were mainly focused on the cell surface rather than the fibers and for some FapC and FapB samples no fibers were observed. These data may suggest that some proteins on the cell surface could exist without going into fiber or aggregate state and bind to Au particles. However, absence of fibers in CsgA sample were not expected. Therefore, a problem in biofilm formation process was probably the reason for absence of fibers. YESCA agar plates were used as a different biofilm induction approach to induce cells. Additionally, nanoparticle detection on cells in both ICC and TEM together with the absence of fibers may suggest that the signal was coming from the cytoplasmic region of dead cells. In

order to avoid leakage of cytoplasmic content due to cell death during sample preparation, fixation prior to sample preparation was applied. ICC was formed as described above. Results were depicted in Figure 54.

In this experimental set, samples other than CsgB gave no signal, verifying our last assumption that the signal was coming from the cytoplasm of dead cells. Therefore, those proteins were either not secreted or not interacting with the cell surface. Especially csgA was quite interesting as it is the native biofilm protein of *E. coli*. In nature, *E. coli* CsgB localizes onto cell surface and CsgA interacts with CsgB to anchor itself to the membrane. I hypothesized that since *csgB* gene was knocked out in the cells, CsgA can only interact with the surface very weakly due to non-covalent weak interactions. It can also be the case for other proteins since their cell anchoring machinery was not available in *E. coli*.

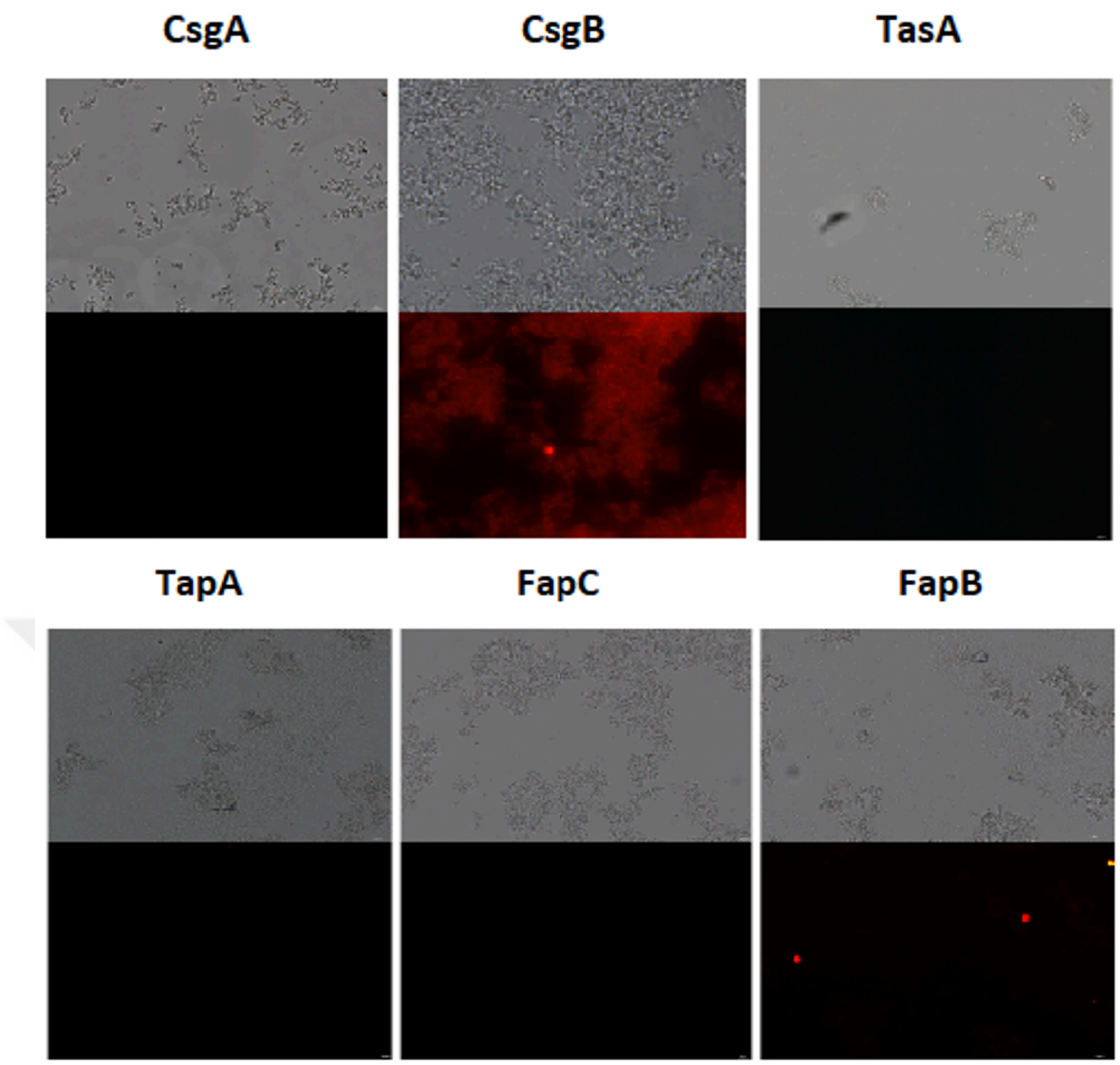


Figure 54. ICC results of biofilm proteins expressed from pZa pBAD tasA, tapA, fapC, fapB, csgA and csgB constructs in ΔcsgAB, prepared from YESCA agar plates. The cells were fixed prior to ICC. The images were taken using Upright Florescence Microscope, 40X magnification.

In order to observe the behavior of CsgA and other proteins in the presence of CsgB, I transformed those plasmids into ΔcsgAB cells, expressing native CsgB. After 4 days induction on YESCA agar, cells were collected and labeled for ICC as previously described. The results were depicted in Figure 55. In those samples, both CsgA and CsgB gave florescence signal, meaning that CsgA requires presence of

CsgB as an anchoring protein to be expressed on cells surface and other proteins cannot be anchored onto the cell surface even in the presence of CsgB.

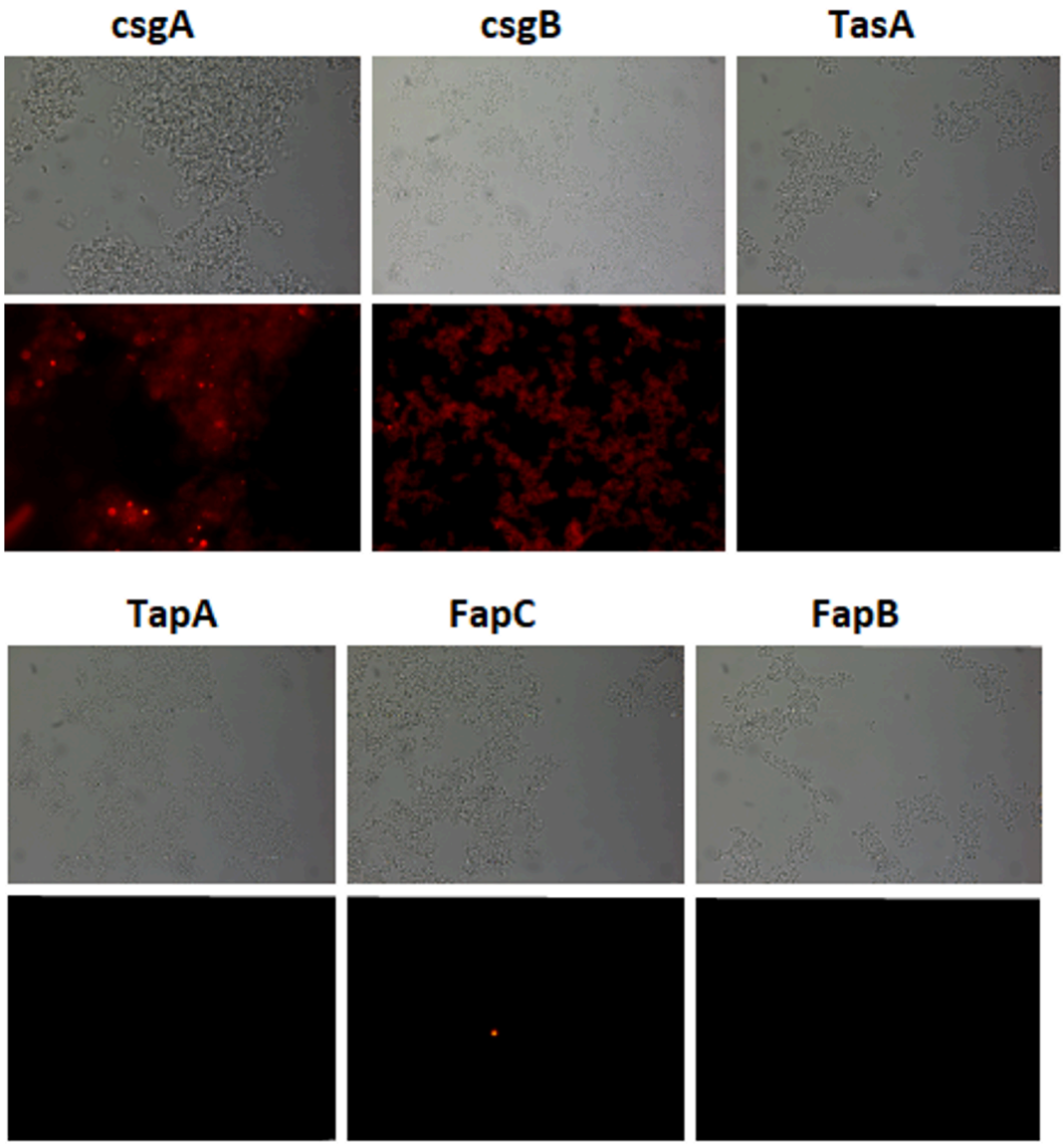


Figure 55. ICC results of biofilm proteins expressed from pZa pBAD tasA, tapA, fapC, fapB, csgA and csgB constructs in ΔcsgA, prepared from YESCA agar plates. The cells were fixed prior to ICC. The images were taken using Upright Florescence Microscope, 40X magnification.

4.4.7 Cloning and expression of functionalized biofilms as fibers

Fiber formation by secreted recombinant proteins were demonstrated in the previous section. Briefly, TasA and TapA proteins can be secreted using native biofilm secretion pathway of E. coli, however they cannot anchor onto cell surface and form amyloid fibers. FapC and FapB, on the other hand, cannot be secreted using native biofilm secretion pathway of E. coli and consequently cannot form amyloid fibers. Therefore, I decided to focus on CsgA fibers for high yield protein purification. In this section, in order to increase yield even more, CsgA His and CsgA RGD proteins were expressed under the control of a stronger promoter with tighter expression control. For this purpose, these genes were cloned into pZa tetO vector. Schematic diagrams of the construct designs were depicted in Figure 56.

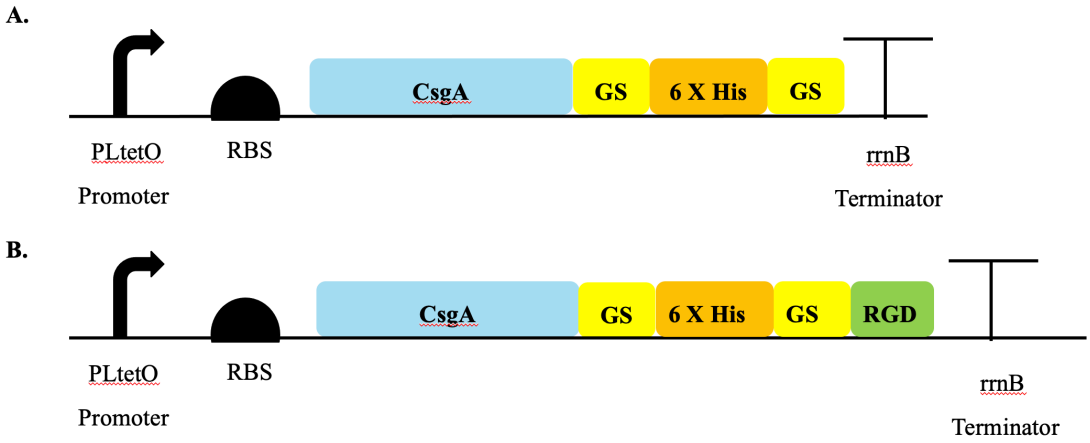


Figure 56. Schematic diagram of biofilm protein expression cassettes from pZa tetO plasmid with 6 X His tag. A. CsgA expression cassette with native secretion signal. B. CgA RGD expression cassettes with native secretion signal. PLtetO promoter and rrnB terminator were used for expression.

csgA and *csgA RGD* genes with native signal sequence were PCR amplified (Figure 57) using previously formed constructs with the primers listed in Table B.6 and cloned into KpnI-MluI digested pZa TetO plasmid (Figure C.17, Figure C.18).

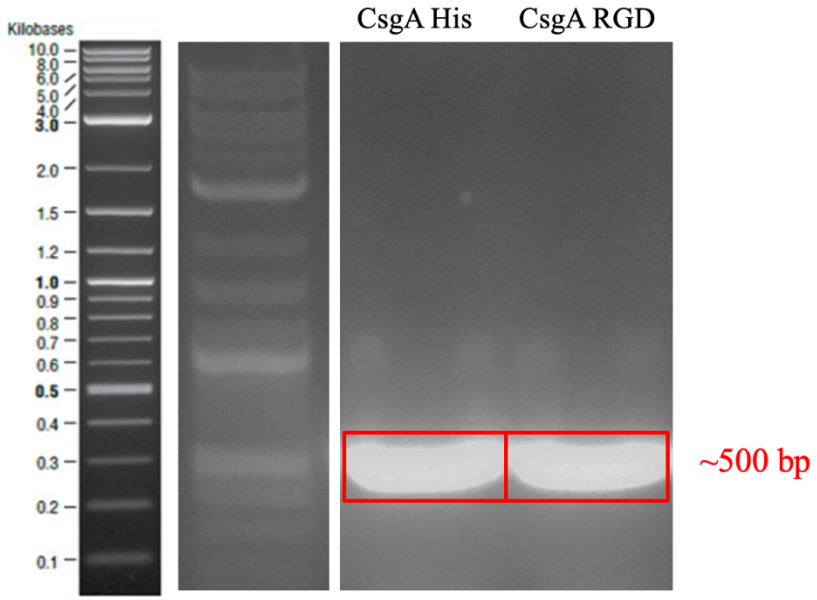


Figure 57. Amplification of genes for His-tagged and RGD tagged expression of CsgA in pZa tetO. 2-log DNA ladder (NEB) was used for detection.

Clonings were verified by Sanger sequencing and the results were aligned at Geneious software. (Figure D.17, Figure D.18) and the match was 100 %.

To investigate if curli subunits were secreted and formed biofilms, I transformed plasmids into ΔcsgA competent cells by chemical transformation. Biofilm formation was induced in M63 minimal media as explained in Section 4.3.4. Firstly, biofilm formation was tested with Congo Red (CR) staining, using induced ΔcsgA cells as control. Cells with biofilm fibers were stained red as control cells without the fibers remained mostly white (Figure 58.A). Quantitative analysis of CR-stained samples also verified amyloid fiber formation for CsgA His and CsgA RGD proteins (Figure 58.B).

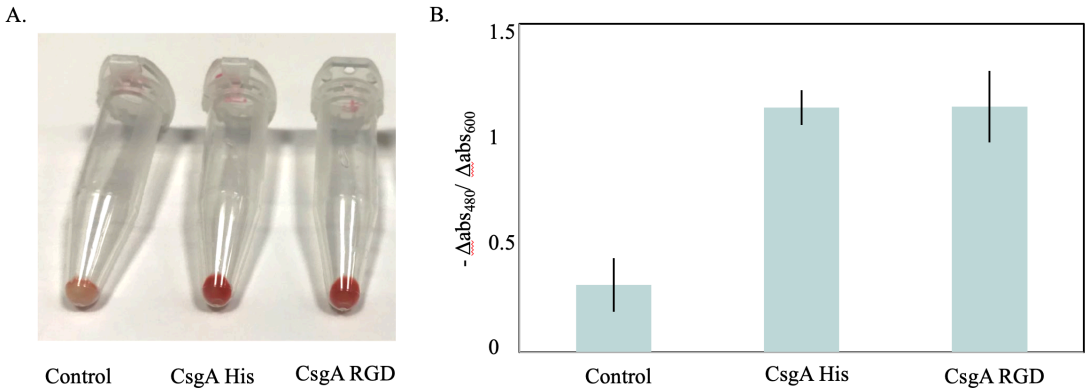


Figure 58. Congo Red staining of cell pellets of CsgA His and CsgA RGD samples after induction in M63 medium, n=3.

4.4.8 Verification of fiber purification

Following verification of fiber formation, functionalized biofilm fibers were purified using the filtration-based method. The filters and silica wafers coated with purified biofilms were examined by SEM. SEM images revealed fibrillar structures in both filters and coated surfaces (Figure **59**).

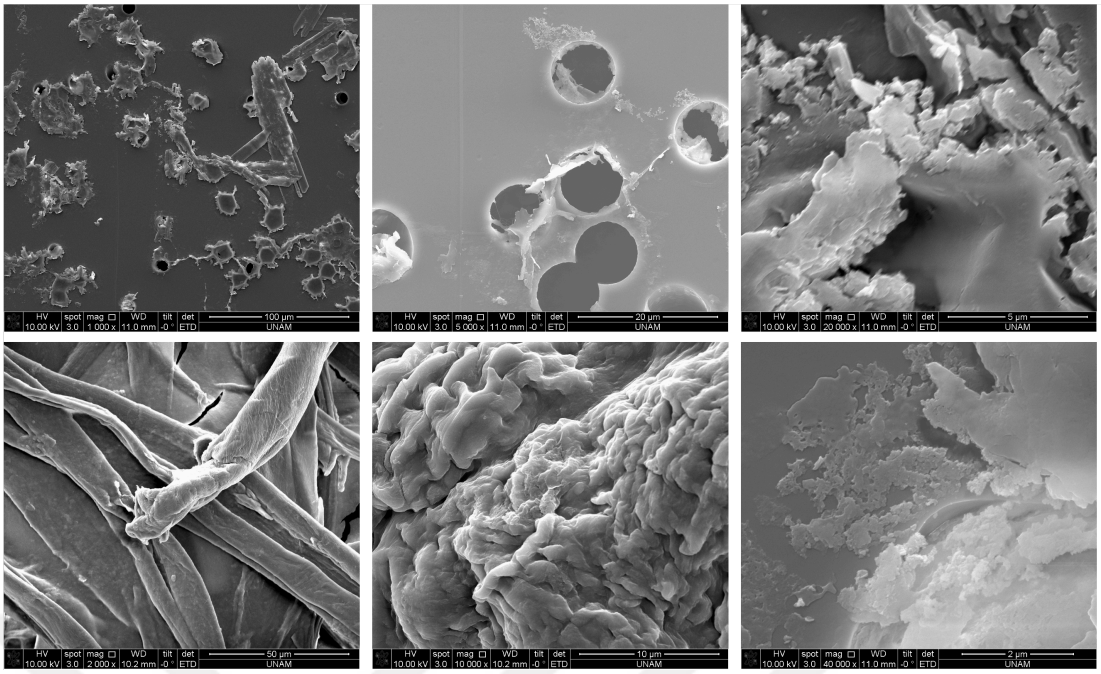


Figure 59. SEM analysis of His-tag and RGD functionalized CsgA fibers. Filters used for purification and Si surfaces coated with purified fibers were analyzed.

4.4.9 Cell adhesion on purified fibers

I determined the cell adhesion capacity of filter purified CsgA-His and CsgA-RGD fibers using HEK293 cells to analyze the effect of RGD peptide addition on on cell adhesive properties of fibers. Representative fluorescent microscopy images of Calcein AM labeled adhered cells are depicted in Figure **60**.A. In addition, the total number of adhered cells are summarized in Figure **60**.B. Those results suggested that RGD peptide addition increased cell adhesion capacity of CsgA fibers compared to CsgA-His and non-treated surfaces, significantly. Number of adhered cells on CsgA-RGD coated surfaces approached the number of cells adhered onto tissue culture treated wells. Even though the number of adhered cells increased by RGD motif, the

variation between each experimental sets were high, as in the case of glycosylated samples. The high variation may arise from non-uniform coating of surfaces with fibrils. Increasing the concentration of the fibers used for coating can help to improve surface coverage of coatings and provide more uniform coatings. Therefore, it is necessary to optimize uniformity of surface coverage of coated surfaces and cell adhesion capacity in response to increase in concentration and surface coverage.

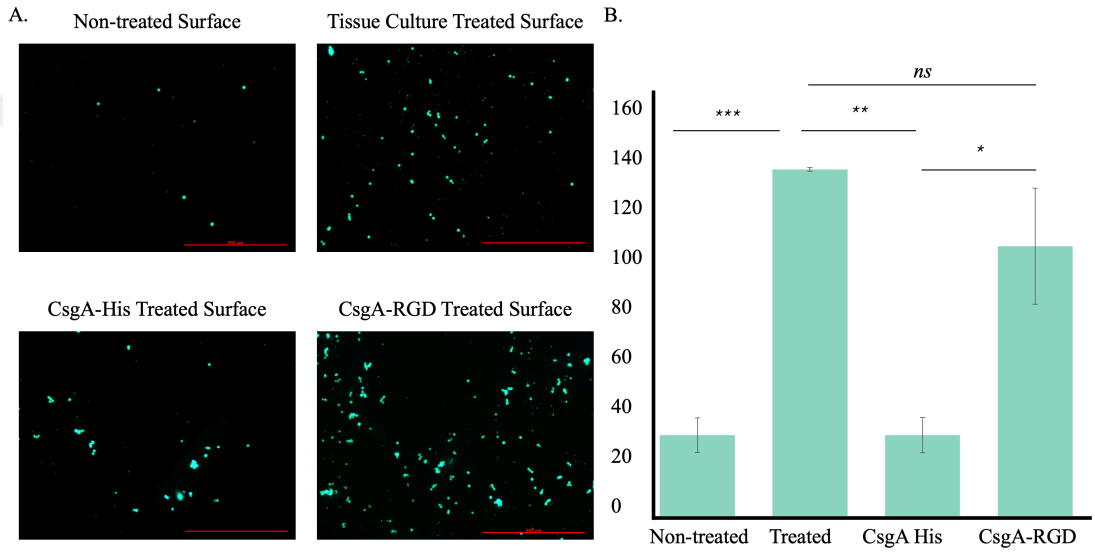


Figure 60. Adhesion of HEK293 cells on surfaces coated with filter purified CsgA-His and CsgA-RGD fibers. A. Representative images of Calcein AM labelled adhered cells and B. Quantitative analysis of adhered number of cells. Significance values are calculated by t-test, n=2. Red bars correspond to 500 µm.

4.5 Conclusion

Curli proteins are functional amyloid structures that possess properties such as high rigidity and mechanical strength and due to those properties, curli proteins have great potential to serve as biomaterials that require mechanical strength, such as tissue

scaffolds and artificial valves. In addition, ease of modification via addition of functional peptide groups with genetic engineering approaches enables functionalization of curli fibers for specialized purposes.

It is of integral importance to characterize cell adhesion and proliferation features of curli fibers prior to their utilization as functional biomaterials. In this study, I characterized cell adhesion properties of surfaces coated with wild type and RGD functionalized CsgA & CsgB fibers. I demonstrated that surfaces coated with RGD functionalized curli fibers can have the potential to serve as a scaffold for HEK293 cells to adhere onto surfaces. However, further characterization was required as the fiber formation was in the form of aggregation.

As a further step, to increase protein purification yields and obtain proteins in fiber form, secretion of biofilm proteins were optimized. *B. subtilis* biofilm proteins were also secreted with *E. coli* biofilm secretion pathway however they did not form amyloid fibers around the cells. *P. aeruginosa* biofilm proteins were not even secreted. Therefore, I only functionalized *E. coli* CsgA protein for analysis. Wild type and RGD functionalized curli proteins were secreted as fibers and collected in high yields using filtration methods. Even though RGD peptide increased the number of adhered HEK293 cells on surfaces, variation between each experiment was high. Therefore, further optimization of coating and adherence processes are required.

5 CHAPTER V

CONCLUSION AND FUTURE PERSPECTIVES

Amyloids are highly ordered protein aggregates that self-assemble into fibrillar structures. Amyloids are found in both disease-associated and functional structures. Biofilm proteins are great examples of functional amyloids. Utilization of amyloid fibers holds great potentials as biomaterials due to their mechanical rigidity and strength. Additionally, modification of physicochemical properties via alteration of amino acid sequences is straightforward therefore, it enables their utilization as functional biomaterials with desired functionalities.

In the first chapter of the study, we analyzed the binding affinity of CsgA and CsgB proteins and their equimolar mixture to surfaces used in biomedical applications. We aimed to get a better understanding of the forces that drives the protein-surface interaction, so we can coat the surfaces in a more controllable manner for designed functions. Silica and gold are used as prosthetics in several areas of the body, such as ear, teeth, knees or bones. Hydroxyapatite based materials are also widely used as implants for teeth and bone, especially for applications that require bone formation and healing. The surface properties of those materials need specialized properties depending on the interacting tissue or cell type. For this reason, biomaterials made of gold, silica or hydroxyapatite are treated with several chemical processes or with different polymer types during production, to control surface properties. In this thesis, we showed that those surfaces can easily be coated with biofilm proteins and

by controlling the concentration and ingredients of protein mixtures, surface coverage can be controlled. However, there are still several questions that needs to be answered before utilization of those proteins as coating on biomaterials.

Utilization of those materials as biomaterial coatings require biocompatibility. Therefore, cell adhesive properties of those amyloid fibers are yet to be determined. The question that whether the surface coatings support cell adhesion, cell growth and cell migration remain yet to be answered. Further studies are required to characterize these properties for different cell types.

One of the advantages using curli proteins is that they can be functionalized with peptide/protein motifs without disrupting the amyloid structure. Therefore, functionalization with different peptide motifs specific for cell or tissue types can further enhance the biocompatibility of the surfaces. For example, bone morphogenetic protein-2 (BMP2) peptide is widely used in bone regeneration and repair applications. Functionalization of curli fibers with BMP-2 peptide could enhance its applicability as implant coatings for bone repair studies. The examples of functional peptide motifs could be broaden depending on the application and tissue type. Optimization of optimal surface coating coverage for tissue interaction with optimal protein components upon peptide group addition would be required for biomaterial applications.

Mechanical and viscoelastic properties of the surfaces are crucial parameters for cell or tissue interaction of surfaces. In a further study, characterization of mechanical and viscoelastic properties of the surfaces coated with curli fibers can hold crucial clues for the optimal surface/cell interactions. Precise control of those properties could also be possible by tuning the proportion of CsgA and CsgB proteins in the protein mixture. Also, using the aforementioned strategy about the genetic fusion of

functional peptide groups, those properties could be optimized for desired interactions.

In the second chapter of the thesis, we worked on effect of glycosylation on the adhesive and viscoelastic properties of biofilm proteins. We showed that glycosylation enhanced binding affinity of TasA fibers to gold surfaces and altered the viscoelastic properties of the films on the surfaces. However, there are still several questions that need to be addressed for a deeper understanding of glycosylation effects on biofilm proteins.

Firstly, a more detailed understanding of the molecular mechanism behind the enhanced gold binding affinity, theoretically and practically, could provide important clues for designing new protein-based biomaterials with higher surface binding affinity. The exploration of adsorption behavior requires determination of differences in structural conformations of protein adsorbed layers. Also, characterization of surfaces in terms of bonding, wettability, roughness and thickness with methods such as XPS, contact angle measurement and ellipsometry can hold crucial information for adsorption mechanism. In addition, all these experimental approaches have several limitations, so understanding of protein adsorption on solid surfaces is relatively limited especially on molecular level. At this point, molecular dynamic simulations can provide the missing understanding for protein-solid surface interactions at molecular level. In brief, exploration of protein adsorption mechanism on solid surfaces is a highly complex problem for future studies.

Secondly, in this thesis we provided a proof-of-concept study that depicted the usability of glycosylation as a tool to alter adhesive and viscoelastic properties of the biofilm proteins. We characterized our system at room temperature on gold surfaces or HEK293 cells. But in a future study, a wider characterization of the system such

as physiological temperature, on different surfaces with solutions of varying pH or salt concentrations could provide a better understanding in terms of biomaterial applications. Thermodynamic characteristics of the proteins may change upon exposure to the different temperatures. Therefore, adhesion kinetics and viscosity at other temperatures such as 37°C could behave differently than room temperature. In addition, even though gold is used as a model surface in this chapter, characterization of the glycosylation effect on other biomedically relevant surfaces such as silica and hydroxyapatite as in the first chapter are equally important.

In the last chapter of the thesis, we tried to enhance cell adhesion capacity of curli fibers by fusion of RGD peptide motif, using different purification methods to enhance yield, purity and convenience of protein purification. In this chapter, we showed that RGD peptide addition enhanced cell adhesive properties of curli fibers, however the variance in the system was very high. Therefore, further characterization of surface coating in terms of the protein concentration and obtained surface coverage is required to obtain optimal coating conditions for scaffold surfaces. In addition, functionalization of curli CsgA and CsgB fibers with other peptide groups for desired applications could provide practical surfaces with varying properties.

In all chapters in this thesis, optimization of biomaterials was conducted for mechanical, viscoelastic and adhesive properties *in vitro*. However, utilization of biomaterials as implants or prosthetics in human body requires other complex *in vivo* characterizations in terms of biocompatibility. Firstly, since the proteins are of bacterial source, their utilization in the human body can induce immune response that can lead to rejection of material or other complications. Therefore, immune reactivity of the materials utilized in this thesis should be defined in future studies, for determination of their biocompatibility *in vivo*. Following, cell adhesive capacities of

the surfaces, functionalized or not, should be determined *in vivo*. In our *in vitro* experimental sets, the microenvironment for cells is under defined conditions, however in the body the microenvironment is much more complex. In addition, in the human body there are several cell types interacting with the biomaterials which can alter the behavior of cell adhesive properties for the designed surfaces. Therefore*, in vivo* characterization of the designed surfaces in the future works is very critical for optimal functionality of biomaterials in the body.

To conclude, in this thesis we characterized and optimized production, secretion, *in vitro* amyloid formation and surface interaction properties of several biofilm proteins. We showed that CsgA and CsgB fibers interact differently with surfaces of different chemical properties. In addition, we functionalized several amyloid forming biofilm proteins with different functional groups for specific applications. We added DQNAT glycosylation tag to TasA protein and depicted that glycosylation increased adhesive capacity of TasA fibers. Finally, we demonstrated that functionalization of CsgA and CsgB proteins with RGD peptide group enhanced their cell adhesion capacity. Our findings hold crucial clues for future design of amyloid based biomaterials with more complex functional requirements in terms of adhesion onto medically relevant surfaces and mammalian cells.

6 BIBLIOGRAPHY

Abdelwahab, M. T., Kalyoncu, E., Onur, T., Baykara, M. Z., & Seker, U. O. S. (2017). Genetically-Tunable Mechanical Properties of Bacterial Functional Amyloid Nanofibers. *Langmuir: The ACS Journal of Surfaces and Colloids*, *33*(17), 4337–4345. https://doi.org/10.1021/acs.langmuir.7b00112

Ahan, R. E., Saltepe, B., Apaydin, O., & Seker, U. O. S. (2019). Cellular Biocatalysts Using Synthetic Genetic Circuits for Prolonged and Durable Enzymatic Activity. *Chembiochem: A European Journal of Chemical Biology*, *20*(14), 1799–1809. https://doi.org/10.1002/cbic.201800767

Alteri, C. J., Xicohténcatl-Cortes, J., Hess, S., Caballero-Olín, G., Girón, J. A., & Friedman, R. L. (2007). Mycobacterium tuberculosis produces pili during human infection. *Proceedings of the National Academy of Sciences of the United States of America*, *104*(12), 5145–5150. https://doi.org/10.1073/pnas.0602304104

An, S., Wu, J., & Zhang, L.-H. (2010). Modulation of Pseudomonas aeruginosa biofilm dispersal by a cyclic-Di-GMP phosphodiesterase with a putative hypoxia-sensing domain. *Applied and Environmental Microbiology*, *76*(24), 8160–8173. https://doi.org/10.1128/AEM.01233-10

Anand, G., Sharma, S., Dutta, A. K., Kumar, S. K., & Belfort, G. (2010). Conformational Transitions of Adsorbed Proteins on Surfaces of Varying Polarity. *Langmuir*, *26*(13), 10803–10811. https://doi.org/10.1021/la1006132

Aung, K. M. M., Ho, X., & Su, X. (2008). DNA assembly on streptavidin modified surface: A study using quartz crystal microbalance with dissipation or resistance measurements. *Sensors and Actuators B: Chemical*, *131*(2), 371–378. https://doi.org/10.1016/j.snb.2007.11.058

Azzopardi, P. V., O'Young, J., Lajoie, G., Karttunen, M., Goldberg, H. A., & Hunter, G. K. (2010). Roles of Electrostatics and Conformation in Protein-Crystal Interactions. *PLoS ONE*, *5*(2). https://doi.org/10.1371/journal.pone.0009330

Balistreri, A., Goetzler, E., & Chapman, M. (2020). Functional Amyloids Are the Rule Rather Than the Exception in Cellular Biology. *Microorganisms*, *8*(12). https://doi.org/10.3390/microorganisms8121951

Balistreri, A., Kahana, E., Janakiraman, S., & Chapman, M. R. (2020). Tuning Functional Amyloid Formation Through Disulfide Engineering. *Frontiers in Microbiology*, *11*. https://doi.org/10.3389/fmicb.2020.00944

Barken, K. B., Pamp, S. J., Yang, L., Gjermansen, M., Bertrand, J. J., Klausen, M., … Tolker-Nielsen, T. (2008). Roles of type IV pili, flagellum-mediated motility and extracellular DNA in the formation of mature multicellular structures in Pseudomonas aeruginosa biofilms. *Environmental Microbiology*, *10*(9), 2331–2343. https://doi.org/10.1111/j.1462-2920.2008.01658.x

Barnhart, M. M., & Chapman, M. R. (2006). Curli biogenesis and function. *Annual Review of Microbiology*, *60*, 131–147. https://doi.org/10.1146/annurev.micro.60.080805.142106

Barraud, N., Hassett, D. J., Hwang, S.-H., Rice, S. A., Kjelleberg, S., & Webb, J. S. (2006). Involvement of nitric oxide in biofilm dispersal of Pseudomonas aeruginosa. *Journal of Bacteriology*, *188*(21), 7344–7353. https://doi.org/10.1128/JB.00779-06

Bian, Z., Brauner, A., Li, Y., & Normark, S. (2000). Expression of and cytokine activation by Escherichia coli curli fibers in human sepsis. *The Journal of Infectious Diseases*, *181*(2), 602–612. https://doi.org/10.1086/315233

Blanco, L. P., Evans, M. L., Smith, D. R., Badtke, M. P., & Chapman, M. R. (2012). Diversity, biogenesis and function of microbial amyloids. *Trends in Microbiology*, *20*(2), 66–73. https://doi.org/10.1016/j.tim.2011.11.005

Bolisetty, S., & Mezzenga, R. (2016). Amyloid-carbon hybrid membranes for universal water purification. *Nature Nanotechnology*, *11*(4), 365–371. https://doi.org/10.1038/nnano.2015.310

Borja, G. M., Meza Mora, E., Barrón, B., Gosset, G., Ramírez, O. T., & Lara, A. R. (2012). Engineering Escherichia coli to increase plasmid DNA production in high cell-density cultivations in batch mode. *Microbial Cell Factories*, *11*, 132. https://doi.org/10.1186/1475-2859-11-132

Borlee, B. R., Goldman, A. D., Murakami, K., Samudrala, R., Wozniak, D. J., & Parsek, M. R. (2010). Pseudomonas aeruginosa uses a cyclic-di-GMP-regulated adhesin to reinforce the biofilm extracellular matrix. *Molecular Microbiology*, *75*(4), 827–842. https://doi.org/10.1111/j.1365-2958.2009.06991.x

Botyanszki, Z., Tay, P. K. R., Nguyen, P. Q., Nussbaumer, M. G., & Joshi, N. S. (2015). Engineered catalytic biofilms: Site-specific enzyme immobilization onto E. coli curli nanofibers. *Biotechnology and Bioengineering*, *112*(10), 2016–2024. https://doi.org/10.1002/bit.25638

Branda, S. S., González-Pastor, J. E., Ben-Yehuda, S., Losick, R., & Kolter, R. (2001). Fruiting body formation by Bacillus subtilis. *Proceedings of the National Academy of Sciences*, *98*(20), 11621–11626. https://doi.org/10.1073/pnas.191384198

Chai, L., Romero, D., Kayatekin, C., Akabayov, B., Vlamakis, H., Losick, R., & Kolter, R. (2013). Isolation, characterization, and aggregation of a structured bacterial matrix precursor. *The Journal of Biological Chemistry*, *288*(24), 17559–17568. https://doi.org/10.1074/jbc.M113.453605

Chai, Y., Beauregard, P. B., Vlamakis, H., Losick, R., & Kolter, R. (2012). Galactose metabolism plays a crucial role in biofilm formation by Bacillus subtilis. *MBio*, *3*(4), e00184-00112. https://doi.org/10.1128/mBio.00184-12

Chai, Y., Chu, F., Kolter, R., & Losick, R. (2008). Bistability and biofilm formation in Bacillus subtilis. *Molecular Microbiology*, *67*(2), 254–263. https://doi.org/10.1111/j.1365-2958.2007.06040.x

Charrier, E. E., Pogoda, K., Wells, R. G., & Janmey, P. A. (2018). Control of cell morphology and differentiation by substrates with independently tunable elasticity and viscous dissipation. *Nature Communications*, *9*(1), 449. https://doi.org/10.1038/s41467-018-02906-9

Cherny, I., Rockah, L., Levy-Nissenbaum, O., Gophna, U., Ron, E. Z., & Gazit, E. (2005). The formation of Escherichia coli curli amyloid fibrils is mediated by prion-like peptide repeats. *Journal of Molecular Biology*, *352*(2), 245–252. https://doi.org/10.1016/j.jmb.2005.07.028

Clegg, J. R., Ludolph, C. M., & Peppas, N. A. (2020). QCM-D assay for quantifying the swelling, biodegradation, and protein adsorption of intelligent nanogels. *Journal of Applied Polymer Science*, *137*(25), 48655. https://doi.org/10.1002/app.48655

Cobley, C. M., Chen, J., Cho, E. C., Wang, L. V., & Xia, Y. (2011). Gold nanostructures: A class of multifunctional materials for biomedical

applications. *Chemical Society Reviews*, *40*(1), 44–56. https://doi.org/10.1039/b821763g

Daley, W. P., & Yamada, K. M. (2013). ECM-modulated cellular dynamics as a driving force for tissue morphogenesis. *Current Opinion in Genetics & Development*, *23*(4), 408–414. https://doi.org/10.1016/j.gde.2013.05.005

Das, S., Jacob, R. S., Patel, K., Singh, N., & Maji, S. K. (2018). Amyloid Fibrils: Versatile Biomaterials for Cell Adhesion and Tissue Engineering Applications. *Biomacromolecules*, *19*(6), 1826–1839. https://doi.org/10.1021/acs.biomac.8b00279

Davies, D. G., Parsek, M. R., Pearson, J. P., Iglewski, B. H., Costerton, J. W., & Greenberg, E. P. (1998). The involvement of cell-to-cell signals in the development of a bacterial biofilm. *Science (New York, N.Y.)*, *280*(5361), 295–298. https://doi.org/10.1126/science.280.5361.295

DeBenedictis, E. P., Liu, J., & Keten, S. (2016). Adhesion mechanisms of curli subunit CsgA to abiotic surfaces. *Science Advances*, *2*(11), e1600998. https://doi.org/10.1126/sciadv.1600998

Dong, X.-L., Zhou, H.-L., Wu, T., & Wang, Q. (2008). Behavior regulation of adsorbed proteins via hydroxyapatite surface texture control. *The Journal of Physical Chemistry. B*, *112*(15), 4751–4759. https://doi.org/10.1021/jp0768672

Donlan, R. M. (2002). Biofilms: Microbial life on surfaces. *Emerging Infectious Diseases*, *8*(9), 881–890. https://doi.org/10.3201/eid0809.020063

Dorval Courchesne, N.-M., Duraj-Thatte, A., Tay, P. K. R., Nguyen, P. Q., & Joshi, N. S. (2017). Scalable Production of Genetically Engineered Nanofibrous Macroscopic Materials via Filtration. *ACS Biomaterials Science & Engineering*, *3*(5), 733–741. https://doi.org/10.1021/acsbiomaterials.6b00437

Drenkard, E., & Ausubel, F. M. (2002). Pseudomonas biofilm formation and antibiotic resistance are linked to phenotypic variation. *Nature*, *416*(6882), 740–743. https://doi.org/10.1038/416740a

Dueholm, M. S., Nielsen, S. B., Hein, K. L., Nissen, P., Chapman, M., Christiansen, G., … Otzen, D. E. (2011). Fibrillation of the major curli subunit CsgA under a wide range of conditions implies a robust design of aggregation. *Biochemistry*, *50*(39), 8281–8290. https://doi.org/10.1021/bi200967c

Dueholm, M. S., Otzen, D., & Nielsen, P. H. (2013). Evolutionary insight into the functional amyloids of the pseudomonads. *PloS One*, *8*(10), e76630. https://doi.org/10.1371/journal.pone.0076630

Dueholm, M. S., Søndergaard, M. T., Nilsson, M., Christiansen, G., Stensballe, A., Overgaard, M. T., … Nielsen, P. H. (2013). Expression of Fap amyloids in Pseudomonas aeruginosa, P. fluorescens, and P. putida results in aggregation and increased biofilm formation. *MicrobiologyOpen*, *2*(3), 365–382. https://doi.org/10.1002/mbo3.81

Eisenberg, D., & Jucker, M. (2012). The amyloid state of proteins in human diseases. *Cell*, *148*(6), 1188–1203. https://doi.org/10.1016/j.cell.2012.02.022

Elahi, N., Kamali, M., & Baghersad, M. H. (2018). Recent biomedical applications of gold nanoparticles: A review. *Talanta*, *184*, 537–556. https://doi.org/10.1016/j.talanta.2018.02.088

Evans, M. L., & Chapman, M. R. (2014). Curli Biogenesis: Order out of Disorder. *Biochimica et Biophysica Acta*, *1843*(8), 1551–1558. https://doi.org/10.1016/j.bbamcr.2013.09.010

Feldman, M. F., Wacker, M., Hernandez, M., Hitchen, P. G., Marolda, C. L., Kowarik, M., … Aebi, M. (2005). Engineering N-linked protein glycosylation with diverse O antigen lipopolysaccharide structures in Escherichia coli. *Proceedings of the National Academy of Sciences of the United States of America*, *102*(8), 3016–3021. https://doi.org/10.1073/pnas.0500044102

Fenoglio, I., Fubini, B., Ghibaudi, E. M., & Turci, F. (2011). Multiple aspects of the interaction of biomacromolecules with inorganic surfaces. *Advanced Drug Delivery Reviews*, *63*(13), 1186–1209. https://doi.org/10.1016/j.addr.2011.08.001

Flemming, H.-C., Neu, T. R., & Wozniak, D. J. (2007). The EPS matrix: The "house of biofilm cells." *Journal of Bacteriology*, *189*(22), 7945–7947. https://doi.org/10.1128/JB.00858-07

Flemming, H.-C., & Wingender, J. (2010). The biofilm matrix. *Nature Reviews. Microbiology*, *8*(9), 623–633. https://doi.org/10.1038/nrmicro2415

Fowler, D. M., Koulov, A. V., Balch, W. E., & Kelly, J. W. (2007). Functional amyloid—From bacteria to humans. *Trends in Biochemical Sciences*, *32*(5), 217–224. https://doi.org/10.1016/j.tibs.2007.03.003

Fox, B. G., & Blommel, P. G. (2009). Autoinduction of protein expression. *Current Protocols in Protein Science*, *Chapter 5*, Unit 5.23. https://doi.org/10.1002/0471140864.ps0523s56

Fuqua, C., & Greenberg, E. P. (2002). Listening in on bacteria: Acyl-homoserine lactone signalling. *Nature Reviews. Molecular Cell Biology*, *3*(9), 685–695. https://doi.org/10.1038/nrm907

Gerwig, J., Kiley, T. B., Gunka, K., Stanley-Wall, N., & Stülke, J. (2014). The protein tyrosine kinases EpsB and PtkA differentially affect biofilm formation in Bacillus subtilis. *Microbiology*, *160*(Pt 4), 682–691. https://doi.org/10.1099/mic.0.074971-0

Gilbert, K. B., Kim, T. H., Gupta, R., Greenberg, E. P., & Schuster, M. (2009). Global position analysis of the Pseudomonas aeruginosa quorum-sensing transcription factor LasR. *Molecular Microbiology*, *73*(6), 1072–1085. https://doi.org/10.1111/j.1365-2958.2009.06832.x

Gras, S. L., Tickler, A. K., Squires, A. M., Devlin, G. L., Horton, M. A., Dobson, C. M., & MacPhee, C. E. (2008). Functionalised amyloid fibrils for roles in cell adhesion. *Biomaterials*, *29*(11), 1553–1562. https://doi.org/10.1016/j.biomaterials.2007.11.028

Greenwald, J., & Riek, R. (2010). Biology of amyloid: Structure, function, and regulation. *Structure (London, England: 1993)*, *18*(10), 1244–1260. https://doi.org/10.1016/j.str.2010.08.009

Hall-Stoodley, L., Costerton, J. W., & Stoodley, P. (2004). Bacterial biofilms: From the Natural environment to infectious diseases. *Nature Reviews Microbiology*, *2*(2), 95–108. https://doi.org/10.1038/nrmicro821

Hammar, M., Arnqvist, A., Bian, Z., Olsén, A., & Normark, S. (1995). Expression of two csg operons is required for production of fibronectin- and congo red-binding curli polymers in Escherichia coli K-12. *Molecular Microbiology*, *18*(4), 661–670.

Hammer, N. D., Schmidt, J. C., & Chapman, M. R. (2007). The curli nucleator protein, CsgB, contains an amyloidogenic domain that directs CsgA polymerization. *Proceedings of the National Academy of Sciences of the*

United States of America, *104*(30), 12494–12499. https://doi.org/10.1073/pnas.0703310104

Hartley, M. D., Schneggenburger, P. E., & Imperiali, B. (2013). Lipid bilayer nanodisc platform for investigating polyprenol-dependent enzyme interactions and activities. *Proceedings of the National Academy of Sciences of the United States of America*, *110*(52), 20863–20870. https://doi.org/10.1073/pnas.1320852110

Hennebert, E., Maldonado, B., Ladurner, P., Flammang, P., & Santos, R. (2015). Experimental strategies for the identification and characterization of adhesive proteins in animals: A review. *Interface Focus*, *5*(1), 20140064. https://doi.org/10.1098/rsfs.2014.0064

Hnilova, M., Oren, E. E., Seker, U. O. S., Wilson, B. R., Collino, S., Evans, J. S., … Sarikaya, M. (2008). Effect of molecular conformations on the adsorption behavior of gold-binding peptides. *Langmuir: The ACS Journal of Surfaces and Colloids*, *24*(21), 12440–12445. https://doi.org/10.1021/la801468c

Hoefling, M., Iori, F., Corni, S., & Gottschalk, K.-E. (2010). Interaction of amino acids with the Au(111) surface: Adsorption free energies from molecular dynamics simulations. *Langmuir: The ACS Journal of Surfaces and Colloids*, *26*(11), 8347–8351. https://doi.org/10.1021/la904765u

Höök, F., Rodahl, M., Kasemo, B., & Brzezinski, P. (1998). Structural changes in hemoglobin during adsorption to solid surfaces: Effects of pH, ionic strength, and ligand binding. *Proceedings of the National Academy of Sciences*, *95*(21), 12271–12276. https://doi.org/10.1073/pnas.95.21.12271

Huang, J., Liu, S., Zhang, C., Wang, X., Pu, J., Ba, F., … Zhong, C. (2019). Programmable and printable Bacillus subtilis biofilms as engineered living materials. *Nature Chemical Biology*, *15*(1), 34–41. https://doi.org/10.1038/s41589-018-0169-2

Huang, S., Hou, Q., Guo, D., Yang, H., Chen, T., Liu, F., … Wang, J. (2017). Adsorption mechanism of mussel-derived adhesive proteins onto various self-assembled monolayers. *RSC Advances*, *7*(63), 39530–39538. https://doi.org/10.1039/C7RA07425E

Huang, W., Anvari, B., Torres, J. H., LeBaron, R. G., & Athanasiou, K. A. (2003). Temporal effects of cell adhesion on mechanical characteristics of the single chondrocyte. *Journal of Orthopaedic Research: Official Publication of the Orthopaedic Research Society*, *21*(1), 88–95. https://doi.org/10.1016/S0736-0266(02)00130-4

Iadanza, M. G., Jackson, M. P., Hewitt, E. W., Ranson, N. A., & Radford, S. E. (2018). A new era for understanding amyloid structures and disease. *Nature Reviews. Molecular Cell Biology*, *19*(12), 755–773. https://doi.org/10.1038/s41580-018-0060-8

Ikeda, T., & Kuroda, A. (2011). Why does the silica-binding protein “Si-tag” bind strongly to silica surfaces? Implications of conformational adaptation of the intrinsically disordered polypeptide to solid surfaces. *Colloids and Surfaces. B, Biointerfaces*, *86*(2), 359–363. https://doi.org/10.1016/j.colsurfb.2011.04.020

Jacob, R. S., Ghosh, D., Singh, P. K., Basu, S. K., Jha, N. N., Das, S., … Maji, S. K. (2015). Self healing hydrogels composed of amyloid nano fibrils for cell culture and stem cell differentiation. *Biomaterials*, *54*, 97–105. https://doi.org/10.1016/j.biomaterials.2015.03.002

Jeong, H., Barbe, V., Lee, C. H., Vallenet, D., Yu, D. S., Choi, S.-H., … Kim, J. F. (2009). Genome sequences of Escherichia coli B strains REL606 and BL21(DE3). *Journal of Molecular Biology*, *394*(4), 644–652. https://doi.org/10.1016/j.jmb.2009.09.052

Jiang, M., Shao, W., Perego, M., & Hoch, J. A. (2000). Multiple histidine kinases regulate entry into stationary phase and sporulation in Bacillus subtilis. *Molecular Microbiology*, *38*(3), 535–542. https://doi.org/10.1046/j.1365-2958.2000.02148.x

John, T., Greene, G. W., Patil, N. A., Dealey, T. J. A., Hossain, M. A., Abel, B., & Martin, L. L. (2019). Adsorption of Amyloidogenic Peptides to Functionalized Surfaces Is Biased by Charge and Hydrophilicity. *Langmuir: The ACS Journal of Surfaces and Colloids*, *35*(45), 14522–14531. https://doi.org/10.1021/acs.langmuir.9b02063

Jolley, C., Klem, M., Harrington, R., Parise, J., & Douglas, T. (2011). Structure and photoelectrochemistry of a virus capsid-TiO2 nanocomposite. *Nanoscale*, *3*(3), 1004–1007. https://doi.org/10.1039/c0nr00378f

Jones, S. E., Paynich, M. L., Kearns, D. B., & Knight, K. L. (2014). Protection from intestinal inflammation by bacterial exopolysaccharides. *Journal of Immunology (Baltimore, Md.: 1950)*, *192*(10), 4813–4820. https://doi.org/10.4049/jimmunol.1303369

Kalyoncu, E., Ahan, R. E., Ozcelik, C. E., & Seker, U. O. S. (2019). Genetic Logic Gates Enable Patterning of Amyloid Nanofibers. *Advanced Materials (Deerfield Beach, Fla.)*, *31*(39), e1902888. https://doi.org/10.1002/adma.201902888

Ke, P. C., Zhou, R., Serpell, L. C., Riek, R., Knowles, T. P. J., Lashuel, H. A., … Mezzenga, R. (2020). Half a century of amyloids: Past, present and future. *Chemical Society Reviews*, *49*(15), 5473–5509. https://doi.org/10.1039/c9cs00199a

Kearns, D. B., Chu, F., Branda, S. S., Kolter, R., & Losick, R. (2005). A master regulator for biofilm formation by Bacillus subtilis. *Molecular Microbiology*, *55*(3), 739–749. https://doi.org/10.1111/j.1365-2958.2004.04440.x

Kelly, J., Jarrell, H., Millar, L., Tessier, L., Fiori, L. M., Lau, P. C., … Szymanski, C. M. (2006). Biosynthesis of the N-linked glycan in Campylobacter jejuni and addition onto protein through block transfer. *Journal of Bacteriology*, *188*(7), 2427–2434. https://doi.org/10.1128/JB.188.7.2427-2434.2006

Khalili, A. A., & Ahmad, M. R. (2015). A Review of Cell Adhesion Studies for Biomedical and Biological Applications. *International Journal of Molecular Sciences*, *16*(8), 18149–18184. https://doi.org/10.3390/ijms160818149

Kim, E.-J., Wang, W., Deckwer, W.-D., & Zeng, A.-P. (2005). Expression of the quorum-sensing regulatory protein LasR is strongly affected by iron and oxygen concentrations in cultures of Pseudomonas aeruginosa irrespective of cell density. *Microbiology (Reading, England)*, *151*(Pt 4), 1127–1138. https://doi.org/10.1099/mic.0.27566-0

Kim, S.-K., & Lee, J.-H. (2016). Biofilm dispersion in Pseudomonas aeruginosa. *Journal of Microbiology (Seoul, Korea)*, *54*(2), 71–85. https://doi.org/10.1007/s12275-016-5528-7

Knowles, T. P. J., & Buehler, M. J. (2011). Nanomechanics of functional and pathological amyloid materials. *Nature Nanotechnology*, *6*(8), 469–479. https://doi.org/10.1038/nnano.2011.102

Kobayashi, K., & Iwano, M. (2012). BslA(YuaB) forms a hydrophobic layer on the surface of Bacillus subtilis biofilms. *Molecular Microbiology*, *85*(1), 51–66. https://doi.org/10.1111/j.1365-2958.2012.08094.x

Kumar, S. T., Meinhardt, J., Fuchs, A.-K., Aumüller, T., Leppert, J., Büchele, B., … Fändrich, M. (2014). Structure and biomedical applications of amyloid oligomer nanoparticles. *ACS Nano*, *8*(11), 11042–11052. https://doi.org/10.1021/nn503960h

Lee, J.-H., Lequette, Y., & Greenberg, E. P. (2006). Activity of purified QscR, a Pseudomonas aeruginosa orphan quorum-sensing transcription factor. *Molecular Microbiology*, *59*(2), 602–609. https://doi.org/10.1111/j.1365-2958.2005.04960.x

Lee, V. T., Matewish, J. M., Kessler, J. L., Hyodo, M., Hayakawa, Y., & Lory, S. (2007). A cyclic-di-GMP receptor required for bacterial exopolysaccharide production. *Molecular Microbiology*, *65*(6), 1474–1484. https://doi.org/10.1111/j.1365-2958.2007.05879.x

Levkovich, S. A., Gazit, E., & Laor Bar-Yosef, D. (2020). Two Decades of Studying Functional Amyloids in Microorganisms. *Trends in Microbiology*. https://doi.org/10.1016/j.tim.2020.09.005

Lewis, R. J., Brannigan, J. A., Smith, I., & Wilkinson, A. J. (1996). Crystallisation of the Bacillus subtilis sporulation inhibitor SinR, complexed with its antagonist, SinI. *FEBS Letters*, *378*(1), 98–100. https://doi.org/10.1016/0014-5793(95)01432-2

Li, C., Born, A.-K., Schweizer, T., Zenobi-Wong, M., Cerruti, M., & Mezzenga, R. (2014). Amyloid-hydroxyapatite bone biomimetic composites. *Advanced Materials (Deerfield Beach, Fla.)*, *26*(20), 3207–3212. https://doi.org/10.1002/adma.201306198

Li, D., Jones, E. M., Sawaya, M. R., Furukawa, H., Luo, F., Ivanova, M., … Eisenberg, D. S. (2014). Structure-based design of functional amyloid materials. *Journal of the American Chemical Society*, *136*(52), 18044–18051. https://doi.org/10.1021/ja509648u

Li, H., Debowski, A. W., Liao, T., Tang, H., Nilsson, H.-O., Marshall, B. J., … Benghezal, M. (2017). Understanding protein glycosylation pathways in bacteria. *Future Microbiology*, *12*, 59–72. https://doi.org/10.2217/fmb-2016-0166

Linton, D., Dorrell, N., Hitchen, P. G., Amber, S., Karlyshev, A. V., Morris, H. R., … Wren, B. W. (2005). Functional analysis of the Campylobacter jejuni N-linked protein glycosylation pathway. *Molecular Microbiology*, *55*(6), 1695–1703. https://doi.org/10.1111/j.1365-2958.2005.04519.x

Lord, M. S., Modin, C., Foss, M., Duch, M., Simmons, A., Pedersen, F. S., … Besenbacher, F. (2006). Monitoring cell adhesion on tantalum and oxidised polystyrene using a quartz crystal microbalance with dissipation. *Biomaterials*, *27*(26), 4529–4537. https://doi.org/10.1016/j.biomaterials.2006.04.006

Lu, Q., Li, S., & Shao, F. (2015). Sweet Talk: Protein Glycosylation in Bacterial Interaction With the Host. *Trends in Microbiology*, *23*(10), 630–641. https://doi.org/10.1016/j.tim.2015.07.003

Ma, L., Conover, M., Lu, H., Parsek, M. R., Bayles, K., & Wozniak, D. J. (2009). Assembly and Development of the Pseudomonas aeruginosa Biofilm Matrix. *PLoS Pathogens*, *5*(3). https://doi.org/10.1371/journal.ppat.1000354

Mankar, S., Anoop, A., Sen, S., & Maji, S. K. (2011). Nanomaterials: Amyloids reflect their brighter side. *Nano Reviews*, *2*. https://doi.org/10.3402/nano.v2i0.6032

Mathé, C., Devineau, S., Aude, J.-C., Lagniel, G., Chédin, S., Legros, V., … Labarre, J. (2013). Structural determinants for protein adsorption/non-adsorption to silica surface. *PloS One*, *8*(11), e81346. https://doi.org/10.1371/journal.pone.0081346

Merighi, M., Lee, V. T., Hyodo, M., Hayakawa, Y., & Lory, S. (2007). The second messenger bis-(3'-5')-cyclic-GMP and its PilZ domain-containing receptor Alg44 are required for alginate biosynthesis in Pseudomonas aeruginosa. *Molecular Microbiology*, *65*(4), 876–895. https://doi.org/10.1111/j.1365-2958.2007.05817.x

Micsonai, A., Wien, F., Bulyáki, É., Kun, J., Moussong, É., Lee, Y.-H., … Kardos, J. (2018). BeStSel: A web server for accurate protein secondary structure prediction and fold recognition from the circular dichroism spectra. *Nucleic Acids Research*, *46*(W1), W315–W322. https://doi.org/10.1093/nar/gky497

Micsonai, A., Wien, F., Kernya, L., Lee, Y.-H., Goto, Y., Réfrégiers, M., & Kardos, J. (2015). Accurate secondary structure prediction and fold recognition for circular dichroism spectroscopy. *Proceedings of the National Academy of Sciences of the United States of America*, *112*(24), E3095-3103. https://doi.org/10.1073/pnas.1500851112

Mielich-Süss, B., & Lopez, D. (2015). Molecular mechanisms involved in Bacillus subtilis biofilm formation. *Environmental Microbiology*, *17*(3), 555–565. https://doi.org/10.1111/1462-2920.12527

Mortaz, E., Adcock, I. M., Tabarsi, P., Masjedi, M. R., Mansouri, D., Velayati, A. A., … Barnes, P. J. (2015). Interaction of Pattern Recognition Receptors with Mycobacterium Tuberculosis. *Journal of Clinical Immunology*, *35*(1), 1–10. https://doi.org/10.1007/s10875-014-0103-7

Nguyen, P. Q., Botyanszki, Z., Tay, P. K. R., & Joshi, N. S. (2014). Programmable biofilm-based materials from engineered curli nanofibres. *Nature Communications*, *5*, 4945. https://doi.org/10.1038/ncomms5945

Nilsson, K. P. R. (2009). Small organic probes as amyloid specific ligands—Past and recent molecular scaffolds. *FEBS Letters*, *583*(16), 2593–2599. https://doi.org/10.1016/j.febslet.2009.04.016

Nothaft, H., & Szymanski, C. M. (2010). Protein glycosylation in bacteria: Sweeter than ever. *Nature Reviews. Microbiology*, *8*(11), 765–778. https://doi.org/10.1038/nrmicro2383

Ogasawara, H., Yamamoto, K., & Ishihama, A. (2011). Role of the biofilm master regulator CsgD in cross-regulation between biofilm formation and flagellar synthesis. *Journal of Bacteriology*, *193*(10), 2587–2597. https://doi.org/10.1128/JB.01468-10

Olmez, Tolga T., Yuca, E., Eyupoglu, E., Catalak, H. B., Sahin, O., & Seker, U. O. S. (2018). Autonomous Synthesis of Fluorescent Silica Biodots Using Engineered Fusion Proteins. *ACS Omega*, *3*(1), 585–594. https://doi.org/10.1021/acsomega.7b01769

Olmez, Tolga Tarkan, Sahin Kehribar, E., Isilak, M. E., Lu, T. K., & Seker, U. O. S. (2019). Synthetic Genetic Circuits for Self-Actuated Cellular Nanomaterial Fabrication Devices. *ACS Synthetic Biology*, *8*(9), 2152–2162. https://doi.org/10.1021/acssynbio.9b00235

Olsén, A., Arnqvist, A., Hammar, M., Sukupolvi, S., & Normark, S. (1993). The RpoS sigma factor relieves H-NS-mediated transcriptional repression of csgA, the subunit gene of fibronectin-binding curli in Escherichia coli. *Molecular Microbiology*, *7*(4), 523–536. https://doi.org/10.1111/j.1365-2958.1993.tb01143.x

Olsén, A., Jonsson, A., & Normark, S. (1989). Fibronectin binding mediated by a novel class of surface organelles on Escherichia coli. *Nature*, *338*(6217), 652–655. https://doi.org/10.1038/338652a0

Onur, T., Yuca, E., Olmez, T. T., & Seker, U. O. S. (2018). Self-assembly of bacterial amyloid protein nanomaterials on solid surfaces. *Journal of Colloid and Interface Science*, *520*, 145–154. https://doi.org/10.1016/j.jcis.2018.03.016

Ostrowski, A., Mehert, A., Prescott, A., Kiley, T. B., & Stanley-Wall, N. R. (2011). YuaB functions synergistically with the exopolysaccharide and TasA amyloid fibers to allow biofilm formation by Bacillus subtilis. *Journal of Bacteriology*, *193*(18), 4821–4831. https://doi.org/10.1128/JB.00223-11

Ozboyaci, M., Kokh, D. B., & Wade, R. C. (2016). Three steps to gold: Mechanism of protein adsorption revealed by Brownian and molecular dynamics simulations. *Physical Chemistry Chemical Physics: PCCP*, *18*(15), 10191–10200. https://doi.org/10.1039/c6cp00201c

Pham, C. L. L., Kwan, A. H., & Sunde, M. (2014). Functional amyloid: Widespread in Nature, diverse in purpose. *Essays in Biochemistry*, *56*, 207–219. https://doi.org/10.1042/bse0560207

Pieters, B. J. G. E., van Eldijk, M. B., Nolte, R. J. M., & Mecinović, J. (2016). Natural supramolecular protein assemblies. *Chemical Society Reviews*, *45*(1), 24–39. https://doi.org/10.1039/c5cs00157a

Prigent-Combaret, C., Brombacher, E., Vidal, O., Ambert, A., Lejeune, P., Landini, P., & Dorel, C. (2001). Complex regulatory network controls initial adhesion and biofilm formation in Escherichia coli via regulation of the csgD gene. *Journal of Bacteriology*, *183*(24), 7213–7223. https://doi.org/10.1128/JB.183.24.7213-7223.2001

Rabe, M., Verdes, D., & Seeger, S. (2011). Understanding protein adsorption phenomena at solid surfaces. *Advances in Colloid and Interface Science*, *162*(1–2), 87–106. https://doi.org/10.1016/j.cis.2010.12.007

Rasamiravaka, T., Labtani, Q., Duez, P., & El Jaziri, M. (2015a). The formation of biofilms by Pseudomonas aeruginosa: A review of the natural and synthetic compounds interfering with control mechanisms. *BioMed Research International*, *2015*, 759348. https://doi.org/10.1155/2015/759348

Rasamiravaka, T., Labtani, Q., Duez, P., & El Jaziri, M. (2015b). The formation of biofilms by Pseudomonas aeruginosa: A review of the natural and synthetic compounds interfering with control mechanisms. *BioMed Research International*, *2015*, 759348. https://doi.org/10.1155/2015/759348

Reichhardt, C., Jacobson, A. N., Maher, M. C., Uang, J., McCrate, O. A., Eckart, M., & Cegelski, L. (2015). Congo Red Interactions with Curli-Producing E. coli and Native Curli Amyloid Fibers. *PloS One*, *10*(10), e0140388. https://doi.org/10.1371/journal.pone.0140388

Romero, D., Aguilar, C., Losick, R., & Kolter, R. (2010). Amyloid fibers provide structural integrity to Bacillus subtilis biofilms. *Proceedings of the National Academy of Sciences*, *107*(5), 2230–2234. https://doi.org/10.1073/pnas.0910560107

Romero, D., Vlamakis, H., Losick, R., & Kolter, R. (2011). An accessory protein required for anchoring and assembly of amyloid fibres in B. *Molecular Microbiology*, *80*, 1155–1168. https://doi.org/10.1111/j.1365-2958.2011.07653.x

Romero, D., Vlamakis, H., Losick, R., & Kolter, R. (2014). Functional analysis of the accessory protein TapA in Bacillus subtilis amyloid fiber assembly. *Journal of Bacteriology*, *196*(8), 1505–1513. https://doi.org/10.1128/JB.01363-13

Sauer, K., Cullen, M. C., Rickard, A. H., Zeef, L. A. H., Davies, D. G., & Gilbert, P. (2004). Characterization of Nutrient-Induced Dispersion in Pseudomonas aeruginosa PAO1 Biofilm. *Journal of Bacteriology*, *186*(21), 7312–7326. https://doi.org/10.1128/JB.186.21.7312-7326.2004

Schmidt, M. A., Riley, L. W., & Benz, I. (2003). Sweet new world: Glycoproteins in bacterial pathogens. *Trends in Microbiology*, *11*(12), 554–561. https://doi.org/10.1016/j.tim.2003.10.004

Seker, U. O. S., Chen, A. Y., Citorik, R. J., & Lu, T. K. (2017). Synthetic Biogenesis of Bacterial Amyloid Nanomaterials with Tunable Inorganic-Organic Interfaces and Electrical Conductivity. *ACS Synthetic Biology*, *6*(2), 266–275. https://doi.org/10.1021/acssynbio.6b00166

Shewmaker, F., McGlinchey, R. P., Thurber, K. R., McPhie, P., Dyda, F., Tycko, R., & Wickner, R. B. (2009). The functional curli amyloid is not based on in-register parallel beta-sheet structure. *The Journal of Biological Chemistry*, *284*(37), 25065–25076. https://doi.org/10.1074/jbc.M109.007054

Singer, A., Eiteman, M. A., & Altman, E. (2009). DNA plasmid production in different host strains of Escherichia coli. *Journal of Industrial Microbiology & Biotechnology*, *36*(4), 521–530. https://doi.org/10.1007/s10295-008-0522-7

Sjöbring, U., Pohl, G., & Olsén, A. (1994). Plasminogen, absorbed by Escherichia coli expressing curli or by Salmonella enteritidis expressing thin aggregative fimbriae, can be activated by simultaneously captured tissue-type plasminogen activator (t-PA). *Molecular Microbiology*, *14*(3), 443–452. https://doi.org/10.1111/j.1365-2958.1994.tb02179.x

Studier, F. W. (2014). Stable expression clones and auto-induction for protein production in E. coli. *Methods in Molecular Biology (Clifton, N.J.)*, *1091*, 17–32. https://doi.org/10.1007/978-1-62703-691-7_2

Szymanski, C. M., Yao, R., Ewing, C. P., Trust, T. J., & Guerry, P. (1999). Evidence for a system of general protein glycosylation in Campylobacter jejuni. *Molecular Microbiology*, *32*(5), 1022–1030. https://doi.org/10.1046/j.1365-2958.1999.01415.x

Taglialegna, A., Lasa, I., & Valle, J. (2016). Amyloid Structures as Biofilm Matrix Scaffolds. *Journal of Bacteriology*, *198*(19), 2579–2588. https://doi.org/10.1128/JB.00122-16

Takahashi, S., Leiss, M., Moser, M., Ohashi, T., Kitao, T., Heckmann, D., … Fässler, R. (2007). The RGD motif in fibronectin is essential for development but dispensable for fibril assembly. *The Journal of Cell Biology*, *178*(1), 167–178. https://doi.org/10.1083/jcb.200703021

Tan, F. Y. Y., Tang, C. M., & Exley, R. M. (2015). Sugar coating: Bacterial protein glycosylation and host-microbe interactions. *Trends in Biochemical Sciences*, *40*(7), 342–350. https://doi.org/10.1016/j.tibs.2015.03.016

Terra, R., Stanley-Wall, N. R., Cao, G., & Lazazzera, B. A. (2012). Identification of Bacillus subtilis SipW as a bifunctional signal peptidase that controls surface-adhered biofilm formation. *Journal of Bacteriology*, *194*(11), 2781–2790. https://doi.org/10.1128/JB.06780-11

Usov, I., & Mezzenga, R. (2015). FiberApp: An Open-Source Software for Tracking and Analyzing Polymers, Filaments, Biomacromolecules, and Fibrous Objects. *Macromolecules*, *48*(5), 1269–1280. https://doi.org/10.1021/ma502264c

Valentin, J. D. P., Qin, X.-H., Fessele, C., Straub, H., van der Mei, H. C., Buhmann, M. T., … Ren, Q. (2019). Substrate viscosity plays an important role in bacterial adhesion under fluid flow. *Journal of Colloid and Interface Science*, *552*, 247–257. https://doi.org/10.1016/j.jcis.2019.05.043

Van Gerven, N., Klein, R. D., Hultgren, S. J., & Remaut, H. (2015). Bacterial amyloid formation: Structural insights into curli biogensis. *Trends in Microbiology*, *23*(11), 693–706. https://doi.org/10.1016/j.tim.2015.07.010

Vivero-Escoto, J. L., Huxford-Phillips, R. C., & Lin, W. (2012). Silica-based nanoprobes for biomedical imaging and theranostic applications. *Chemical Society Reviews*, *41*(7), 2673–2685. https://doi.org/10.1039/c2cs15229k

Vogler, E. A. (2012). Protein adsorption in three dimensions. *Biomaterials*, *33*(5), 1201–1237. https://doi.org/10.1016/j.biomaterials.2011.10.059

Wacker, M., Linton, D., Hitchen, P. G., Nita-Lazar, M., Haslam, S. M., North, S. J., … Aebi, M. (2002). N-linked glycosylation in Campylobacter jejuni and its functional transfer into E. coli. *Science (New York, N.Y.)*, *298*(5599), 1790–1793. https://doi.org/10.1126/science.298.5599.1790

Walters, M. C., Roe, F., Bugnicourt, A., Franklin, M. J., & Stewart, P. S. (2003). Contributions of antibiotic penetration, oxygen limitation, and low metabolic activity to tolerance of Pseudomonas aeruginosa biofilms to ciprofloxacin and tobramycin. *Antimicrobial Agents and Chemotherapy*, *47*(1), 317–323. https://doi.org/10.1128/aac.47.1.317-323.2003

Wang, Q., Wang, M., Lu, X., Wang, K., Fang, L., Ren, F., & Lu, G. (2017). Effects of atomic-level nano-structured hydroxyapatite on adsorption of bone morphogenetic protein-7 and its derived peptide by computer simulation. *Scientific Reports*, *7*(1), 15152. https://doi.org/10.1038/s41598-017-15219-6

Wang, Xinyu, Li, Y., & Zhong, C. (2015). Amyloid-directed assembly of nanostructures and functional devices for bionanoelectronics. *Journal of Materials Chemistry. B*, *3*(25), 4953–4958. https://doi.org/10.1039/c5tb00374a

Wang, Xuan, & Chapman, M. R. (2008). Sequence determinants of bacterial amyloid formation. *Journal of Molecular Biology*, *380*(3), 570–580. https://doi.org/10.1016/j.jmb.2008.05.019

Whitchurch, C. B., Tolker-Nielsen, T., Ragas, P. C., & Mattick, J. S. (2002). Extracellular DNA required for bacterial biofilm formation. *Science (New York, N.Y.)*, *295*(5559), 1487. https://doi.org/10.1126/science.295.5559.1487

Xue, W.-F., Homans, S. W., & Radford, S. E. (2008). Systematic analysis of nucleation-dependent polymerization reveals new insights into the mechanism of amyloid self-assembly. *Proceedings of the National Academy of Sciences of the United States of America*, *105*(26), 8926–8931. https://doi.org/10.1073/pnas.0711664105

Yan, Z., Yin, M., Chen, J., & Li, X. (2020). Assembly and substrate recognition of curli biogenesis system. *Nature Communications*, *11*. https://doi.org/10.1038/s41467-019-14145-7

Yang, X., Li, Z., Xiao, H., Wang, N., Li, Y., Xu, X., … Li, J. (2018). A Universal and Ultrastable Mineralization Coating Bioinspired from Biofilms. *Advanced Functional Materials*, *28*(32), 1802730. https://doi.org/10.1002/adfm.201802730

Yoon, S. S., Hennigan, R. F., Hilliard, G. M., Ochsner, U. A., Parvatiyar, K., Kamani, M. C., … Hassett, D. J. (2002). Pseudomonas aeruginosa anaerobic respiration in biofilms: Relationships to cystic fibrosis pathogenesis. *Developmental Cell*, *3*(4), 593–603. https://doi.org/10.1016/s1534-5807(02)00295-2

Yuca, E., Şahin Kehribar, E., & Şeker, U. Ö. Ş. (2020). Interaction of microbial functional amyloids with solid surfaces. *Colloids and Surfaces. B, Biointerfaces*, *199*, 111547. https://doi.org/10.1016/j.colsurfb.2020.111547

Zhang, Y., Wang, A., DeBenedictis, E. P., & Keten, S. (2017). Bending energy penalty enhances the adhesive strength of functional amyloid curli to surfaces. *Nanotechnology*, *28*(46), 464002. https://doi.org/10.1088/1361-6528/aa8f72

Zhong, C., Gurry, T., Cheng, A. A., Downey, J., Deng, Z., Stultz, C. M., & Lu, T. K. (2014). Strong underwater adhesives made by self-assembling multi-protein nanofibres. *Nature Nanotechnology*, *9*(10), 858–866. https://doi.org/10.1038/nnano.2014.199

Zhou, H., Wu, T., Dong, X., Wang, Q., & Shen, J. (2007). Adsorption mechanism of BMP-7 on hydroxyapatite (001) surfaces. *Biochemical and Biophysical Research Communications*, *361*(1), 91–96. https://doi.org/10.1016/j.bbrc.2007.06.169

7 APPENDIX A

DNA SEQUENCES OF GENES AND GENE FRAGMENTS

Table A.1. Nucleotide sequences of *csgA* and *csgB* genes.

E. coliK12 csgA gene nucleotide sequence with signal sequence and with 6X His-Tag and GS Linkers	ATGTCTGAGCTGAACATTTACCAGTACGGTGGCGGTA ACTCTGCACTTGCTCTGCAAACTGATGCCCGTAACTC TGACTTGACTATTACCCAGCATGGCGGCGGTAATGGT GCAGATGTTGGTCAGGGCTCAGATGACAGCTCAATC GATCTGACCCAACGTGGCTTCGGTAACAGCGCTACTC TTGATCAGTGGAACGGCAAAAATTCTGAAATGACGG TTAAACAGTTCGGTGGTGGCAACGGTGCTGCAGTTGA CCAGACTGCATCTAACTCCTCCGTCAACGTGACTCAG GTTGGCTTTGGTAACAACGCGACCGCTCATCAGTACG GTACCGGCGGTAGCGGTGGCGGTAGCGGAGGCGGTA GCGGCGAAAACCTGTATTTTCAGGGCGGCGGTAGCG GTGGCGGTAGCGGAGGCGGTAGCGGCGGATCCCACC ACCACCACCACCAC

Table A.1 (cont'd)

E. coli K12 csgB gene nucleotide sequence without signal sequence and with 6X His-Tag and GS Linkers	ATGAAAAACAAATTGTTATTTATGATGTTAACAATAC TGGGTGCGCCTGGGATTGCAGCCGCAGCAGGTTATG ATTTAGCTAATTCAGAATATAACTTCGCGGTAAATGA ATTGAGTAAGTCTTCATTTAATCAGGCAGCCATAATT GGTCAAGCTGGGACTAATAATAGTGCTCAGTTACGG CAGGGAGGCTCAAAACTTTTGGCGGTTGTTGCGCAA GAAGGTAGTAGCAACCGGGCAAAGATTGACCAGACA GGAGATTATAACCTTGCATATATTGATCAGGCGGGC AGTGCCAACGATGCCAGTATTTCGCAAGGTGCTTATG GTAATACTGCGATGATTATCCAGAAAGGTTCTGGTA ATAAAGCAAATATTACACAGTATGGTACTCAAAAAA CGGCAATTGTAGTGCAGAGACAGTCGCAAATGGCTA TTCGCGTGACACAACGTGGTACCGGCGGTAGCGGTG GCGGTAGCGGAGGCGGTAGCGGCGAAAACCTGTATT TTCAGGGCGGCGGTAGCGGTGGCGGTAGCGGAGGCG GTAGCGGCGGATCCCACCACCACCACCACCAC

Table A.2. Nucleotide sequences of *tasA* and *tasA-DQNAT* genes

B. subtilis tasA gene nucleotide sequence without signal sequence and with 6X His-Tag and GS Linker	ATGGCATTTAACGACATTAAATCAAAGGATGC TACTTTTGCATCAGGTACGCTTGATTTATCTGC TAAAGAGAATTCAGCGAGTGTGAACTTATCAA ATCTAAAGCCGGGAGATAAGTTGACAAAGGAT TTCCAATTTGAAAATAACGGATCACTTGCGAT CAAAGAAGTTCTAATGGCGCTTAATTATGGAG ATTTTAAAGCAAACGGCGGCAGCAATACATCT CCAGAAGATTTCCTCAGCCAGTTTGAAGTGAC ATTGTTGACAGTTGGAAAAGAGGGCGGCAATG GCTACCCGAAAAACATTATTTTAGATGATGCG AACCTTAAAGACTTGTATTTGATGTCTGCTAAA AATGATGCAGCGGCTGCTGAAAAAATCAAAAA ACAAATTGACCCTAAATTCTTAAATGCAAGCG GTAAAGTCAATGTAGCAACAATTGATGGTAAA ACCGCTCCTGAATATGATGGTGTTCCAAAAAC ACCAACTGACTTCGATCAGGTTCAAATGGAAA TCCAATTCAAGGATGATAAAACAAAAGATGAA AAAGGGCTTATGGTTCAAAATAAATATCAAGG CAACTCCATTAAGCTTCAATTCTCATTCGAAGC TACACAGTGGAACGGCTTGACAATCAAAAAGG ACCATACTGATAAAGATGGTTACGTGAAAGAA AATGAAAAAGCGCATAGCGAGGATAAAAATG GCGGTAGCGGTCTCGAGCACCACCACCACCAC CAC

Table A.2 (cont'd)

B. subtilis tasA gene nucleotide sequence without signal sequence and with 6X His-Tag, DQNAT tag and GS Linker	ATGGCATTTAACGACATTAAATCAAAGGATGC TACTTTTGCATCAGGTACGCTTGATTTATCTGC TAAAGAGAATTCAGCGAGTGTGAACTTATCAA ATCTAAAGCCGGGAGATAAGTTGACAAAGGAT TTCCAATTTGAAAATAACGGATCACTTGCGAT CAAAGAAGTTCTAATGGCGCTTAATTATGGAG ATTTTAAAGCAAACGGCGGCAGCAATACATCT CCAGAAGATTTCCTCAGCCAGTTTGAAGTGAC ATTGTTGACAGTTGGAAAAGAGGGCGGCAATG GCTACCCGAAAAACATTATTTTAGATGATGCG AACCTTAAAGACTTGTATTTGATGTCTGCTAAA AATGATGCAGCGGCTGCTGAAAAAATCAAAAA ACAAATTGACCCTAAATTCTTAAATGCAAGCG GTAAAGTCAATGTAGCAACAATTGATGGTAAA ACCGCTCCTGAATATGATGGTGTTCCAAAAAC ACCAACTGACTTCGATCAGGTTCAAATGGAAA TCCAATTCAAGGATGATAAAACAAAAGATGAA AAAGGGCTTATGGTTCAAAATAAATATCAAGG CAACTCCATTAAGCTTCAATTCTCATTCGAAGC TACACAGTGGAACGGCTTGACAATCAAAAAGG ACCATACTGATAAAGATGGTTACGTGAAAGAA AATGAAAAAGCGCATAGCGAGGATAAAAATG GCGGTAGCGGTCTCGAGCACCACCACCACCAC CACCCTAGGGGCGGTAGCGGTGATCAGAACGC GACCACTAGT

Table A.3. Nucleotide sequences of *csgA-RGD* and *csgB-RGD* genes

E. coli K12 csgA gene nucleotide sequence without signal sequence and with 6X His-Tag, GS Linker and RGD peptide tag	ATGTCTGAGCTGAACATTTACCAGTACGGTG GCGGTAACTCTGCACTTGCTCTGCAAACTGA TGCCCGTAACTCTGACTTGACTATTACCCAG CATGGCGGCGGTAATGGTGCAGATGTTGGTC AGGGCTCAGATGACAGCTCAATCGATCTGAC CCAACGTGGCTTCGGTAACAGCGCTACTCTT GATCAGTGGAACGGCAAAAATTCTGAAATG ACGGTTAAACAGTTCGGTGGTGGCAACGGTG CTGCAGTTGACCAGACTGCATCTAACTCCTC CGTCAACGTGACTCAGGTTGGCTTTGGTAAC AACGCGACCGCTCATCAGTACGGCGGTAGCG GTCTCGAGCACCACCACCACCACCACGGCGG TAGCGGTGGGCGCGGTGACAGCCCC

Table A.3 (cont'd)

E. coli K12 csgB gene nucleotide sequence without signal sequence and with 6X His-Tag, GS Linker and RGD peptide tag	ATGCAGGCAGCCATAATTGGTCAAGCTGGGA CTAATAATAGTGCTCAGTTACGGCAGGGAGG CTCAAAACTTTTGGCGGTTGTTGCGCAAGAA GGTAGTAGCAACCGGGCAAAGATTGACCAG ACAGGAGATTATAACCTTGCATATATTGATC AGGCGGGCAGTGCCAACGATGCCAGTATTTC GCAAGGTGCTTATGGTAATACTGCGATGATT ATCCAGAAAGGTTCTGGTAATAAAGCAAATA TTACACAGTATGGTACTCAAGGCGGTAGCGG TCTCGAGCACCACCACCACCACCACGGCGGT AGCGGTGGGCGCGGTGACAGCCCC

Table A.4. Nucleotide sequences of *tasA, tapA, csgA* and *csgB* genes with N42 signal sequence.

E. coli EcN csgA gene nucleotide sequence with native N42 signal sequence	ATGAAACTTTTAAAAGTAGCAGCAATTGCAG CAATCGTATTCTCCGGTAGCGCTCTGGCAGG TGTTGTTCCTCAGTACGGCGGCGGCGGTGGC AACCACGGTGGTGGCGGTAATAACAGCGGT CCGAATTCAGAGCTGAATATTTACCAGTACG GTGGCGGTAACTCTGCTCTTGCTCTGCAAGC TGACGCCCGTAACTCTGATCTGACCATTACC CAGCACGGCGGCGGTAATGGCGCAGATGTG GGCCAAGGTTCTGATGACAGCTCAATCGATC TGACTCAGCGTGGTTTCGGCAACAGCGCTAC TCTTGATCAGTGGAATGGTAAAGATTCTACT ATGACTGTTAAACAGTTCGGTGGCGGTAACG GTGCTGCTGTTGACCAGACTGCATCTAACTC CAGCGTTAACGTCACTCAGGTTGGCTTTGGT AACAACGCGACCGCTCATCAGTACTAA

Table A.4 (cont'd)

E. coli EcN csgB gene nucleotide sequence with native signal sequence	ATGAAAAACAAATTGTTATTTATGATGTTAA CAATACTGGGTGCGCCTGGGATTGCAGCCGC AGCAGGTTATGATTTAGCTAATTCAGAATAT AACTTTGCGGTAAATGAATTGAGTAAGTCTT CATTTAATCAGGCAGCCATAATTGGTCAAGC TGGGACTAATAATAGTGCTCAGTTACGGCAG GGAGGCTCAAAACTTTTGACGGTTGTTGCGC AAGAAGGTAGTAGCAACTGGGCAAAGATTG ATCAGACAGGAGATTATAACCTTGCATATAT TGATCAGGCGGGCAGTGCCAACGATGCCAGT ATTTCGCAAGGTGCTTATGGTAATACTGCGA TGATTATCCAGAAAGGTTCTGGTAATAAAGC AAATATTACACAGTATGGTACTCAAAAAACG GCAATTGTAGTGCAGAGACAGTCGCAAATG GCTATTCGCGTGACACAACGT

Table A.4 (cont'd)

B. subtilis tasA gene nucleotide sequence without native signal sequence and with N42 signal sequence	ATGAAACTTTTAAAAGTAGCAGCAATTGCAGCAAT CGTATTCTCCGGTAGCGCTCTGGCAGGTGTTGTTCC TCAGTACGGCGGCGGCGGTAACCACGGTGGTGGCG GTAATAATAGCGGCCCAAATGCATTTAACGACATT AAATCAAAGGATGCTACTTTTGCATCAGGTACGCT TGATTTATCTGCTAAAGAGAATTCAGCGAGTGTGA ACTTATCAAATCTAAAGCCGGGAGATAAGTTGACA AAGGATTTCCAATTTGAAAATAACGGATCACTTGC GATCAAAGAAGTTCTAATGGCGCTTAATTATGGAG ATTTTAAAGCAAACGGCGGCAGCAATACATCTCCA GAAGATTTCCTCAGCCAGTTTGAAGTGACATTGTTG ACAGTTGGAAAAGAGGGCGGCAATGGCTACCCGA AAAACATTATTTTAGATGATGCGAACCTTAAAGAC TTGTATTTGATGTCTGCTAAAAATGATGCAGCGGCT GCTGAAAAAATCAAAAAACAAATTGACCCTAAATT CTTAAATGCAAGCGGTAAAGTCAATGTAGCAACAA TTGATGGTAAAACCGCTCCTGAATATGATGGTGTTC CAAAAACACCAACTGACTTCGATCAGGTTCAAATG GAAATCCAATTCAAGGATGATAAAACAAAAGATG AAAAAGGGCTTATGGTTCAAAATAAATATCAAGGC AACTCCATTAAGCTTCAATTCTCATTCGAAGCTACA CAGTGGAACGGCTTGACAATCAAAAAGGACCATAC TGATAAAGATGGTTACGTGAAAGAAAATGAAAAA GCGCATAGCGAGGATAAAAAT

Table A.4 (cont'd)

B. subtilis tapA gene nucleotide sequence without native signal sequence and with N42 signal sequence	ATGAAACTTTTAAAAGTAGCAGCAATTGCAGCAATCG TATTCTCCGGTAGCGCTCTGGCAGGTGTTGTTCCTCAG TACGGCGGCGGCGGTAACCACGGTGGTGGCGGTAAT AATAGCGGCCCAAATATATGCTTACAATTTTCCGATG ATACAAGCGCTGCTTTTCATGATATTGAAACATTTGA TGTCTCACTTCAAACGTGTAAAGACTTTCAGCATACA GATAAAAACTGCCATTATGATAAACGCTGGGATCAAA GTGATTTGCACATATCAGATCAAACGGATACGAAAGG CACTGTATGCTCACCTTTCGCCTTATTTGCTGTGCTCG AAAATACAGGTGAGAAACTTAAGAAATCAAAGTGGA AGTGGGAGCTTCATAAGCTTGAAAATGCCCGCAAACC GTTAAAGGATGGGAACGTGATCGAAAAAGGATTTGT CTCCAATCAAATCGGCGATTCACTTTATAAAATTGAG ACCAAGAAAAAAATGAAACCCGGCATTTATGCATTTA AAGTATATAAACCGGCAGGCTACCCGGCAAACGGCA GTACATTTGAGTGGTCGGAGCCTATGAGGCTTGCAAA ATGCGATGAAAAACCGACAGTCCCTAAAAAAGAAAC AAAGTCGGACGTCAAAAAGGAGAATGAAACAACACA AAAAGATATACCGGAAAAAACAATGAAAGAAGAAAC ATCTCAAGAAGCTGTAACCAAAGAAAAAGAAACTCA ATCAGACCAGAAGGAAAGCGGGGAAGAGGATGAAA AAAGCAATGAAGCTGATCAG

Table A.5. Nucleotide sequences of *tasA, tapA, csgA*, *csgB, fapC* and *fapB* genes with N42 signal sequence and N-terminal 6X His tag.

E. coli EcN csgA gene nucleotide sequence with native N42 signal sequence, GS linker and 6X His tag	ATGAAACTTTTAAAAGTAGCAGCAATTGCAG CAATCGTATTCTCCGGTAGCGCTCTGGCAGG TGTTGTTCCTCAGTACGGCGGCGGCGGTGGC AACCACGGTGGTGGCGGTAATAACAGCGGT CCGAATTCAGAGCTGAATATTTACCAGTACG GTGGCGGTAACTCTGCTCTTGCTCTGCAAGC TGACGCCCGTAACTCTGATCTGACCATTACC CAGCACGGCGGCGGTAATGGCGCAGATGTG GGCCAAGGTTCTGATGACAGCTCAATCGATC TGACTCAGCGTGGTTTCGGCAACAGCGCTAC TCTTGATCAGTGGAATGGTAAAGATTCTACT ATGACTGTTAAACAGTTCGGTGGCGGTAACG GTGCTGCTGTTGACCAGACTGCATCTAACTC CAGCGTTAACGTCACTCAGGTTGGCTTTGGT AACAACGCGACCGCTCATCAGTACGGCGGTA GCGGTCACCACCACCACCACCAC

Table A.5 (cont'd)

E. coli EcN csgB gene nucleotide sequence with native N42 signal sequence, GS linker and 6X His tag	ATGAAAAACAAATTGTTATTTATGATGTTAA CAATACTGGGTGCGCCTGGGATTGCAGCCGC AGCAGGTTATGATTTAGCTAATTCAGAATAT AACTTTGCGGTAAATGAATTGAGTAAGTCTT CATTTAATCAGGCAGCCATAATTGGTCAAGC TGGGACTAATAATAGTGCTCAGTTACGGCAG GGAGGCTCAAAACTTTTGACGGTTGTTGCGC AAGAAGGTAGTAGCAACTGGGCAAAGATTG ATCAGACAGGAGATTATAACCTTGCATATAT TGATCAGGCGGGCAGTGCCAACGATGCCAGT ATTTCGCAAGGTGCTTATGGTAATACTGCGA TGATTATCCAGAAAGGTTCTGGTAATAAAGC AAATATTACACAGTATGGTACTCAAAAAACG GCAATTGTAGTGCAGAGACAGTCGCAAATG GCTATTCGCGTGACACAACGTGGCGGTAGCG GTCACCACCACCACCACCAC

Table A.5 (cont'd)

B. subtilis tasA gene nucleotide sequence with N42 signal sequence, GS linker and 6X His tag	ATGAAACTTTTAAAAGTAGCAGCAATTGCAGCAATCGT ATTCTCCGGTAGCGCTCTGGCAGGTGTTGTTCCTCAGT ACGGCGGCGGCGGTAACCACGGTGGTGGCGGTAATAA TAGCGGCCCAAATGCATTTAACGACATTAAATCAAAGG ATGCTACTTTTGCATCAGGTACGCTTGATTTATCTGCTA AAGAGAATTCAGCGAGTGTGAACTTATCAAATCTAAA GCCGGGAGATAAGTTGACAAAGGATTTCCAATTTGAA AATAACGGATCACTTGCGATCAAAGAAGTTCTAATGGC GCTTAATTATGGAGATTTTAAAGCAAACGGCGGCAGCA ATACATCTCCAGAAGATTTCCTCAGCCAGTTTGAAGTG ACATTGTTGACAGTTGGAAAAGAGGGCGGCAATGGCT ACCCGAAAAACATTATTTTAGATGATGCGAACCTTAAA GACTTGTATTTGATGTCTGCTAAAAATGATGCAGCGGC TGCTGAAAAAATCAAAAAACAAATTGACCCTAAATTCT TAAATGCAAGCGGTAAAGTCAATGTAGCAACAATTGA TGGTAAAACCGCTCCTGAATATGATGGTGTTCCAAAAA CACCAACTGACTTCGATCAGGTTCAAATGGAAATCCAA TTCAAGGATGATAAAACAAAAGATGAAAAAGGGCTTA TGGTTCAAAATAAATATCAAGGCAACTCCATTAAGCTT CAATTCTCATTCGAAGCTACACAGTGGAACGGCTTGAC AATCAAAAAGGACCATACTGATAAAGATGGTTACGTG AAAGAAAATGAAAAAGCGCATAGCGAGGATAAAAATG GCGGTAGCGGTCACCACCACCACCACCAC

Table A.5 (cont'd)

B. subtilis tapA gene nucleotide sequence with N42 signal sequence, GS linker and 6X His tag	ATGAAACTTTTAAAAGTAGCAGCAATTGCAGCAATC GTATTCTCCGGTAGCGCTCTGGCAGGTGTTGTTCCTC AGTACGGCGGCGGCGGTAACCACGGTGGTGGCGGT AATAATAGCGGCCCAAATATATGCTTACAATTTTCC GATGATACAAGCGCTGCTTTTCATGATATTGAAACA TTTGATGTCTCACTTCAAACGTGTAAAGACTTTCAGC ATACAGATAAAAACTGCCATTATGATAAACGCTGGG ATCAAAGTGATTTGCACATATCAGATCAAACGGATA CGAAAGGCACTGTATGCTCACCTTTCGCCTTATTTGC TGTGCTCGAAAATACAGGTGAGAAACTTAAGAAATC AAAGTGGAAGTGGGAGCTTCATAAGCTTGAAAATGC CCGCAAACCGTTAAAGGATGGGAACGTGATCGAAA AAGGATTTGTCTCCAATCAAATCGGCGATTCACTTT ATAAAATTGAGACCAAGAAAAAAATGAAACCCGGC ATTTATGCATTTAAAGTATATAAACCGGCAGGCTAC CCGGCAAACGGCAGTACATTTGAGTGGTCGGAGCCT ATGAGGCTTGCAAAATGCGATGAAAAACCGACAGT CCCTAAAAAAGAAACAAAGTCGGACGTCAAAAAGG AGAATGAAACAACACAAAAAGATATACCGGAAAAA ACAATGAAAGAAGAAACATCTCAAGAAGCTGTAAC CAAAGAAAAAGAAACTCAATCAGACCAGAAGGAAA GCGGGGAAGAGGATGAAAAAAGCAATGAAGCTGAT CAGGGCGGTAGCGGTCACCACCACCACCACCAC

Table A.5 (cont'd)

P. aeruginosa	ATGAAACTTTTAAAAGTAGCAGCAATTGCAGCAATCGT
fapC gene	ATTCTCCGGTAGCGCTCTGGCAGGTGTTGTTCCTCAGT
nucleotide	ACGGCGGCGGCGGTAACCACGGTGGTGGCGGTAATAA
sequence with	TAGCGGCCCAAATGGTAATGAGGGCGGCTGGCATCCG
N42 signal	CCGAAACCGAATCCTCAGAGTAACAACAAGGGCGGTG
sequence, GS	CCACCGCACTGGTGGTTGATACCCAGCAGAATTACAAT
linker and 6X His	AACAAGGTTAGCAACTTCGGCACTCTGAACAATGCCAG
tag	CGTTAGCGGCAGCATCAAAGATGCCAGCGGTAACGTG
	GGTGTTAATGTGGCCGCAGGCGACAATAACCAGCAGG
	CAAATGCCGCAGCCCTGGCAAGCGCAGATGCAAGCTT
	CGTGTTTGGCACCGCAACCGCAAGCACCAGCGTGCTGC
	AGAGCGGCTATGGCAACACCCTGAATAACTATAGCAA
	CCCGAACACCGCCAGTCTGAGCAACAGCGCCAACAAT
	GTGAGCGGTAACCTGGGTGTGAACGTGGCCGCCGGCA
	ACTTCAATCAGCAGAAAAACGACCTGGCAGCCGCCGT
	GAGCAATGGCCAGTATAGCACCGCAGGTAGCGCCGCC
	AGCCAGACAAGCACCGGCAACACCACCGTGAATAGCG
	CCAATTATGCCTATGGCGGCACCTATGTGAGCCTGAAG
	CTGAATGCCGACGGCAGCTATAAAGGCACCAGCGACC
	AAATCGGTGATGTGTACCTGGATACCTGGGAAGGTCAG
	ACCCATCCGGGTGGCAGCAATACCGGCCATATCGATGT
	GGATAGCCAGGCCCAGGGCGCAAAAGACCTGAACCAT
	GACGGCGGTGCCTTTGCCTTCAAAGAAAAAGGCGACG
	TGGACCTGAAAGGCACCGTTAGCGGCTTTATTCCGGCC

Table A.5 (cont'd)

	ATTGTGGGCTTTAAGACCCCGGTGACCAACAACGCAAGC CTGAGCAATAGTCTGCAGAACGTGAGCGGCAATGTTGGC GTTAATATCGCCGCAGGCGGTGGTAACCAGCAGAGCAAT AGCCTGAGCATTGCAGCAGGTTGCAGTAGCTGTCCGGCC GGTGGCGAAAGCCTGGGTTTTGGCGGTAGCGGTCACCAC CACCACCACCAC
P. aeruginosa *fapB* gene nucleotide sequence with N42 signal sequence, GS linker and 6X His tag	ATGAAACTTTTAAAAGTAGCAGCAATTGCAGCAATCGTA TTCTCCGGTAGCGCTCTGGCAGGTGTTGTTCCTCAGTACG GCGGCGGCGGTAACCACGGTGGTGGCGGTAATAATAGCG GCCCAAATGACCCGCTGGCCAGCCGTAATCGCGCAAGCA TCGATGATAGCGGCACCTATCGCGGTAATTTCGCCCTGAA TCAGGCCGCAGGTGATGCCCAGCAACAGAGCAATGTGCG CGTTGTGGCCGTTGGTAGCGCCGCACTGGTGGGTAGTGAT CAGCGCCAGCATCTGCAGCTGGATGCCAGCCAGCCGATT GCCGCAAGCGCCAGTATTAGCGGTGCCGCCCTGCGTGGT AGCGGTATTCTGGGTGTGAATCAGGGCGCCGGTCTGGGC AACCAGCAGATCAATGCCTTTCGCCTGAGCCTGAGCAAT GGTCCGGAAAGTCTGGACGATAGCGTTCTGGCCCAGAGT GTGGCACTGACCAAAGTGAGCGGTAGTGCAACCCCGGTT CCTGGTGGCCGTAGCGTGAGCACCGATGATCGTGCATTTG CCGGCAGCAGCGGTGTTGTGCAGGTGAATCAGAGCGCCG GTGTGGGTAACCAGAGCATGAATACCCTGAGCGTGCGCG TGATGGAAGGCGGTAGCGGTCACCACCACCACCACCAC

Table A.6. Nucleotide sequences of *csgA* genes with N42 signal sequence, RGD peptide tag and N-terminal 6X His tag.

E. coli K12 csgA gene nucleotide sequence with native N42 signal sequence, GS linker and 6X His tag	ATGAAACTTTTAAAAGTAGCAGCAATTGCAGC AATCGTATTCTCCGGTAGCGCTCTGGCAGGTGT TGTTCCTCAGTACGGCGGCGGCGGTAACCACG GTGGTGGCGGTAATAATAGCGGCCCAAATTCT GAGCTGAACATTTACCAGTACGGTGGCGGTAA CTCTGCACTTGCTCTGCAAACTGATGCCCGTAA CTCTGACTTGACTATTACCCAGCATGGCGGCG GTAATGGTGCAGATGTTGGTCAGGGCTCAGAT GACAGCTCAATCGATCTGACCCAACGTGGCTT CGGTAACAGCGCTACTCTTGATCAGTGGAACG GCAAAAATTCTGAAATGACGGTTAAACAGTTC GGTGGTGGCAACGGTGCTGCAGTTGACCAGAC TGCATCTAACTCCTCCGTCAACGTGACTCAGGT TGGCTTTGGTAACAACGCGACCGCTCATCAGT ACGGATCCCACCACCACCACCACCACCTAGG GGCGGTAGCGGT

Table A.6 (cont'd)

E. coli K12 csgA gene nucleotide sequence with native N42 signal sequence, GS linker, RDG peptide tag and 6X His tag	ATGAAACTTTTAAAAGTAGCAGCAATTGCAGC AATCGTATTCTCCGGTAGCGCTCTGGCAGGTGT TGTTCCTCAGTACGGCGGCGGCGGTAACCACG GTGGTGGCGGTAATAATAGCGGCCCAAATTCT GAGCTGAACATTTACCAGTACGGTGGCGGTAA CTCTGCACTTGCTCTGCAAACTGATGCCCGTAA CTCTGACTTGACTATTACCCAGCATGGCGGCG GTAATGGTGCAGATGTTGGTCAGGGCTCAGAT GACAGCTCAATCGATCTGACCCAACGTGGCTT CGGTAACAGCGCTACTCTTGATCAGTGGAACG GCAAAAATTCTGAAATGACGGTTAAACAGTTC GGTGGTGGCAACGGTGCTGCAGTTGACCAGAC TGCATCTAACTCCTCCGTCAACGTGACTCAGGT TGGCTTTGGTAACAACGCGACCGCTCATCAGT ACGGATCCCACCACCACCACCACCACCCTAGG GGCGGTAGCGGTGGGCGCGGTGACAGCCCC

8 APPENDIX B

LIST OF PRIMERS

Table B.1. Nucleotide sequences of primers used in cloning of *csgA* and *cgsB* genes into pEt22b.

Primer Name	**Primer Sequence**	
csgA_F (66)	Forward Primer	5' AAAAAAGGTACCATGTCTGAGCTGAACATTTACCAGT 3'
pZa csgA cmr aTc REV	Reverse Primer	5' ATTAAGGTAACTAAAAAACTCCTTTTTAGTACTGATGAGCGGTCGCGTTG 3'
csgB_F (63)	Forward Primer	5' AAAAAAGGTACCATGCAGGCAGCCATAATTG 3'
csgB_R (61)	Reverse Primer	5' AAAAAACTCGAGACCGCTACCGCCTTGAGTACCATACTGTGT 3'

Table B.2. Nucleotide sequences of primers used in *tasA* and *tasA DQNAT* genes into pEt22b (+).

Primer Name	**Primer Sequence**
TasA01 FWD	5' ATATATGGTACCATGGCATTTAACGACATTAAATCAAAG 3'
TasA01 REV	5' ATATATCTCGAGACCGCTACCGCCATTTTTATCCTCGCTATGCG 3'
DQNAT_pet22b_F (66)	5'AAAAAACCTAGGGGCGGTAGCGGTGATCAGAACGCGACCACTAGTTGAGATCCGGCTGCT AACAA 3'
RGD_pet22b_R (69)	5' AAAAAACCTAGGGTGGTGGTGGTGGTGGTG 3'

Table B.3. Nucleotide sequences of primers used in cloning of *csgA-RGD* and *csgB-RGD* genes into pET22b (+) vector.

Primer Name	**Primer Sequence**
csgA_F (66)	5' AAAAAAGGTACCATGTCTGAGCTGAACATTTACCAGT 3'
csgA_R (68)	5' AAAAAACTCGAGACCGCTACCGCCGTACTGATGAGCGGT 3'
csgB_F (63)	5' AAAAAAGGTACCATGCAGGCAGCCATAATTG 3'
csgB_R (61)	5' AAAAAACTCGAGACCGCTACCGCCTTGAGTACCATACTGTGT 3'
RGD_F (66)	5' AAAAAACCTAGGGGCGGTAGCGGTGGGCGCGGTGACAGCCCCTGAGATCCGGCTGCTAACA 3'
RGD_R (68)	5' AAAAAACCTAGGGTGGTGGTGGTG 3'

Table B.4. Nucleotide sequences of primers used in cloning of *csgA*, *cgsB, tasA* and *tapA* genes with N42 signal sequence into pZa pBAD vector.

Primer Name	**Primer Sequence**
cgA pBD FWD	5' GAGCACGGGTACCATGAAACTTTTAAAAGTAGCA 3'
cgA pBD REV	5' ATTCATCTCGAGTTAGTACTGATGAGCGGT 3'
cgB pBD FWD	5’ CCGGCAGGTACCATGAAAAACAAATTGTTATTTATGATGTTAAC 3’
cgB pBD REV	5’ TTCGAACTCGAGTTAACGTTGTGTCACGCG 3’
P1 FWD *(for tasA)*	5' GGTGGCGGTAATAATAGCGGCCCAAATGCATTTAACGACATTAAATCAAAGGATGC 3'
R1 REV *(for tasA)*	5' GCGCGCATGCTCCCGGGCCCCTCGAGTTATTATTAATTTTTATCCTCGCTATGCGCTTTTTCA 3'

Table B.4 (cont'd)

P1 FWD2 *(for tapA)*	5' GGTGGCGGTAATAATAGCGGCCCAAATATATGCTTACAATTTTCCGATGATACAAG CGC 3'
R2 REV *(for tapA)*	5' CTCGAGTTATTATTACTGATCAGCTTCATTGCTTTTTTCATCC 3'
P2 FWD *(for N42)*	5' TGTTCCTCAGTACGGCGGCGGCGGTAACCACGGTGGTGGCGGTAATAATAGCGG 3'
P3 FWD *(for N42)*	5' CAGCAATCGTATTCTCCGGTAGCGCTCTGGCAGGTGTTGTTCCTCAGTACGGCGG 3'
P4 FWD *(for N42)*	5' GCGCGGCACCGGTACCATGAAACTTTTAAAAGTAGCAGCAATTGCAGCAATCGTA TTCTCCGGT 3'

Table B.5. Nucleotide sequences of primers used in cloning of *csgA*, *cgsB, tasA, tapA, fapC* and *fapB* genes with N42 signal sequence and with C terminal 6X His tag into pZa pBAD vector.

Primer Name	**Primer Sequence**
cgA pBD FWD	5' GAGCACGGGTACCATGAAACTTTTAAAAGTAGCA 3'
cgA pBD His REV	5' ATATATCTCGAGTCAGTGGTGGTGGTGGTGGTGACCGCTACCGCCGTACTGATGAGCGGTCGC 3'
cgB pBD FWD	5’ CCGGCAGGTACCATGAAAAACAAATTGTTATTTATGATGTTAAC 3’
cgB pBD His REV	5’ ATATATCTCGAGTCAGTGGTGGTGGTGGTGGTGACCGCTACCGCCACGTTGTGTCACGCGAATAG 3’
pBD Tas His REV	5' GGTGGCGGTAATAATAGCGGCCCAAATGCATTTAACGACATTAAATCAAAGGATGC 3'
pBD Tap His REV	5' GCGCGCATGCTCCCGGGCCCCTCGAGTTATTATTAATTTTTATCCTCGCTATGCGCTTTTTCA 3'
pBD fpC His REV	5’ GGTGGCGGTAATAATAGCGGCCCAAATATATGCTTACAATTTTCCGATGATACAAGCGC 3’
pBD fpB His REV	5’ CTCGAGTTATTATTACTGATCAGCTTCATTGCTTTTTTCATCC 3’

Table B.6. Nucleotide sequences of primers used in cloning of *csgA and cgsA RGD* genes with N42 signal sequence and with C terminal 6X His tag into pZa atc vector.

Primer Name	**Primer Sequence**
P4 FWD	5’ GCGCGGCACCGGTACCATGAAACTTTTAAAAGTAGCAGCAATTGCAGCAATCGTATTCTCCGGT 3’
ESK 008 REV1	5' CTGATCACCGCTACCGCCCCTAGGGTGGTGGTGGTGGTGGTGGGATCCGTACTGATGAGCGGTCG C 3'
ESK010 REV2	5’ GATGCCACGCGTTCAGGGGCTGTCACCGCGCCCACCGCTACCGCCCCTAGGGTG 3’
ESK011 REV2	5’ TCGATGCCACGCGTTCATCAACCGCTACCGCCCCTAGGGT 3’

9 APPENDIX C

PLASMID MAPS



Figure C.1. Schematic representation of pEt22b-CsgA plasmid.



Figure C.2. Schematic representation of pEt22b-CsgB plasmid.

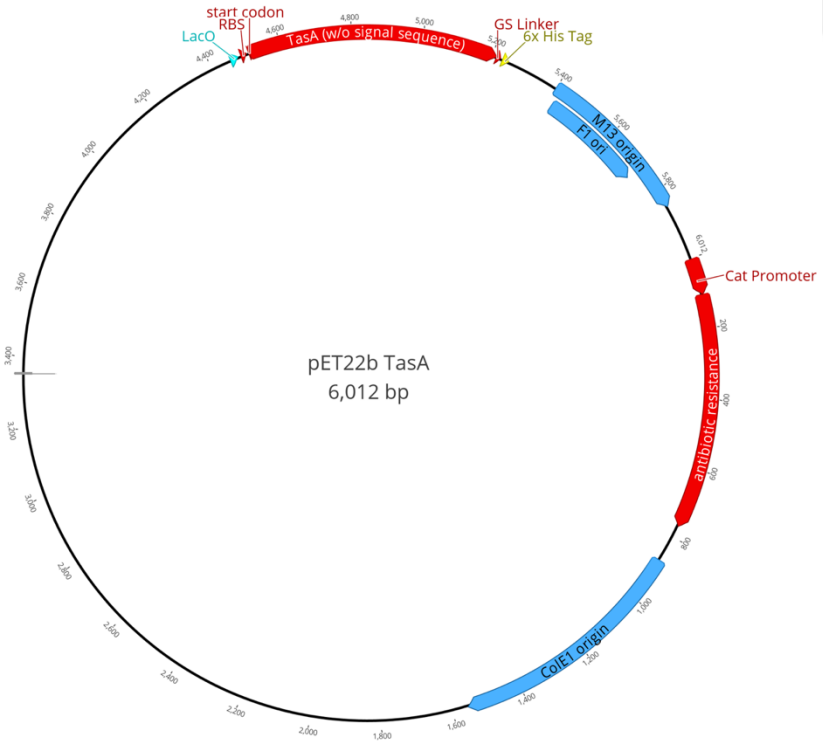


Figure C.3. Schematic representation of pEt22b-TasA plasmid.

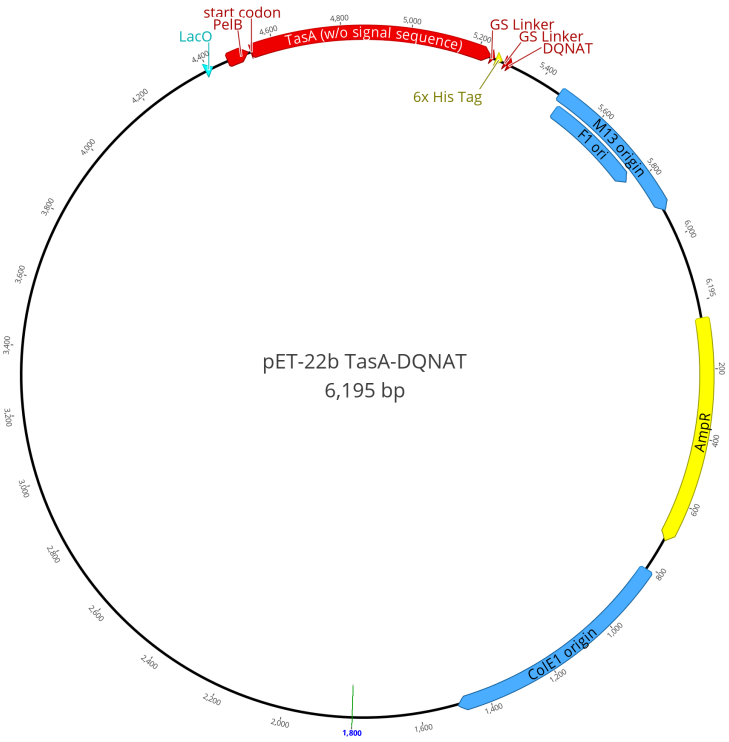


Figure C.4. Schematic representation of pEt22b-TasA DQNAT plasmid.

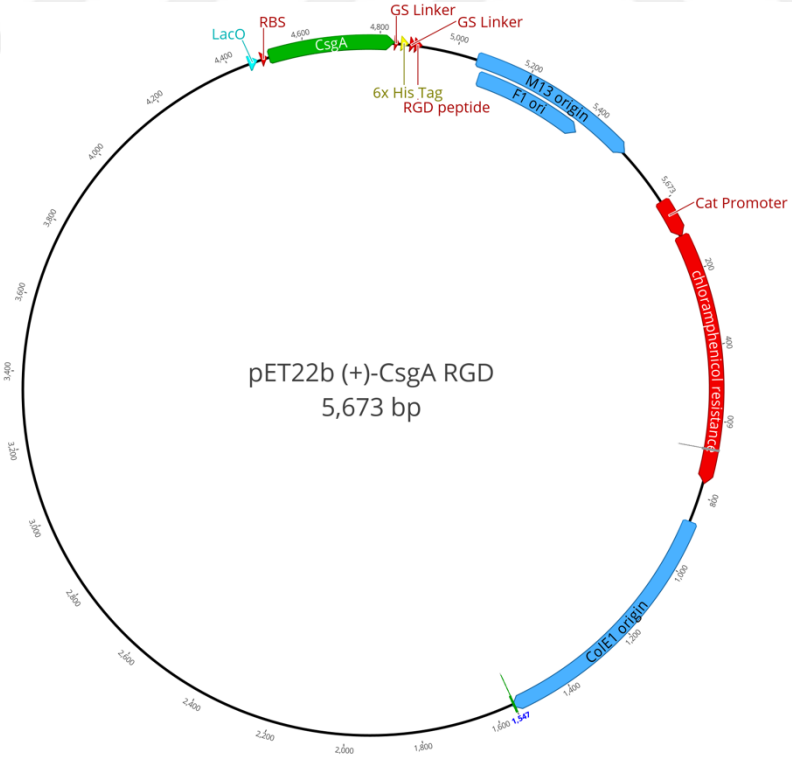


Figure C.5. Schematic representation of pEt22b-CsgA RGD plasmid.

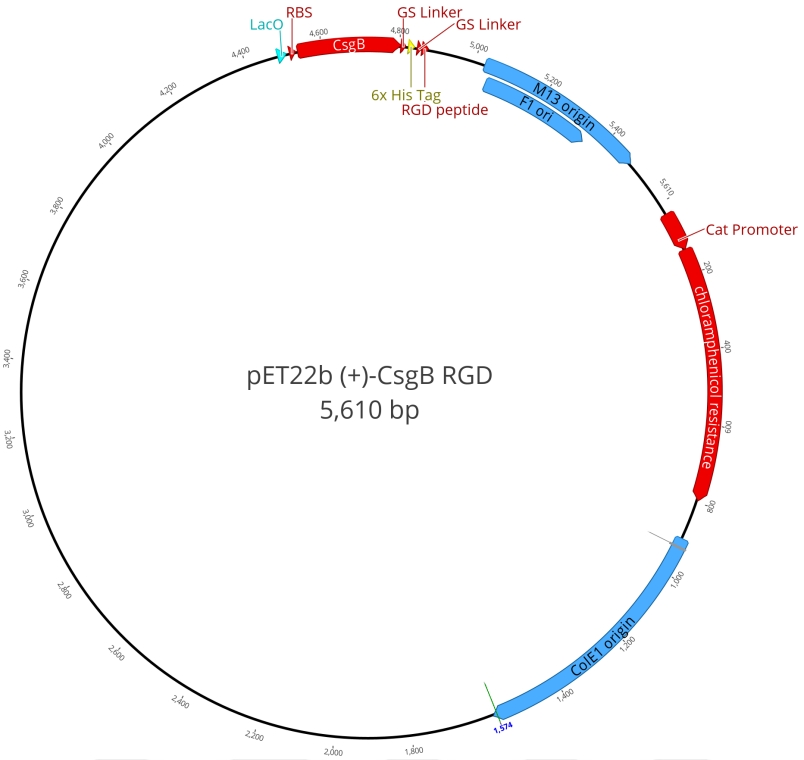


Figure C.6. Schematic representation of pEt22b-CsgB RGD plasmid.

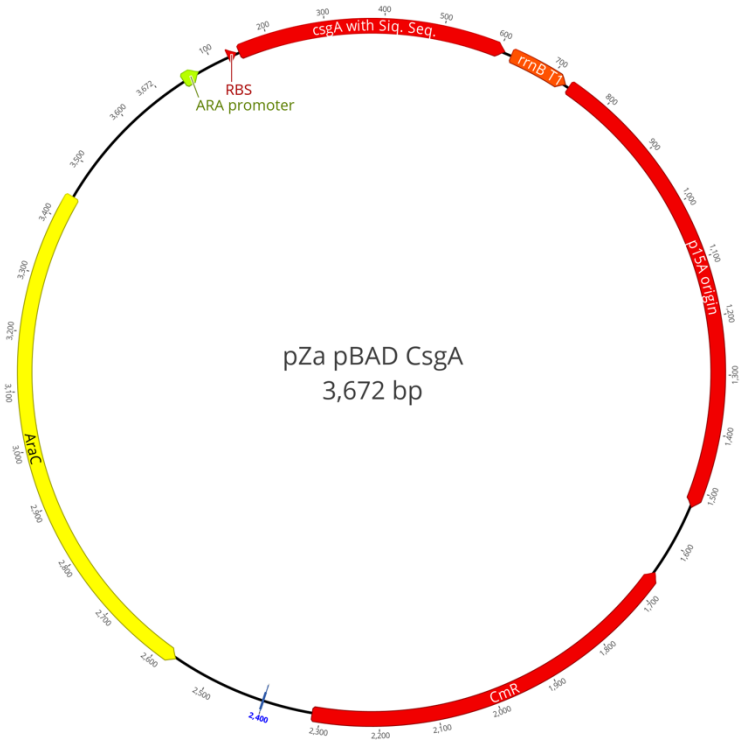


Figure C.7. Schematic representation of pZa pBAD CsgA plasmid.

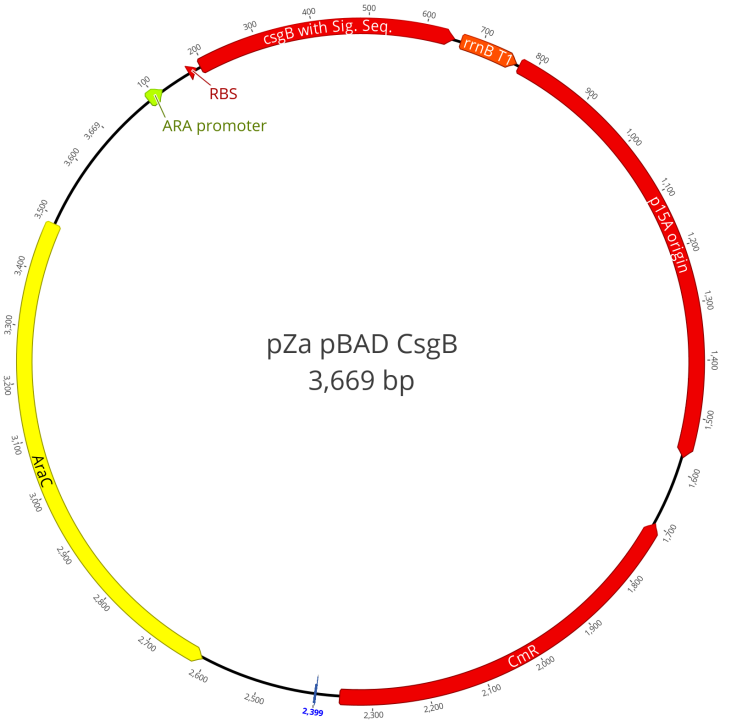


Figure C.8. Schematic representation of pZa pBAD CsgB plasmid.



Figure C.9. Schematic representation of pZa pBAD TasA plasmid.

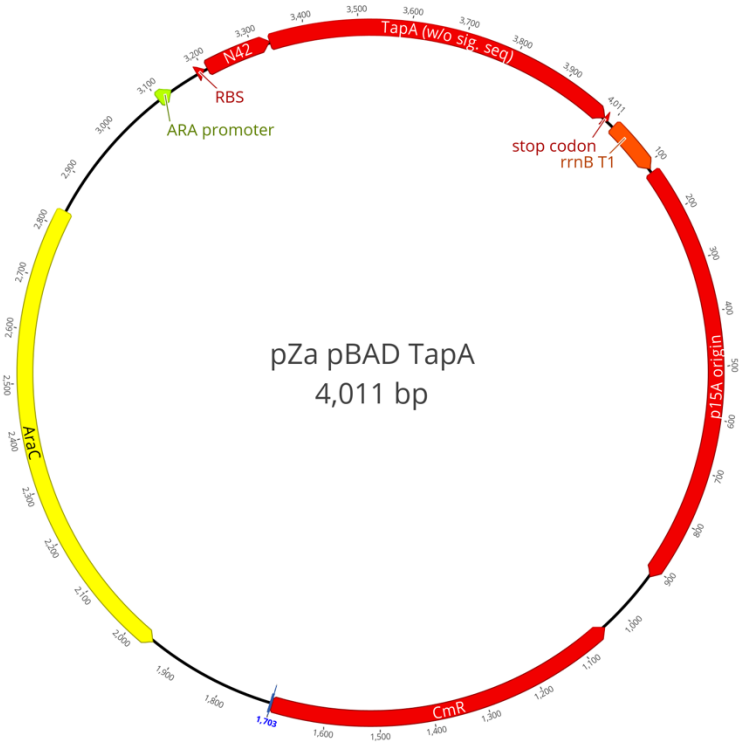


Figure C.10. Schematic representation of pZa pBAD TapA plasmid.

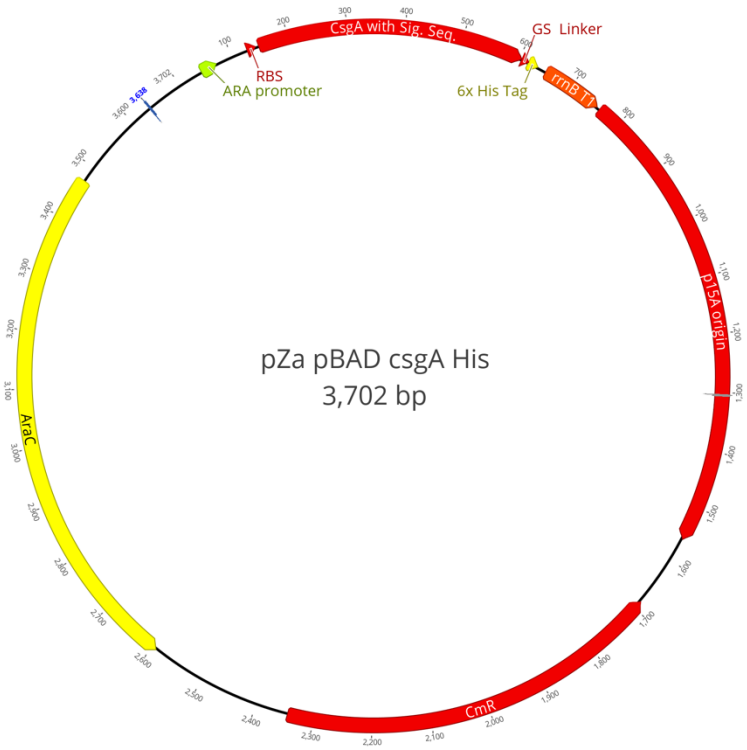


Figure C.11. Schematic representation of pZa pBAD csgA His plasmid.

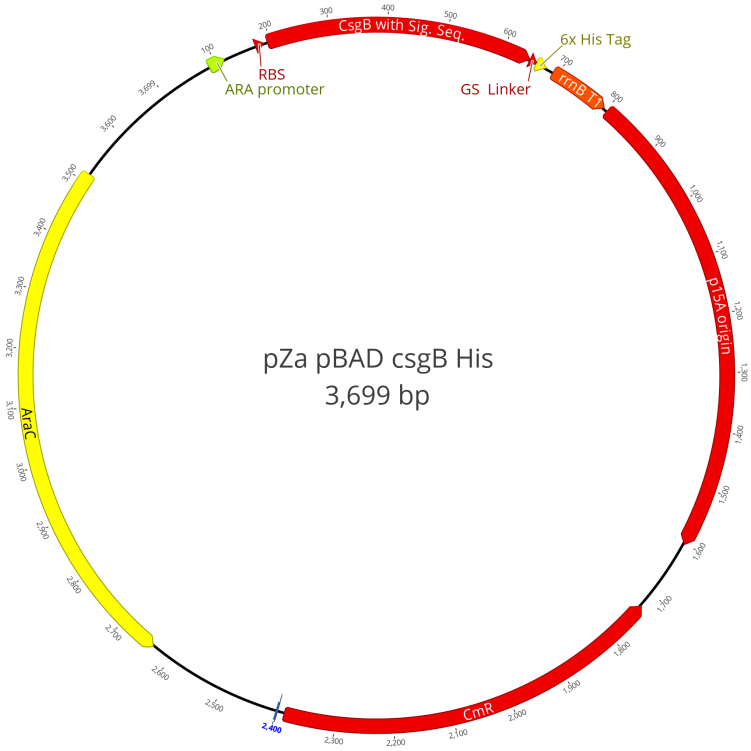


Figure C.12. Schematic representation of pZa pBAD csgB His plasmid.

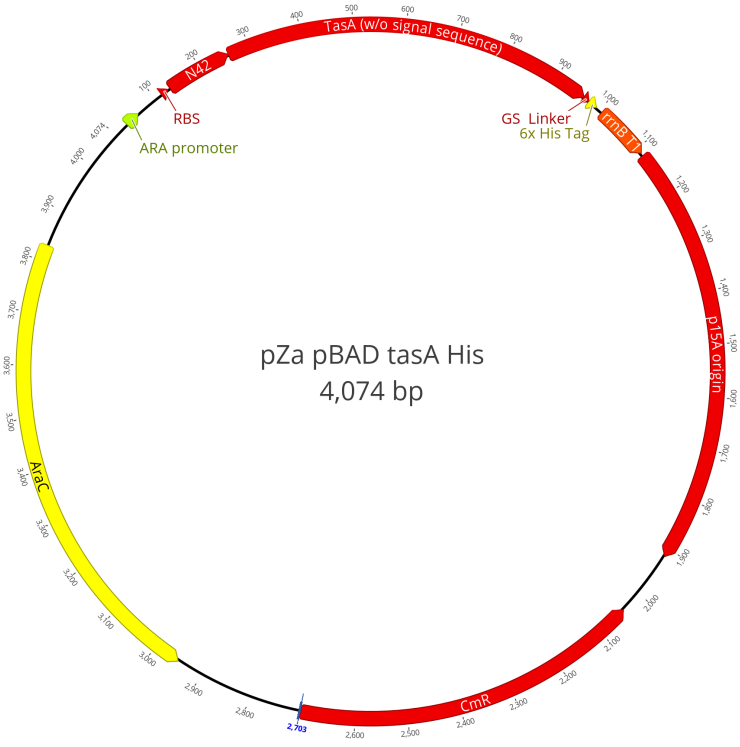


Figure C.13. Schematic representation of pZa pBAD tasA His plasmid.

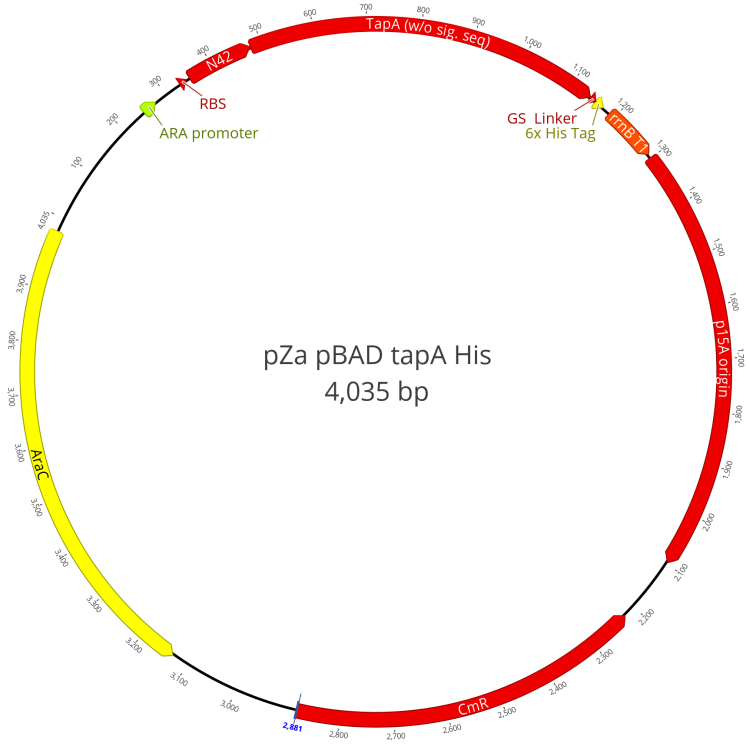


Figure C.14. Schematic representation of pZa pBAD tapA His plasmid.

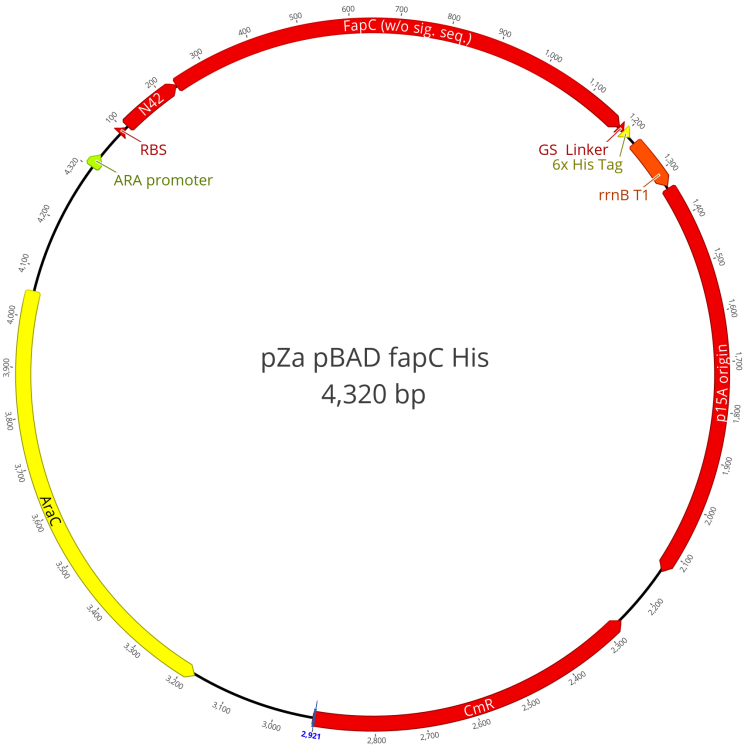


Figure C.15. Schematic representation of pZa pBAD fapC His plasmid.

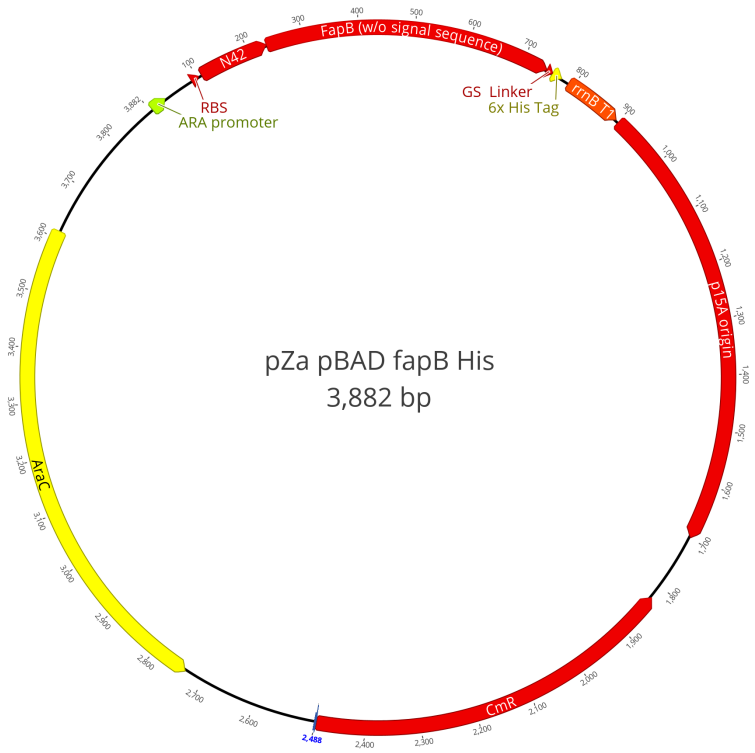


Figure C.16. Schematic representation of pZa pBAD fapB His plasmid.

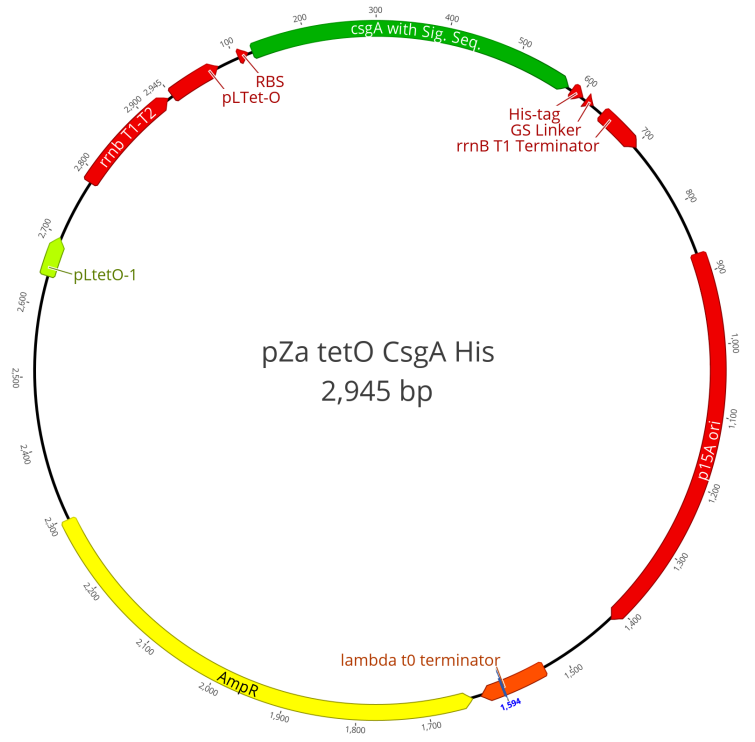


Figure C.17. Schematic representation of pZa tetO csgA His plasmid.



Figure C.18. Schematic representation of pZa tetO csgA RGD plasmid.

10 APPENDIX D

SANGER SEQUENCING RESULTS

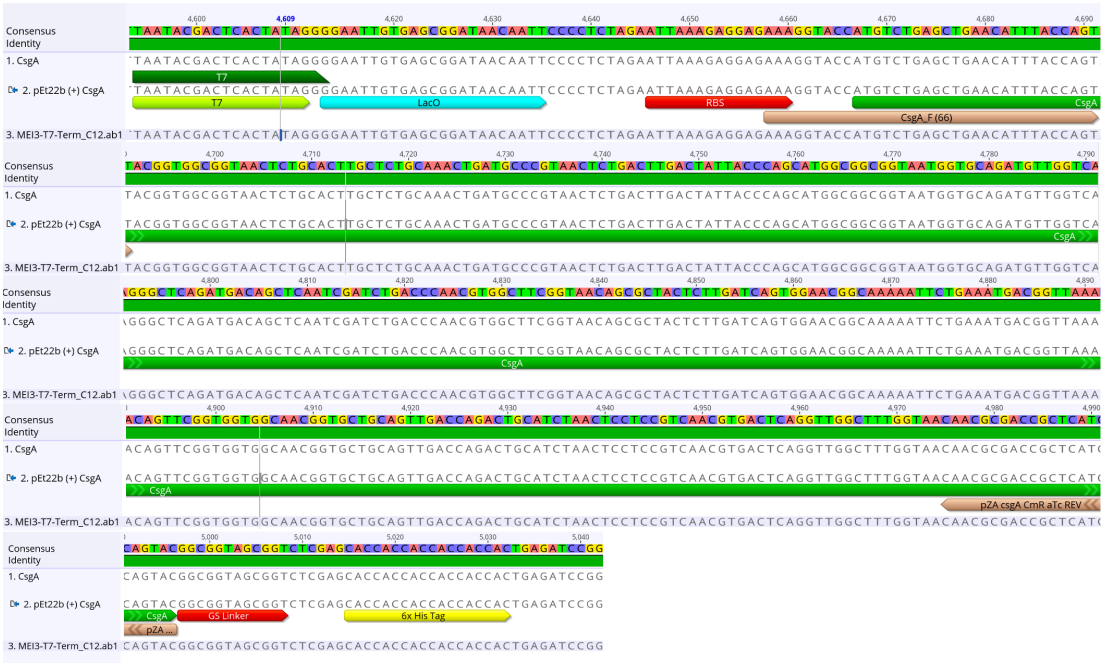


Figure D 1. Sequencing alignment of pEt22b-CsgA construct. Analysis performed in Geneious R9.0.5 Software. Identity was 100%.

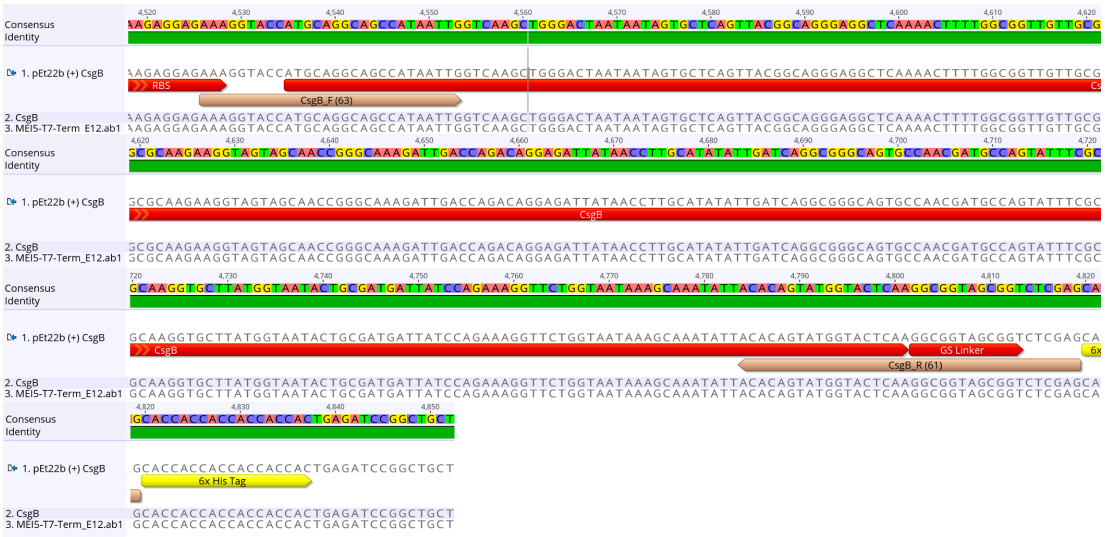


Figure D 2. Sequencing alignment of pEt22b-CsgB construct. Analysis performed in Geneious R9.0.5 Software. Identity was 100%.

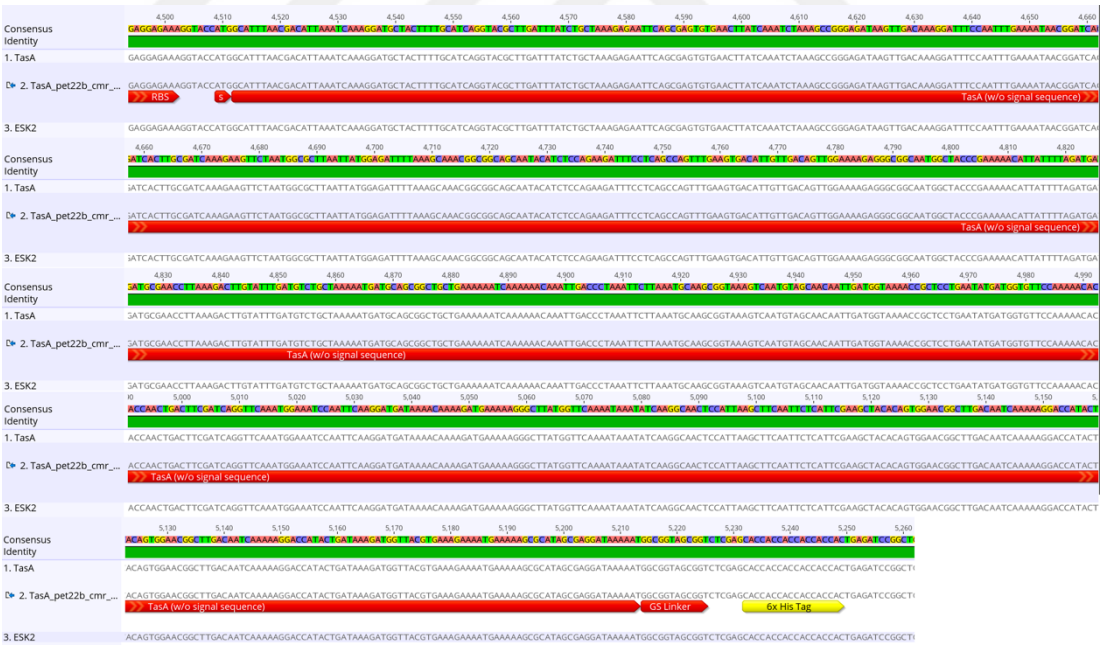


Figure D.3. Sequencing alignment of pEt22b-TasA construct. Analysis performed in Geneious R9.0.5 Software. Identity was 100%.



Figure D.4. Sequencing alignment of pEt22b-TasA DQNAT construct. Analysis performed in Geneious R9.0.5 Software. Identity was 100%.

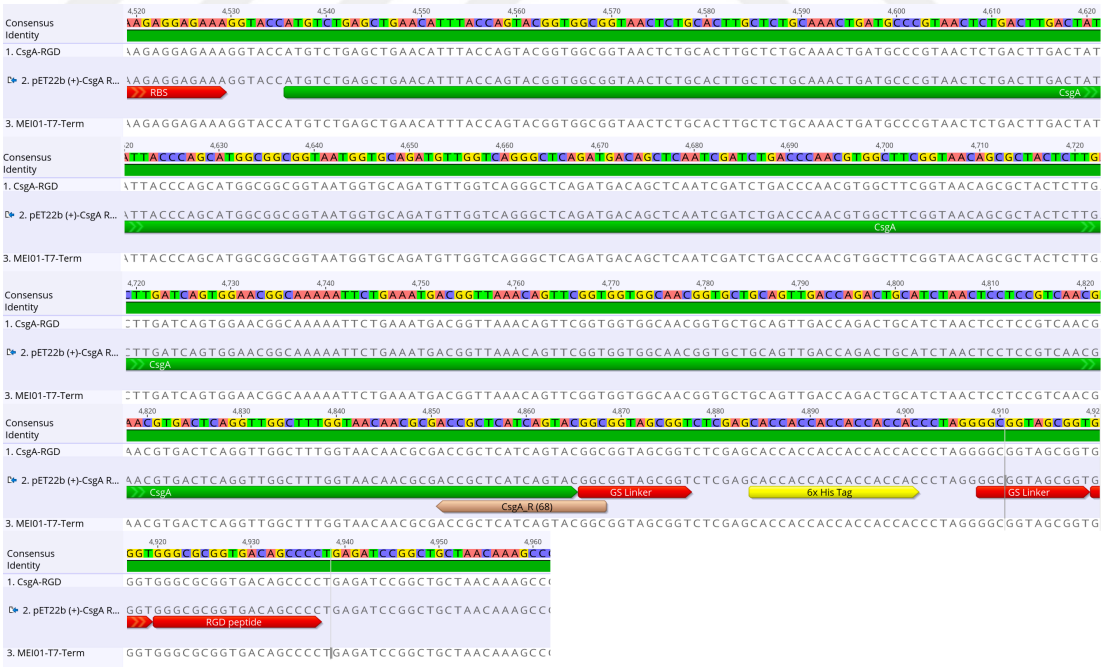


Figure D.5. Sequencing alignment of pEt22b-CsgA RGD construct. Analysis performed in Geneious R9.0.5 Software. Identity was 100%.

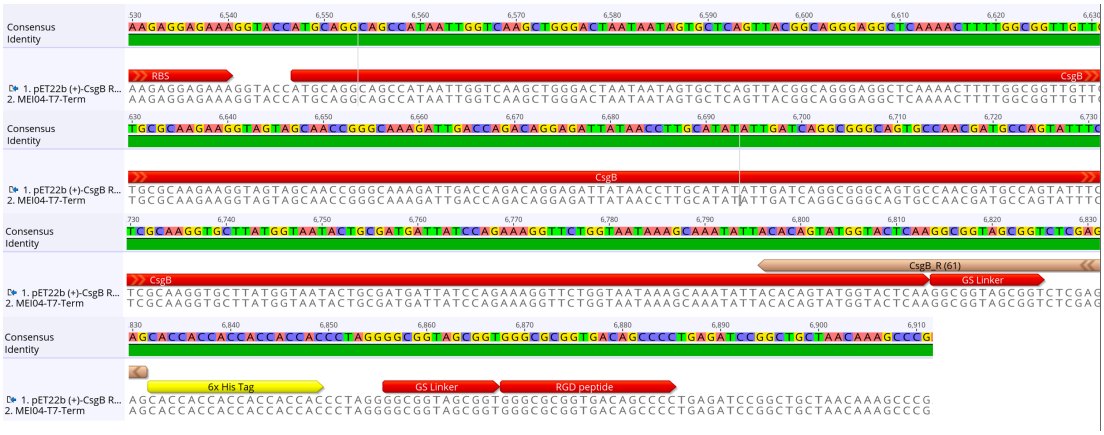


Figure D.6. Sequencing alignment of pEt22b-CsgB RGD construct. Analysis performed in Geneious R9.0.5 Software. Identity was 100%.

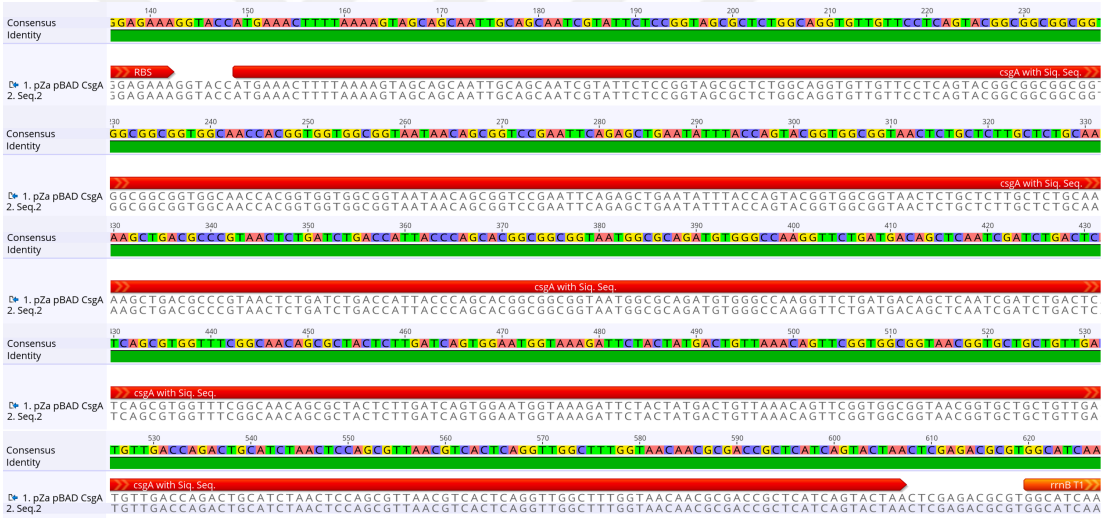


Figure D.7. Sequencing alignment of pZa pBAD CsgA construct. Analysis performed in Geneious R9.0.5 Software. Identity was 100%.

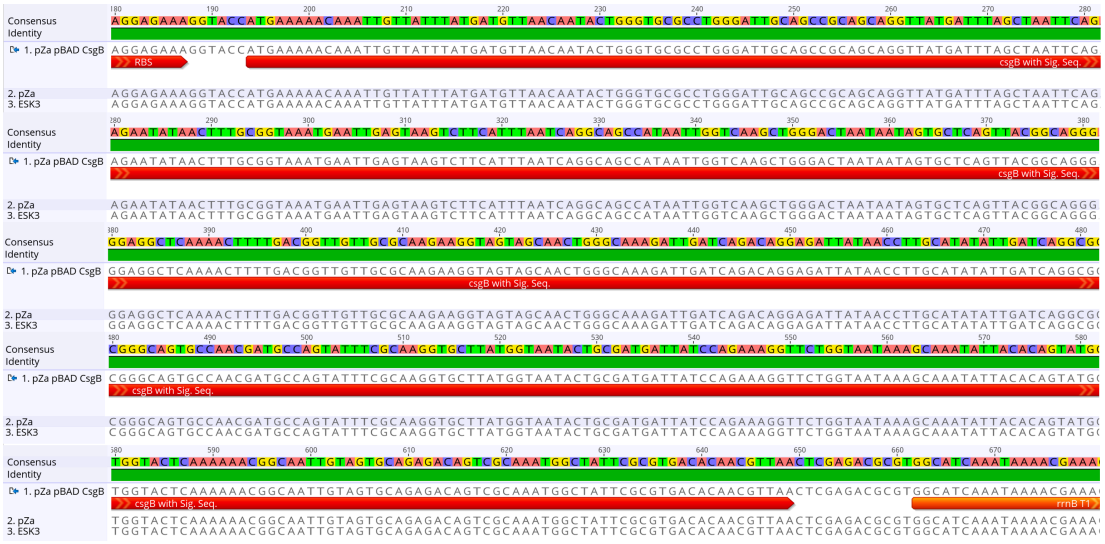


Figure D.8. Sequencing alignment of pZa pBAD CsgB construct. Analysis performed in Geneious R9.0.5 Software. Identity was 100%.



Figure D.9. Sequencing alignment of pZa pBAD TasA construct. Analysis performed in Geneious R9.0.5 Software. Identity was 100%.

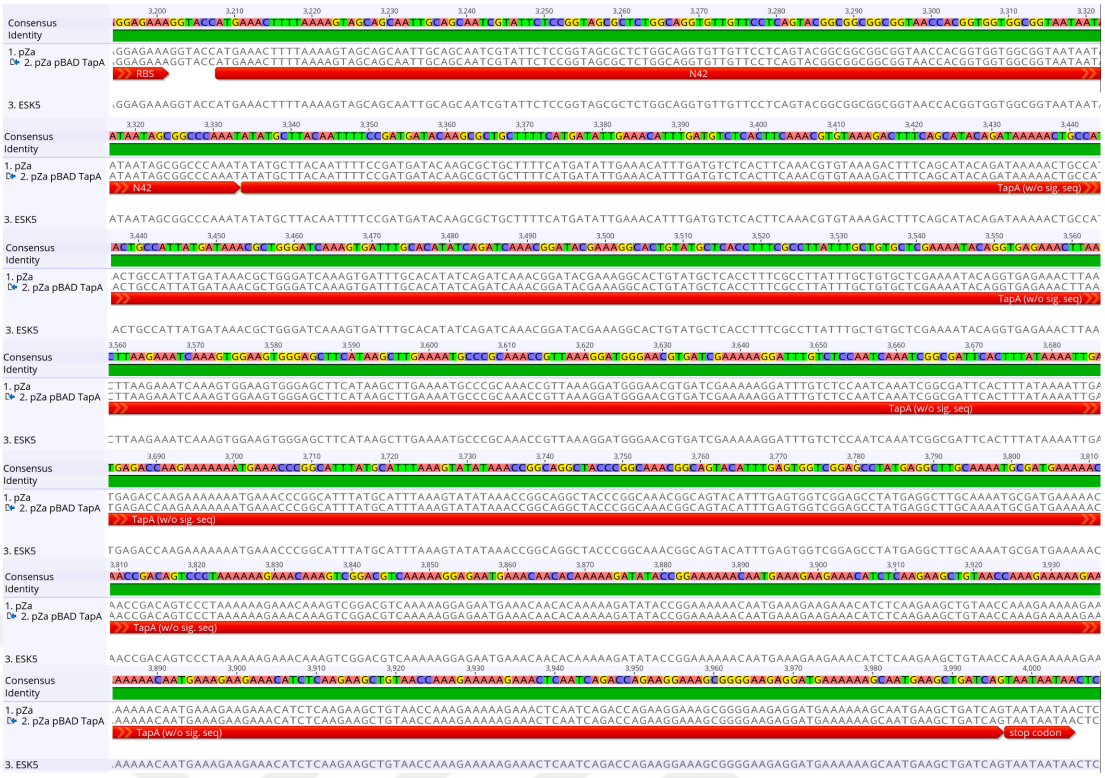


Figure D.10. Sequencing alignment of pZa pBAD TapA construct. Analysis performed in Geneious R9.0.5 Software. Identity was 100%.

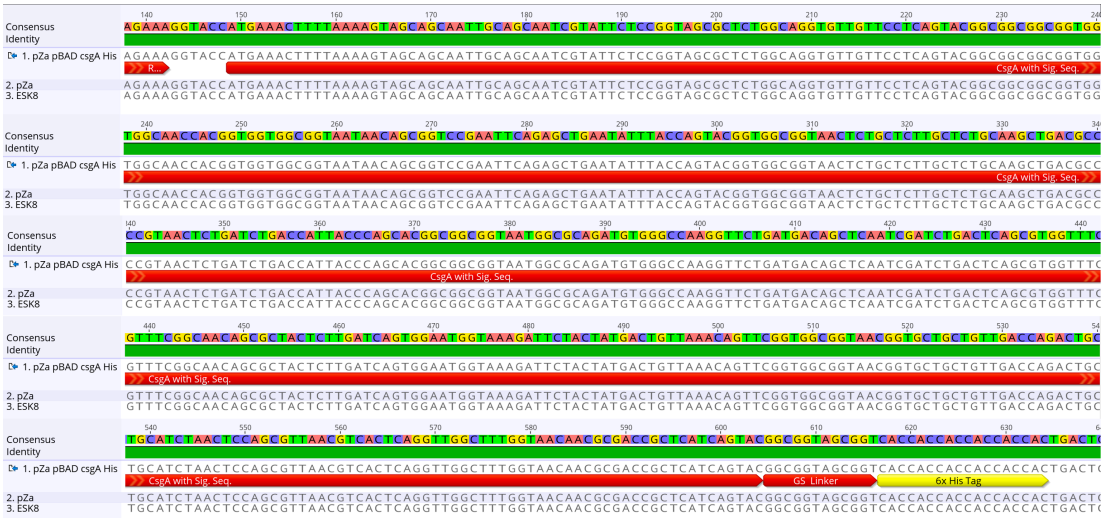


Figure D.11. Sequencing alignment of pZa pBAD csgA His construct. Analysis performed in Geneious R9.0.5 Software. Identity was 100%.

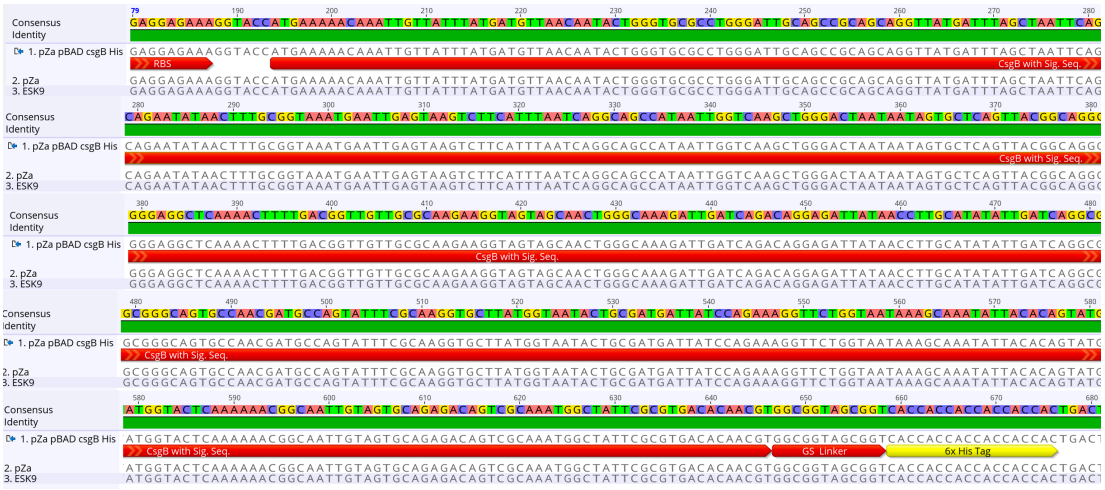


Figure D.12. Sequencing alignment of pZa pBAD csgB His construct. Analysis performed in Geneious R9.0.5 Software. Identity was 100%.

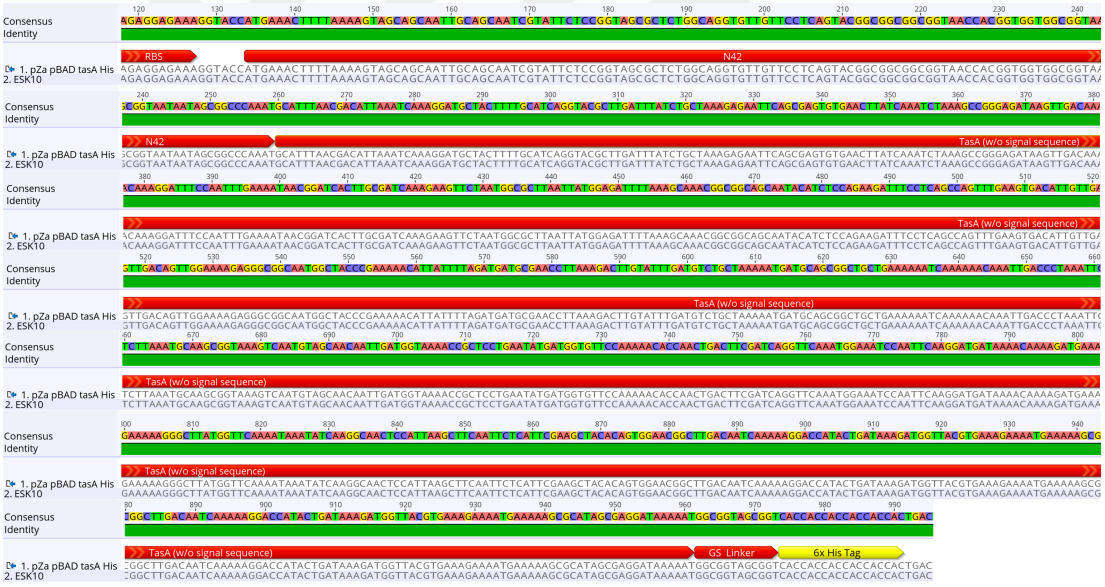


Figure D.13. Sequencing alignment of pZa pBAD tasA His construct. Analysis performed in Geneious R9.0.5 Software. Identity was 100%.

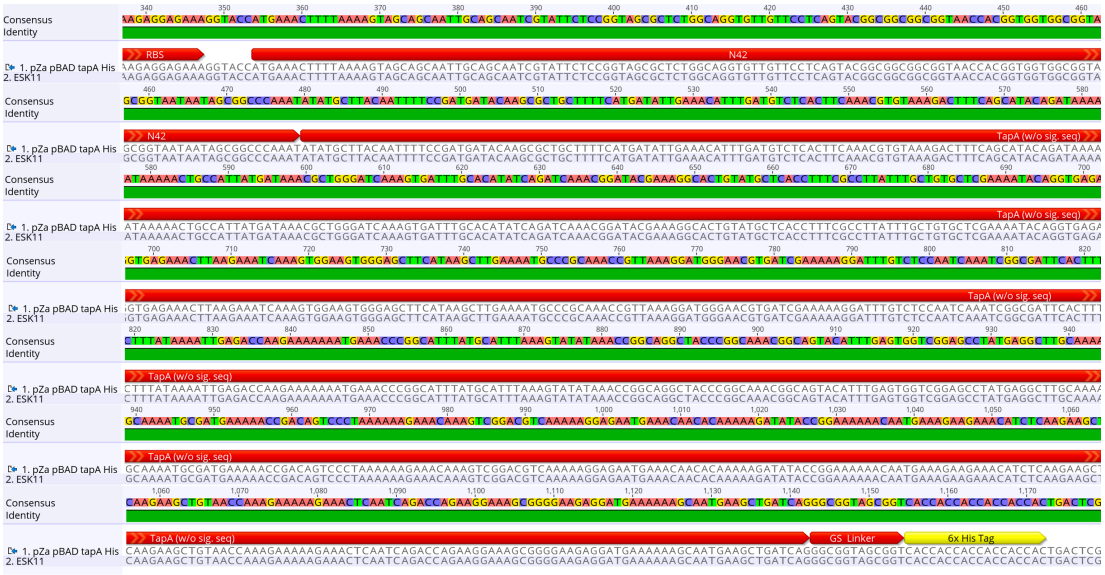


Figure D.14. Sequencing alignment of pZa pBAD tapA His construct. Analysis performed in Geneious R9.0.5 Software. Identity was 100%.

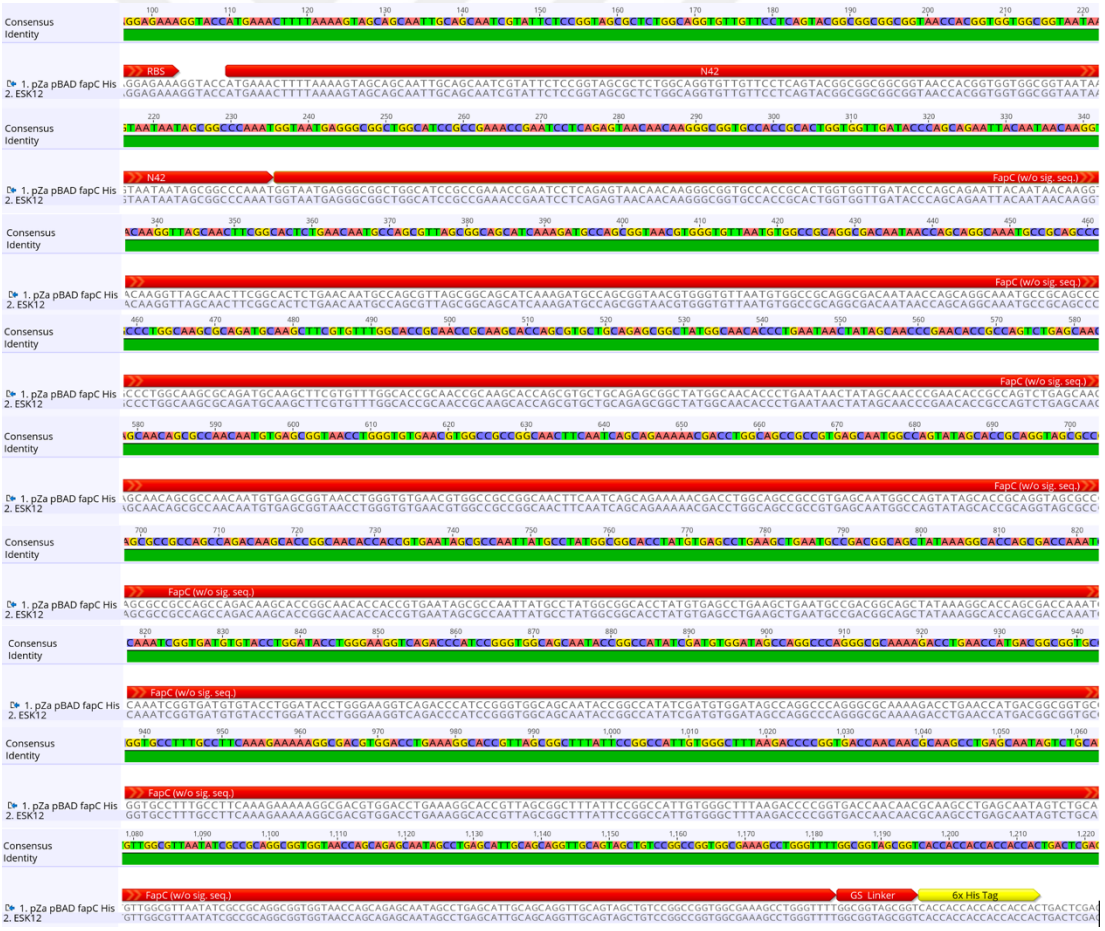


Figure D.15. Sequencing alignment of pZa pBAD fapC His construct. Analysis performed in Geneious R9.0.5 Software. Identity was 100%.

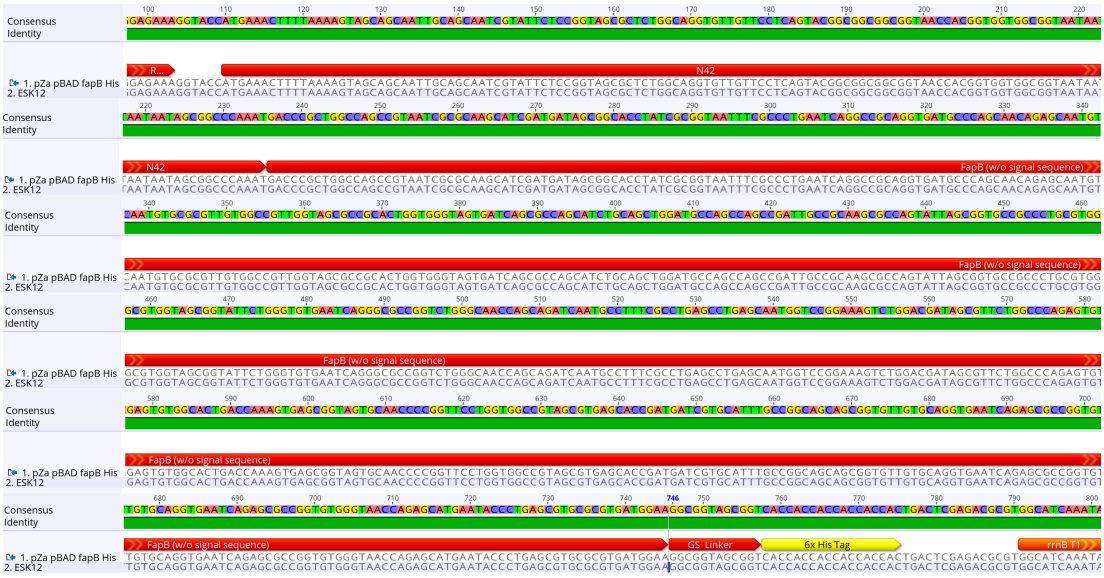


Figure D.16. Sequencing alignment of pZa pBAD fapB His construct. Analysis performed in Geneious R9.0.5 Software. Identity was 100%.

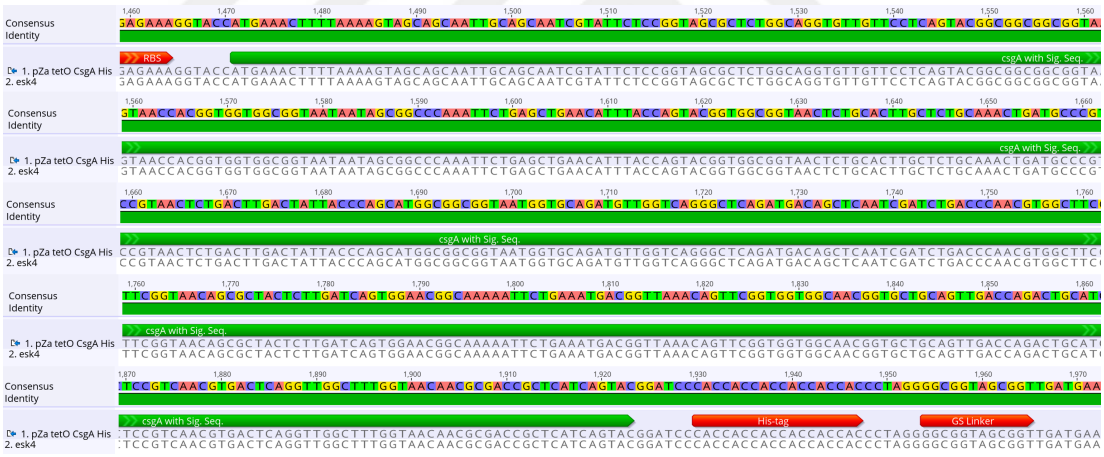


Figure D.17. Sequencing alignment of pZa tetO csgA His construct. Analysis performed in Geneious R9.0.5 Software. Identity was 100%.

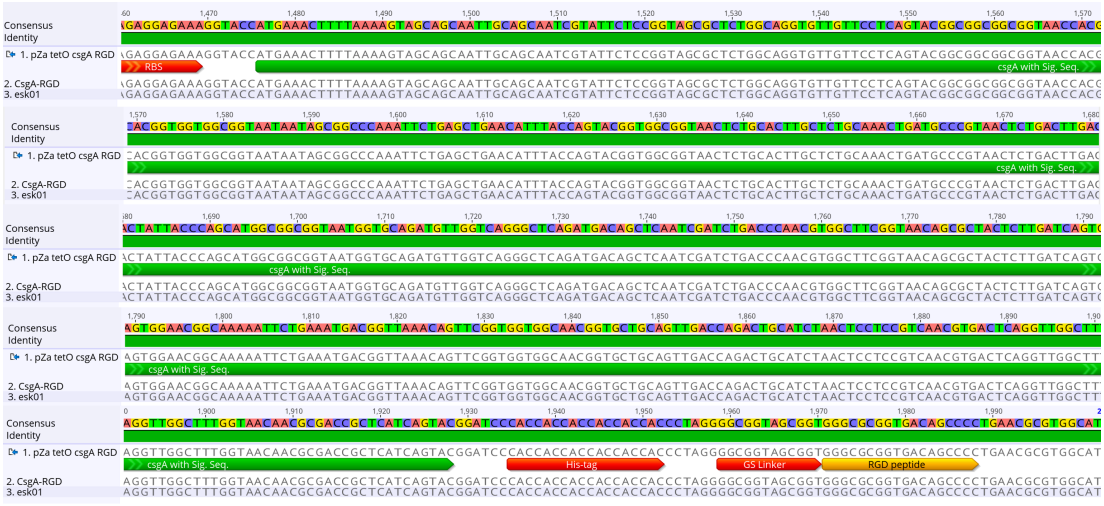


Figure D.18. Sequencing alignment of pZa tetO csgA RGD construct. Analysis performed in Geneious R9.0.5 Software. Identity was 100%.

11 APPENDIX E

AMINO ACID SEQUENCES OF PROTEINS

Table E.1. Amino acid sequences of proteins used in Chapter 2. Color code corresponds to red for positively charged amino acids, blue for negatively charged amino acids, black for nonpolar aliphatic amino acids, green for polar uncharged amino acids, and orange for nonpolar aromatic amino acids.

E. coli CsgA amino acid sequence with, 6X His-Tag and GS Linker	MSELNIYQYGGGNSALALQTDARNSDLTITQHGGGNGADVGQ GSDDSSIDLTQRGFGNSATLDQWNGKNSEMTVKQFGGGNGA AVDQTASNSSVNVTQVGFGNNATAHQYGTGGSGGGSGGGSG ENLYFQGGGSGGGSGGGSGGSLEHHHHHH
E.coli CsgB amino acid sequence with, 6X His-Tag and GS Linker	MQAAIIGQAGTNNSAQLRQGGSKLLAVVAQEGSSNRAKIDQT GDYNLAYIDQAGSANDASISQGAYGNTAMIIQKGSGNKANITQ YGTQGTGGSGGGSGGGSGENLYFQGGGSGGGSGGGSGGSLE HHHHHH

Table E.2. TasA Amino acid sequences of proteins used in Chapter 3.

TasA amino acid sequence with GS linker and 6X His tag	MAFNDIKSKDATFASGTLDLSAKENSASVNLSNLKP GDKLTKDFQFENNGSLAIKEVLMALNYGDFKANGG SNTSPEDFLSQFEVTLLTVGKEGGNGYPKNIILDDAN LKDLYLMSAKNDAAAAEKIKKQIDPKFLNASGKVN VATIDGKTAPEYDGVPKTPTDFDQVQMEIQFKDDK TKDEKGLMVQNKYQGNSIKLQFSFEATQWNGLTIK KDHTDKDGYVKENEKAHSEDKNGGSGLEHHHHHH
TasA amino acid sequence with GS linker, 6X His tag and DQNAT tag.	MAFNDIKSKDATFASGTLDLSAKENSASVNLSNLKP GDKLTKDFQFENNGSLAIKEVLMALNYGDFKANGG SNTSPEDFLSQFEVTLLTVGKEGGNGYPKNIILDDAN LKDLYLMSAKNDAAAAEKIKKQIDPKFLNASGKVN VATIDGKTAPEYDGVPKTPTDFDQVQMEIQFKDDK TKDEKGLMVQNKYQGNSIKLQFSFEATQWNGLTIK KDHTDKDGYVKENEKAHSEDKNGGSGLEHHHHHH PRGGSGDQNATTS

Table E.3. Amino acid sequences of proteins used in Chapter 4.

CsgA amino acid sequence with GS linker, 6X His tag and RGD peptide tag	MSELNIYQYGGGNSALALQTDARNSDLTITQHGGG NGADVGQGSDDSSIDLTQRGFGNSATLDQWNGKNS EMTVKQFGGGNGAAVDQTASNSSVNVTQVGFGNN ATAHQYGGSGLEHHHHHHPRGGSGGRGDSP
CsgB amino acid sequence with GS linker, 6X His tag and RGD peptide tag	MQAAIIGQAGTNNSAQLRQGGSKLLAVVAQEGSSN RAKIDQTGDYNLAYIDQAGSANDASISQGAYGNTA MIIQKGSGNKANITQYGTQGGSGLEHHHHHHPRGG SGGRGDSP
CsgA amino acid sequence with native signal sequence	MKLLKVAAIAAIVFSGSALAGVVPQYGGGGGNHGG GGNNSGPNSELNIYQYGGGNSALALQADARNSDLTI TQHGGGNGADVGQGSDDSSIDLTQRGFGNSATLDQ WNGKDSTMTVKQFGGGNGAAVDQTASNSSVNVTQ VGFGNNATAHQY
CsgB amino acid sequence with native signal sequence	MKNKLLFMMLTILGAPGIAAAAGYDLANSEYNFAV NELSKSSFNQAAIIGQAGTNNSAQLRQGGSKLLTVV AQEGSSNWAKIDQTGDYNLAYIDQAGSANDASISQ GAYGNTAMIIQKGSGNKANITQYGTQKTAIVVQRQ SQMAIRVTQR

Table E.3 (cont'd)

TasA amino acid sequence with N42 signal sequence	MKLLKVAAIAAIVFSGSALAGVVPQYGGGGNHGGG GNNSGPNAFNDIKSKDATFASGTLDLSAKENSASVN LSNLKPGDKLTKDFQFENNGSLAIKEVLMALNYGD FKANGGSNTSPEDFLSQFEVTLLTVGKEGGNGYPKN IILDDANLKDLYLMSAKNDAAAAEKIKKQIDPKFLN ASGKVNVATIDGKTAPEYDGVPKTPTDFDQVQMEI QFKDDKTKDEKGLMVQNKYQGNSIKLQFSFEATQ WNGLTIKKDHTDKDGYVKENEKAHSEDKN
TapA amino acid sequence with N42 signal sequence	MKLLKVAAIAAIVFSGSALAGVVPQYGGGGNHGGG GNNSGPNICLQFSDDTSAAFHDIETFDVSLQTCKDFQ HTDKNCHYDKRWDQSDLHISDQTDTKGTVCSPFAL FAVLENTGEKLKKSKWKWELHKLENARKPLKDGN VIEKGFVSNQIGDSLYKIETKKKMKPGIYAFKVYKP AGYPANGSTFEWSEPMRLAKCDEKPTVPKKETKSD VKKENETTQKDIPEKTMKEETSQEAVTKEKETQSDQ KESGEEDEKSNEADQ
CsgA amino acid sequence with native signal sequence, GS linker and 6X His tag	MKLLKVAAIAAIVFSGSALAGVVPQYGGGGGNHGG GGNNSGPNSELNIYQYGGGGNSALALQADARNSDLTI TQHGGGNGADVGQGSDDSSIDLTQRGFGNSATLDQ WNGKDSTMTVKQFGGGNGAAVDQTASNSSVNVTQ VGFGNNATAHQYGGSGHHHHHH

Table E.3 (cont'd)

CsgB amino acid sequence with native signal sequence, GS linker and 6X His tag	MKNKLLFMMLTILGAPGIAAAAGYDLANSEYNFAV NELSKSSFNQAAIIGQAGTNNSAQLRQGGSKLLTVV AQEGSSNWAKIDQTGDYNLAYIDQAGSANDASISQ GAYGNTAMIIQKGSGNKANITQYGTQKTAIVVQRQ SQMAIRVTQRGGSGHHHHHH
TasA amino acid sequence with N42 signal sequence, GS linker and 6X His tag	MKLLKVAAIAAIVFSGSALAGVVPQYGGGGNHGGG GNNSGPNAFNDIKSKDATFASGTLDLSAKENSASVN LSNLKPGDKLTKDFQFENNGSLAIKEVLMALNYGD FKANGGSNTSPEDFLSQFEVTLLTVGKEGGNGYPKN IILDDANLKDLYLMSAKNDAAAAEKIKKQIDPKFLN ASGKVNVATIDGKTAPEYDGVPKTPTDFDQVQMEI QFKDDKTKDEKGLMVQNKYQGNSIKLQFSFEATQ WNGLTIKKDHTDKDGYVKENEKAHSEDKNGGSGH HHHHH
TapA amino acid sequence with N42 signal sequence, GS linker and 6X His tag	MKLLKVAAIAAIVFSGSALAGVVPQYGGGGNHGGG GNNSGPNICLQFSDDTSAAFHDIETFDVSLQTCKDFQ HTDKNCHYDKRWDQSDLHISDQTDTKGTVCSPFAL FAVLENTGEKLKKSKWKWELHKLENARKPLKDGN VIEKGFVSNQIGDSLYKIETKKKMKPGIYAFKVYKP AGYPANGSTFEWSEPMRLAKCDEKPTVPKKETKSD VKKENETTQKDIPEKTMKEETSQEAVTKEKETQSDQ KESGEEDEKSNEADQGGSGHHHHHH

Table E.3 (cont'd)

FapC amino acid sequence with N42 signal sequence, GS linker and 6X His tag	MKLLKVAAIAAIVFSGSALAGVVPQYGGGGNHGGG GNNSGPNGNEGGWHPPKPNPQSNNKGGATALVVD TQQNYNNKVSNFGTLNNASVSGSIKDASGNVGVNV AAGDNNQQANAAALASADASFVFGTATASTSVLQS GYGNTLNNYSNPNTASLSNSANNVSGNLGVNVAAG NFNQQKNDLAAAVSNGQYSTAGSAASQTSTGNTTV NSANYAYGGTYVSLKLNADGSYKGTSDQIGDVYLD TWEGQTHPGGSNTGHIDVDSQAQGAKDLNHDGGA FAFKEKGDVDLKGTVSGFIPAIVGFKTPVTNNASLS NSLQNVSGNVGVNIAAGGGNQQSNSLSIAAGCSSCP AGGESLGFGGSGHHHHHH
FapB amino acid sequence with N42 signal sequence, GS linker and 6X His tag	MKLLKVAAIAAIVFSGSALAGVVPQYGGGGNHGGG GNNSGPNDPLASRNRASIDDSGTYRGNFALNQAAG DAQQQSNVRVVAVGSAALVGSDQRQHLQLDASQPI AASASISGAALRGSGILGVNQGAGLGNQQINAFRLS LSNGPESLDDSVLAQSVALTKVSGSATPVPGGRSVS TDDRAFAGSSGVVQVNQSAGVGNQSMNTLSVRVM EGGSGHHHHHH

Table E.3 (cont'd)

CsgA amino acid sequence with native signal sequence, GS linker and 6X His tag	MKLLKVAAIAAIVFSGSALAGVVPQYGGGGNHGGG GNNSGPNSELNIYQYGGGNSALALQTDARNSDLTIT QHGGGNGADVGQGSDDSSIDLTQRGFGNSATLDQ WNGKNSEMTVKQFGGGNGAAVDQTASNSSVNVTQ VGFGNNATAHQYGSHHHHHHPRGGSG
CsgA amino acid sequence with native signal sequence, GS linker, 6X His tag and RGD peptide tag	MKLLKVAAIAAIVFSGSALAGVVPQYGGGGNHGGG GNNSGPNSELNIYQYGGGNSALALQTDARNSDLTIT QHGGGNGADVGQGSDDSSIDLTQRGFGNSATLDQ WNGKNSEMTVKQFGGGNGAAVDQTASNSSVNVTQ VGFGNNATAHQYGSHHHHHHPRGGSGGRGDSP

12 APPENDIX F

REACTION CONDITIONS

Table F.1. PCR reaction setup of Q5 DNA Polymerase

Component	***Final Concentration***
5 X Q5 Reaction Buffer	1 X
10 mM dNTPs	200 µM
10 µM Forward Primer	0.5 µM
10 µM Reverse Primer	0.5 µM
Template DNA	< 1 µg
Q5 DNA Polymerase	0.02 U/ µl
5 X Q5 GC Enhancer (Optional)	1 X
Nuclease free water	To reaction volume

Table F.2. PCR conditions of Q5 DNA Polymerase

Step	***Temperature***	***Time***
Initial Denaturation	98 ºC	
Denaturation	98 ºC	5-10 s
Annealing	50-72 ºC	10-30 s
Extension (25-35 cycles)	72 ºC	20-30 s/kb
Final Extension	72 ºC	5 min
Hold	+4 ºC	

Table F.3. Restriction digestion reaction setup with NEB restriction enzymes

Component	***Volume (20 µl Reaction)***
10 X Buffer	2 µl
DNA	1 µg
Restriction Enzyme 1	0.4 µl
Restriction Enzyme 2	0.4 µl
Nuclease free water	to 20 µl

Table F.4. T4 (NEB) ligation reaction setup

Component	***Volume (20 µl Reaction)***
10 X T4 DNA Ligase Buffer	2 µl
DNA (Total of insert and vector)	100 ng
T4 DNA Ligase	1 µl
Nuclease free water	to 20 µl

13 APPENDIX G

ADDITIONAL RESULTS

Table G.1. Dynamic light scattering analysis of CsgA protein at different concentrations and at different maturation times.

		Day0				Day1			
CsgA		Meas1	Intensity (%)	Meas2	Intensity (%)	Meas1	Intensity (%)	Meas2	Intensity (%)
4 nM	Peak1	234.9	89.7	340.2	79.2	391.3	100	391.4	100
	Peak2	3.1	5.7	2553	13.3	0	0	0	0
	Peak3	2780	4.6	1.6	5.8	0	0	0	0
	Z-average (d.nm)	360.5		390.6		739.3		713.5	
	PdI	0.609		0.509		0.465		0.531	
40 nM	Peak1	216.4	96.8	228.5	97.2	307.1	96.4	323.8	94.2
	Peak2	2701	3.2	2686	2.8	0.7	5.4	0.5	5.8
	Peak3	0	0	0	0	0	0	0	0
	Z-average (d.nm)	197.9		194.5		392.9		499.2	
	PdI	0.479		0.456		0.536		0.578	
400 nM	Peak1	292.5	88.2	303.9	87.8	295.5	100	318.9	100
	Peak2	56.6	7.3	67.9	8.8	0	0	0	0
	Peak3	2623	4.5	2632	3.4	0	0	0	0
	Z-average (d.nm)	266.8		256.9		498.1		471.5	
	PdI	0.371		0.361		0.456		0.385	

Table G.2. Dynamic light scattering analysis of CsgB protein at different concentrations and at different maturation times.

		Day0				Day1			
CsgB		Meas1	Intensity (%)	Meas2	Intensity (%)	Meas1	Intensity (%)	Meas2	Intensity (%)
4 nM	Peak1	537.8	100	430.7	100	5264	36.8	0.9	43.7
	Peak2	0	0	0	0	0.7	26.3	5295	30.6
	Peak3	0	0	0	0	161.6	22.5	152.2	1.7
	Z-average (d.nm)	803		891.3		1152		1169	
	PdI	0.534		0.708		1		1	
40 nM	Peak1	553.3	85.2	549	89.2	310.8	100	320.3	100
	Peak2	4697	14.8	4909	10.8	0	0	0	0
	Peak3	0	0	0	0	0	0	0	0
	Z-average (d.nm)	540.1		564.1		473.5		485.3	
	PdI	0.470		0.403		0.417		0.411	
400 nM	Peak1	277.3	76.3	351	95.7	1308	100	1277	100
	Peak2	1519	23.7	4460	4.3	0	0	0	0
	Peak3	0	0	0	0	0	0	0	0
	Z-average (d.nm)	268.9		256.5		2127		2205	
	PdI	0.353		0.324		0.416		0.414	

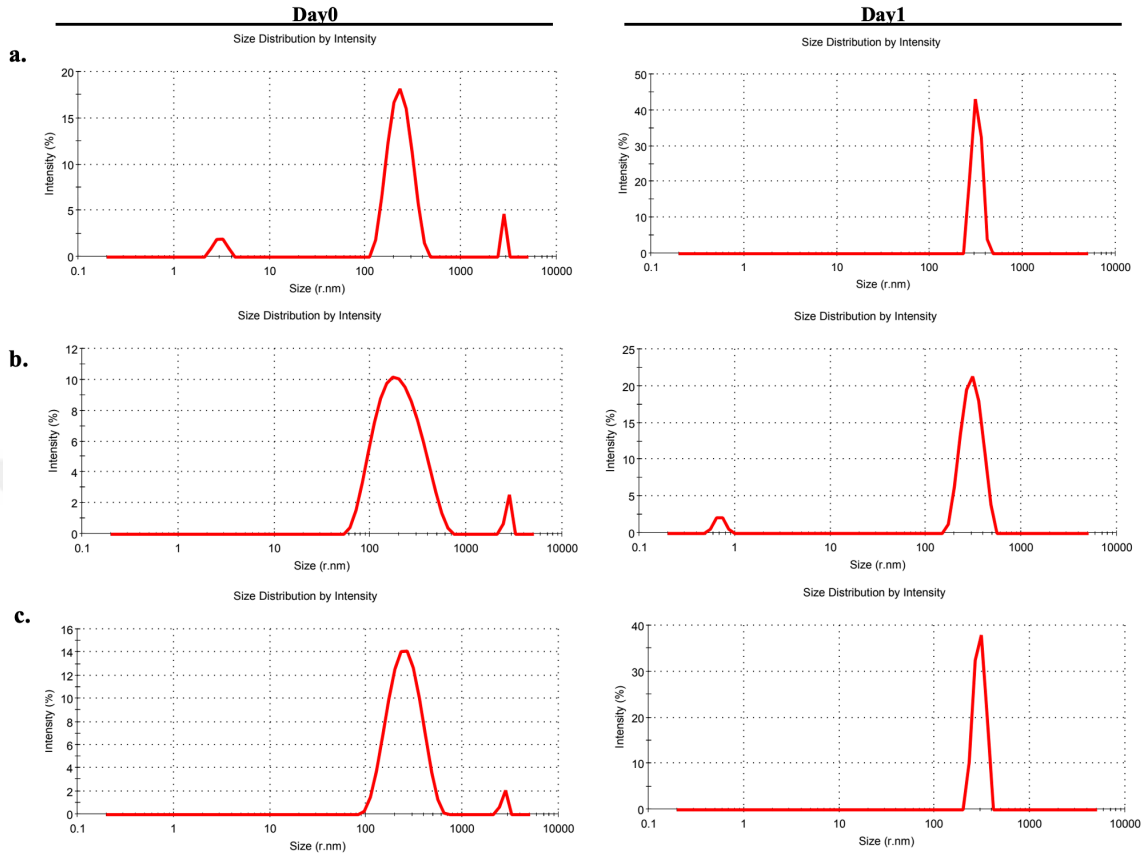


Figure G.1. Intensity distribution of CsgA samples with different aging time at a. 4 nM, b. 40 nM and c. 400 nM.

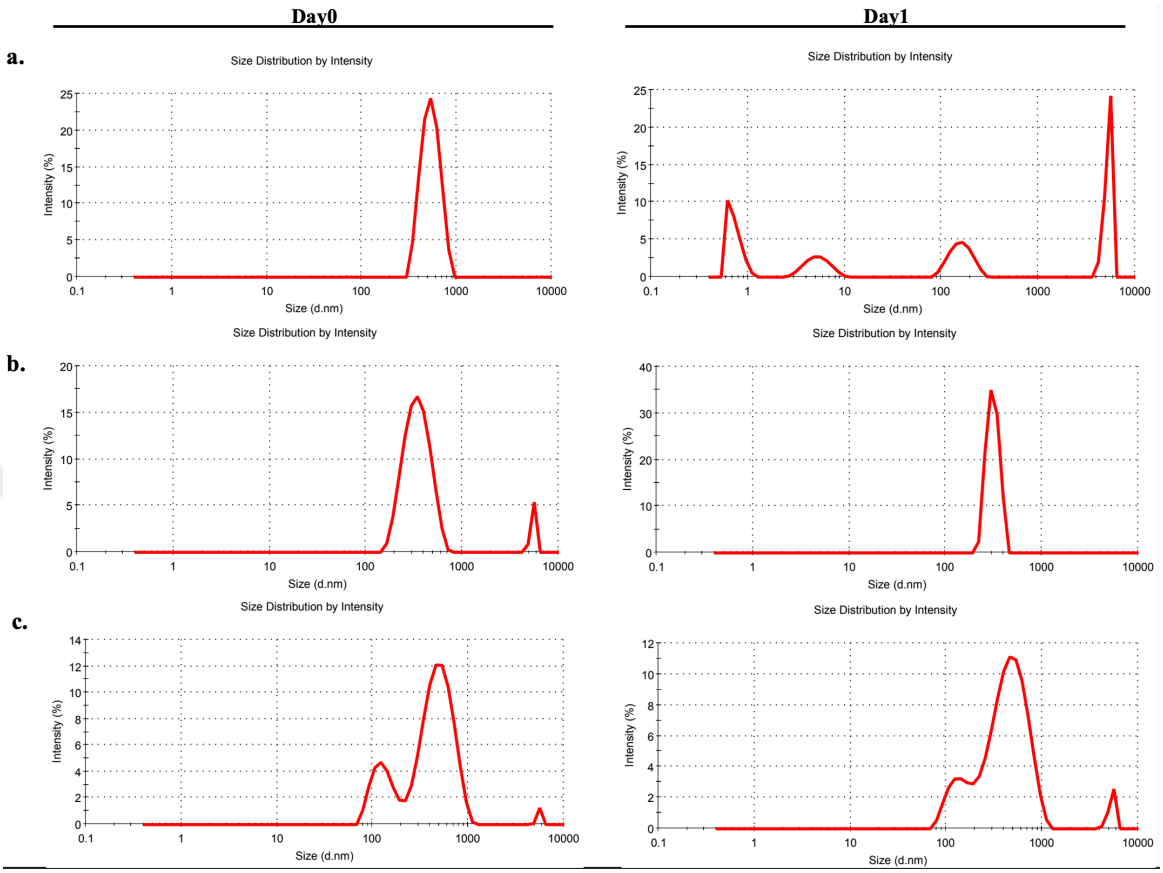


Figure G.2. Intensity distribution of CsgB samples with different aging time at a. 4 nM, b. 40 nM and c. 400 nM.

Table G.3. Desorption constant (k_d) of matured TasA, TasA D and TasA DP samples. Significance values are calculated by t-test, n=3.

	k_d (μM), mean ± SD			
	Day 1	Day 7	Day 14	Day 28
TasA	2.94 ± 0.19	5.22 ± 0.07	5.12 ± 0.54	3.39 ± 0.09
TasA D	3.83 ± 0.06	4.24 ± 0.13	4.10 ± 0.15	3.03 ± 0.14
TasA DP	1.48 ± 0.07	1.62 ± 0.07	1.70 ± 0.18	1.32 ± 0.06

Table G.4. Gibbs free energy (ΔG^o) calculations of matured TasA, TasA D and TasA DP samples. Significance values are calculated by t-test, n=3.

	ΔG^o (kcal/mol), mean ± SD			
	Day 1	Day 7	Day 15	Day 28
TasA	-3.28±0.02	-3.13±0.01	-3.13±0.03	-3.24±0.01
TasA D	-3.21±0.01	-3.18±0.01	-3.19±0.01	-3.27±0.01
TasA DP	-3.45±0.01	-3.43±0.01	-3.42±0.03	-3.48±0.01